Vapour Compression Cycle Technology for Aviation
Automated Design Methods and a New Experimental Setup

Ascione, F.

DOI
10.4233/uuid:39ef6ce1-d97f-4197-83ab-96d1e766de61

Publication date
2024

Document Version
Final published version

Citation (APA)
Ascione, F. (2024). *Vapour Compression Cycle Technology for Aviation: Automated Design Methods and a New Experimental Setup*. [Dissertation (TU Delft), Delft University of Technology]. Delft University of Technology. https://doi.org/10.4233/uuid:39ef6ce1-d97f-4197-83ab-96d1e766de61

VAPOUR COMPRESSION CYCLE TECHNOLOGY FOR AVIATION

AUTOMATED DESIGN METHODS AND A NEW EXPERIMENTAL SETUP

VAPOUR COMPRESSION CYCLE TECHNOLOGY FOR AVIATION

AUTOMATED DESIGN METHODS AND A NEW EXPERIMENTAL SETUP

Dissertation

for the purpose of obtaining the degree of doctor
at Delft University of Technology
by the authority of the Rector Magnificus, prof. dr. ir. T.H.J.J. van der Hagen,
chair of the Board for Doctorates
to be defended publicly on
Tuesday, 26th of November 2024 at 10:00 o'clock

by

Federica ASCIONE

Master of Science in Mechanical Engineering,
Universitá di Napoli Federico II, Scuola Politecnica e delle Scienze di Base, Italy
born in Scafati, Italy

This dissertation has been approved by the promotors.

Composition of the doctoral committee:

Rector Magnificus	chairperson
Prof. dr. ir. P. Colonna	Delft University of Technology, *promotor*
Dr. ir. C. M. De Servi	Delft University of Technology, *copromotor*
Independent members:	
Prof. dr. ir. W. De Jong	Delft University of Technology
Prof. dr. A. Bardow	ETH Zurich, Switzerland
Prof. dr. D. Laboureur	Von Karman Institute for Fluid Dynamics, Belgium
Dr. D. Zimmer	German Aerospace Centre, Germany
Dr. K. Dietl	Airbus Operations GmbH, Germany
Prof. dr. D. von Terzi	Delft University of Technology, reserve member

This research was performed at the Propulsion & Power group within the Flight Performance and Propulsion Section, Department of Flow Physics and Technology, Faculty of Aerospace Engineering. The work is part of the research project "Novel Electrically Driven Environmental Control System for Aircraft" (NEDEFA), supported by Aeronamic BV and by the Applied and Engineering Sciences Division (TTW) of the Dutch Organization for Scientific Research (NWO), Technology Program of the Ministry of Economic Affairs of the Netherlands (Grant No. 17091).

Keywords: Aircraft/Rotorcraft Environmental Control System, More Electric Aircraft, Vapour Compression Cycle, high-speed centrifugal compressor, system modelling, integrated design optimization, low-GWP refrigerants, IRIS setup.

Printed by: Ipskamp Drukkers B.V.

Cover design by: F. Ascione

ISBN 978-94-6366-964-1

---

[1] Author e-mail address: `fedy.asci@gmail.com`

A te, zia.
Ti porto nel cuore.

CONTENTS

SUMMARY

THE environmental emergency is one of the most critical challenges of modern times. The exponential increase of industrial activities is the primary cause of anthropogenic climate change, with negative consequences for the environment, society and economy. In the transport sector, decarbonization is the most significant challenge. In aviation, the environmental objectives are to halve international CO_2 emissions by 2030, and to reach net-zero carbon emissions by 2050. The achievement of these goals implies a step-change in the traditional practice of aircraft design, with many resources invested in research for promoting the use of fossil fuel-free propulsion systems and electrified auxiliary systems.

In this framework, the research presented in this dissertation is on methods for automated design optimization with applications to a novel electrically-driven Environmental Control System (ECS) for aircraft cabin cooling. The ECS is the main consumer of non-propulsive power onboard aircraft. The founding idea of the project, which has been carried out in collaboration with several companies, is to replace the traditional ECS equipping airliners, which is based on Air Cycle Machine (ACM) technology, with Vapour Compression Cycle (VCC) systems powered by high-speed centrifugal compressors. Work performed within this project demonstrated that such a VCC-based ECS can be more efficient and lighter than an ACM-based ECS in the case of mainstream passenger airplanes. The main goal of the research documented in this dissertation is to provide design methods and guidelines for the optimal design of aircraft ECS whose core is a VCC system powered by novel high-speed electrically-driven compressors and using low-Global Warming Potential (GWP) working fluids in place of the conventional R-134a refrigerant. Additionally, the study encompasses the analysis of the impact of the selected working fluid on the optimal design of the main system components, i.e., the heat exchangers and the centrifugal compressor. For this purpose, a novel integrated design optimization framework has been developed: it allows to perform the multi-objective optimization of the aircraft ECS across different points of the aircraft operating envelope. This method enables the concurrent automated optimization of thermodynamic cycle, preliminary component sizing and working fluid selection. Moreover, the successful application of the method to this complex case demonstrates that the approach is generally applicable to any thermal energy conversion system.

The method was applied to the design of the ECS of two different aircraft to demonstrate its capabilities: a large passenger rotorcraft and a single-aisle short-haul aircraft, i.e., the A320. Results show that it is possible to design an efficient VCC system for aircraft ECS that is powered by an electrically-driven centrifugal compressor and uses low-GWP refrigerants as working fluids. In particular, in the case of a small-capacity ECS for large rotorcraft, it was demonstrated that the use of high-molecular complexity refrigerants, such as haloolefins, enables the design of lighter and more efficient VCC systems if compared to the state-of-the-art. The test case of the airliner ECS provided the specifications to further develop and test the methodology: a so-called physics-based equation of state model was adopted for the computation of the thermodynamic properties of the working fluid. Molecular parameters allow to define the fluid, therefore they can be optimized as part of the global optimization of the design of the system. Parameters are constrained so as to define a realistic molecule, though non-existing, called *pseudo-fluid*. Actual working fluids whose molecular parameters are similar to those of the optimal *pseudo-fluid* are selected in a following step of the design procedure. Optimal working fluids are therefore natural refrigerants. The use of these working fluids with null GWP would reduce the environmental footprint of the considered environmental control systems, while enabling an (albeit small, in the considered case) reduction of specific fuel consumption.

Complementary to the numerical investigation, a novel experimental setup called IRIS (Inverse organic Rankine cycle Integrated System) was designed, realized and successfully commissioned at the Propulsion & Power laboratory of Delft University of Technology. The setup was conceived to enable testing and performance analysis of VCC-based aircraft ECS and to validate *in-house* software for system and components design. The setup hosts two main test sections: one to test compressors and another to test air-cooled condensers. The results of the commissioning show that it is possible to continuously operate the IRIS setup in steady-state conditions at temperature levels which are very close to those at the design point, thus achieving a Coefficient of Performance (COP) equal to 3.76±0.48.

SAMENVATTING

De milieucrisis is een van de meest kritieke uitdagingen van de moderne tijd. De exponentiële toename van industriële activiteiten is de belangrijkste oorzaak van antropogene klimaatverandering, met negatieve gevolgen voor het milieu, de samenleving en de economie. In de transportsector is decarbonisatie de grootste uitdaging. In de luchtvaart zijn de milieudoelstellingen om de internationale CO_2-uitstoot tegen 2030 te halveren en tegen 2050 volledig terug te brengen. Het behalen van deze doelen vereist een ommekeer in het ontwerp van toekomstige vliegtuigen. Hiervoor wordt groots geïnvesteerd in onderzoek omtrend fossielvrije voortstuwingssystemen en geëlektrificeerde hulpsystemen.

In dit kader richt het onderzoek, gepresenteerd in dit proefschrift, zich op methoden voor geautomatiseerde ontwerpoptimalisatie met toepassingen voor een nieuw elektrisch aangedreven Environmental Control System (ECS) voor de koeling van vliegtuigcabines. Het ECS gebruikt het meeste vermogen naast de voorstuwing aan boord van vliegtuigen. Het basisidee van het project, dat is uitgevoerd in samenwerking met verschillende bedrijven, is om het traditionele ECS dat airliners uitrust, gebaseerd op Air Cycle Machine (ACM) technologie, te vervangen door Vapour Compression Cycle (VCC) systemen. Deze worden aangedreven door hogesnelheids-centrifugaalcompressoren. Het werk uitgevoerd binnen dit project toonde aan dat een dergelijk VCC-gebaseerd ECS efficiënter en lichter kan zijn dan een ACM-gebaseerd ECS in het geval van reguliere passagiersvliegtuigen. Het hoofddoel van het onderzoek gedocumenteerd in dit proefschrift is om ontwerpmethoden en richtlijnen te bieden voor het optimale ontwerp van vliegtuig-ECS. De crux van dit systeem is een VCC-systeem, aangedreven door nieuwe hogesnelheids elektrisch aangedreven compressoren en gebruikmakend van lage Global Warming Potential (GWP) werkvloeistoffen in plaats van het conventionele R-134a koelmiddel. Daarnaast omvat de studie de analyse van de impact van de geselecteerde werkvloeistof op het optimale ontwerp van de belangrijkste systeemcomponenten, onder andere de warmtewisselaars en de centrifugaalcompressor. Hiervoor is een nieuw geïntegreerd ontwerpoptimalisatiekader ontwikkeld: het stelt in staat om de meervoudige optimalisatie van het vliegtuig-ECS uit te voeren over verschillende punten van de operationele envelop van het vliegtuig. Deze methode maakt de gelijktijdige geautomatiseerde optimalisatie van thermodynamische cyclus, voorlopige componentafmetingen en werkvloeistofselectie mogelijk. Bovendien toont de succesvolle toepassing van de methode op dit complexe geval aan dat de aanpak in het algemeen toepasbaar is op elk thermisch energieomzetsysteem.

De methode werd toegepast op het ontwerp van de ECS van twee verschillende vliegtuigen om de capaciteiten ervan aan te tonen: een groot passagiershelikopter en een kortafstandsvliegtuig, in dit geval de A320. De resultaten laten zien dat het mogelijk is om een efficiënt VCC-systeem voor vliegtuig-ECS te ontwerpen dat wordt aangedreven door een elektrisch aangedreven centrifugaalcompressor en lage-GWP koelmiddelen als werkvloeistoffen gebruikt. In het bijzonder werd in het geval van een kleinschalig ECS voor grote helikopters aangetoond dat het gebruik van koelmiddelen met hoge moleculaire complexiteit, zoals haloolefinen, het mogelijk maakt om lichtere en efficiëntere VCC-systemen te ontwerpen vergeleken met de hedendaagse opties. De toepassing van de ontwerpmethode in passagiersvliegtuigen leverde de specificaties op om de methodologie verder te ontwikkelen en te testen: een zogenaamd natuurkundig geinspireerd model van de toestandsvergelijking werd gebruikt voor de berekening van de thermodynamische eigenschappen van de werkvloeistof. Moleculaire parameters definiëren de vloeistof en kunnen daarom worden geoptimaliseerd als onderdeel van de globale optimalisatie van het systeemontwerp. Hierbij

werden de parameters beperkt om een realistisch, doch niet-bestaand, molecuul te definiëren: een zogenaamde pseudo-stof. Bestaande werkstoffen waarvan de moleculaire parameters vergelijkbaar zijn met die van het optimale pseudo-vloeistof worden geselecteerd in een volgende stap van de ontwerpprocedure. Optimale werkvloeistoffen zijn dus natuurlijke koelmiddelen. Het gebruik van deze werkstoffen met nul GWP zou de ecologische voetafdruk van de beschouwde milieubeheersystemen verminderen, met een bijkomend voordeel van vermindering brandstofgebruik (in elk geval in de huidige toepassing).

Aanvullend op het numerieke onderzoek werd een nieuwe experimentele opstelling genaamd IRIS (Inverse organic Rankine cycle Integrated System) ontworpen, gerealiseerd en met succes in gebruik genomen in het Propulsion & Power-laboratorium van de Technische Universiteit Delft. De opstelling was bedoeld om het testen en prestatieanalyse van VCC-gebaseerde vliegtuig-ECS mogelijk te maken en in-house software voor systeem- en componentontwerp te valideren. De opstelling herbergt twee hoofdtestsecties: één om compressoren te testen en een andere om luchtgekoelde condensors te testen. De resultaten van de ingebruikname tonen aan dat het mogelijk is om de IRIS-opstelling continu te bedienen in stationaire omstandigheden op temperatuurniveaus die zeer dicht bij het ontwerp liggen, met als gevolg een Coëfficiënt van Prestatie (COP) gelijk aan 3.76±0.48.

1

INTRODUCTION

> *We are living on this planet as if*
> *we had another one to go to.*
>
> Terri Swearingen

Climate change is an emergency. In the transport sector, decarbonization is a critical challenge. Aviation is calling for a step-change in aircraft design practice to reduce the environmental footprint of air traffic. The next generation of aircraft begins with the more electric aircraft, where all the sub-systems are electrified. Onboard aircraft, the non-propulsive systems are responsible for 5% of the total specific fuel consumption. Their electrification may considerably enhance the energy performance of aircraft.

The Environmental Control System (ECS) is the auxiliary system providing cabin air pressurization, passengers thermal comfort and avionics thermal management. The traditional ECS is the pneumatically-driven Air Cycle Machine (ACM). It is the main user of non-propulsive energy among all the aircraft subsystems. Recently, novel ECS architectures have been investigated to improve the system efficiency, e.g., the bleed-less ACM. Another option is the Vapour Compression Cycle (VCC) system, based on the inverse Rankine cycle concept. Its efficiency can be twofold the one of the ACM, independently from the aircraft flying condition, and it guarantees high cooling capacity even at ground operating conditions. The main challenge is the selection of a working fluid combining the requirements of allowing for good thermodynamic efficiency, low weight, small volume, environmental sustainability and safety.

This dissertation documents the development of a novel integrated design and optimization method and its application to a novel concept of aircraft ECS, whose core is an electrically-driven VCC system. The system features an oil-free high-speed centrifugal compressor, and light-weight compact heat exchangers. The design feasibility is tested by considering different low-GWP refrigerants as working fluid, as alternatives to the state-of-the-art R-134a. The test cases are a large helicopter and one of the most common passenger aircraft. A novel experimental test rig, called the Inverse organic Rankine cycle Integrated System (IRIS), has been designed and commissioned. It can accommodate compressors varying in capacity from 5 to 10 kW. The setup will be used for several purposes: system models validation, ECS performance analysis, compressor and condenser testing, control design and validation.

1.1. ENVIRONMENTAL EMERGENCY: A CALL FOR SUSTAINABLE AVIATION

Since the start of the Industrial Revolution, anthropogenic activities have had a dramatic impact on the Earth climate change. Thus far, the average global warming has reached 1.1 °C with respect to pre-industrial times [1]. NASA's Goddard Institute for Space Studies (GISS) announced that July 2023 was the hottest month ever recorded: 0.24 °C warmer than any other July in NASA's database, and 1.18 °C hotter than the average July between 1951 and 1980 [2]. The consequences of this phenomenon are evident worldwide, e.g., severe air temperature and humidity levels, extreme climate events, excessively dry lands and high risk of fire hazards with detrimental repercussions on eco-systems and socio-economic activities. In such a scenario, the scientific community is warning about the risks associated with global warming by defining 2 °C of warming as the critical threshold to avoid irreversible anthropogenic climate change consequences [3].

In response to this emergency, in 2015, 196 parties of the United Nations (UN) signed the Paris Climate Agreement at the Climate Change Conference COP 21. This international treaty set the collective goal *"to hold warming well below* 2 °C, *with efforts to limit warming to* 1.5 °C *above pre-industrial averages"* [4]. The need to accelerate the actions towards the goals of the Paris Agreement was recognised at the 26th UN Climate Change Conference COP 26 held in Glasgow in 2021. Despite the approved texts have been defined as *"a compromise"* by the UN secretary, they contain some important steps in cutting global Greenhouse Gas (GhG) emissions. In the transport sector, decarbonization was recognized as an urgency. The common goal is to promote the development of alternative low-emission and fossil fuel-free technologies. In this regard, the first milestone is the electrification of road transport by 2035 in leading markets of over 30 countries [5]. In 2023, at the COP28, the International Civil Aviation Organization (ICAO) and its member states agreed on a strategy to facilitate the global scale-up in the development, production and deployment of sustainable aviation fuels and other aviation cleaner energies. The long-term environmental objectives are the 50% reduction of international aviation CO_2 emissions by 2030, and the achievement of net-zero carbon emissions by 2050 [6]. In 2020, the countries of the European Union (EU) signed the European Green Deal. The document introduced new policies to achieve the twofold objective of reducing by 55% the net GhG emissions by 2030, compared to 1990 levels, and becoming the first world climate-neutral continent by 2050. One of the ambitions is to force a rapid acceleration to zero-emission mobility by cutting 90% of CO_2 emissions by 2050 [7]. The emissions of CO_2 and non-CO_2 GhG emissions, i.e., NO_x, H_2O, from the aviation sector are considered responsible for 3.5% of net anthropogenic effective radiative forcing [8]. In the EU, aviation is recognized as the second biggest source of transport GhG emissions after road transport, accounting for 13.9% of the total transport emissions [9]. The environmental impact of this sector has been significantly growing until 2019, when the COVID-19 pandemic caused a decline in air transport demand. Nowadays, the sector has resumed its growth even faster and emissions are expected to double or even triple in the coming 30 years [10]. Decarbonization of aviation is clearly the most challenging endeavor from a technological point of view.

In view of these considerations, actions have been taken to face the increasing air transportation demand. The ICAO agreed on a global market-based measure known as the Carbon Offsetting and Reduction Scheme for International Aviation (CORSIA) to counterbalance the growth of airlines CO_2 emissions after 2020 [11]. The Advisory Council for Aeronautic Research in Europe (ACARE) published a strategic roadmap for aviation research in Europe, known as FlightPath 2050. Among the 5 goals outlined in the report, the long-term environmental objective is threefold: reduction by 65% of noise emissions at cruise conditions, 90% cut of NO_x emissions and 75% reduction in CO_2 emissions per passenger km, relative to a typical new aircraft in 2000 [12]. Therefore, a call for a step-change in the traditional aircraft design practice is imperative. Novel technologies, sustainable low-carbon fuels, more efficient aircraft operations and improved infrastructures are pivotal to reducing the environmental footprint of aviation. In this regard, the aerospace industry and academia have oriented significant research efforts toward aircraft electrification to reduce global weight and specific fuel consumption. The next generation aircraft begins with the More Electric Aircraft (MEA), where only the sub-systems are electrified. The Hybrid Electric Aircraft (HEA) and the All Electric Aircraft (AEA) will follow, featuring hybrid and fully electrified propulsion systems, respectively [13].

In conventional civil aircraft, gas turbines do not only provide thrust, but a part of their mechanical power output is used to power auxiliary sub-systems. Hence, the energy provided by the engines is converted into other four energy sources, e.g., electric energy for avionics, lighting and entertainment; pneumatic energy for the Environmental Control System (ECS) and the Wing Ice Protection System (WIPS); hydraulic energy to operate the actuation systems; and mechanical energy for fuel and oil pumping (Fig. 1.1 (left)) [14]. The non-propulsive systems are responsible for approximately 5% of the total specific fuel consumption. Their electrification may provide a considerable reduction of the aircraft fuel consumption [15]. This paradigmatic change of non-propulsive equipment technology is at the basis of the MEA concept. Thanks to the progress in power electronics technology, electric energy can be stored and distributed throughout the aircraft (Fig. 1.1 (right)). Examples of MEA have already been launched on the market. For instance, the Airbus A380, which was certified in 2007, features partially electrified flight control systems. Similarly, the Boeing 787-8 Dreamliner, launched in 2011, utilizes electrified versions of the traditional WIPS and ECS [15].

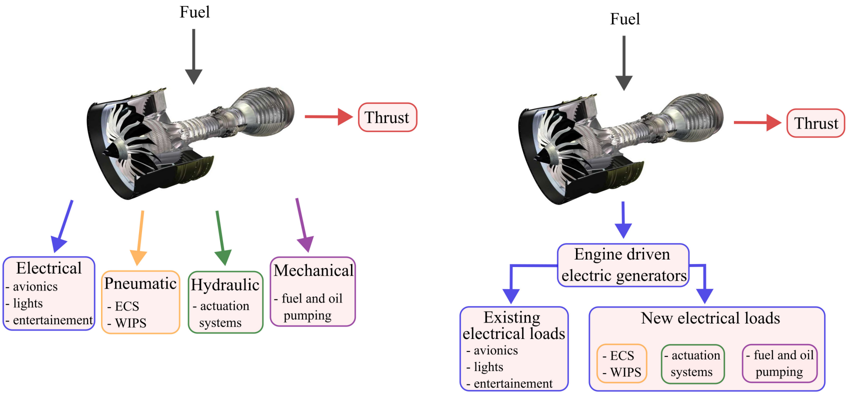

Figure 1.1.: Left: conventional aircraft power distribution. Right: More Electric Aircraft power distribution [14]

The ECS is the auxiliary system providing cabin air pressurization and passengers thermal comfort. The ECS must ensure the correct supply of air and temperature control of cabin and cockpit, even for the most critical environmental conditions, not only for passengers comfort but also for avionics reliability. The traditional ECS is based on the pneumatically-driven Air Cycle Machine (ACM), whose thermodynamic cycle derives from the reverse Joule cycle concept for open systems. It is currently the main onboard user of non-propulsive energy [16], accounting for 3-5% of the total energy usage among all the aircraft subsystems [17]. Therefore, novel and optimized ECS architectures have been investigated to improve the efficiency of this sub-system, such as the bleed-less ACM installed onboard the Boeing 787-8 Dreamliner [18], and the combined ACM and electrically-driven Vapour Compression Cycle (VCC) system [19].

1.2. NOVEL ENVIRONMENTAL CONTROL SYSTEMS FOR THE NEXT-GENERATION AIRCRAFT

Throughout the flight envelope, air conditions undergo significant variations, ranging from ambient conditions on the ground to rarefied and cold air during cruise. Therefore, the aircraft must be provided with a proper Heating, Ventilation and Air Conditioning (HVAC) system to guarantee comfort to the aircraft occupants and to ensure the avionics correct functionality. Onboard aircraft, this system is known as ECS. It is responsible for the regulation of air temperature and humidity levels in the cabin, pressurization during flight, and air ventilation for acceptable air quality [20]. The conventional ECS onboard large aircraft is the based on the ACM, whose working principle is the inverse Brayton thermodynamic cycle. In the most common system configuration, the air is bled from the engine compressor via a flow control valve at approximately 250 kPa. Its temperature is higher than 200 °C, hence, a precooler is used to lower the air temperature to approximately 180 °C [21].

In recent times, considerable research efforts have been dedicated to reducing the environmental impact of pneumatic ACM systems. As a result, various novel technologies have been developed. One of the solutions, currently installed onboard the Boeing 787-8 Dreamliner, is the bleedless ACM [18]. The bleedless ACM configuration allows for a 5% fuel saving (approximately 5000 kg) with respect to the bleed-air system [21].

Figure 1.2 shows a simplified process flow diagram of the system. Figure 1.3 shows the associated T–s thermodynamic charts depicting the processes undergone by the working fluid (air) for the case of aircraft at ground (Fig. 1.3, left) and at cruise (Fig. 1.3, right) conditions. Instead of achieving air pressurization with air bled from the engine compressor, high pressure air is obtained with an independent electrically-driven compressor. Moreover, due to the low air temperature level at the inlet of the system, a precooler is no longer required. After being compressed, air goes through the inverse Brayton cycle: it enters the primary heat exchanger (PHEX), where it is further cooled; afterwards, a compressor increases the air temperature to almost 210 °C; then, in the secondary heat exchanger (SHEX), the air temperature is lowered down to 100 °C before entering the turbine, where the flow is expanded to the target temperature and pressure. Finally, the air is sent to the mixing manifold, where it is blended with the recirculated air from the cabin.

In the case of ground and low-altitude operating conditions, a dehumidification system is activated to remove the water condensate from the cabin air stream. A condenser removes the moisture from the high-pressure air upstream of the turbine. The moisture droplets are collected and then sprayed in the ram air stream to lower the temperature and enhance the heat transfer efficiency. The ram air is used as a heat sink in both the PHEX and the SHEX, which are typically compact plate and fins cross-flow heat exchangers (HEXs). A fan sucks the ram air from the environment in the diffuser, flowing through the two system HEXs and finally, it is discharged to the environment through an exhaust nozzle [19]. The EASA CS-25 [22] prescribes that at least 6 $\mathrm{g \cdot s^{-1}}$ of fresh air per passenger are supplied. Therefore, the ram air mass flow rate is typically twice or three times the mass flow rate delivered to the cabin. Normally, two air conditioning packs are installed on the aircraft to provide redundancy in case one pack fails.

An ECS configuration alternative to the bleedless ACM is based on the inverse Rankine thermodynamic cycle, and it is known as the VCC system. The VCC system is already employed for the air conditioning system onboard business jets and helicopters [23]. This

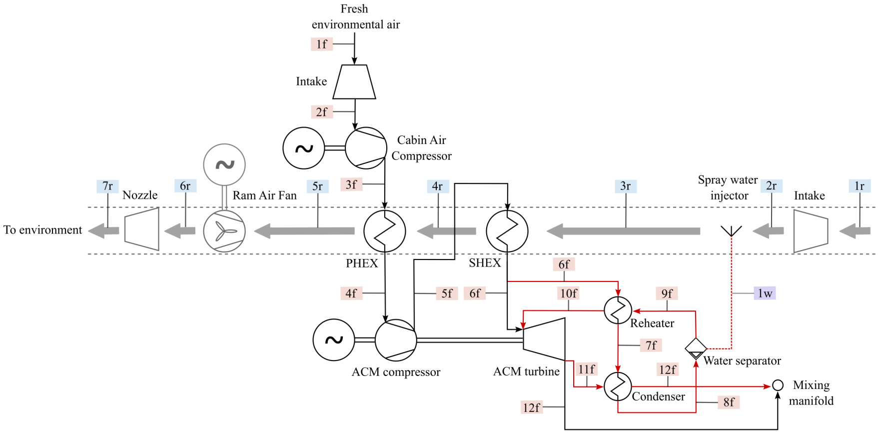

Figure 1.2.: Simplified process flow diagram of the aircraft ECS based on the bleedless ACM configuration for ground (—) and cruise (—) operating conditions.

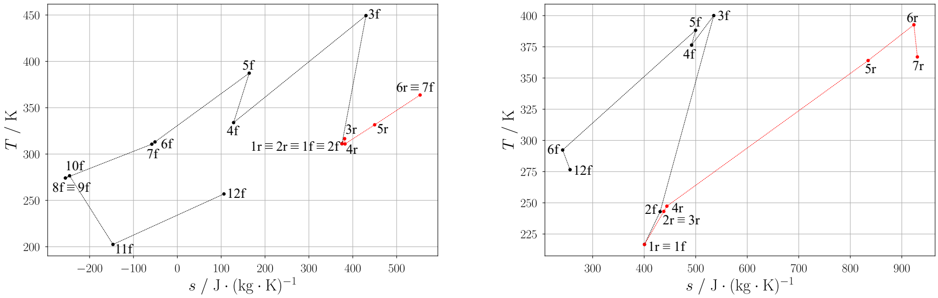

Figure 1.3.: T-s thermodynamic charts illustrating the processes undergone by air through the ram air duct (—) and the cabin air (—) streams at ground (left) and cruise (right) operating conditions. The numbering of the state points refers to Fig. 1.2.

system was employed onboard large passenger aircraft, such as the Boeing 707, during the early 1960s. Nevertheless, the use of such a technology was limited because of the heavy and low-efficient refrigerant compressors available at the time [24]. This system is based on the same working principle as those used for refrigeration in the food industry and domestic or industrial air conditioning. The cooling capacity of the system depends on the aircraft type and operating point. For instance, at the design point, a cooling capacity of approximately 12 kW per ECS pack is considered for the case of helicopter ECS. In contrast, the cooling capacity of each ECS of a passenger aircraft, like the A320, is almost 70 kW.

Figure 1.4 shows a simplified process flow diagram of a two-compression stages VCC system. Figure 1.5 shows the associated T-s thermodynamic charts displaying the processes undergone by the refrigerant (top of Figure 1.5), and those related to the air streams for the case of aircraft at ground (bottom of Figure 1.5, left), and at cruise (bottom of Figure 1.5, right) conditions.

The environmental air enters through an air scoop and, in case of cruise conditions, is

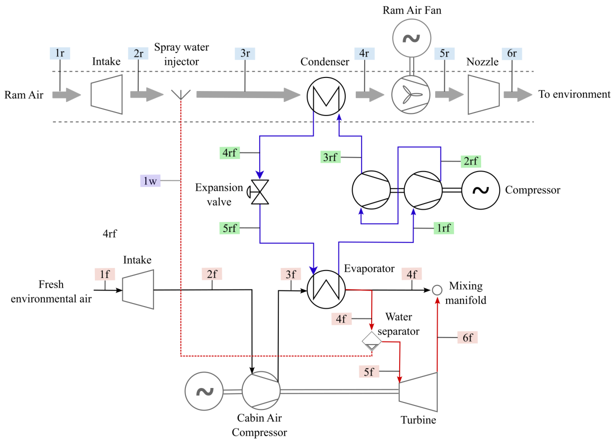

Figure 1.4.: Aircraft ECS based on a two-compression stages VCC system. The process flow diagram changes depending on the operating conditions: ground (—) and cruise (—) operating conditions.

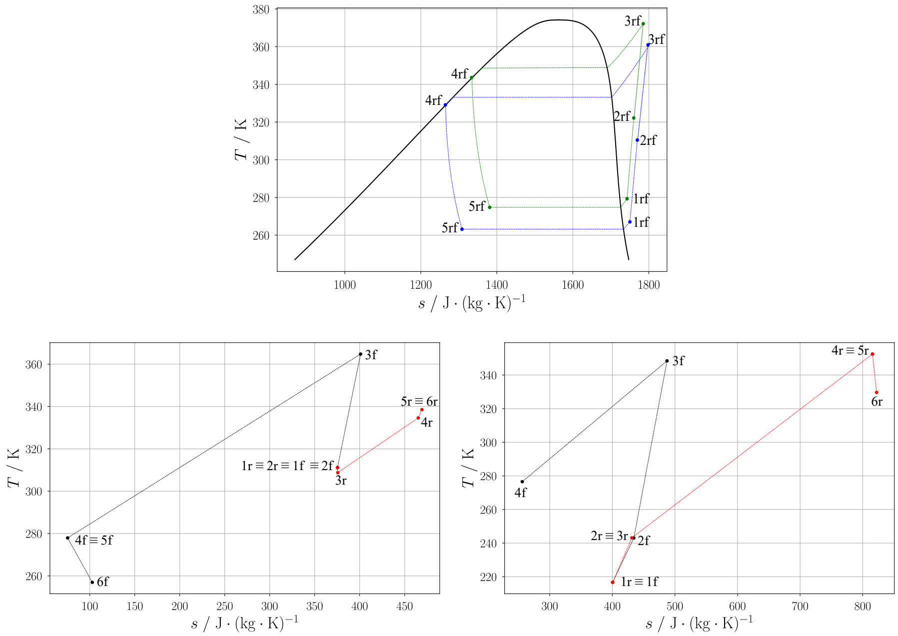

Figure 1.5.: Top: T-s thermodynamic charts depicting the thermodynamic cycle for the ground (—) and the cruise (—) aircraft operating conditions. The working fluid is R-134a. Bottom: T-s thermodynamic charts related to the ram air (—) and cabin air (—) streams at ground (left) and cruise (right) operating conditions. The numbering of the state points refers to Fig. 1.4.

pressurized by the cabin air compressor. If the aircraft is on the ground or at low altitude, the air directly enters the duct leading to the evaporator where it cools down to the desired temperature before entering the mixing manifold. Thanks to its low normal boiling point, the refrigerant completely evaporates within the evaporator before entering the compressor suction port. The turbomachinery is designed to match the target temperature lift between condensation and evaporation at the most demanding operating condition of the ECS. The ram air serves as the heat sink for the condenser, where the refrigerant is cooled down from superheated vapour states to subcooled liquid states. Once the refrigerant has transitioned into the subcooled liquid phase, it is throttled through an expansion valve until it reaches the evaporation pressure. In the case of ground operation or low flying altitude, a dehumidification system is required to achieve prescribed comfort conditions of the cabin air. The cabin airstream flows over the evaporator coil, where it is cooled down to a temperature lower than that of the dewpoint. The condensate is then drained out and sprayed into the ram air stream.

The Coefficient Of Performance (COP) of the VCC system can be enhanced by adopting more complex system configurations. In the case of high-temperature lift, a two-stage compression VCC system is commonly employed. Furthermore, an additional HEX, known as economizer or intercooler, can be installed to further subcool the refrigerant at the outlet of the condenser. This allows for a reduction of the refrigerant vapour quality at the evaporator inlet. In this way, given the system cooling capacity, the refrigerant mass flow rate required in the system is lower with a beneficial effect on both the compressor power demand and the evaporator size [25]. Figure 1.6 shows a simplified process flow diagram of a two-compression stages VCC system with intercooler. Figure 1.7 shows the associated T-s thermodynamic charts displaying the processes undergone by the refrigerant (top of Fig. 1.7), and those related to the air streams for the case of aircraft at ground (bottom of Fig. 1.7, left), and at cruise (bottom of Fig. 1.7, right) conditions.

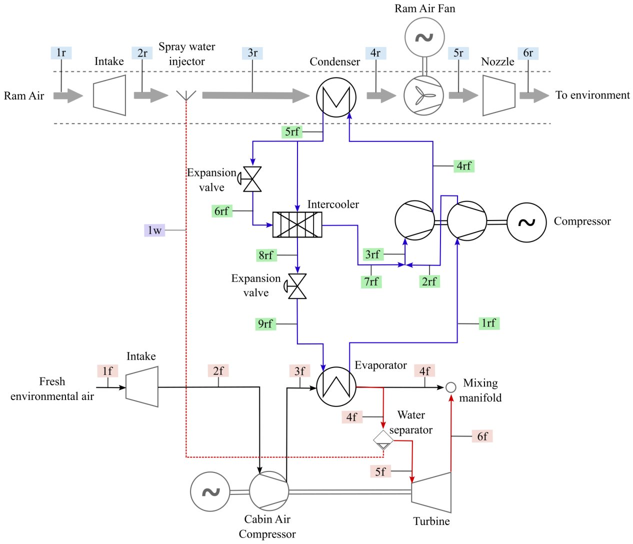

Figure 1.6.: Aircraft ECS based on a two-compression stages VCC system with intercooler. The process flow diagram changes depending on the operating conditions: ground (—) and cruise (—) operating conditions.

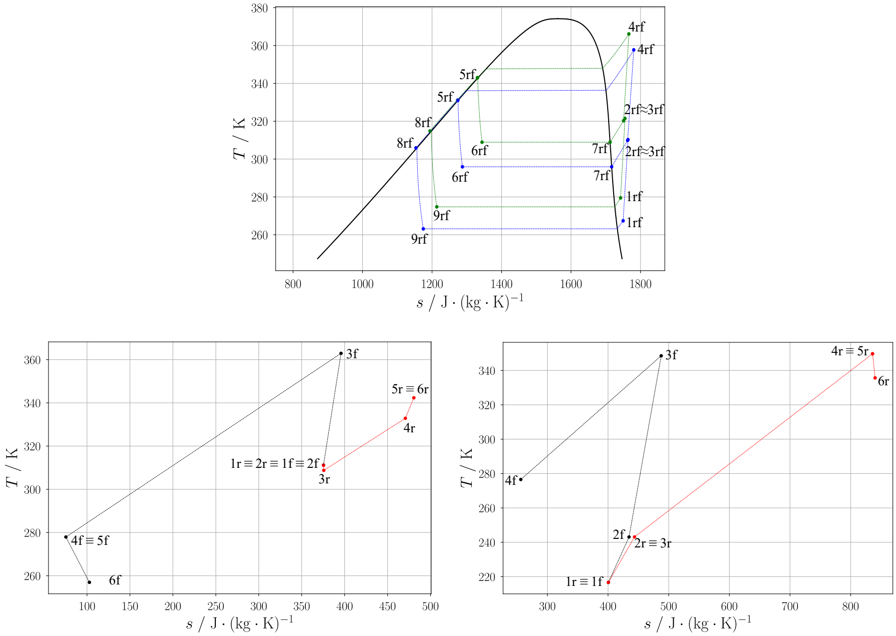

Figure 1.7.: Top: T-s thermodynamic charts depicting the thermodynamic cycle for the ground (—) and the cruise (—) aircraft operating conditions. The working fluid is R-134a. Bottom: T-s thermodynamic charts related to the ram air (—) and cabin air (—) streams at ground (left) and cruise (right) operating conditions. The state points refer to Fig. 1.6.

In 2016, Airbus patented a novel ECS which combines the features of both the ACM and the VCC, hereinafter referred to as hybrid ACM-VCC system [26, 27]. Figure 1.8 shows a simplified process flow diagram of the system architecture. The air enters the inlet scoop at ambient conditions. In the case of cruise conditions, it is first compressed by the cabin air compressor and then cooled down in the PHEX. Otherwise, the air is directly compressed by the ACM compressor. Then, a reheater is used to cool down the air before it reaches the SHEX. In the case of ground operation or low flying altitude, further cooling is provided by the evaporator of the VCC system. Here the air is also dehumidified. In this case, the VCC compressor is single-stage.

In the literature, the ACM is presented as the more robust solution for passenger aircraft ECS and current practice substantiates this evaluation. However, the novel ECS solutions described thus far offer many advantages, and research efforts to study their potential and to overcome any technological challenge are arguably justified: the VCC system is characterized by a COP values which can be twice those of the ACM, independently from the flying condition of the aircraft. Furthermore, the use of a VCC system guarantees high cooling capacity even at ground operating conditions. The aspects deserving investigation are those related to the choice of the working fluid, which must satisfy the requirements of enabling the achievement of low fuel weight penalty, of environmental sustainability and safety [25]. In the case of the hybrid ACM-VCC solution, the design cooling capacity is split between the ACM and the VCC systems. Thus, it enables the use of smaller HEXs, which do not require to be

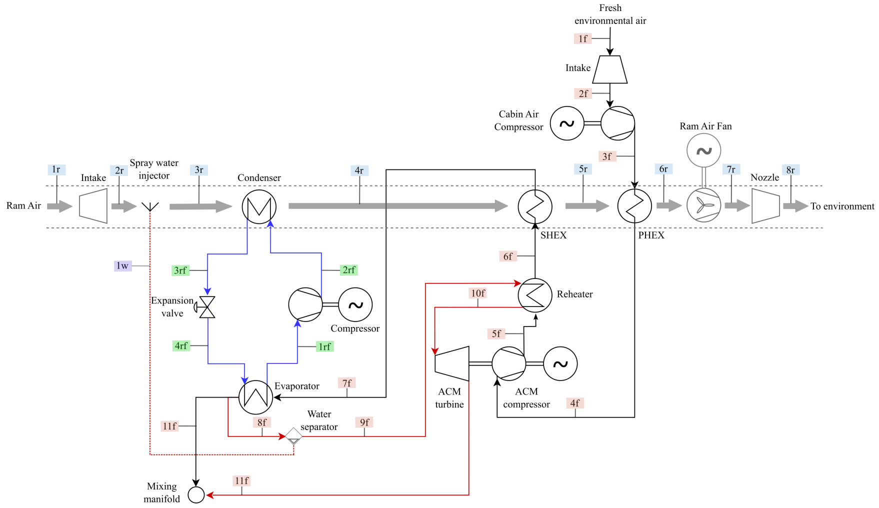

Figure 1.8.: Simplified process flow diagram of the aircraft ECS based on the hybrid ACM-VCC configuration for ground (—) and cruise (—) operating condition.

oversized to correctly operate in the most demanding operating conditions. Furthermore, the combined use of the evaporator and the ACM turbine for cabin air cooling allows overcoming the limitations on the evaporator operating temperature level. The main drawbacks are system complexity and possibly larger system weight [27].

1.3. MOTIVATION AND SCOPE

The work documented in this thesis is conducted within the framework of a research project concerning the assessment of a novel concept of aircraft ECS. The idea is that the efficiency and the environmental footprint of the ECS can be improved by recurring to an electrically-driven VCC system configuration in place of the currently adopted ACM. This system is already installed onboard business jets and helicopters, e.g., Piaggio Avanti, Socata TBM 850, Socata TBM 700, Citation Mustang, Phenom 300, and Cessna Citation Jet [23, 25]. The idea of this study is to prove the feasibility of this technology if applied to airliners, thus considerably impacting the emissions reduction that are now mandatory for the avaition sector. The test case is a single-aisle, short-haul passenger aircraft, e.g., the Airbus A320. Furthermore, the proposed VCC system features two main novelties: i) the prime mover is an electrically-driven high-speed and oil-free centrifugal compressor, in place of the traditional mechanically-driven scroll compressor, ii) the working fluid is a low-Global Warming Potential[1] (GWP) refrigerant, thus a potential replacement for the state-of-the-art R-134a fluid.

The assessment of novel aerospace systems is subjected to three main phases: system requirements definition, design and simulations, and ground testing. Modern aviation relies on modular software simulation tools based on component models which are assembled together to form systems of different degrees of complexity. Performing system simulations over the entire aircraft operating envelope is a common practice. The objective of these simulations is usually to minimize the specific fuel consumption or to maximize system efficiency while

---

[1] The author refers to the index GWP$_{100}$, which indicates the environmental impact of a substance compared to that of the CO$_2$ over 100 years.

minimizing drag penalties and system weight. Furthermore, the optimal system design must obey safety regulations. This translates into a complex multi-point and multi-objective optimization problem. The last design phase is the system ground testing. The purpose is to verify that the system is compliant with the design requirements and analyse the performance in *off-design* conditions. The experimental data are generally used to validate the numerical models and improve the robustness of the computer programs used for system simulations.

The aircraft ECS is a complex system, whose design should rely on a sizing and simulation framework capable of simultaneously optimizing the thermodynamic cycle and the preliminary design of components, for both *on-design* and *off-design* operating conditions. The documented first attempt at developing and testing such a complex methodology was conducted by Vargas and Bejan [28], who proposed an integrated system optimization method for the ECS of commercial aeroplanes. Both the cycle operating parameters and the preliminary design of the HEXs were considered within the optimization procedure which aimed at minimizing the exergy destruction associated with performance and weight of the ECS. This approach not only allows for the definition of an optimal system operating point but also for the design analysis of the most critical components, e.g., the HEXs. Using the same approach, Pérez-Grande and Leo [29] described the results of a multi-objective optimization of a bleed-less ACM. The functions to be minimized were the system weight and the entropy generation. However, the design optimization method is limited solely to the geometrical design and thermodynamic characterization of the two HEXs. Finally, Sielemann *et al.* [30] described an integrated design optimization methodology for an unconventional aircraft ECS architecture, coupling the features of the ACM and of the VCC systems. The system is optimized by accounting for the minimization of two objective functions, namely the additional specific fuel consumption and the weight associated with the ECS at cruise conditions. The authors draw conclusions about the influence of the HEXs geometrical design on the specific fuel consumption related to the ECS. However, the study neglects the preliminary design of turbomachinery components and the analysis of its impact on the overall system performance and design.

The state-of-the-art refrigerant for aircraft ECS is R-134a [25]. This refrigerant belongs to the class of the hydrofluorocarbons (HFCs). R-134a is characterized on the one hand by null Ozone Depletion Potential (ODP), and on the other hand by GWP equal to 1300. The global warming emergency has pushed for the global deployment of regulations on the use of Fluorinated greenhouse gases (F-gas) [31, 32]. The target is to gradually phase out the high-GWP HFCs from the market by encouraging the use of alternative substances, known as *forth-generation refrigerants*, i.e., hydrofluoroolefins (HFOs), hydrochlorofluoro-olefins (HCFOs), natural refrigerants and blends. All these compounds are characterized by similar environmental properties, i.e., null ODP and GWP lower than two. The selection of alternative working fluids depends on both the application and the combination of their chemical, environmental, thermodynamics, and safety properties. For these reasons, a few recent studies concern the transition to low-GWP refrigerants for VCC systems, investigating the use of HFOs, HCFOs, natural refrigerants, or blends, as replacements for the traditional HFCs. Roy and Mandal [33] carried out a thermo-economic optimization of a single-stage VCC system, by evaluating the possible use of three refrigerants: R-152a, isobutane (R-600a) and R-1234ze. On the one hand, their results show that R-152a is the best option in terms of system energy efficiency. On the other hand, if the environmental impact is accounted for, the other two working fluids are more appealing alternatives. de Paula *et al.* [34] investigated the optimal design of a VCC system for air conditioning and chilled water, featuring two coaxial HEXs and a reciprocating compressor. They tested both natural and synthetic refrigerants. The environmental, energy, and exergy analysis of the results shows that the system performance is comparable if R-1234yf or R-134a are the working fluids. Propane (R-290) allows for the best system performance, as well as the smallest refrigerant charge within the refrigeration loop.

Mateu-Royo *et al.* [35] performed a numerical study on the best system configuration for high-temperature heat pumps for industrial waste heat recovery, taking into account the effect of the working fluid. They investigated the effect of using nine low-GWP refrigerants as working fluid alternatives to R-245fa. R-1233zd(E) and R-1224yd(Z) are identified as the refrigerants enabling the best trade-off between system efficiency and volumetric heating capacity. Yan *et al.* [36] investigated the design and performance of high-temperature heat pumps for residential use, by considering five low-GWP refrigerants as replacements for R-134a. From the numerical analysis of the system performance, it resulted that R-1234ze(E) is the best working fluid candidate. The use of this refrigerant was then tested in the experimental setup implementing a single-stage VCC system. The results show that using R-1234ze(E) as the working fluid leads to a larger compressor capacity as compared to R-134a, and it allows for a significant increase in the system COP at high temperatures. However, none of these studies concerns the use of VCC system for airborne application.

Despite the large number of numerical works concerning innovative aircraft ECS architectures, only a few examples of experimental investigations are available in the literature. Zhao *et al.* [37] carried out an experimental study on the performance of a bootstrap ACM with high-pressure water separation. They simulated different flight conditions to evaluate the *off-design* performance and the dynamic response of the system to test its efficiency and reliability. Chowdhury *et al.* [38] document the design and realization of an experimental ground test facility reproducing the bleedless ACM of a Boeing 737-400. The system was tested to simulate various operating conditions. The outcome of the experimental campaign was used for the validation of the physics-based component models implemented into a commercial software [39]. An example of VCC system for aircraft applications is proposed by Mancin *et al.* [40]. They describe a mini-VCC system for avionics thermal management. The system is designed for a cooling capacity ranging from 37 W to 374 W, and the working fluid is R-134a. The condenser is water-cooled, the compressor is oil-free, and a cold plate is used to meet the requirements of compactness and reliability.

The main documented studies about the use of a VCC system in an ECS concern helicopters. The considered working fluid is R-134a [41, 42]. However, the latest literature offers a few examples of research work about the use of this technology for passenger aircraft thermal management. Ablanque *et al.* [43] developed a Modelica library for steady-state and transient simulations of VCC systems for aircraft ECS. Hu *et al.* [44] numerically investigated the use of VCC technology as a supplementary cooling system for the cooling of galley carts and avionics. Xu *et al.* [45] developed a model to study a cabin heating system in which a VCC system uses engine lubrication oil as the heat source to recover thermal energy. Finally, Tayfun *et al.* [46] performed a numerical and experimental study on the performance of a VCC system for avionics thermal management. The electronic components are located in an unventilated bay, where the maximum air temperature reaches 50 °C.

From the literature review presented thus far, it is possible to conclude that despite the large number of numerical investigations about aircraft ECS optimization, a few works explore the use of the VCC technology. Furthermore, in the studies regarding the integrated system optimization and accounting for the simultaneous optimization of thermodynamic process and system components, the analysis is usually limited to the preliminary design of the HEXs, while the turbomachinery is simply treated by assuming constant values of isentropic efficiency to roughly determine the system power consumption [28–30]. Few research studies have addressed the design of centrifugal compressors for VCC systems operating with low-GWP refrigerants [47, 48]. If working fluid selection is included in the VCC system analysis, investigations are limited to studies considering just two working fluids belonging to the class of the HFOs, i.e., R-1234yf and R-1234ze(E), treated as drop-in replacements of R-134a [49, 50]. Furthermore, there is a lack of experimental investigation on VCC systems powered by high-speed centrifugal compressors and tailored for airborne cabin cooling applications.

The objective of the research documented in this dissertation is to bridge these knowledge gaps. The investigation concerns the feasibility and performance of an ECS based on the electrically-driven VCC system adopting low-GWP refrigerants, featuring an oil-free high-speed centrifugal compressor and compact HEXs. The selected optimization test cases are the ECS of a large helicopter (20 passengers and 2 pilots) and that of a common passenger aircraft (Airbus A320). An in-house integrated system design optimization framework has been developed. The software allows to simultaneously optimize the working fluid, the thermodynamic cycle, and the preliminary design of all the main system components, i.e., the HEXs, the piping and the centrifugal compressor. A novel experimental test rig, called the Inverse organic Rankine cycle Integrated System (IRIS), has been designed and commissioned at the Propulsion & Power Laboratories of the TU Delft Aerospace Engineering faculty. The setup was conceived for the performance analysis and validation of VCC systems (the capacity of the system is in the range typical of helicopter ECS). The facility consists of a single-stage compression refrigeration cycle. A single Balance of Plant (BoP) was designed to accommodate two test sections: a piston compressor testing setup and an air-cooled condenser test bed. The working fluid is the low-GWP refrigerant R-1233zd(E). The aim is to investigate the performance of the system, as well as the aerothermal characterization of the condenser and the performance maps of the compressor. Furthermore, the data will be used for the validation of the *in-house* numerical models. The test rig is conceived to accommodate, in the future, an oil-free and electrically-driven high-speed centrifugal compressor designed in collaboration with Aeronamic.

1.4. OUTLINE

This dissertation is divided into two parts. Part I concerns the design optimization methods developed for passenger aircraft and high-payload rotorcraft ECS. Part 2 documents the design, realization and commissioning of the IRIS setup. The content is organized into seven chapters, whose subjects are summarized as follows.

Chapter 2 provides a detailed overview of the electrically-driven VCC system for aeronautical applications. A detailed description of the cutting-edge technology of the system, i.e., the compact HEXs, and the high-speed and oil-free centrifugal compressor, is also provided. An extensive review of alternative low-GWP refrigerants and their properties is presented.

PART I: Integrated design optimization methods for novel aircraft ECS

Chapter 3 describes numerical models and methods developed for VCC-based aircraft ECS system simulations. The first part of the chapter includes a detailed description of the component models. The second part illustrates three different integrated design optimization methods used for VCC system analysis. Methodological differences and pros and cons of each method are discussed, focusing on robustness and computational cost.

Chapter 4 concerns the effect of adopting low-GWP refrigerants as working fluids on the design optimization of novel helicopter ECS based on this VCC system technology. First, a detailed description of the helicopter ECS is provided, highlighting the design novelties of the new technology with respect to the traditional one. Then, the results of a multi-objective optimization considering a new working fluid as alternative to the state-of-the-art R-134a is reported.

Chapter 5 documents the multi-point multi-objective integrated design optimization of VCC-based aircraft ECS using low-GWP working fluids. The optimal working fluid is identified by optimizing the PC-SAFT parameters of the medium. Both natural and synthetic refrigerants are analysed. The results are compared with those computed in case of R-134a is the working fluid.

PART II: Inverse organic Rankine cycle Integrated System (IRIS) setup.

Chapter 6 documents the detailed design and commissioning of the Inverse organic Rankine cycle Integrated System (IRIS) setup. Both the hardware and the software are described. Then, the facility operation and commissioning are discussed.

Chapter 7 provides an outline of the original contributions of the research, together with an overlook about limitations and potential future works.

NOMENCLATURE

Acronyms

ACARE	Advisory Council for Aeronautic Research in Europe
ACM	Air Cycle Machine
AEA	All Electric Aircraft
BoP	Balance of Plant
CO_2	Carbon dioxide
COP	Coefficient Of Performance
CORSIA	Carbon Offsetting and Reduction Scheme for International Aviation
ECS	Environmental Control System
EU	European Union
F-gas	Fluorinated greenhouse gases
GISS	Goddard Institute for Space Studies
GhG	Greenhouse Gas
GWP	Global Warming Potential
HCFO	Hydrochlorofluoro-olefin
HEX	Heat Exchanger
HEA	Hybrid Electric Aircraft
HFC	Hydrofluorocarbon
HFO	Hydrofluoroolefin
HVAC	Heating Ventilation and Air Conditioning
H_2O	Water
ICAO	International Civil Aviation Organization
IRIS	Inverse organic Rankine cycle Integrated System
MEA	More Electric Aircraft
NO_x	Nitrogen oxide
ODP	Ozone Depletion Potential
PHEX	Primary Heat Exchanger
R-1224yd(Z)	cis-1-Chloro-2,3,3,3-Tetrafluoropropane
R-1234ze(Z)	cis-1,3,3,3-Tetrafluoropropene
R-1234yf	2,3,3,3-Tetrafluoropropene
R-1234ze(E)	trans-1,3,3,3-Tetrafluoropropene
R-1233zd(E)	trans-1-Chloro-3,3,3-trifluoropropene
R-134a	1,1,1,2-Tetrafluoroethane
R-152a	1,1-Difluoroethane
R-245fa	1,1,1,3,3-Pentafluoropropane
R-290	Propane
R-600a	Isobutane
SHEX	Secondary Heat Exchanger
UN	United Nations
VCC	Vapour Compression Cycle
WIPS	Wing Ice Protection System

Roman letters

s	Specific entropy $[\mathrm{J}\cdot(\mathrm{kg}\cdot\mathrm{K})^{-1}]$
T	Temperature [K]

REFERENCES

[1] United Nations. *COP26: Together for our planet*. 2021. URL: https://www.un.org/en/climatechange/cop26.

[2] NASA's Jet Propulsion Laboratory. *NASA Clocks July 2023 as Hottest Month on Record Ever Since 1880*. Aug. 2023. URL: https://climate.nasa.gov/news/3279/nasa-clocks-july-2023-as-hottest-month-on-record-ever-since-1880/.

[3] T. Park, H. Hashimoto, W. Wang, B. Thrasher, A. R. Michaelis, T. Lee, I. G. Brosnan, and R. R. Nemani. "What Does Global Land Climate Look Like at 2°C Warming?" In: *Earth's Future* 11.5 (May 2023). ISSN: 23284277. DOI: 10.1029/2022EF003330.

[4] United Nations Framework Convention on Climate Change. *The Paris Agreement*. Tech. rep. Paris: Paris Climate Change Conference COP 21, Nov. 2016.

[5] United Nations Framework Convention on Climate Change. *Glasgow Climate Pact*. Tech. rep. Glasgow, Nov. 2021. URL: https://www.ipcc.ch/report/ar6/wg1/..

[6] ICAO. *Emissions from fuel used for international aviation and maritime transport*. Tech. rep. Dubai, United Arab Emirates: International Civil Aviation Organization, 2023.

[7] European Commission. *European Green Deal: Commission proposes transformation of EU economy and society to meet climate ambitions*. Tech. rep. Brussels: European Commission, July 2021.

[8] S. Gössling and C. Lyle. "Transition policies for climatically sustainable aviation". In: *Transport Reviews* 41.5 (2021), pp. 643–658. ISSN: 14645327. DOI: 10.1080/01441647.2021.1938284.

[9] European Commission. *European Green Deal: new rules agreed on applying the EU emissions trading system in the aviation sector*. Dec. 2022. URL: https://ec.europa.eu/commission/presscorner/detail/en/ip_22_7609.

[10] International Civil Aviation Organization. *Trends in Emissions that affect Climate Change*. URL: https://www.icao.int/environmental-protection/Pages/ClimateChange_Trends.aspx.

[11] International Civil Aviation Organization. *Carbon Offsetting and Reduction Scheme for International Aviation (CORSIA)*. URL: https://www.icao.int/environmental-protection/CORSIA/pages/default.aspx.

[12] O. Zaporozhets, V. Isaienko, and K. Synylo. "PARE preliminary analysis of ACARE FlightPath 2050 environmental impact goals". In: *CEAS Aeronautical Journal* 12.3 (Aug. 2021), pp. 653–667. ISSN: 18695590. DOI: 10.1007/s13272-021-00525-7.

[13] G. Buticchi, P. Wheeler, and D. Boroyevich. "The More-Electric Aircraft and beyond". In: *Proceedings of the IEEE* 111.4 (Apr. 2023), pp. 356–370. ISSN: 15582256. DOI: 10.1109/JPROC.2022.3152995.

[14] P. W. Wheeler, J. C. Clare, A. Trentin, and S. Bozhko. "An overview of the more electrical aircraft". In: *Proceedings of the Institution of Mechanical Engineers, Part G: Journal of Aerospace Engineering* 227.4 (Apr. 2013), pp. 578–585. ISSN: 09544100. DOI: 10.1177/0954410012468538.

[15] H. Schefer, L. Fauth, T. H. Kopp, R. Mallwitz, J. Friebe, and M. Kurrat. “Discussion on Electric Power Supply Systems for All Electric Aircraft”. In: *IEEE Access* 8 (2020), pp. 84188–84216. ISSN: 21693536. DOI: 10.1109/ACCESS.2020.2991804.

[16] SAE International Information Report. *Aircraft Fuel Weight Penalty Due to Air Conditioning*. June 2011. DOI: 10.4271/AIR1168/8A.

[17] D. Bender. “Integration of exergy analysis into model-based design and evaluation of aircraft environmental control systems”. In: *Energy* 137 (Oct. 2017), pp. 739–751. ISSN: 03605442. DOI: 10.1016/j.energy.2017.05.182.

[18] M. Sinnett. *787 No-bleed systems: saving fuel and enhancing operational efficiencies*. Tech. rep. 2007.

[19] D. Bender. “Exergy-Based Analysis of Aircraft Environmental Control Systems and its Integration into Model-Based Design”. PhD thesis. Berlin: Technischen Universität Berlin, 2019.

[20] E. Zavaglio, M. Le Cam, C. Thibaud, G. Quartarone, Y. Zhu, G. Franzini, P. Roux, M. Dinca, A. Walte, and P. Rothe. “Innovative Environmental Control System for Aircraft”. In: *49th International Conference on Environmental Systems*. Boston, Massachusetts, July 2019.

[21] I. Martinez. *Aircraft environmental control system*. Tech. rep. 2014.

[22] European Aviation Safety Agency. *Certification specifications for large aeroplanes CS-25*. Brussels, Oct. 2003.

[23] M. Mohanraj and J. D. A. P. Abraham. “Environment friendly refrigerant options for automobile air conditioners: a review”. In: *Journal of Thermal Analysis and Calorimetry* 147.1 (2022), pp. 47–72. ISSN: 1588-2926. DOI: 10.1007/s10973-020-10286-w.

[24] K. Linnett and R. Crabtree. “What’s Next in Commercial Aircraft Environmental Control Systems?” In: *SAE Transactions* 102 (1993), pp. 639–653.

[25] ARP292. “Air Conditioning Helicopter General Requirements”. In: *SAE International* (2014). DOI: 10.4271/ARP292.

[26] S. Golle, U. Hesse, E. Klausner, M. Raddatz, F. Klimpel, and H. Brunswig. *Aircraft air-conditioning system controllable according to operating phases and method of operating such an aircraft air-conditioning system*. 2016.

[27] S. A. Schmidt, J. Riedel, F. Hepcke, W. Casas, J. Bonhora, D. Lavergne, F. Sanchez, and G. Ricard. “New Air Systems for More Electric Aircraft”. In: *More Electric Aircraft, MEA*. Bordeaux, France, Oct. 2021.

[28] J. V. Vargas and A. Bejan. “Integrative thermodynamic optimization of the environmental control system of an aircraft”. In: *International Journal of Heat and Mass Transfer* 44.20 (Oct. 2001), pp. 3907–3917. ISSN: 0017-9310. DOI: 10.1016/S0017-9310(01)00033-3.

[29] I. Pérez-Grande and T. J. Leo. “Optimization of a commercial aircraft environmental control system”. In: *Applied Thermal Engineering* 22.17 (Dec. 2002), pp. 1885–1904. ISSN: 1359-4311. DOI: 10.1016/S1359-4311(02)00130-8.

[30] M. Sielemann, T. Giese, B. Oehler, and M. Gräber. “Optimization of an Unconventional Environmental Control System Architecture”. In: *SAE International Journal of Aerospace* 4.2 (2011), pp. 1263–1275. DOI: 10.4271/2011-01-2691.

[31] E. A. Heath. “Amendment to the Montreal Protocol on Substances that Deplete the Ozone Layer (Kigali Amendment)”. In: *International Legal Materials* 56 (Feb. 2017), pp. 193–205.

[32] European Commission. *Proposal for a regulation of the European parliament and of the council on fluorinated greenhouse gases, amending Directive (EU) 2019/1937 and repealing Regulation (EU) No 517/2014*. Tech. rep. May 2022.

[33] R. Roy and B. K. Mandal. "Thermo-economic Assessment and Multi-Objective Optimization of Vapour Compression Refrigeration System using Low GWP Refrigerants". In: *2019 8th International Conference on Modeling Simulation and Applied Optimization (ICMSAO)*. Ed. by B. Manama. 2019, pp. 1–5.

[34] C. H. de Paula, W. M. Duarte, T. T. M. Rocha, R. N. de Oliveira, and A. A. T. Maia. "Optimal design and environmental, energy and exergy analysis of a vapor compression refrigeration system using R290, R1234yf, and R744 as alternatives to replace R134a". In: *International Journal of Refrigeration* 113 (May 2020), pp. 10–20. ISSN: 0140-7007. DOI: 10.1016/J.IJREFRIG.2020.01.012.

[35] C. Mateu-Royo, C. Arpagaus, A. Mota-Babiloni, J. Navarro-Esbrí, and S. S. Bertsch. "Advanced high temperature heat pump configurations using low GWP refrigerants for industrial waste heat recovery: A comprehensive study". In: *Energy Conversion and Management* 229 (Feb. 2021), p. 113752. ISSN: 0196-8904. DOI: 10.1016/J.ENCONMAN.2020.113752.

[36] H. Yan, D. Wu, J. Liang, B. Hu, and R. Z. Wang. "Selection and validation on low-GWP refrigerants for a water-source heat pump". In: *Applied Thermal Engineering* 193 (July 2021), p. 116938. ISSN: 1359-4311. DOI: 10.1016/J.APPLTHERMALENG.2021.116938.

[37] H. Zhao, Y. Hou, Y. Zhu, L. Chen, and S. Chen. "Experimental study on the performance of an aircraft environmental control system". In: *Applied Thermal Engineering* 29.16 (Nov. 2009), pp. 3284–3288. ISSN: 1359-4311. DOI: 10.1016/J.APPLTHERMALENG.2009.05.002.

[38] S. H. Chowdhury, F. Ali, and I. K. Jennions. "Development of a Novel Ground Test Facility for Aircraft Environmental Control System". In: *Journal of Thermal Science and Engineering Applications* 15.8 (June 2023). ISSN: 1948-5085. DOI: 10.1115/1.4062553.

[39] Documentation Simulink. *Simulation and Model-Based Design*. 2020.

[40] S. Mancin, C. Zilio, G. Righetti, and L. Rossetto. "Mini Vapor Cycle System for high density electronic cooling applications". In: *International Journal of Refrigeration* 36.4 (June 2013), pp. 1191–1202. ISSN: 0140-7007. DOI: 10.1016/J.IJREFRIG.2012.12.008.

[41] A. Mannini. "Vapor Cycle versus Air Cycle Environmental Control System: selection criteria on modern helicopters". In: *Twentieth European Rotorcraft Forum*. Amsterdam, 1994, p. 14.

[42] A. Mannini. "The Environmental Control System for a modern helicopter: a blend of new technologies". In: *Twenty-first European Rotorcraft Forum*. Saint-Petersburg, Russia, 1995, p. 11.

[43] N. Ablanque, S. Torras, C. Oliet, J. Rovira, C. David Pérez-Segarra, N. Ablanque, J. Rigola, and C.-D. Perez-Segarra. "Purdue e-Pubs Vapor Compression System Modelica Library for Aircraft ECS Vapor Compression System Modelica Library for Aircraft ECS". In: *17th International Refrigeration and Air Conditioning Conference*. Pardue, July 2018.

[44] H. Hu, H. Sun, C. Wu, X. Wang, and Z. Lv. "A steady-state simulation model of supplemental cooling system integrated with vapor compression refrigeration cycles for commercial airplane". In: *Applied Thermal Engineering* 166 (Feb. 2020), p. 114692. ISSN: 1359-4311. DOI: 10.1016/J.APPLTHERMALENG.2019.114692.

[45] Y. Xu, Z. Yan, and W. Xia. “A novel system for aircraft cabin heating based on a vapor compression system and heat recovery from engine lubricating oil”. In: *Applied Thermal Engineering* 212 (July 2022), p. 118544. ISSN: 1359-4311. DOI: `10.1016/J.APPLTHERMALENG.2022.118544`.

[46] E. Tayfun, C. Fethiye, C. Aykut, O. Recep, and S. Mustafa Fazil. “Experimental and numerical investigation of a compact vapor compression refrigeration system for cooling avionics in harsh environment”. In: *Applied Thermal Engineering* (Sept. 2023), p. 121663. ISSN: 1359-4311. DOI: `10.1016/J.APPLTHERMALENG.2023.121663`.

[47] A. Giuffré, P. Colonna, and M. Pini. “The Effect of Size and Working Fluid on the Multi-Objective Design of High-Speed Centrifugal Compressors”. In: *International Journal of Refrigeration* 143 (Nov. 2022), pp. 43–56. ISSN: 01407007. DOI: `10.1016/j.ijrefrig.2022.06.023`.

[48] A. Giuffré, P. Colonna, and M. Pini. “Design Optimization of a High-Speed Twin-Stage Compressor for Next-Gen Aircraft Environmental Control System”. In: *Journal of Engineering for Gas Turbines and Power* 145.3 (Mar. 2023). ISSN: 0742-4795. DOI: `10.1115/1.4056022`.

[49] F. Molés, J. Navarro-Esbrí, B. Peris, A. Mota-Babiloni, and Á. Barragán-Cervera. “Theoretical energy performance evaluation of different single stage vapour compression refrigeration configurations using R1234yf and R1234ze(E) as working fluids”. In: *International Journal of Refrigeration* 44 (Aug. 2014), pp. 141–150. ISSN: 0140-7007. DOI: `10.1016/J.IJREFRIG.2014.04.025`.

[50] A. Yataganbaba, A. Kilicarslan, and I. Kurtbaş. “Exergy analysis of R1234yf and R1234ze as R134a replacements in a two evaporator vapour compression refrigeration system”. In: *International Journal of Refrigeration* 60 (Dec. 2015), pp. 26–37. ISSN: 0140-7007. DOI: `10.1016/J.IJREFRIG.2015.08.010`.

2

VAPOUR COMPRESSION CYCLE FOR AIRCRAFT ECS: NOVELTIES AND CHALLENGES

> *In nature's economy, the currency is not money;*
> *it is life.*
>
> Vandana Shiva

Historically, the main obstacle preventing the application of the Vapour Compression Cycle concept to the realization of aircraft Environmental Control Systems has been its higher overall weight compared to the Air Cycle Machine. This limitation can now be overcome by designing and realizing novel lightweight and high-performance components: the specific fuel consumption attributable to Environmental Control Systems based on the vapour compression thermodynamic cycle can be significantly reduced by adopting ultra-compact heat exchangers and an electrically-driven high-speed centrifugal compressor in place of a heavier and less efficient scroll compressor. Additionally, to comply with recent regulations on the use of fluorinated refrigerants (so-called F-gases), a novel low-GWP working fluid must be employed and a list of new refrigerants is presented and their properties are discussed. Innovative integrated system optimization and components design methods further contribute to solving the challenge of bringing these ECS to fruition.

Since the 1960s, the Vapour Compression Cycle (VCC) was already employed as a solution for aircraft Environmental Control Systems (ECS). Notable examples are the Boeing 707 and the Grumman E-2C aircraft [1]. However, with advancements in technology, the Air Cycle Machine (ACM) has rapidly developed and become the preferred option for large passenger aircraft ECS due to its simplicity and low maintenance requirements. With high-efficiency and lightweight turbomachinery, along with a neutral coolant like air, the ACM is a reliable and efficient choice [2], though the inverse Brayton thermodynamic cycle is bound to be less thermodynamically efficient than the vapour compression cycle, or inverse organic Rankine cycle. In the past, the limitations of refrigerant compressor technology made the VCC-based ECS impractical for large passenger aircraft. Heavy and low-efficiency volumetric compressors were used, and electrically driven solutions were limited by the low rotational speed of the electric motor, heavy power electronics, and complex control systems. Therefore, the use of the VCC system was restricted to the case of small aircraft applications, i.e., high-payload helicopters and business jets, where the availability of bleed air was insufficient for the use of the ACM [3]. In 1993, Linnett and Crabtree [2] foresaw that in the future VCC-based ECSs for aircraft would rely on the technological advancement of lightweight centrifugal compressors employing gas bearings for the support of the high-speed shaft. Today, this prediction has become a reality as many aerospace companies are investing resources in the development of novel and more efficient ECS solutions. Liebheer and Airbus have pioneered research on this topic and have started investigating the development of more efficient and lightweight ACM coupled with an electrically-driven VCC system and employing novel components such as oil-free high-speed centrifugal compressors and highly efficient compact heat exchangers (HEXs) [4]. Additionally, to comply with the F-gas regulation, novel low-Global Warming Potential (GWP) refrigerants are being studied as an alternative to the traditionally used R-134a.

2.1. COMPACT HEAT EXCHANGERS

In recent years, there has been a growing demand for thermal devices that are both lightweight and highly efficient, particularly in the aviation and automotive sectors [5]. As a result, the development of ultra-compact HEXs has become increasingly important. These devices are designed to optimize heat transfer between two fluid streams while minimizing their size and weight. Compact HEXs have proven to be a viable solution to meet the challenging requirements of modern aircraft thermal management systems, where space and weight constraints are critical. By utilizing novel materials and manufacturing techniques, compact HEXs can deliver significant improvements in terms of specific fuel consumption. A HEX is considered compact if its compactness factor β, defined as the ratio of total heat transfer surface to volume, is higher than 700 $\mathrm{m}^2 \cdot \mathrm{m}^{-3}$ [6]. Compact HEXs designs feature complex internal fins geometries, microchannels, and high porosity internal structures that allow for large heat transfer surfaces within a fixed volume. The main design challenge is to ensure a compromise between maximizing heat transfer efficiency and minimizing losses due to flow resistance.

Much research is dedicated to developing numerical tools to design these components in detail and comprehend the influence of geometrical parameters, such as fin pitch, fin and plate thickness, on the overall performance. Multidisciplinary optimization methods, such as shape and topology optimization, have made it possible to develop HEX designs with superior performance. Thanks to progress in manufacturing techniques and new materials, Additive Manufacturing (AM) can now be used to create customized HEX prototypes with complex internal structures [5]. Experimental investigation is being conducted to support the development of these products, including tests for the aerothermal performance characterization of novel samples of 3D printed HEXs [7]. Boeing has been actively assessing innovative thermal management devices using both AM and traditional techniques [7]. Honeywell has recently started a collaboration with Reaction Engines Limited to incorporate the microtube heat exchanger technology developed by the British company into their sustainable aviation thermal management solutions. This unique heat exchange technology would reduce weight by more than 30%, leading to lower fuel consumption, longer range, and increased aircraft capacity [8].

2.2. HIGH-SPEED CENTRIFUGAL COMPRESSOR

The recent development of high-speed permanent-magnet electric motors and gas bearings technologies has stimulated research in the field of small-scale centrifugal compressors, which feature many advantages if compared to larger and heavier positive displacement machines. For example, high-speed radial compressors are an attractive solution as components of refrigeration and heat pump systems, air management systems of fuel cells, electric superchargers, and fuel delivery systems [9]. Small-scale radial compressors can reach an efficiency of up to 85%, higher than that of volumetric compressors, and can be reliable and durable due to the absence of sliding surfaces and complex kinematics. As demonstrated by Casey *et al.* [9], radial compressors are characterized by high-power density and compact impeller designs. Moreover, the use of foil or magnetic bearings, compared to traditional oil bearings, eliminates the need for lubrication. This is particularly attractive for refrigeration and heat pump systems, as it avoids all the problems associated with the presence of oil within the working fluid loop, and, in particular, in the evaporator whose aerothermal efficiency is negatively affected by oil accumulation on the surface of its tubes [10]. Furthermore, in oil bearings, the viscosity of the lubricant can decrease at high operating temperatures, which is often the case in high-speed rotating machines. This issue is mitigated with foil bearings, as they can operate at significantly higher temperatures without the need for lubrication. Additionally, being oil-free, foil bearings require less maintenance since there is no need to check or replace lubricant fluids [11]. However, the use of gas bearings implies some design constraints associated with their limited load capacity. For example, on the one hand, in the case of low-density and high molecular complexity refrigerants, the thermodynamic properties of these fluids lead to relatively large impeller designs. Hence, the maximum bearings load imposes feasibility constraints on the overall dimensions of the compressor [12]. On the other hand, the adoption of simple-molecule refrigerants as working fluid can lead to significantly high rotational speeds. Thus, to comply with the gas bearings maximum load, they are usually designed for lower work coefficients, which limits the device efficiency [13]. Other design constraints depend on manufacturability associated with the material mechanical properties and manufacturing techniques.

Casey and Robinson [14] document several examples of recent high-speed small-scale centrifugal compressor applications. The largest market is that of turbochargers for automotive gasoline engines. Centrifugal compressors can reach a compression ratio of up to 4. The impeller diameter is usually smaller than 40 mm with a rotational speed larger than 250 krpm. Onboard the Boeing 787-Dreamliner, centrifugal compressors have been employed to pressurise the cabin air delivered by the ECS, thus replacing the traditional bleed air system [15]. Liebherr has developed an electrical single-stage centrifugal compressor of 25 kW for the air supply of fuel cell systems for aerospace and automotive applications [16].

Other important applications employing high-speed centrifugal compressors are small-size VCC systems and heat pumps, especially for domestic heating and cooling. Differently from turbochargers, the working fluid is a refrigerant, therefore the molecular weight of the working fluid is larger, while its associated speed of sound is lower. Therefore, optimal compressor designs feature larger compression ratios and transonic flow even though the blade speeds are moderate. Schiffmann and Favrat [10] designed and tested a small-scale oil-free turbocompressor for domestic heat pump applications. The refrigerant is R-134a. The radial turbocompressor features gas bearings, a 20 mm tip diameter and it was tested with a rotational speed of up to 210 krpm. The total-to-total pressure ratio was 3.3 and the internal isentropic efficiency reached a maximum value of 79%. Demierre *et al.* [17] designed and tested a thermally-driven heat pump, which combines into the same system a heat pump cycle and an organic Rankine cycle. Both compressor and turbine are mounted on a common shaft supported on gas bearings. The working fluid is R-134a. The compressor wheel diameter is around 20 mm, and its power demand is of the order of 2 kW. The component has been tested up to a speed of 206 krpm reaching a compression ratio of around 2.8 and an efficiency of 73%. Javed *et al.* [18] demonstrated the use of two mechanically-driven small-scale turbocompressors running on gas bearings for a 6.5 kW heat pump for domestic applications. The system operates with R-134a as the working fluid. The twin-stage centrifugal compressor was tested for a wide range of operating conditions, reaching a maximum rotational speed of 280 krpm. More recently, Essa *et al.* [19] investigated the performance of air conditioning systems for electric vehicles using ultra-light high-speed centrifugal compressors. The authors used the compressor maps for a commercial turbocharger to determine the refrigerant mass flow rate. In case R-134a is the working fluid, the numerical results demonstrate an increase in cooling capacity with a corresponding reduction of power demand with respect to the system featuring a volumetric machine as compressor. Low-GWP refrigerants have been tested to evaluate possible alternatives to R-134a.

One of the objectives of the research program for which the work documented in this dissertation has been carried out was the definition of design guidelines for high-speed centrifugal compressors for VCC-based aircraft ECS. This investigation belongs to a separate work package of the project [13, 20], and it has been carried out in partnership with Aeronamic, a Dutch aerospace company specialised in high-speed rotating machinery and components.

Aeronamic recently developed and tested a prototype of a high-speed centrifugal compressor for helicopter ECS, operating with R-134a. Currently, another high-speed compressor prototype is being finalized. This compressor, hereinafter named after WAHTAS (Warmtepomp voor Hoge Temperatuur Afgifte Systeem[1]) compressor, has been designed for isobutane (R-600a) as working fluid and a maximum electric power of 15 kW. The weight of the device including the Electronic Control Unit (ECU) is 9 kg. The company successfully tested this device to operate with R-1233zd(E) up to a maximum rotational speed of 85 krpm, reaching a compression ratio almost equal to 5 at a refrigerant mass flow rate of approximately 0.15 $\mathrm{kg \cdot s^{-1}}$. This turbomachinery will be installed in the Inverse organic Rankine cycle Integrated System (IRIS) facility of the TU Delft Aerospace Propulsion & Power laboratories for further investigations. The two impeller wheels are mounted on the same shaft and they run on gas bearings. To cope with the maximum allowable design load of the gas bearings, the two impellers are mounted in a back-to-back configuration to balance their axial thrust. The compressor design is compact and the refrigerant is used for cooling both the electric motor and the bearings. At the outlet of the first stage, a small amount of the total mass flow of refrigerant is diverted to cool the bearings, and then redirected to the compressor suction port. The remaining part of the refrigerant already compressed by the first compressor stage is used to cool the electric motor, before entering the second stage. However, since the refrigerant is heated between the two stages, the overall compressor efficiency is penalised.

---

[1] Dutch acronym which stands for "heat pump for high temperature supply system".

The baseline design of Aeronamic has been improved using the *in-house* tool *TurboSim* for detailed centrifugal compressor design, developed in another work package of this research project by Giuffré [20]. The compressor, conceived to be tested in the IRIS setup and therefore referred to as the IRIS compressor, features the same assembly layout as the WAHTAS compressor, but was specifically designed to operate with R-1233zd(E). Giuffré [20] proved that it is possible to design such a compressor for a much higher compression ratio, i.e., 8.5, a design mass flow rate of 0.1 $\mathrm{kg \cdot s^{-1}}$, and an overall efficiency higher than 65%. The manufacturing constraints provided by the industrial partner of maximum rotation speed (103 krpm), fixed value of inlet impeller hub radius (4.5 mm), and minimum outlet blade height (1.5 mm) make the compressor design quite challenging. Furthermore, because of the lower values of volumetric flow rate, the design of the second stage is more challenging than the first stage, therefore also its efficiency is negatively affected. Figure 2.1 shows the three-dimensional rendering of the two impellers of the compressor and its operating map. The efficiency and the operating range of the second stage of the compressor are always penalized by the high values of volumetric flow rate, with respect to the first stage. Therefore, the design guideline suggests to design the first stage with the highest compression ratio. Furthermore, since both stages rotate at the same speed, their work coefficient is set to the same value. In this way, the flow coefficient of the second impeller lies in a region of the optimal range, thus the compressor overall efficiency is enhanced. Finally, the authors emphasise the detrimental effect of the tip clearance gap and the maximum rotational speed on the maximum allowable compression ratio of the compressor [21].

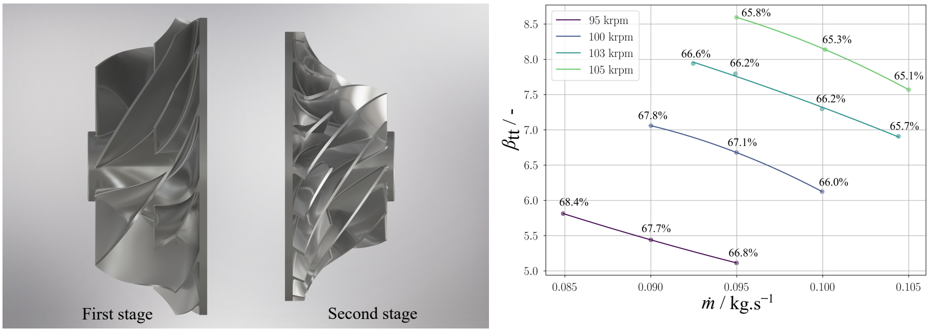

Figure 2.1.: Left: 3-dimensional rendering of the IRIS compressor impeller wheels. Courtesy of A. Giuffré. Right: performance map of the IRIS compressor [20].

2.3. NEXT-GENERATION REFRIGERANTS

During the 1830s, Perkins invented the VCC system. At that time, the *first-generation of refrigerants* included any natural substance suitable for the purpose of refrigeration, i.e., ammonia (NH_3), carbon dioxide (CO_2), Freon 10 (CCl_4), hydrocarbons (HCs). During the 1930s, The Chemours company (now Du Pont) proposed a new class of fluids, the chlorofluorocarbons. They are often classified either as CFCs (HCFCs if hydroclorofluorocarbons) or Rs fluids and were marketed as Freon™ products. The most common *second-generation refrigerants* were CFC-11 (or R11), CFC-12 (or R12), HCFC-22 (or R22) and they solved the safety problems associated with the previous generation of refrigerants. These fluids have been employed in the refrigeration and air conditioning sector for almost one century before the scientific community became aware of the detrimental effect that chlorine was having on the atmospheric ozone layer [22]. In response to this environmental emergency, in 1987, the Montréal Protocol imposed the phase-out of CFCs, and the refrigeration industry substituted them with the *third-generation refrigerants*: the hydrofluorocarbons (HFCs). However, their high GWP values and the increase of their atmospheric concentrations generated international concern about their radiative forcing. Therefore, the Kigali Amendment to the Montréal Protocol [23] established a roadmap to gradually phase out high-GWP fluorinated greenhouse gases (F-gases) from the market and to encourage the use of other substances, known as *fourth-generation refrigerants*, i.e., natural refrigerants, haloolefins, and blends. The ambition is to cut emissions by 55% by 2030 and to achieve net carbon neutrality by 2050 [24].

The selection of the most suitable working fluid depends on the application and the combination of its chemical, thermodynamic, environmental, and safety properties. In the case of haloolefins, thanks to their chemistry, these compounds have a short atmospheric lifetime (ALT), ranging from a few days to weeks, hence GWP values are lower than one [25]. However, during the atmospheric degradation of haloolefins, trifluoroacetic acid (TCA), a substance harmful to aquatic life, is produced [26]. The molar yield of the degradation of haloolefins in the atmosphere depends on the refrigerant. It can be as low as 2% in the case of R-1233zd(E) [27–29], or up to 97% for R-1224yd(Z) [29]. Therefore, the general opinion is that haloolefins could only be considered a temporary solution for the refrigeration sector, while natural refrigerants would represent a permanent solution to atmospheric problems caused by refrigerants. These fluids have excellent thermodynamic and environmental properties, although they are highly flammable and, in some cases such as Ammonia (R-717), also toxic. Among the natural fluids, Ammonia is the most used refrigerant in the food industry and for industrial refrigeration in general. CO_2 (R-744) is employed in a wide range of applications, e.g., supermarkets chillers, heat pumps, ice rinks and industrial freezers. In recent years, propane (R-290) and isobutane (R-600a) have become the leading solution for domestic refrigerators, since the refrigerant mass charge never exceeds 150 g and the flammability hazard is simple to handle [25]. Table 2.1 summarizes the environmental properties of the different classes of refrigerants.

Table 2.1.: Environmental and safety properties of the different refrigerant classes [30].

Refrigerant class	**Examples**	**GWP**	**ODP**	**ALT**	**Safety**
CFCs	R-11, R-12, R-115	4750-14400	0.6-1	45-1700 years	Not toxic Not flammable
HCFCs	R-22, R-123, R-410A	400-1800	0.02-0.11	1-20 years	Not toxic Not flammable
HFCs	R-32, R-134a	140-11700	0	1-300 years	Not toxic Not flammable
Haloolefins	R-1234yf, R-1234ze, R-1233zd(E)	<0-2	0	Few days	Not toxic Flammable / Not flammable
Natural Refrigerants	R-744, R-717, R-600a, R-290	0	0	Few days	Highly flammable Toxic / Not toxic

The state-of-the-art refrigerant for aircraft ECS is R-134a [31]. This refrigerant belongs to the class of HFCs. R-134a is characterized on the one hand by null Ozone Depletion Potential (ODP), and on the other hand by GWP equal to 1300. So far, the aviation sector has not considered the use of alternative refrigerants due to the strict regulations in terms of safety and certification.

2.4. SHORT-CHAIN HALOOLEFINS

Short-chain haloolefins are alkens characterized by null ODP and GWP values lower than two. These unsaturated organic compounds are composed of hydrogen, fluorine, carbon and, in some cases, chlorine atoms. They are used as refrigerants and they are classified as hydrofluoroolefins (HFOs) and hydrochlorofluoroolefins (HCFOs) [32]. Their low GWP values result from the combination of two chemical characteristics of the olefins, namely, low radiative efficiency (RE) and short ALT [33]. The RE measures the effect that a unitary change of the substance concentration in the atmosphere has on the climate forcing, i.e., energy fluxes in the atmosphere associated with human activities [34]. In the case of halolefins, this efficiency is one order of magnitude lower than that of HFCs. Haloolefins are a subset of the halocarbons class of fluids, with a double bond between carbon atoms, which is highly reactive to the natural hydroxyl radicals (OH) present in the atmosphere, thus allowing for an ALT of these compounds of few days [25]. In the ANSI/ASHRAE Standard 34 [35] classification, these compounds belong to the safety classes A1, A2L, and A2. Therefore, they are not toxic. However, the nature of the double carbon atoms bond can be responsible for the relatively high reactivity of these substances, which can make them flammable. To comply with the safety codes of the aerospace sector, research on the use of these working fluids onboard aircraft is usually limited to low-pressure refrigerants, with high Normal Boiling Point (NBP).

Table 2.2.: Thermodynamic properties of selected haloolefins and those of R-134a for comparison.

Refrigerant	**Fluid class**	T_C **/ K**	p_C **/ bar**	**NBP / K**	N **/ -**[a]	M **/ g·mol**$^{-1}$
R-134a	HFC	374.21	40.6	247.08	−1.10	102.0
R-1243zf	HFO	376.93	35.18	247.73	0.097	96.05
R-1234ze(Z)	HFO	423.27	35.31	282.88	1.49	114.04
R-1234ze(E)	HFO	382.51	36.35	254.18	1.78	114.04
R-1233zd(E)	HCFO	439.6	36.24	291.41	3.92	130.05
R-1224yd(Z)	HCFO	428.69	33.37	287.77	4.91	148.49
R-1336mzz(Z)	HFO	444.5	29.03	306.6	9.24	164.06

---

[a] The values of molecular complexity are estimated by assuming that low reduced-pressure saturated vapour properties comply with the ideal gas model, therefore $N \approx \frac{Cp}{0.7R} - \frac{\log 10}{0.49}\,\frac{7}{3}\,(\omega + 1)$ [36].

To discuss the thermodynamic properties of these compounds, six exemplary refrigerants have been chosen among those indicated as promising by one of the lead manufacturers in the cooling industry [37], e.g., R-1243zf, R-1234ze(Z), R-1234ze(E), R-1233zd(E), R-1224yd(Z), and R-1336mzz(Z). With reference to Tab. 2.2, the main thermodynamic properties of the selected haloolefins, benchmarked against those of R-134a, can be summarized as i) higher critical temperature and lower critical pressure; ii) lower saturation pressure (Fig. 2.3, left), iii) significantly lower saturated vapour density ρ_V (Fig. 2.3, right), iv) larger molar mass M; v) higher molecular complexity N.

The molecular complexity N has been defined by [38] as

$$N = \frac{T_\mathrm{C}}{R}\left[\frac{ds}{dT}\right]_{x=1,T_\mathrm{r}=0.7} = \frac{T_\mathrm{C}}{R}\left[\frac{c_p}{T} - \left(\frac{\partial V}{\partial T}\right)_p \frac{\mathrm{d}p}{\mathrm{d}T}\right]_{x=1,T_\mathrm{r}=0.7}. \tag{2.1}$$

It is a fluid thermodynamic property derived semi-empirically and related to the complexity of fluid molecules. Complexity refers to the number of atoms in a molecule and their

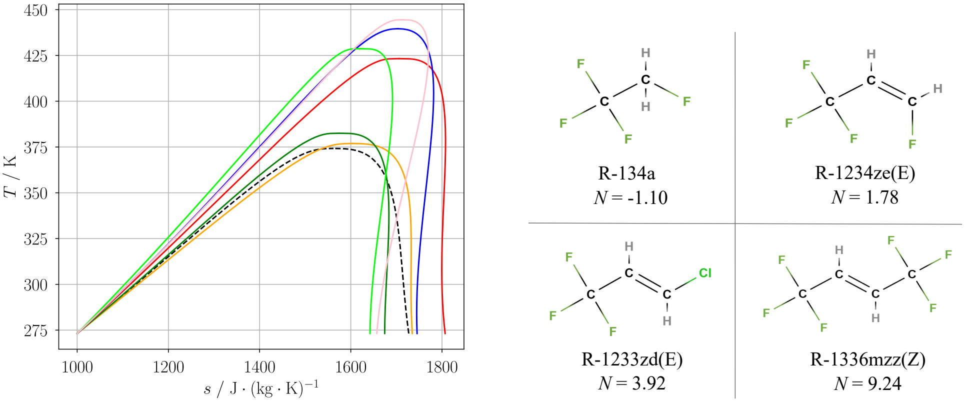

Figure 2.2.: Left: representation of the saturation line on the fluid T-s chart. Working fluids: R-134a (– –), R-1243zf (—), R-1234ze(Z) (—), R-1234ze(E) (—), R-1233zd(E) (—), R-1224yd(Z) (—), R-1336mzz(Z) (—). Right: molecular structure and associated molecular complexity N for several fluids.

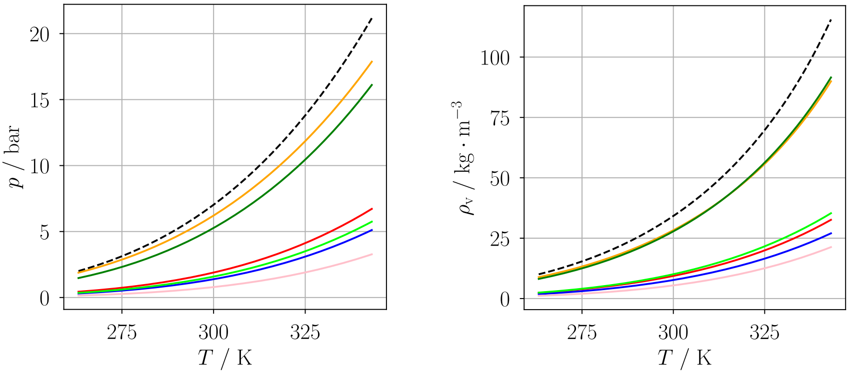

Figure 2.3.: Left: saturation pressure as a function of temperature. Right: saturated vapour density as a function of temperature. Working fluids: R-134a (– –), R-1243zf (—), R-1234ze(Z) (—), R-1234ze(E) (—), R-1233zd(E) (—), R-1224yd(Z) (—), R-1336mzz(Z) (—).

arrangement. Substances with high molecular complexity are characterized by large specific heat capacity (c_p) since the large number of atoms in a molecule increases their degree of freedom in terms of rotational and vibrational modes [34]. As an example, Fig. 2.2 (right) shows how the increased complexity of the fluid molecule corresponds to higher values of N. At macroscopic level, the molecular complexity N is proportional to the slope of the saturated vapour line in the T-s plane calculated at the reduced temperature of 0.7, and to the critical temperature.

With reference to Eqn. 2.1, high and positive values of N are typical for substances known as dry fluids (fluids whose isentropically expanding vapour remains dry), i.e., R-1224yd(Z) and R-1336mzz(Z). These classes of compounds are characterized by large critical temperature and low critical pressure in the opposite fashion of those fluids featuring low molecular complexity, i.e. wet fluids (R-134a). Figure 2.2 (left) shows a comparison of the T-s charts of the exemplary refrigerants to R-134a. Thanks to these properties, in the case of low-temperature small-capacity VCC systems, the losses associated with vapour superheating along the compression process are limited if the working fluid is made of complex molecules.

Furthermore, the selected haloolefins also feature low values of saturated vapour density which, for a fixed mass flow rate within the refrigeration loop, correspond to a large volumetric cooling capacity. This affects the size of the components, which feature larger flow passages to reduce the flow velocity and avoid high friction losses. For the application under analysis, given the small capacity of the system and the low operating temperatures, the use of low-density refrigerants allows for a good compromise between impeller wheels diameter and rotational speed for small-scale centrifugal compressors design. The fluid molecular complexity also affects the speed of sound, which is low in the case of fluids made of complex molecules. This therefore makes the design of turbomachinery components more challenging, due to the likely occurrence of transonic flow through the cascades, leading to a reduction of both isentropic efficiency and choke margin.

2.5. NATURAL REFRIGERANTS

Natural refrigerants are organic substances and include the classes of HCs and of ethers. HCs consist of only two atoms, e.g., carbon and hydrogen; ethers are formed by two HCs groups bonded to an oxygen atom. In the early days of the refrigeration industry, natural refrigerants were the prevailing working fluids, thanks to the excellent suitability of their thermodynamic properties for the requirements of the applications. Because of the hazards caused by their high flammability, their use was gradually discontinued in favor of synthetic refrigerants. In response to the climate emergency, both research and therefore industry have resumed their study and application, because they are characterized by negligible GWP and null ODP. According to the ANSI/ASHRAE Standard 34 [35], organic refrigerants are classified as low-toxicity and high-flammability fluids (A3). However, in the case of accidental release in the atmosphere, their autoignition is possible only in case the air mixture is within a given concentration range, the ignition source has an energy greater than 0.29 mJ or the mixture is in contact with a surface whose temperature exceeds 495 °C [30]. Safety standards prescribe the correct procedures for the design, realization and maintenance of refrigeration systems in the case of flammable refrigerants [39, 40]. To prevent any risk of explosion, the following safety precautions are mandatory: i) hydrocarbons must be stored in sealed components, and separated from the rest of the system; ii) ventilation is mandated to guarantee that, in the case of leakage, the refrigerant concentration is insufficient for autoignition; iii) the maximum allowable refrigerant charge in the system is limited; iv) any potential external source of ignition is absent. In compliance with the safety standards, in the last decade, HCs have been used for both domestic and industrial refrigeration. Their compatibility with the majority of common metals and polymers used in components for HFCs systems represents another advantage of these compounds [41]. Isobutane (R-600a) is employed as a working fluid for domestic refrigerators in many North European countries. Cyclopropane (RC-270) is suitable for low-temperature heat pump applications, while propane (R-290) and propene (R-1270) are mostly chosen for commercial applications [41].

A general overview of the thermodynamic properties of the natural refrigerants most commonly used in the refrigeration sector, as well as R-134a for comparison, is provided in Tab. 2.3.

In the same fashion as the haloolefins, the critical temperatures of the selected natural compounds are much higher than that of R-134a. Propene and propane are exceptions since

Table 2.3.: Thermodynamic properties of selected natural refrigerants and those of R-134a for comparison.

Refrigerant	T_c / K	p_c / bar	**NBP / K**	N/ -	M / g·mol^{-1}
R-134a	374.21	40.6	247.08	−1.10	102.0
Cyclopropane (RC-270)	398.3	55.80	241.67	−3.45	42.08
Propene (R-1270)	364.21	45.55	225.53	−2.62	42.08
Dimethyl ether (RE-170)	400.38	53.37	248.37	−2.20	46.07
Propane (R-290)	369.89	42.51	231.04	−1.31	44.10
Isobutane (R-600a)	407.81	36.29	261.40	3.03	58.12
Butane (R-600)	425.12	37.96	272.66	3.73	58.12
Pentane (R-601)	469.7	33.67	309.21	8.58	72.15

the shape of the T-s plane of these refrigerants is similar to the one of the HFC (Fig. 2.4). The values of critical pressure are similar for all the fluids, but cyclopropane and dimethyl ether. The NBP depends on the size of the molecule and the intermolecular bonds, therefore it is higher for complex molecules, i.e., pentane, and for cycloalkanes as compared to their acyclic isomers, i.e., cyclopropane with respect to propene. Since natural refrigerants are mainly formed by atoms of carbon and hydrogen, the molar mass of these compounds is significantly lower if compared to that of HFCs and haloolefins. The shape of the C-H molecular chains of natural refrigerants influences their molecular complexity, therefore the values of molecular complexity N can vary within a wide range. Figure 2.4 (right) shows the molecular structure of four exemplary substances and the corresponding molecular complexity. In the case of the selected refrigerants, there are examples of wet fluids, namely, propane, dimethyl ether, and propane; and dry fluids, such as isobutane, butane and pentane. However, it is important to remark that in case of high-molecular-complexity fluids, such as pentane, condensation might occur during compression and this is very problematic if the compressor is a high-speed radial machine because droplets cause blade erosion [42].

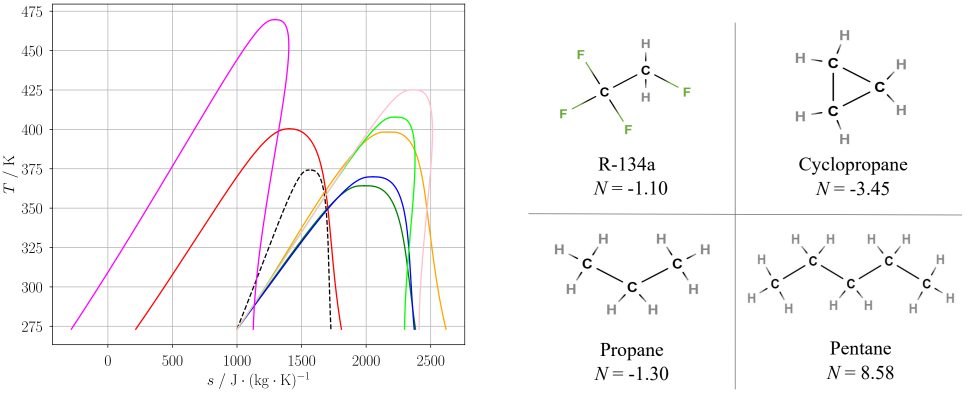

Figure 2.4.: Left: $T-s$ chart. Working fluids: R-134a (- -), cyclopropane (—), propene (—), dimethylether(—), propane (—), isobutane (—), butane (—), pentane (—). Right: molecular structure and molecular complexity of cyclopropane, propane, pentane as compared to R-134a.

The charts of Fig. 2.4 (left) show that the latent heat of evaporation of natural refrigerants is almost double that of HFCs and haloolefins. Therefore, for a fixed cooling capacity of the system, the required refrigerant mass flow rate is comparatively small, thus allowing for the use of compact system components. However, with the commercial introduction of small capacity systems, the use of these refrigerants raises another technological challenge related to the need for components specifically designed for the application.

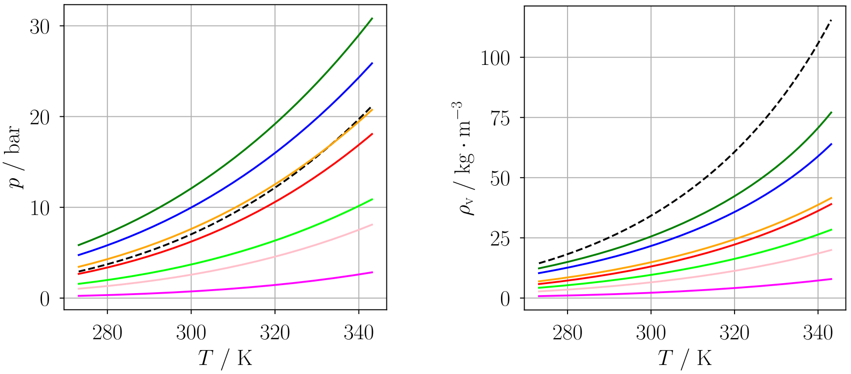

Figure 2.5.: Left: saturation pressure as a function of temperature. Right: saturated vapour density as a function of temperature. Working fluids: R-134a (- -), cyclopropane (—), propene (—), dimethylether(—), propane (—), isobutane (—), butane (—), pentane (—).

The variation of the vapour density as a function of the saturation temperature is illustrated in Fig. 2.5 (right). The saturated vapour density of natural refrigerants varies similarly to that of haloolefins: its values are lower than that of R-134a, and they increase in the case of simple molecules refrigerants. As a result of these two properties, the refrigerant volumetric cooling capacity is significantly high. This implies the need for novel design solutions of compact and lightweight system components. In Fig. 2.5 (left), the trend of saturation pressure as a function of the temperature is shown for each refrigerant. For high molecular complexity fluids, the pressure values are similar to those of haloolefins, and they increase with the refrigerant molecular complexity. This means that, for a fixed temperature lift, simple molecule refrigerants will correspond to high pressure ratio, thus lower compressor efficiency.

A simplified analysis has been conducted to discuss the effect of the natural refrigerants and the haloolefins on the performance of a single-stage VCC system. This analysis focuses solely on the thermodynamic cycle calculations, using a fixed isentropic efficiency value for the centrifugal compressor. Other factors such as pressure drops in the heat exchangers and component sizing have been overlooked. The operating conditions are similar to those of the VCC system for aircraft ECS, i.e., the evaporation and condensation temperatures are chosen respectively equal to 20 °C and 60 °C, and the compressor isentropic efficiency is 0.78. The superheating and the subcooling degrees are kept constant to 5 K. The cooling capacity of the system is 10 kW. Figure 2.6 shows the results in terms of non-dimensional percentage variation of system efficiency for each refrigerant with respect to R-134a, together with the ratio of the refrigerant volumetric flow rate to the volumetric flow rate in the case of R-134a. The results show that the efficiency of a VCC system increases in the case of natural refrigerants classified as dry fluids (positive molecular complexity). The system efficiency that

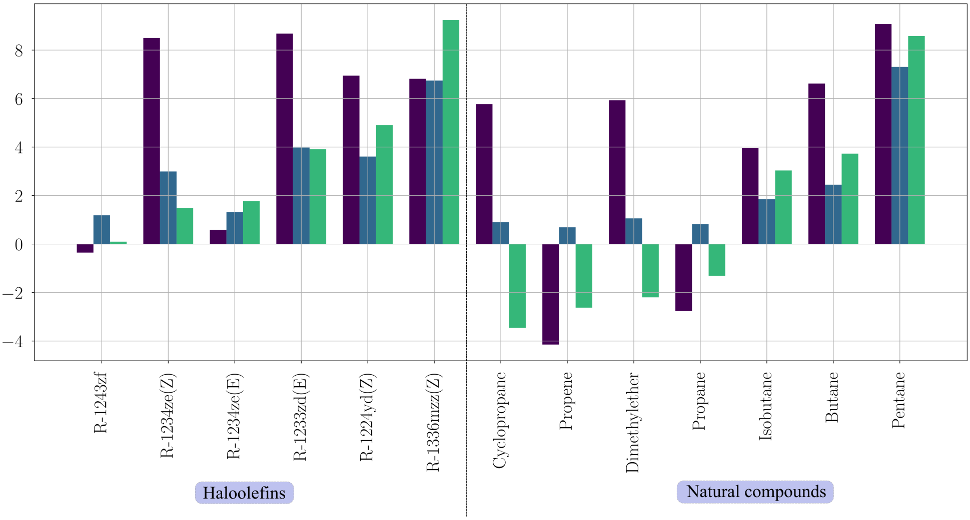

Figure 2.6.: Exemplary case of a single-stage VCC system, with evaporation temperature of 20 °C, condensation temperature of 60 °C, and compressor isentropic efficiency equal to 0.78. The superheating degree and the subcooling degree are both equal to 5 K. The results show a comparison in terms of i) percentage variation of system COP with respect to R-134a (🟪), ii) ratio refrigerant volumetric flow rate to volumetric flow rate of R-134a (🟦), iii) fluid molecular complexity (🟩), in the case haloolefins and natural refrigerants are adopted as working fluids.

can be achieved with these fluids is higher than the one obtained with haloolefins with similar molecular complexity. Furthermore, the significantly lower saturated vapour density allows for large volumetric flow rates. This affects the size of the system components, which feature larger flow passages to reduce the flow velocity and avoid high friction losses. In the case of small-scale centrifugal compressor design, the use of low-density refrigerants allows for a good compromise between impeller wheel diameter and rotational speed. However, the heat exchangers weight may be penalised, since larger flow passages are necessary to moderate the refrigerant flow velocity and the associated pressure drop, especially for the evaporator which operates at the lowest temperature level of the system [42]. The main drawback of these refrigerants is that the existing Heating, Ventilation and Air Conditioning (HVAC) systems would need to be redesigned accounting for both thermodynamic properties and hazard safety measures [25].

NOMENCLATURE

Acronyms

ACM	Air Cycle Machine
ALT	Atmospheric Life Time
AM	Additive Manufacturing
CFC	Chlorofluorocarbon
ECS	Environmental Control System
GWP	Global Warming Potential
HC	Hydrocarbon
HCFC	Hydrochlorofluorocarbon
HCFO	Hydrochlorofluoroolefins
HEX	Heat exchanger
HFC	Hydrofluorocarbon
HFO	Hydrofluoroolefin
HVAC	Heating, Ventilation and Air Conditioning
IRIS	Inverse organic Rankine cycle Integrated System
NBP	Normal Boiling Point [K]
ODP	Ozone Depletion Potential
OH	Hydroxyl radicals
RC-270	Cyclopropane
RE	Radiative Efficiency
RE-170	Dimethyl ether
R-1224yd(Z)	cis-1-Chloro-2,3,3,3-Tetrafluoropropane
R-1234ze(Z)	cis-1,3,3,3-Tetrafluoropropene
R-1234ze(E)	trans-1,3,3,3-Tetrafluoropropene
R-1233zd(E)	trans-1-Chloro-3,3,3-trifluoropropene
R-1243zf	3,3,3-trifuoropropene
R-1270	Propene
R-1336mzz(Z)	cis-1,1,1,4,4,4-hexafluoro-2-butene
R-134a	1,1,1,2-Tetrafluoroethane
R-290	Propane
R-600	Butane
R-600a	Isobutane
R-601	Pentane
TCA	Trifluoroacetic acid
VCC	Vapour Compression Cycle

Roman letters

a	Speed of sound [m·s^{-1}]
c_p	Isobaric specific heat capacity [J·(kg·K)$^{-1}$]
D	Diameter [m]
M	Molar mass [g·mol^{-1}]
N	Molecular complexity [-]
$\dot{m}$	Mass flow rate [kg·s^{-1}]
p	Pressure [Pa]
R	Gas constant [J·(kg·K)$^{-1}$]
s	Entropy [J·(kg·K)$^{-1}$]
T	Temperature [K]
x	Vapour quality [-]

Greek letters

β	Compactness factor [m^{2}·m^{-3}]
β_{tt}	Total-to-total compression ratio [-]
ρ	Density [kg·m^{-3}]
ω	Acentric factor [-]

Superscripts and subscripts

C	Critical point
r	Reduced thermodynamic property
V	Saturated vapour

REFERENCES

[1] P. F. Dexter, R. J. Watts, and W. L. Haskin. “Vapor Cycle Compressors for Aerospace Vehicle Thermal Management”. In: *SAE Transactions* 99 (1990), pp. 1987–1995.

[2] K. Linnett and R. Crabtree. “What’s Next in Commercial Aircraft Environmental Control Systems?” In: *SAE Transactions* 102 (1993), pp. 639–653.

[3] M. Merzvinskas, C. Bringhenti, J. T. Tomita, and C. R. De Andrade. *Air conditioning systems for aeronautical applications: A review*. Apr. 2020. DOI: `10.1017/aer.2019.159`.

[4] Clean Sky 2. *A breath of fresh air with Clean Sky’s Environmental Control System*. Tech. rep. Brussels, 2021.

[5] F. Careri, R. H. Khan, C. Todd, and M. M. Attallah. “Additive manufacturing of heat exchangers in aerospace applications: a review”. In: *Applied Thermal Engineering* 235 (Nov. 2023), p. 121387. ISSN: 1359-4311. DOI: `10.1016/J.APPLTHERMALENG.2023.121387`.

[6] B. Zohuri. “Heat Exchangers”. In: *Application of Compact Heat Exchangers For Combined Cycle Driven Efficiency In Next Generation Nuclear Power Plants* (2016), pp. 125–160. DOI: `10.1007/978-3-319-23537-0`.

[7] K. Kasim, A. Muley, M. Stoia, and F. Ladeinde. “Advanced Heat Transfer Devices for Aerospace Applications”. In: *ASME International Mechanical Engineering Congress and Exposition, Proceedings (IMECE)* 8 (Jan. 2018). DOI: `10.1115/IMECE2017-72382`.

[8] J. Collins-Achong. *Honeywell, Reaction Engines To Collaborate On Sustainable Thermal Management Technologies*. Aug. 2022.

[9] M. V. Casey, D. Krähenbühl, and C. Zwyssig. “The Design of Ultra-High-Speed Miniature Centrifugal Compressors”. In: *European Conference on Turbomachinery Fluid Dynamics and Thermodynamics ETC 10*. 2013.

[10] J. Schiffmann and D. Favrat. “Experimental investigation of a direct driven radial compressor for domestic heat pumps”. In: *International Journal of Refrigeration* 32.8 (Dec. 2009), pp. 1918–1928. ISSN: 01407007. DOI: `10.1016/j.ijrefrig.2009.07.006`.

[11] G. L. Agrawal. “Foil Air/Gas Bearing Technology - An Overview”. In: *Proceedings of the ASME Turbo Expo* 1 (Dec. 2014). DOI: `10.1115/97-GT-347`.

[12] J. Schiffmann, K. Kontomaris, C. Arpagaus, F. Bless, and S. Bertsch. “Scale limitations of gas bearing supported turbocompressors for vapor compression cycles”. In: *International Journal of Refrigeration* 109 (Jan. 2020), pp. 92–104. ISSN: 0140-7007. DOI: `10.1016/J.IJREFRIG.2019.09.019`.

[13] A. Giuffré, P. Colonna, and M. Pini. “The Effect of Size and Working Fluid on the Multi-Objective Design of High-Speed Centrifugal Compressors”. In: *International Journal of Refrigeration* 143 (Nov. 2022), pp. 43–56. ISSN: 01407007. DOI: `10.1016/j.ijrefrig.2022.06.023`.

[14] M. Casey and C. Robinson. *Radial Flow Turbocompressors: design, analysis and applications*. First edition. Cambridge University Press, 2021. ISBN: 9781108416672. DOI: `0.1017/9781108241663`.

[15] M. Sinnett. *787 No-bleed systems: saving fuel and enhancing operational efficiencies*. Tech. rep. 2007.

[16] Liebherr-Aerospace & Transportation SAS. “Technology for Next Generation Fuel Cell Powered Automobile Electrical Single Stage Air Compressor 25 kW ”. In: (2018).

[17] J. Demierre, A. Rubino, and J. Schiffmann. “Modeling and Experimental Investigation of an Oil-Free Microcompressor-Turbine Unit for an Organic Rankine Cycle Driven Heat Pump”. In: *Journal of Engineering for Gas Turbines and Power* 137.3 (Oct. 2014). ISSN: 0742-4795. DOI: 10.1115/1.4028391.

[18] A. Javed, C. Arpagaus, S. Bertsch, and J. Schiffmann. “Small-scale turbocompressors for wide-range operation with large tip-clearances for a two-stage heat pump concept”. In: *International Journal of Refrigeration* 69 (Sept. 2016), pp. 285–302. ISSN: 0140-7007. DOI: 10.1016/J.IJREFRIG.2016.06.015.

[19] D. Essa, B. Spickler, C. Depcik, and M. B. Shiflett. “Air conditioning cycle simulations using a ultrahigh-speed centrifugal compressor for electric vehicle applications”. In: *International Journal of Refrigeration* 131 (Nov. 2021), pp. 803–816. ISSN: 0140-7007. DOI: 10.1016/J.IJREFRIG.2021.07.030.

[20] A. Giuffré. “Integrated design optimization of electrically-driven vapour compression cycle systems for aircraft: powered by high-speed centrifugal compressors”. PhD thesis. Delft: Delft University of Technology, 2024. DOI: 10.4233/uuid:b4f6a4a4-2e48-4bbe-9093-3f1368282f63.

[21] A. Giuffré, P. Colonna, and M. Pini. “Design Optimization of a High-Speed Twin-Stage Compressor for Next-Gen Aircraft Environmental Control System”. In: *Journal of Engineering for Gas Turbines and Power* 145.3 (Mar. 2023). ISSN: 0742-4795. DOI: 10.1115/1.4056022.

[22] M. Molina and F. Rowland. “Stratospheric sink for chlorofluoromethanes: chlorine atom-catalysed destruction of ozone”. In: *Nature* 249 (1974), pp. 810–812. DOI: 10.1038/249810a0.

[23] E. A. Heath. “Amendment to the Montreal Protocol on Substances that Deplete the Ozone Layer (Kigali Amendment)”. In: *International Legal Materials* 56 (Feb. 2017), pp. 193–205.

[24] European Commission. *Proposal for a regulation of the European parliament and of the council on fluorinated greenhouse gases, amending Directive (EU) 2019/1937 and repealing Regulation (EU) No 517/2014*. Tech. rep. May 2022.

[25] M. O. Mclinden, C. J. Seeton, and A. Pearson. “New refrigerants and system configurations for vapor-compression refrigeration”. In: *Science* 370.6518 (Nov. 2020), pp. 791–796. DOI: 10.1126/science.abe3692.

[26] M. Mohanraj and J. D. A. P. Abraham. “Environment friendly refrigerant options for automobile air conditioners: a review”. In: *Journal of Thermal Analysis and Calorimetry* 147.1 (2022), pp. 47–72. ISSN: 1588-2926. DOI: 10.1007/s10973-020-10286-w.

[27] M. P. Sulbaek Andersen, J. A. Schmidt, A. Volkova, and D. J. Wuebbles. “A three-dimensional model of the atmospheric chemistry of E and Z-CF3CH=CHCl (HCFO-1233(zd) (E/Z))”. In: *Atmospheric Environment* 179 (Apr. 2018), pp. 250–259. ISSN: 1352-2310. DOI: 10.1016/J.ATMOSENV.2018.02.018.

[28] C. Arpagaus, R. Kuster, M. Prinzing, F. Bless, M. Uhlmann, E. Büchel, S. Frei, J. Schiffmann, and S. S. Bertsch. "High temperature heat pump using HFO and HCFO refrigerants-system design and experimental results". In: *Refrigeration science and technology proceedings. 25th IIR international congress of refrigeration.* 2019, pp. 4239–4247.

[29] C. Arpagaus and S. Bertsch. "Experimental comparison of HCFO and HFO R-1224yd(Z), R-1233zd(E), R-1336mzz(Z), and HFC R-245fa in a high temperature heat pump up to 150 ○C supply temperature". In: *18th International Refrigeration and Air Conditioning Conference.* Purdue University, 2021.

[30] K. Harby. "Hydrocarbons and their mixtures as alternatives to environmental unfriendly halogenated refrigerants: An updated overview". In: *Renewable and Sustainable Energy Reviews* 73 (June 2017), pp. 1247–1264. ISSN: 1364-0321. DOI: 10.1016/J.RSER.2017.02.039.

[31] ARP292. "Air Conditioning Helicopter General Requirements". In: *SAE International* (2014). DOI: 10.4271/ARP292.

[32] T. J. Wallington, M. P. Sulbaek Andersen, and O. J. Nielsen. "Atmospheric chemistry of short-chain haloolefins: Photochemical ozone creation potentials (POCPs), global warming potentials (GWPs), and ozone depletion potentials (ODPs)". In: *Chemosphere* 129 (June 2015), pp. 135–141. ISSN: 0045-6535. DOI: 10.1016/J.CHEMOSPHERE.2014.06.092.

[33] A. Cavallini. "The state-of-the-art on Refrigerants". In: *Journal of Physics: Conference Series 1599* (2001). DOI: 10.1088/1742-6596/1599/1/012001.

[34] Hodnebrog, B. Aamaas, J. S. Fuglestvedt, G. Marston, G. Myhre, C. J. Nielsen, M. Sandstad, K. P. Shine, and T. J. Wallington. "Updated Global Warming Potentials and Radiative Efficiencies of Halocarbons and Other Weak Atmospheric Absorbers". In: *Reviews of Geophysics* 58.3 (Sept. 2020). ISSN: 1944-9208. DOI: 10.1029/2019RG000691.

[35] ANSI/ASHRAE Standard 34. *ASHRAE Standard 34-2022 - Designation and Safety Classification of Refrigerants.* 2022.

[36] C. M. Invernizzi. *Closed Power Cycles Thermodynamic Fundamentals and Applications.* Londono: Springer, 2013. ISBN: 978-1-4471-5139-5. DOI: 10.1007/978-1-4471-5140-1.

[37] Danfoss. "Refrigerant options now and in the future". In: (Dec. 2023).

[38] G. Angelino and C. Invernizzi. "General method for the thermodynamic evaluation of heat pump working fluids". In: *International Journal of Refrigeration* 11.1 (Jan. 1988), pp. 16–25. ISSN: 0140-7007. DOI: 10.1016/0140-7007(88)90007-2.

[39] ASHRAE 15.2. *Safety Standard for Refrigeration Systems in Residential Applications.* 2022.

[40] ISO 5149-1. *Refrigerating systems and heat pumps: safety and environmental requirements.* 2014.

[41] E. Granryd. "Hydrocarbons as refrigerants — an overview". In: *International Journal of Refrigeration* 24.1 (Jan. 2001), pp. 15–24. ISSN: 0140-7007. DOI: 10.1016/S0140-7007(00)00065-7.

[42] F. Ascione, C. M. De Servi, O. Meijer, V. Pommé, and P. Colonna. "Assessment of an Inverse Organic Rankine cycle system for the ECS of a large rotorcraft adopting a high-speed centrifugal compressor and a low GWP refrigerant". In: *Proceedings of the 6th International Seminar on ORC Power Systems.* Ed. by Technical University of Munich. Technical University of Munich, 2021. DOI: 10.14459/2021mp1633127.

I

INTEGRATED DESIGN OPTIMIZATION METHODS FOR NOVEL AIRCRAFT ECS

3

DESIGN OPTIMIZATION METHODS FOR VCC-BASED AIRCRAFT ECS

Environment is no one's property to destroy;
it is everyone's responsibility to protect.

Mohith Agadi

The design and optimization of aircraft Environmental Control Systems is a complex problem, which involves multiple disciplines and depends on the aircraft operating conditions as well as on manufacturing and integration constraints. The objective is threefold: thermodynamic efficiency maximization, overall weight reduction, and minimization of the drag associated with the ram air. This multi-objective problem greatly benefits from the application of a novel integrated system design optimization method encompassing at the same time the thermodynamic cycle, the selection of the working fluid, and the preliminary design of all the main system components. For this purpose, four different in-house computer programs coupling Modelica system models to a Python open-source genetic optimization algorithm have been developed. In the case all the system components are modelled in the Modelica language, the complexity of the set of equations describing the system model may compromise the robustness of the simulations. Therefore, one solution is to decouple the compressor design model from the Modelica-based system model using the in-house software TurboSim. Furthermore, the computational cost of such a complex optimization problem can be significantly reduced by resorting to a data-driven compressor model. In addition, an independent framework for multi-point integrated system optimization which simultaneously integrates and verifies the performance of the system for different aircraft operating points is also documented here. Finally, a methodology for the preliminary scouting of optimal new refrigerants as working fluids of Vapour Compression Cycle-based Environmental Control Systems has been implemented. The method relies on PC-SAFT equation of state models for the calculation of the thermodynamic properties of the fluids.

Parts of this chapter have been published in

- **F. Ascione**, P. Colonna, and C. M. De Servi. “Integrated design optimization method for novel vapour-compression-cycle-based environmental control systems”. In: Applied Thermal Engineering 236 (Jan. 2024), p. 121261. ISSN: 1359-4311. DOI: 10.1016/J.APPLTHERMALENG.2023.121261.
- A. Giuffré, **F. Ascione**, C. D. Servi, and M. Pini. “Data-driven modeling of high-speed centrifugal compressors for aircraft Environmental Control Systems”. In: International Journal of Refrigeration 151 (July 2023), pp. 354–369. ISSN: 0140-7007. DOI:10.1016/J.IJREFRIG.2023.03.019.

3.1. INTRODUCTION

RElevant research about the aircraft Environmental Control System (ECS) mainly focuses on system design optimization to improve the thermodynamic efficiency, reduce the overall weight and minimize the drag associated with the ram air. Such a study poses a complex challenge, as it depends on various operating conditions of the aircraft and must comply with technological constraints regarding manufacturing and integration. Therefore, many research efforts have been made to assess integrated design optimization methods encompassing at the same time the thermodynamic cycle, the working fluid, and the preliminary design of all the main system components.

Vargas and Bejan [1] proposed an integrated system optimization method for the ECS of commercial aeroplanes, whereby both the cycle operating parameters and the preliminary design of the heat exchangers (HEXs) are considered within the optimization procedure. The exergy destruction associated with the performance and weight of the ECS is minimized. This approach not only allows for the definition of an optimal system operating point but also for the design analysis of the most critical components within the system, e.g., the HEXs. Using the same approach, Pérez-Grande and Leo [2] described the results of the application of a multi-objective optimization method to a bleed-less Air Cycle Machine (ACM) system. The functions to be minimized are the system weight and the entropy generation. However, their study focuses solely on the geometrical design and thermodynamic characterization of the two HEXs. Sielemann *et al.* [3] described an integrated design optimization methodology for an unconventional aircraft ECS architecture, coupling the features of the ACM and of the Vapour Compression Cycle (VCC) systems. The models of the main system components are developed using the equation-based object-oriented Modelica language [4]. The system is optimized by accounting for the minimization of two objective functions, namely the additional specific fuel consumption and the weight associated with the ECS at cruise conditions. The authors draw conclusions about the influence of the HEXs geometrical design on the specific fuel consumption related to the ECS. However, the study neglects the turbomachinery preliminary design and the analysis of its impact on the overall system performance and design. Duan *et al.* [5] investigated the performance of a bleed-air three-wheel bootstrap ACM. They developed custom models for the main components of the system, i.e., turbomachinery and HEXs, together with a dehumidification model of the cabin air stream. The level of detail of the models is limited to the implementation of equations describing the thermodynamic processes, without accounting for components design. The authors assessed an integrated design optimization tool where the objectives are the minimization of the entropy generation rate and the number of heat transfer units. Chen *et al.* [6] developed a modified binary-coded genetic algorithm (GA) for the thermo-economic optimization of a three-wheel ECS for the A330/A340 aircraft. The objective function is the total fuel energy rate calculated as the weighted sum of the shaft power extraction and the propulsive power loss for a fixed cooling capacity of the system. The method does take into account the preliminary design of components, and it accounts only for four optimization variables, i.e., the heat transfer area of the primary and HEXs of the ACM, the ram air mass flow rate, and the ratio of bleed air temperature to total ambient air temperature. Planès *et al.* [7] developed a method for the integrated design optimization of a bleed-less ACM system. The author developed detailed models of system components encompassing both the sizing and the thermodynamics. A single-objective GA optimization method has been utilized. The system has been optimized in two separate steps in the case of hot and cold days for two operating conditions, i.e., aircraft at cruise in case of faulty pack, and aircraft at cruise in normal operation. However, the authors point out the limitation of such an approach, and they assert that a multipoint optimization which simultaneously integrates and verifies the performance of the system for each operating point would be more accurate, even if more computationally expensive.

All the mentioned literature illustrates methods for the optimization of ECS performance, accounting at the same time for the design of the main system components. However, the analysis is usually limited to the design of the HEXs, and the turbomachinery is simply treated by assuming constant values of isentropic efficiency to roughly determine the system power consumption. Moreover, the available studies only pertain to the ACM technology, and a limited number of works concern the optimization of the VCC technology for aircraft ECS [8, 9]. The objective of the work documented in this dissertation is to bridge this knowledge gap by proposing four different integrated optimization design methods for the electrically-driven VCC-based aircraft ECS described in Ch. 1. The *in-house* numerical frameworks allow for the optimization of the thermodynamic cycle, the working fluid, and the preliminary design of all the main system components, i.e., the HEXs, the air intakes, the piping and the centrifugal compressor in an integrated fashion. The system model comprises lumped parameter component models coded by means of the acausal modelling language Modelica [4]. All four optimization methods rely on a Genetic Algorithm (GA), and the differences among them pertain to the integration of the centrifugal compressor model within the system, and the criteria used for the working fluid selection. The number of optimization variables varies depending on the specific application and design objectives being addressed.

This chapter is structured as follows. First, the design methodology implemented for the models of the main system components is illustrated in detail. Then, the different multi-objective integrated design optimization frameworks are described, and their pros and cons discussed. Finally, the main outcomes are summarized in the conclusions.

3.2. MODELS

Two applications were chosen as test cases of the novel electrically-driven VCC-based ECS, i.e., the ECS of a high-payload rotorcraft (Fig. 1.6), and the ECS of a passenger aircraft (Fig. 1.4). The developed steady-state system models have been coded using the equation-based, acausal, object-oriented Modelica language [4]. The Modelica language, being acausal, allows for the use of the same model of a component for both *on-design* and *off-design* simulations[1]. The *in-house* library *DeSimECS* (Design and Simulation of Energy Conversion Systems) featuring multi-domain lumped-parameters models of components, e.g., thermal, hydraulic, mechanical, and electrical components for steady-state simulations was further developed for this purpose. All the models are mathematically described by systems of non-linear algebraic equations including conservation and constitutive equations. Component models can be assembled to build systems of different complexity.

All the models of the main components of the VCC-based ECS model, i.e., HEXs, piping, valves, and intakes are based on the Modelica language and they are all included in the *DeSimECS* library. The models for the preliminary design of the centrifugal compressor rely on a mean-line approach, and three design tools have been developed: i) a Modelica model of the component belonging to the *DeSimECS* library, ii) a more sophisticated Python-based *in-house* tool called *TurboSim*, and iii) a data-driven model of the component. The last two models have been developed within another work package of this research project.

3.2.1. AIR INTAKE

Air intakes supply the cabin with fresh air and provide ram air to the HEXs of the ECS packs. For the design of the aircraft ECS, to comply with the need to minimize the ram air drag

---

[1] Input variables can be freely chosen before running the simulation without modifying the code, provided that they comply with the mathematical constraints that allow for the numerical solution of the system of equations associated with the model.

penalty, flush intakes have been preferred to scoop intakes since they allow for larger total pressure recovery. The geometry selected for the flush intake is the one installed on the Boeing 747, i.e., a rectangular entry and a NACA curved-divergent ramp (Fig. 3.1).

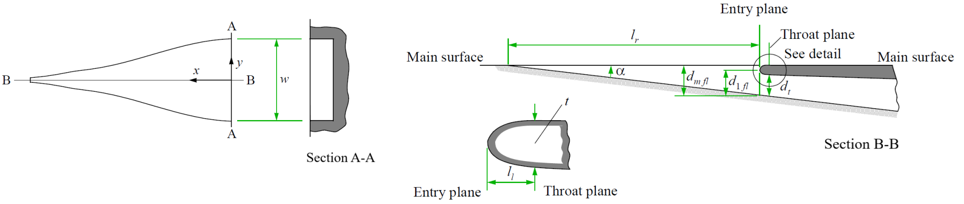

Figure 3.1.: Schematic of the flush intake with a rectangular entry and a NACA curved-divergent ramp [10].

The air intakes are modelled following the methodology documented by the Engineering Sciences Data Unit (ESDU) [10]. This method is only valid in the case of subsonic speed and it is based on semi-empirical correlations fitted to the sets of experimental data. The drag penalty associated with the air mass flow rate ingested by the intake is defined as

$$D = \dot{m}_\infty v_\infty \frac{C_\mathrm{D}}{2}, \tag{3.1}$$

where $\dot{m}_\infty$ and v_∞ are the mass flow rate and velocity of the air in free-stream conditions. The drag coefficient C_D is estimated by summing the terms associated with the ram drag $C_\mathrm{D,ram}$, the spillage drag $C_\mathrm{D,sp}$, the increase of drag in the case of mass flow rate close to the intake chocking condition ΔC_D.

$$C_\mathrm{D} = C_\mathrm{D,ram} + C_\mathrm{D,sp} + \Delta C_\mathrm{D} = 2k_\mathrm{fl}\frac{\dot{m}}{\dot{m}_\infty} + k_\alpha k_\mathrm{m} k_\mathrm{sp,fl} C'_\mathrm{D} + \Delta C_\mathrm{D}. \tag{3.2}$$

The ESDU [10] provides semi-empirical correlations for the estimation of the coefficients of Eq. (3.2). In particular, k_fl is associated with the ram drag component, and its value depends on the intake geometry. The coefficients k_α, k_m, and $k_\mathrm{sp,fl}$ are correction factors of the spillage drag coefficient at zero mass flow C'_D, used to account for the real values of the ramp angle, Mach number, and mass flow ratio $\dot{m}/\dot{m}_\infty$. The term ΔC_D is obtained as a function of the mass flow ratio.
The air intake pressure recovery factor C_p is defined as

$$C_p = \frac{p_\mathrm{t,1} - p_\infty}{p_\mathrm{t,\infty} - p_\infty}. \tag{3.3}$$

The ESDU [10] illustrates a methodology to calculate the pressure recovery factor as

$$C_p = C_{p,\mathrm{m}} + \Delta C_{p,\mathrm{mf}} + \Delta C_{p,\alpha} + \Delta C_{p,\mathrm{w}}. \tag{3.4}$$

The terms on the right-hand side of Eq. 3.4 are coefficients defined with semi-empirical correlations. More specifically, $C_{p,\mathrm{m}}$ is the ideal value of the pressure recovery factor when the intake geometry is optimized for the mass flow rate design value. The coefficients $\Delta C_{p,\mathrm{mf}}$, $\Delta C_{p,\alpha}$, and $\Delta C_{p,\mathrm{w}}$ are used to consider the real values of the mass flow ratio, ramp angle, and aspect ratio. Both the correlations for the drag penalty and the pressure recovery factor estimation are applicable only in the case of flush intakes with a maximum ramp angle of 11.5°. Tables 3.1 and 3.2 list the range of validity of the equations proposed by the ESDU for the drag penalty and the pressure recovery factor estimation, respectively.

Table 3.1.: Ranges of applicability for the drag coefficient estimation [10].

Derivation	**Lip shape**	**Entry cross-section**	$w/d_{1\mathrm{fl}}$ / –	α / °	$\delta/d_{1\mathrm{fl}}$ / –	M / –
Mossman *et al.* [11]	round	rectangular	2, 4, 6	7	∼0.4 - 0.8	< 0.23
Mossman *et al.* [11]	round	curved-divergent	4	5, 7, 9, 11.5	∼0.5	< 0.23
Dennard [12]	round	rectangular	4	7	∼0.8	0.55 - 0.9
Dennard [12]	round	curved-divergent	4	7	∼0.8	0.55 - 0.9

Table 3.2.: Ranges of applicability for the pressure recovery factor estimation [10].

Derivation	**Lip shape**	**Ramp profile**	w/d_{t} / –	α / °	δ/d_{t} / –	M / –
Mossman *et al.* [11]	round	curved-divergent	4	5-11.5	0.05	< 0.23
Delany [13]	round	curved-divergent	4	7	0.02 - 0.03	0.2
Axelson and Taylor [14]	round	curved-divergent	4	6.5	0.012 - 0.044	0.8 - 0.9
Frank [15]	round	curved-divergent	4	7	0.02 - 0.065	0.3 - 0.9
Selna and Schlaff [16]	round	curved-divergent	4	7	0.03	0.8 - 0.9
McCreath and Smith [17]	round	curved-divergent	3.8, 4, 4.6	7, 8	0.04 - 0.424	0.1

The flush intake model can be used for both *on-design* and *off-design* simulations. In design mode, the intake geometry is a function of a given operational requirement at the design point mass flow rate. In the case of *off-design* simulations, the performance metrics of the intake depend on the intake geometry and the selected operating point. This procedure can be iterated for different operating points until the choking occurs.

3.2.2. HEAT EXCHANGERS

A VCC-based ECS typically includes two HEXs, i.e., a condenser, and an evaporator. In the case of the helicopter application, the system encompasses a third HEX known as intercooler. The need for lightweight and highly efficient systems calls for the adoption of compact heat exchangers (CHEXs) [18].

CONDENSER AND EVAPORATOR

The condenser and the evaporator are finned-tube CHEXs. The working fluids, namely air and refrigerant, circulate according to a cross-flow arrangement. More specifically, the refrigerant flows into flat tubes featuring small internal passages, i.e., minichannels with rectangular section (the hydraulic diameter ranges from 3 mm to 0.2 mm [19]), while the air flows outside the channels. The fins are of the multilouvered type: several louvers along the fin length increase the heat transfer surface on the air side. The continuous breaking of the boundary layer of the flow passing through the louvers promotes the enhancement of the heat transfer coefficient by two to four times with respect to unlouvered surfaces with the same dimensions. The CHEXs equipping aircraft ECSs are derived from the CHEXs employed on board automotive vehicles as radiators and their typical compactness factor is around 1100 $\mathrm{m}^2 \cdot \mathrm{m}^{-3}$ [18]. Figure 3.2 shows the main geometrical parameters of the CHEX core. Its geometrical characterization, as well as the weight estimation, are based on the guidelines by Shah and Sekulic [20]. The condenser model implemented in the *DeSimECS* library has been validated by comparing the numerical results to the outcome of the experimental campaign documented in the work by Kim and Bullard [21], who tested microchannel condensers for a room air conditioning system. The results show a discrepancy lower than 4% in the calculation of the heat transfer surface and a 10% deviation in the estimation of the pressure drop. It was not possible to carry out a comparison in terms of heat transfer coefficient, as this quantity was not reported in the aforementioned study.

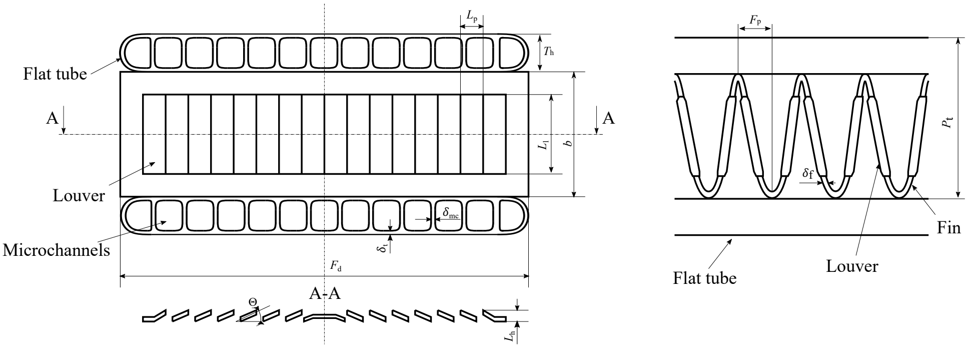

Figure 3.2.: Minichannels flat tubes and multilouvered fins HEX geometry.

The HEXs are critical components for what concerns the evaluation of the performance and the weight of an aircraft ECS, hence their models should achieve an optimal trade-off between results accuracy and numerical complexity. The Moving Boundary (MB) method has been preferred to a Finite Volume (FV) discretization method as it allows for lower computational cost without compromising model accuracy, as demonstrated by Bendapudi *et al.* [22]. The MB models of the evaporator and condenser are obtained by dividing the HEX length in a number of control volumes equal to the number of thermodynamic phases of the refrigerant. For instance, the condenser features three control volumes (CVs) for the refrigerant side, namely a dry vapour (desuperheating) CV, a two-phase flow (condensation) CV and a liquid flow (subcooling) CV, as displayed in Fig. 3.3. Mass and energy balance equations are solved for each control volume, whose length depends on the refrigerant vapour quality. The main modelling assumptions are: i) both the refrigerant and the air flows are one-dimensional; ii) the specific enthalpy distribution is linear with the length within each CV, therefore thermodynamic properties are computed as an average of the ones at the inlet and the outlet of each CV; iii) the void fraction of the two-phase flow refrigerant is calculated by assuming that the homogeneous flow model holds. More specifically, the slip ratio (s), expressed as the ratio between the velocity of the gaseous flow (v_V) to the velocity of the liquid (v_L), is assumed equal to one, meaning that the two flow phases are perfectly mixed [23][2]; iv) the air outlet temperature is computed according to the assumption of ideal mixing of the air streams exiting each control volume.

Heat transfer coefficient and pressure drop are evaluated using specific correlations for each refrigerant phase. These correlations have been selected following the guidelines provided by two well-known handbooks about heat transfer and heat exchanger design, i.e., Shah and Sekulic [20] and the “VDI Heat Atlas” [24]. The correlations are formulated in non-dimensional terms, i.e., Colburn factor j or Nusselt number Nu for the heat transfer coefficient, and friction factor f for the pressure drop. Tables 3.3 and 3.4 list the set of correlations implemented in the HEXs models, for both the refrigerant and the air side. Notice that the

---

[2] This simplified approach could lead to an underestimation of the refrigerant charge within the HEX, potentially resulting in the downsizing of the component, as demonstrated by Bendapudi *et al.* [22]. Alternatively, the heterogeneous flow model could be employed to incorporate more detailed methods for estimating the void fraction. However, this would increase the complexity of the set of equations to be solved in the model, without yielding significant improvements in the accuracy of the HEX performance predictions.

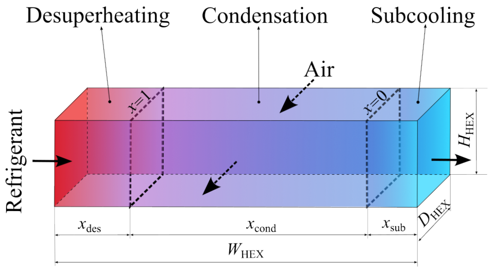

Figure 3.3.: Schematic of the Moving Boundary modelling approach applied to the refrigerant channels of the condenser. The vapour quality x distinguishes the different control volumes depending on the fluid phase.

correlation by Kim and Bullard [25] has been preferred to that of Chang and Wang [26] to predict the friction factor on the air side of the HEXs, as it accounts also for the effect of the fin depth. Moreover, regarding the prediction of the two-phase flow friction factor inside the flat tubes, the correlation by Schmidt *et al.* [23] has been selected in place of those proposed by Lockhard and Martinelli [27] and Chisholm [28], given its independence from the range of the mass flux G.

In each control volume, the heat transfer rate is estimated according to the relation between the effectiveness (ϵ) and the number of thermal units (NTU) of the heat exchanger. The definition of ϵ depends on both the flow arrangement and the phase of the refrigerant [25]. In case of unmixed cross-flow and single-phase flow, it is expressed as

$$\epsilon = 1 - \exp\left\{ \frac{\mathrm{NTU}^{0.22}}{C_{\mathrm{r}}} \left[\exp\left(-C_{\mathrm{r}} \mathrm{NTU}^{0.78} \right) - 1 \right] \right\}. \tag{3.5}$$

In the case evaporation or condensation occurs within the heat exchanger tubes, the heat capacity ratio C_{r} is zero, and the effectiveness can be calculated as

$$\epsilon = 1 - e^{-\mathrm{NTU}}. \tag{3.6}$$

The NTU is defined as the product of the overall heat transfer coefficient U and the total heat transfer surface A, divided by the minimum heat transfer capacity between the two working fluids. The overall heat transfer coefficient UA accounts for both the effect of convection and conduction, due to the presence of the fins and the tubes

$$\frac{1}{UA} = \frac{1}{h_{\mathrm{air}} \eta_{\mathrm{c}} A_{\mathrm{air}}} + \frac{1}{h_{\mathrm{refr}} A_{\mathrm{refr}}} + R_{\mathrm{t}}. \tag{3.7}$$

The fins surface effectiveness η_{c} is a function of the fin efficiency η_{f} [25] and is given by

$$\eta_c = 1 - \frac{A_{\mathrm{f}}}{A_{\mathrm{air}}} \left(1 - \eta_{\mathrm{f}}\right) = 1 - \frac{A_{\mathrm{f}}}{A_{\mathrm{air}}} \left(1 - \frac{\tanh m l_{\mathrm{f}}}{m l_{\mathrm{f}}}\right), \tag{3.8}$$

where

$$m = \sqrt{\frac{2 h_{\mathrm{air}}}{k_{\mathrm{f}} \delta_{\mathrm{f}}} \left(1 + \frac{\delta_{\mathrm{f}}}{F_{\mathrm{d}}}\right)}, \tag{3.9}$$

$$l_{\mathrm{f}} = \frac{H}{2} - \delta_{\mathrm{f}}. \tag{3.10}$$

Table 3.3.: List of empirical correlations selected for the condenser and evaporator heat transfer coefficient estimation.

Heat transfer correlations		
Working fluid	**Reference**	**Equation**
Air	Chang and Wang [26]	$j = Re_{\mathrm{Lp}}^{-0.487} \left(\frac{\Theta}{90}\right)^{0.257} \left(\frac{F_\mathrm{p}}{L_\mathrm{p}}\right)^{-0.13} \left(\frac{b}{L_\mathrm{p}}\right)^{-0.29} \left(\frac{F_\mathrm{d}}{L_\mathrm{p}}\right)^{-0.235} \times \left(\frac{L_\mathrm{l}}{L_\mathrm{p}}\right)^{0.68} \left(\frac{T_\mathrm{p}}{L_\mathrm{p}}\right)^{-0.279} \left(\frac{\delta_\mathrm{f}}{L_\mathrm{p}}\right)^{-0.05}$
Single-phase refrigerant	Gnielinski [29]	• $\begin{cases} Nu = \left\{4.364^3 + \left(1.953\sqrt[3]{RePrD_\mathrm{i}/l} - 1\right)^3 + \left(0.924\sqrt[3]{Pr}\sqrt{Re(D_\mathrm{i}/l)}\right)^3\right\}^{1/3}, \\ Re < 2300 \end{cases}$ • $\begin{cases} Nu = 0.0214(Re^{0.8} - 100)Pr^{0.4}[1 + (D_\mathrm{i}/l)^{2/3}], \\ 0.5 \leq Pr \leq 1.5; 2300 \leq Re \leq 10^4 \end{cases}$ • $\begin{cases} Nu = 0.012(Re^{0.87} - 280)Pr^{0.4}[1 + (D_\mathrm{i}/l)^{2/3}], \\ 1.5 \leq Pr \leq 500; 2300 \leq Re \leq 10^4 \end{cases}$ • $\begin{cases} Nu = \frac{(\xi/8)RePr}{1 + 12.7\sqrt{(\xi/8)}(Pr^{2/3} - 1)}[1 + (D_\mathrm{i}/l)^{2/3}], \\ \xi = (1.8\log_{10} Re - 1.5)^{-2}, \\ Re > 10^4 \end{cases}$
Evaporation	Kandlikar [30]	$\begin{cases} h = h_\mathrm{L}[\mathrm{C_1 Co^{C_2}}(25Fr_\mathrm{L})^{\mathrm{C_5}} + \mathrm{C_3}Bo^{\mathrm{C4}}\mathrm{F_{fl}}], \\ h_\mathrm{L} = 0.023Re_\mathrm{L}^{0.8}Pr_\mathrm{L}^{0.4}(k_\mathrm{L}/D_\mathrm{i}) \end{cases}$
Condensation	Shah [31]	$h = 0.023\frac{k_\mathrm{L}}{D_\mathrm{i}}Re_\mathrm{L}^{0.8}Pr_\mathrm{L}^{0.4}\left\{(1-x)^{0.8} + \frac{3.8x^{0.76}(1-x)^{0.04}}{(p_\mathrm{sat}/p_\mathrm{cr})^{0.38}}\right\}$

The thermal resistance of the microchannel walls is calculated as [34]

$$R_\mathrm{t} = \frac{1}{2\pi k}\left(\frac{1}{l_\mathrm{t}\mathrm{N_{mc}N_t}}\right)\log\left(\frac{D_\mathrm{ext,mc}}{D_\mathrm{ext,mc} - 2\delta_\mathrm{mc}}\right). \tag{3.11}$$

The heat exchanger models include also a method to estimate their dry weight. Once the geometry has been fully determined, the volume of the material forming the HEX core can be computed as the sum of the volume occupied by the fins V_f, and that of the microchannels tubes V_t. With reference to Fig. 3.2, these two volumes are calculated as

$$\begin{cases} V_\mathrm{f} = \delta_\mathrm{f}\left[\left(b^2 + F_\mathrm{p}^2\right)^{1/2} - \delta_\mathrm{f}\right]F_\mathrm{d}\mathrm{N_f} \\ V_\mathrm{t} = x_\mathrm{HEX}\left[\frac{\pi}{2}\delta_\mathrm{t}\mathrm{N_t}\left(T_\mathrm{h} + F_\mathrm{d} - 2\delta_\mathrm{t}\right) + \delta_\mathrm{mc}\left(T_\mathrm{h} - 2\delta_\mathrm{t}\right)\left(\mathrm{N_{mc}} - 1\right)\right]. \end{cases} \tag{3.12}$$

Then, based on the prescribed material, the weight of the heat exchanger is computed as the product of the material density and the total volume. Finally, the result is multiplied by an empirical coefficient, to account for casing, manifold, and soldering in the weight estimation.

The flow chart in Fig. 3.4 shows the computational scheme, depending on the type

Table 3.4.: List of empirical correlations selected for the friction factor estimation of condenser and evaporator.

Pressure drop correlations		
Working fluid	**Reference**	**Equation**
Air	Kim and Bullard [25]	$f = Re_{\mathrm{Lp}}^{-0.487}\left(\frac{\Theta}{90}\right)^{0.444}\left(\frac{F_\mathrm{p}}{L_\mathrm{p}}\right)^{-1.682}\left(\frac{b}{L_\mathrm{p}}\right)^{-1.22}\left(\frac{F_\mathrm{d}}{L_\mathrm{p}}\right)^{0.818}\left(\frac{L_\mathrm{l}}{L_\mathrm{p}}\right)^{1.97}$
Single phase refrigerant	Kast *et al.* [32]	• $f = \frac{64}{Re},\ Re < 3000$ • $f = \frac{0.3164}{\sqrt[4]{Re}},\ 3000 \le Re \le 10^4$ • $f = 0.0054 + \frac{0.3964}{Re^{0.3}},\ 2 \cdot 10^4 \le Re \le 2 \cdot 10^6$ • $\frac{1}{\sqrt{f}} = -0.8 + 2\log\left(Re\sqrt{f}\right),\ Re > 10^6$
Two-phase refrigerant	Schmidt and Friedel [33]	$\begin{cases} \left(\frac{\Delta p}{l}\right) = \Phi_\mathrm{L}^2\left(\frac{\Delta p}{l}\right)_\mathrm{L}, \\ \Phi_\mathrm{L}^2 = E + \frac{3.24FH}{Fr^{0.045}We^{0.035}}, \\ E = (1-x)^2 + x^2(f_\mathrm{V}/f_\mathrm{L})(\rho_\mathrm{L}/\rho_\mathrm{V}), \\ F = x^{0.78}(1-x)^{0.24}, \\ H = (\rho_\mathrm{L}/\rho_\mathrm{V})^{0.91}(\mu_\mathrm{V}/\mu_\mathrm{L})^{0.19}(1-\mu_\mathrm{V}/\mu_\mathrm{L})^{0.7} \end{cases}$

of calculation, thus either an *on-design* or *off-design* calculation. More specifically, in *on-design* mode, the operating conditions at the inlet and outlet of the HEXs are provided as input values, and the main dimensions are estimated (e.g., the HEX width) to match the required thermal load. In *off-design* mode, the geometry is fully specified, while one of the thermodynamic input variables (e.g., the air mass flow rate) is calculated.

INTERCOOLER

The other heat exchanger of the system is the intercooler, or economizer. It consists of a chevron gasketed Plate Heat Exchanger (PHEX). A number of gasketed metal plates of rectangular shape are clamped together. A corrugated surface is stamped on each thin plate to create interconnected parallel flow channels where the refrigerant flows with multiple changes in direction. The chevron-type corrugation, in particular, features a sinusoidal pattern, whose crests and troughs are oriented with a certain angle against the main flow direction in one or several strips of fixed width, as shown in Fig. 3.5 [35].

At each corner of the plates, there are circular ports where the refrigerant enters the HEX to be directed through the channels formed in the space between two plates, before exiting. PHEXs operate at moderate temperature and pressure. They are typically employed for liquid-to-liquid or liquid-to-two phase heat transfer and their compactness factor ranges from 120 to 230 $\mathrm{m}^2 \cdot \mathrm{m}^{-3}$ [18]. For the selected application, the refrigerant is liquid on one side and two-phase on the other side. The model is zero-dimensional and, depending on the refrigerant phase, different correlations have been implemented in the code to estimate the heat transfer coefficient and the pressure drop, as listed in Tab. 3.5. This set of equations has been chosen according to the recommendations by Palm *et al.* [36].

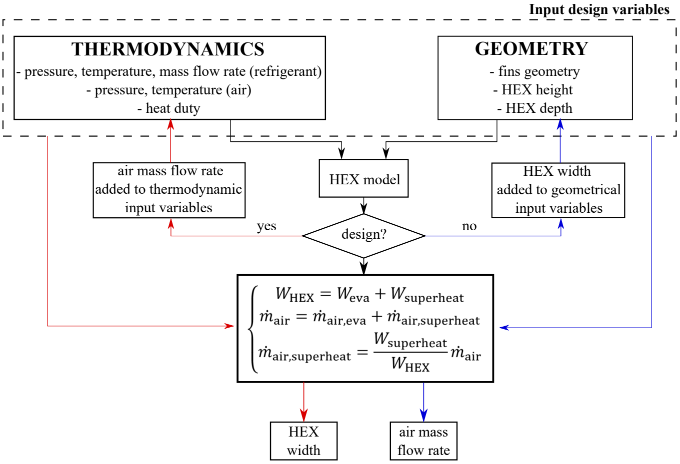

Figure 3.4.: Flow chart illustrating the *on/off-design* calculation methodology implemented in the HEXs model (exemplary case: evaporator).

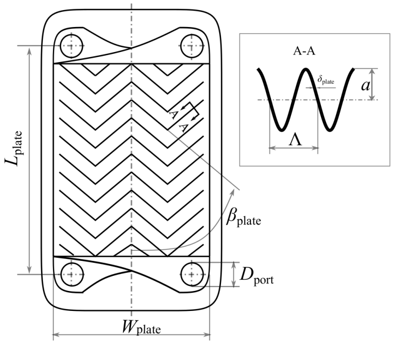

Figure 3.5.: Chevron-type plate heat exchanger geometry.

Also in this case, the effectiveness-NTU method is used to calculate the heat duty. The geometrical characterization of the PHEX follows the procedure described by Shah and Sekulic [20]. The model has been verified by comparing the results with those obtained using a well-established commercial software for HEX design and rating [39]. The comparison shows a 2% deviation in the calculation of the heat transfer surface and a deviation of less than 1% in the computation of the outlet flow temperature. The heat transfer coefficient of the single-phase and of the two-phase refrigerant flows are estimated with an uncertainty approximately equal to 18% and 5%, respectively.

In the case of PHEXs, due to the complexity of the chevron corrugation patterns, the volume is approximated as the number of plates times the volume of a single plate, computed without accounting for the additional volume due to corrugations. Thus, as shown in (Eqn. 3.13), the weight is obtained by multiplying the HEX dry volume by the density of the material as

Table 3.5.: List of empirical correlations selected for the aerothermal characterization of the chevron gasketed PHEX.

Heat transfer correlations

Working fluid	**Reference**	**Equation**
Single-phase refrigerant	Martin [37]	$Nu = 1.615 \left[\left(f \frac{Re}{64} \right) Re Pr \left(\frac{D_\mathrm{h}}{\Lambda} \right) \sin(2\beta_\mathrm{plate}) \right]^{1/3}$
Two-phase flow refrigerant	Cooper [38]	$h = 55(Pr^{0.12-0.2\log_{10}\mathrm{Ra}})(-\log_{10} Pr)^{-0.55} M_\mathrm{r}{}^{-0.5} q^{0.8}$

Pressure drop

Working fluid	**Reference**	**Equation**
Single-phase refrigerant	Martin [37]	$\begin{cases} \frac{1}{\sqrt{f}} = \frac{\cos\beta_\mathrm{plate}}{\sqrt{0.18\tan\beta_\mathrm{plate} + 0.36\sin\beta_\mathrm{plate} + f_0(Re)/\cos\beta_\mathrm{plate}}} + \frac{1-\cos\beta_\mathrm{plate}}{\sqrt{f_1(Re)}}, \\ f_0(Re) = 64/Re, \ \ Re < 2000 \\ f_0(Re) = (1.8\ln Re - 1.5)^{-2}, \ \ Re \geq 2000 \\ f_1(Re) = 3.8(597/Re) + 3.85, \ \ Re < 2000 \\ f_1(Re) = 3.8(39/Re^{0.289}), \ \ Re \geq 2000 \end{cases}$
Two-phase flow refrigerant	Lockhard and Martinelli [27]	$\begin{cases} \left(\frac{\Delta p}{l} \right) = \phi_\mathrm{L}^2 \left(\frac{\Delta p}{l} \right)_\mathrm{L}, \\ \phi_\mathrm{L}^2 = 1 + \frac{\mathrm{K}}{X} + \frac{1}{X^2}, \\ X = \left(\frac{1-x}{x} \right)^{(2-n)/2} \left(\frac{\mu_\mathrm{L}}{\mu_\mathrm{V}} \right)^{n/2} \left(\frac{\rho_\mathrm{V}}{\rho_\mathrm{L}} \right)^{0.5} \end{cases}$

$$\begin{cases} \mathrm{weight}_\mathrm{PHEX} = \rho_\mathrm{material} V_\mathrm{PHEX} \\ V_\mathrm{PHEX} = \delta_\mathrm{plate} H_\mathrm{plate} W_\mathrm{plate} N_\mathrm{plate} \end{cases} \tag{3.13}$$

3.2.3. PIPELINE

The performance of a VCC system may be significantly affected by the pressure drop due to the working fluid flowing through the pipelines of the system, as they are usually quite long. In particular, if the working fluid is a low-density refrigerant enabling the design of a more efficient compressor, the friction losses in the pipeline operating at the lowest temperature level (e.g., the one connected to the evaporator) may become critical. In this regard, the correct sizing of the hoses is of fundamental importance to evaluate the influence of pressure drops in the refrigerant loop on system efficiency. The duct model is zero-dimensional. It can be used either in *on-design* mode to size the pipe internal diameter given the length, surface roughness and thermodynamic conditions, or in *off-design* mode to calculate the pressure drop given the duct dimensions. The friction factor is estimated from the set of correlations listed in Tab. 3.6, depending on the flow regime.

The pipeline weight is calculated from the tube thickness estimation. The ASME B31.5 standard [40] provides the relation

$$\delta_\mathrm{pipe} = \frac{p_\mathrm{gauge} D_\mathrm{out}}{2(\sigma_\mathrm{max} + p_\mathrm{gauge} y)} \tag{3.14}$$

Table 3.6.: List of correlations selected for the friction factor estimation in straight pipes [32].

Flow regime	**Friction factor**	**Equation**
Laminar	$f = \frac{64}{Re}, Re < 2300$	Hagen-Poiseuille
Transitional	$f = \frac{0.316}{Re^{0.25}}, 2300 < Re < 4000$	Blasius
Turbulent	$\frac{1}{\sqrt{f}} = -2 - \ln\left(\frac{\epsilon}{3.71D} + \frac{2.51}{Re\sqrt{f}}\right), Re > 4000$	Colebrook and White

to calculate the minimum allowable thickness (δ_{pipe}) of straight pipes to withstand the internal design gauge pressure (p_{gauge}). In the case of aerospace applications, specific guidelines are set out for the estimation of the internal design gauge pressure. The CS-25 (Amendment 3) certification manual [41] advises to account for a multiplication safety factor equal to 3 for the system design pressure.

3.2.4. CENTRIFUGAL COMPRESSOR

Three different models have been developed for the preliminary design and simulation of twin-stage back-to-back centrifugal compressor (Fig. 3.6). The models are different because they are coded with different programming languages and their level of complexity and thus of accuracy is also different.

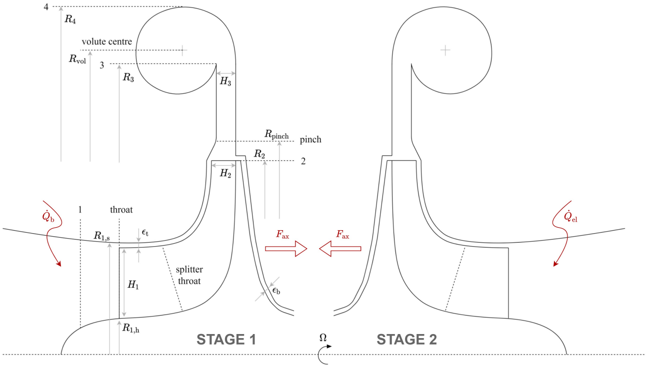

Figure 3.6.: Meridional view of a centrifugal compressor featuring two stages mounted in a back-to-back configuration on the same shaft [42].

In all cases, the compressor design method is based on the guidelines documented in Refs. [42, 43]. This method relies on a mean-line approach, whereby a centrifugal compressor stage can be designed as a function of a vector $\mathbf{X}_{\text{C}}$ of eight design variables

$$\mathbf{X}_{\text{C}} = \left[\phi_{\text{t1}}, \psi_{\text{is}}, k, \alpha_2, N_{\text{bl}}, R_3/R_2, R_{\text{r,pinch}}, H_{\text{r,pinch}}\right]. \tag{3.15}$$

where ϕ_{t1} is the swallowing capacity

$$\phi_{\mathrm{t1}} = \frac{\dot{m}}{\rho_{\mathrm{t1}} U_2 D_2^2}, \tag{3.16}$$

ψ_{is} is the isentropic loading coefficient

$$\psi_{\mathrm{is}} = \frac{\Delta h_{\mathrm{tt,is}}}{U_2^2}, \tag{3.17}$$

k is the impeller shape factor

$$k = 1 - \left(\frac{R_{1,\mathrm{h}}}{R_{1,\mathrm{s}}}\right)^2, \tag{3.18}$$

and $R_{\mathrm{r,pinch}}$ and $H_{\mathrm{r,pinch}}$ are non-dimensional parameters used to characterize the diffuser shape

$$\begin{aligned} R_{\mathrm{r,pinch}} &= \frac{R_{\mathrm{pinch}} - R_2}{R_3 - R_2} \\ H_{\mathrm{r,pinch}} &= \frac{H_3 - H_2}{H_2(R_2/R_{\mathrm{pinch}} - 1)}. \end{aligned} \tag{3.19}$$

The design method requires some specifications, such as the nominal total-to-total pressure ratio β_{tt}, the nominal mass flow rate $\dot{m}$, the working fluid, the nominal total inlet conditions, and geometrical parameters imposed by manufacturing constraints, e.g., the impeller tip clearance gap. Additionally, since the two compressor wheels are mounted on the same shaft, the rotational speed of the second impeller is constrained by the design of the first stage. Therefore, the work coefficient chosen for the second stage is univocally related to its flow coefficient, or vice-versa.

Assuming that the compressor is vaneless, the flow is taken as uniform at the impeller inlet section. The design of the impeller inlet geometry follows the approach proposed by Rusch and Casey [44]. The swallowing capacity ϕ_{t1} is proportional to the compressor flow coefficient (Eq. 3.16). The design of highly loaded centrifugal compressors with large swallowing capacity must account for limitations on the maximum inlet relative Mach number at the shroud. In particular, a Mach number higher than approximately 1.35 may trigger boundary layer separation due to shock interaction within the rotor flow channels, causing additional losses associated with secondary flows and mixing. To account for this effect, Rusch and Casey [44] have defined a modified mass flow Φ' as

$$\Phi' = \Phi_{\mathrm{t}} \frac{4M_{u2}^2}{k\pi} = \frac{M_{w_{1,\mathrm{s}}}^3 \sin^2\beta_{1,\mathrm{s}} \cos\beta_{1,\mathrm{s}}}{\left(1 + \dfrac{\gamma_{Pv} - 1}{2} M_{w_{1,\mathrm{s}}}^2 \cos^2\beta_{1,\mathrm{s}}\right)^{1/(\gamma_{Pv}-1)+3/2}}, \tag{3.20}$$

which is thus a function of the inlet blade metal angle at the impeller inlet casing ($\beta_{1,\mathrm{s}}$) and of the relative inlet Mach number at the shroud ($M_{w_{1,\mathrm{s}}}$). The authors demonstrate that, for a given Φ', it is possible to univocally determine the $\beta_{1,\mathrm{s}}$ which minimizes $M_{w_{1,\mathrm{s}}}$. Hence, to reduce the effect of shock losses, an optimal inlet blade metal angle corresponding to the lowest impeller inlet relative Mach number can be defined for each design point as

$$\cos\beta_{1\mathrm{s,opt}} = \frac{\sqrt{3+\gamma_{Pv} M^2_{w_{1,\mathrm{s}}} + 2M_{w_{1,\mathrm{s}}}} - \sqrt{3+\gamma_{Pv} M^2_{w_{1,\mathrm{s}}} - 2M_{w_{1,\mathrm{s}}}}}{2M_{w_{1,\mathrm{s}}}}. \tag{3.21}$$

Given this information, the static thermodynamic state and the velocity triangle at the inlet of the impeller can be obtained. The meanline model considers the effect of the slip at the impeller outlet to estimate the velocity triangle by accounting for the flow angular momentum reduction. The slip factor, calculated using the model proposed by von Backström [45], quantifies the deviation of the outlet relative flow angle from the impeller outlet blade metal angle. Downstream of the impeller, a vaneless diffuser with parallel walls is considered.

The compressor model includes a method for the estimation of the axial thrust, whose maximum value is a design constraint for the bearings. Newton's second law is commonly used for axial thrust calculation, which gives

$$F_{\mathrm{axial}} = F_{\mathrm{eye+nose}} + F_{\mathrm{shroud}} + F_{\mathrm{impulse}} - F_{\mathrm{backdisk}}. \tag{3.22}$$

A reliable prediction of the pressure distribution over the shroud and the back disk of the impeller is needed to estimate the various force terms in the equation. The model, therefore, includes the calculation procedure proposed by Tiainen *et al.* [46], which consists of a set of equations combining different analytical models. More in detail, the force acting on the impeller eye and nose is calculated using the model by Nguyen-Schäfer [47]. The impulse force and the force acting on the shroud are retrieved with the model proposed by Japikse [48]. The back disk force is computed by means of the model by Larjola [49], which is based on the assumption that a fluid element is in radial equilibrium so that the pressure force balances the centrifugal force. Note also that the axial thrust is computed without accounting for the presence of labyrinth seals. Finally, the twin-stage centrifugal compressor model also takes into account the electric motor cooling by assuming that the electric motor efficiency is equal to 95% and that all the electromagnetic losses are dissipated as heat. The refrigerant mass flow rate exiting the first stage of the compressor is used to cool the electric motor.

The methodology described thus far is common to both the centrifugal compressor models developed in the *DeSimECS* Modelica library and in the Python *TurboSim* program. However, the two models are characterized by some differences:

- both the design methods are based on the lumped parameters approach. However, the model in *TurboSim* features a span-wise discretization of the flow properties at the inducer section and a stream-wise discretization along the diffuser radial evolution;

- the two models rely on a different set of semi-empirical correlations for the impeller loss prediction. The compressor model of the *DeSimECS* library utilizes the list proposed by Oh *et al.* [50] (Tab. 3.7), while the *TurboSim* model leverages on the correlations reported in Ref. [43];

- in *TurboSim*, the flow in the vaneless diffuser is modelled by integrating the system of two-dimensional differential equations derived by Stanitz [51]. In the *DeSimECS* compressor model, a non-iterative approach proposed by De Bellis *et al.* [52] is used for the same purpose, but simplifying the aforementioned classical set of conservation equations.

- *TurboSim* allows for performing both the preliminary design of a new compressor prototype, as well as for computing the operating map of a prescribed compressor, while the Modelica compressor model can only be used for design analysis.

Table 3.7.: List of semi-empirical correlations selected for the estimation of the impeller losses in the centrifugal compressor model implemented in the *DeSimECS* library.[a]

Internal losses

Loss mechanism	**Loss model**
Blade loading	Coppage *et al.* [53]
Skin friction	Jansen [54]
Clearance	Jansen [54]
Mixing	Johnston and Dean [55]

External losses

Loss mechanism	**Loss model**
Disc friction	Daily and Nece [56]
Recirculation	Oh, Yoon, and Chung [50]
Leakage	Aungier [57]

---

[a] Incidence and shock losses are neglected since the model can be only used for *on-design* simulations.

The compressor model implemented in *TurboSim* has additional features which have not been implemented in the *DeSimECS* model. In particular, at the diffuser outlet, the flow undergoes an additional pressure recovery thanks to the presence of the volute and the exit cone. Furthermore, it includes a method to preliminary estimate the weight of the turbomachinery, using the open-source Python library CadQuery [58]. Given the dimensions of the main parts of the compressor, the routine generated a simplified CAD model of the turbomachinery assembly. Then, the weight of the components is estimated from their volume for the selected material. The computation of the electric motor weight relies on the data of power density reported by Van Der Geest *et al.* [59] for high-speed permanent magnet synchronous machines. This method is based on the assumptions that the magnet is air-cooled and its temperature never exceeds 150 °C, the surface speed of the rotor is maximum $200\ \mathrm{m \cdot s^{-1}}$ and the electric power is up to 1 MW. The total weight of the entire compressor assembly also includes the weight of the Electronic Control Unit (ECU), whose weight is assumed as fixed, based on the suggestion of the industrial partners.

Three test cases from the literature [60–65], and the results of the CFD simulation of a new compressor prototype [42] have been used to verify the accuracy of the *TurboSim* compressor model. The validation study shows that over 95% of both experimental and CFD data points fall within the ± 5% uncertainty bands of the model predictions, as indicated by Giuffré *et al.* [42]. The output of the centrifugal compressor model belonging to the *DeSimECS* library has been verified by comparison with the output of *TurboSim*, obtaining a maximum discrepancy of the results equal to 8%.

A data-driven model of the centrifugal compressor has been developed as a task of another work package of the project. The surrogate model of the compressor was trained using a dataset of 240k compressor stage designs generated using the *in-house* software *TurboSim*. This database includes designs obtained for compressors designed with different working fluids, i.e., R-134a, R-1233zd(E), CO_2 and H_2. The Multi-Layer Perceptron (MLP) method technique has been used for the data regression. Two models have been tested to predict compressor performance parameters and geometrical constraints, with a mean absolute percentage error respectively equal to 2.32% and 0.72%. Detailed information about the model training can be found in Ref. [66]. The use of a data-driven model significantly reduces the time required for designing the centrifugal compressor compared to *TurboSim*. Moreover, integrating this model within the Modelica system model cuts the number of equations for the compressor from 165 to just 97. This reduction substantially decreases the complexity of the numerical problems encountered during system simulations, leading to a notable decrease in computational cost.

3.3. INTEGRATED SYSTEM DESIGN OPTIMIZATION METHODS

The *in-house* software *DesOptECS* (Design and Optimization of Energy Conversion Systems) has been developed to allow for the preliminary integrated design optimization of aircraft/rotorcraft ECS. It includes several methods, all relying on an interface between an open-source optimization algorithm coded in Python and the executable of the system model generated by means of a Modelica-based commercial software [67]. The approach and framework are applicable to any thermal energy conversion system, and in particular if the optimal performance results from the combination of thermodynamic efficiency, low weight and reduced drag.

First, specific component models from the *DeSimECS* library are assembled into a system model which reproduces the ECS configuration of the case study of interest. Since the Modelica Standard Library (MSL) includes a limited number of fluid models, the open-source *ExternalMedia* library [68] is used to compute thermodynamic and transport properties of the working fluid selected for the Modelica model of the ECS. In this way, it is possible to interface external fluid properties databases, i.e., CoolProp, RefProp and FluidProp, to the system component models of the *DeSimECS* library. Then, the optimization design problem is formulated in terms of objective functions $f_{\mathrm{q}}(x)$, given a set of design variables x_{n}. The optimization design problem is restricted by inequality constraints $g_{\mathrm{j}}(x)$. The associated mathematical problem can be expressed as

$$\begin{aligned} \min/\max \quad & f_{\mathrm{q}}(x), \quad \mathrm{q}=1,\dots,\mathrm{Q} \quad \forall x \in \mathbb{R}, \\ \text{s.t.} \quad & \begin{cases} g_{\mathrm{j}}(x) \le 0, & \mathrm{j}=1,\dots,\mathrm{J} \\ x_{\mathrm{n}}^{(\mathrm{L})} \le x_{\mathrm{n}} \le x_{\mathrm{n}}^{(\mathrm{U})}, & \mathrm{n}=1,\dots,\mathrm{N}. \end{cases} \end{aligned} \tag{3.23}$$

The differences between the versions of the software *DesOptECS* developed for integrated system design and optimization of ECS consist of i) the way in which the compressor model is integrated and used to optimize the component within the system, ii) the operating conditions for which the aircraft can be optimized, and iii) how the working fluids are selected.

In the first version, called *DesOptECS Lite*, all the components of the system model belong to the *DeSimECS* library, including the centrifugal compressor model. The *in-house* computer program used for the integrated optimization framework relies on a GA to determine the non-dominated solutions populating the Pareto front. More specifically, when running the GA, for each generation a matrix $\mathbf{X_{M\times N}}$ is created to store the vectors of $\mathbf{N}$ system design variables for each of the $\mathbf{M}$ individuals. These values are provided as input to the Modelica model that is executed at each iteration of the optimization program. The results of the simulations are then stored in an output matrix $\mathbf{Y_{M\times N}}$. More in detail, the GA initializes a population of solutions and, through the repetitive application of selection, crossover, mutation, and evaluation, improves each generation towards the defined objective. This process is iterated until the optimizer convergence termination criteria are satisfied and the optimal non-dominated solutions of the objective functions are found, see Fig. 3.7.

This approach has been successfully tested for the case study of the helicopter ECS [69], however, the authors have pointed out the drawback associated with the need to correctly initialize steady-state simulations of complex Modelica system models to enable the convergence of the simulation. The choice of a consistent set of initial conditions is not trivial, and it may be a limiting factor for the application of stochastic optimization algorithms since it is difficult to define *a priori* such values for each vector of design variables. Consequently, due to the limited convergence capability of the model, the resulting design space could be smaller than the actual one.

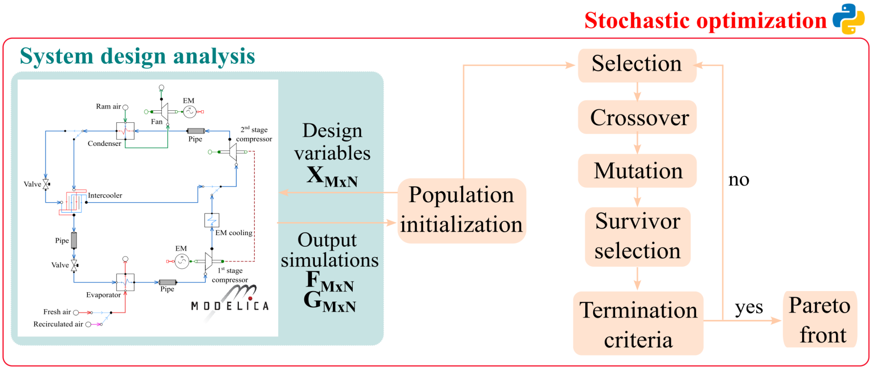

Figure 3.7.: Flowchart illustrating the *DesOptECS Lite* integrated system design optimization framework coupling the ECS Modelica model to the stochastic optimization algorithm coded in Python.

To overcome this problem, the software *DesOptECS Lite* has been modified in version *DesOptECS TurboEd*. The complexity of the system model implemented in Modelica has been reduced by replacing the Modelica model of the compressor with a simplified model, in which the efficiency and the compression ratio are the only input parameters. These values are preliminarily computed with *TurboSim* [42]. This approach offers the advantage of simplifying the simulation of the system model by decoupling the centrifugal compressor thermo-fluid dynamic design. In this way, the complexity of the set of equations associated with the ECS model is reduced without compromising the accuracy of the compressor design. Figure 3.8 illustrates the logic underpinning the integrated system optimization framework implemented in *DesOptECS TurboEd*.

When the simulation starts, the optimization algorithm assigns to each individual **M** of a generation, a vector of **N** design variables $\mathbf{X}_{\mathbf{M}\times\mathbf{N}}$. Each vector groups the variables related to the system components ($\mathbf{X}_{\mathbf{sys}}$) and the centrifugal compressor ($\mathbf{X}_{\mathbf{C}}$) design

$$\mathbf{X}_{\mathbf{M}\times\mathbf{N}} = \left[\mathbf{X}_{\mathbf{sys}}, \mathbf{X}_{\mathbf{C}}\right]. \tag{3.24}$$

For each vector of design variables, the software executes a routine for the preliminary calculation of the reduced inlet thermodynamic properties of both compressor stages and the refrigerant mass flow rate of the second stage. These values, together with the set of variables $\mathbf{X}_{\mathbf{C}}$, are given as input to *TurboSim*. Once, the compressor design is finalized, the values of total-to-total efficiency, compression ratio, and refrigerant mass flow rate of both stages are added to the vector of design variables $\mathbf{X}_{\mathbf{sys}}$. This new group of design variables includes all the input data necessary to simulate the Modelica model of the VCC system. Note that the VCC system compressor model is much simplified with respect to that implemented in *TurboSim*, having the efficiency and the compression ratio as the only input variables. Once initialized, the GA algorithm continues with the processes of selection, crossover, and mutation. This routine is iterated until the termination criteria are reached and the Pareto front of optimal solutions is obtained. This framework has been utilized for the optimization of helicopter ECS using low-GWP refrigerants, the case study discussed in Ch. 4.

This methodology is robust, but the computational cost of a simulation can be high depending on the number of optimization variables. To overcome this issue and make the optimization process of such intricate systems more computationally efficient, a new

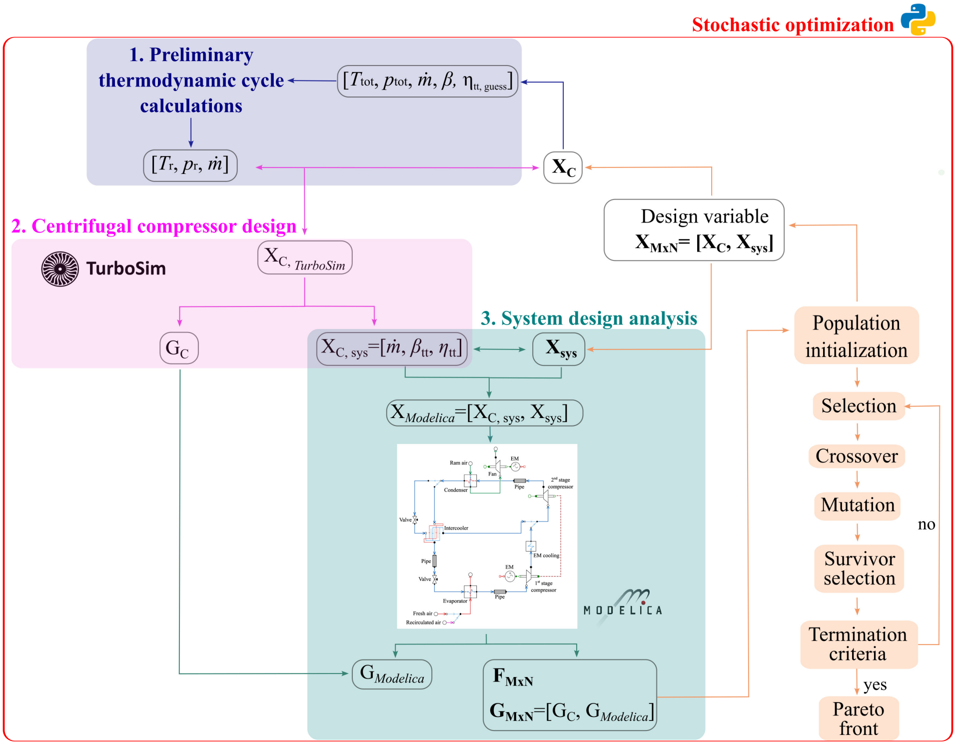

Figure 3.8.: Flowchart illustrating the *DesOptECS TurboEd* integrated design optimization framework which de-couples the centrifugal compressor design performed with *TurboSim* from the rest of the system model. The optimization is based on a stochastic algorithm coded in Python.

optimization framework called *DeSimECS TurboAI* has been designed and tested. The novelty of this approach lies in the integration into the system model of a data-driven model of the centrifugal compressor. A flowchart illustrating the *DeSimECS TurboAI* framework is provided in Fig. 3.9.

Also in this case the optimization framework is based on a GA. Once initialized, a matrix $\mathbf{X_{M\times N}}$ is generated. It consists of a vector of **N** design variables for **M** individuals of a generation. Each vector of design variables is split into two sub-vectors, i.e., $\mathbf{X_C}$ and $\mathbf{X_{sys}}$. $\mathbf{X_C}$ includes the set of design variables necessary for the compressor design, and $\mathbf{X_{sys}}$ lists the inputs necessary to the remaining components of the ECS. The optimization of the data-driven centrifugal compressor model is decoupled from that of the system. It is performed with a constrained gradient-based algorithm, and the objective functions are the total-to-total efficiency (η_{tt}) and the operating range (OR). For each individual of a generation, the optimal values of the total-to-total compression ratio (β_{tt}) and efficiency (η_{tt}) are appended to the vector of design variables used for the stochastic optimization of the design of the entire system. This approach reduces the computational cost by decoupling the compressor design optimization from that of the entire system, thereby lowering the number of design variables selected by the stochastic algorithm and reducing the number of function evaluations needed

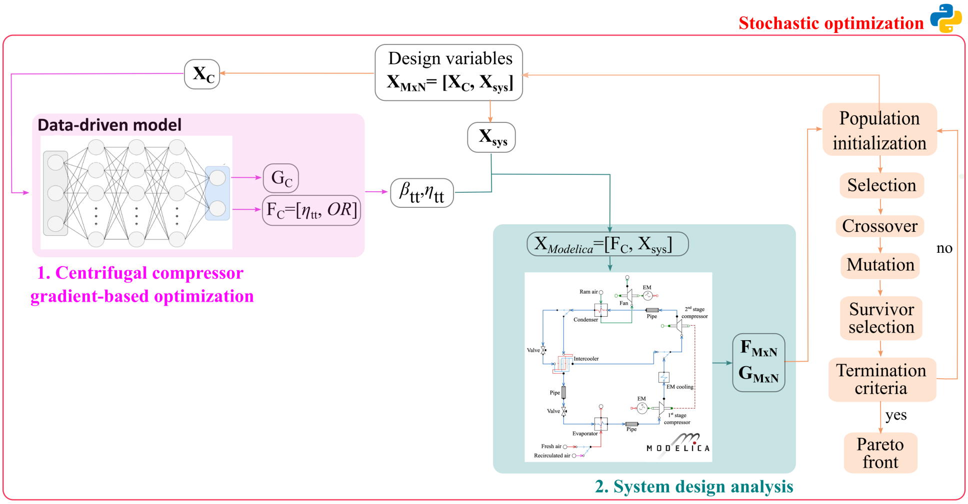

Figure 3.9.: Flowchart illustrating the *DeSimECS TurboAI* integrated design optimization method in which the centrifugal compressor design model is de-coupled from the models of the rest of the system. The model of the compressor is data-driven.

to identify the Pareto front. However, the validity of this approach is always constrained by the initial dataset used for training the data-driven compressor model, i.e., thermodynamic conditions, working fluids, and range of input design parameters. This optimization framework has been applied to the multi-objective optimization of an ECS for a single-aisle, short-haul aircraft, e.g. A320, operating at cruise conditions [66].

The optimization frameworks described thus far serve the sole purpose of optimizing the system design at its nominal point. Nevertheless, for a comprehensive evaluation of the system performance, it is imperative to optimize its performance not just at the design point but also at other conditions within the operating envelope. For such a purpose, the design optimization framework called *DesOptECS MultiPoint* has been developed, and its methodology is illustrated in Fig. 3.10.

Analogously to other versions of *DesOptECS* described thus far, also the *DesOptECS MultiPoint* optimal design framework relies on a stochastic optimization algorithm. The methodology to design the ECS is analogous to *DesOptECS TurboEd*, where *TurboSim* is used for the centrifugal compressor design. For the multi-point optimization test case, three aircraft operating points have been identified, i.e., ground, standard cruise and faulty-pack at cruise conditions. Of these, the ground scenario on a hot and humid day is the most critical, ultimately dictating the sizing of all the components. However, the system must also function efficiently in the other two operating conditions. Therefore, a comprehensive simulation of system operation across all three cases is required to analyze the corresponding system performance. To this end, first the GA generates a matrix of $\mathbf{X}_{\mathbf{M}\times\mathbf{N}}$ design variables for all the individuals of a generation for the case of system design at ground level. Then, the results of the HEXs and the compressor sizing are used as input parameters for the system simulation in the other two operating points. If the compressor feasibility is verified, therefore the compressor operating point corresponds to a stable operating point of the compressor map, the system simulation is executed. Afterwards, the objective functions related to all three cases are averaged based on assigned weights and optimized until the convergence criteria are met. This methodology has

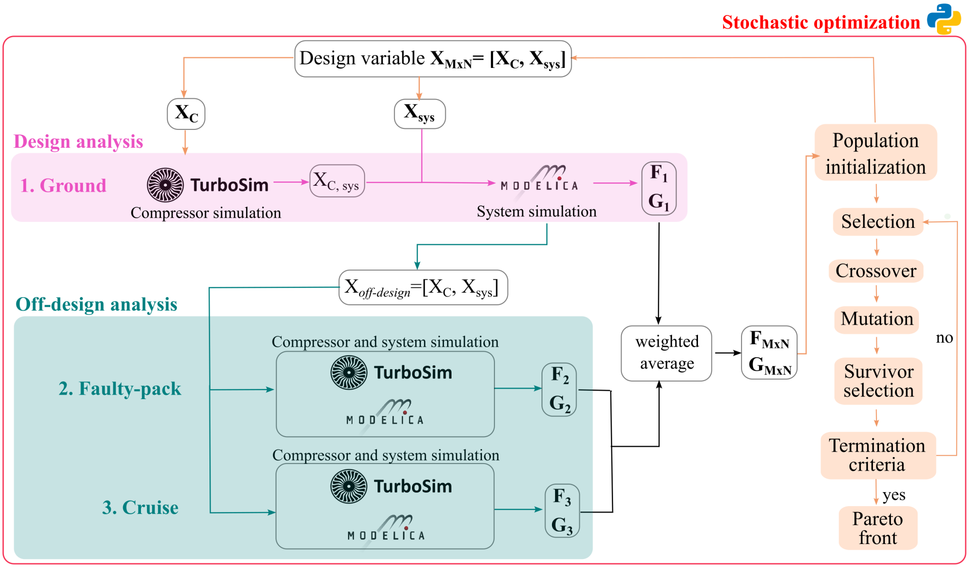

Figure 3.10.: Flowchart illustrating the methodology implemented in *DesOptECS MultiPoint* for the multi-point integrated design optimization of ECS.

been implemented and tested for the case of the ECS of the A320 aircraft [70].

All the versions of *DesOptECS* do not account for the optimal selection of the working fluid, which is a most important design variable for these systems. To overcome this limitation, an automated framework for selecting the refrigerant for the VCC-based ECS has been developed and implemented into the Python code called *OptiFluidECS*. Figure 3.11 illustrates the main elements of this procedure.

The purpose of this method is to identify the most suitable refrigerants from a list of several fluids without the need to perform integrated system design optimization calculations for each of them. The method allows to investigate the possible benefit of adopting a working fluid that has never been considered for a given application. For this purpose, the Continuous Molecular Targeting-Computer Aided Molecular Design (CoMT-CAMD) proposed by Bardow *et al.* [71] has been implemented in *OptiFluidECS*. Fluid thermodynamic properties are calculated using the physically-based Perturbed-Chain Statistical Associating Fluid Theory (PC-SAFT) equation of state model [72]. This molecular-based model allows to estimate the thermodynamic properties of any fluid by determining only three parameters, i.e., the number of segments per chain molecule (m), the segment diameter (σ), and the dispersion energy (ϵ_k). In this work, the dipole moment (μ) has been neglected, and only non-polar molecules have been considered. Linear combinations of the molecular parameters have been used to determine the molecular mass (M) and the isobaric specific heat capacity (c_p) of the *pseudo-fluid*. Given these as inputs, transport properties are estimated using the approach proposed by Chung *et al.* [73] and the surface tension is calculated according to the method described by Sastri and Rao [74].

The working fluid selection procedure is as follows. A list of working fluids is identified as suitable working fluids based on common considerations regarding thermodynamic properties and other desirable technical characteristics. This list of fluids defines the design space of the

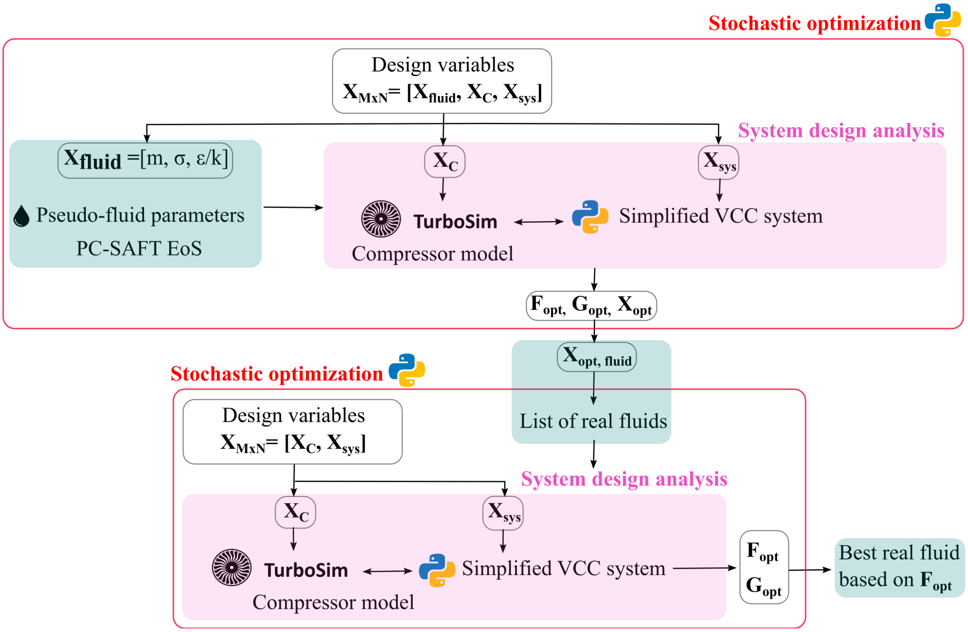

Figure 3.11.: Flowchart illustrating the methodology implemented in *OptiFluidECS* for the selection of the optimal refrigerant for the VCC-based aircraft ECS.

three molecular parameters.

The VCC system is modelled in the *OptiFluidECS* Python code, which supports an interface with *TurboSim* for the centrifugal compressor design. The HEXs sizing is neglected. The refrigerant used for the system simulation is a hypothetical molecule, referred to as *pseudo-fluid*. The three molecular describers of the *pseudo-fluid* ($\mathbf{X_{fluid}}$) are included among the set of design variables of the system ($\mathbf{X_C}$ and $\mathbf{X_{sys}}$ in Fig. 3.11). A GA has been chosen for the system COP maximization. The optimization problem is constrained to account for the centrifugal compressor design feasibility. The optimal molecular describers for the pseudo-fluid are used to identify the corresponding real fluids, which are mapped as those with molecular describers equal to ±10% of the optimal values found for the *pseudo-fluid*. Then, the system optimization is reiterated with each one of the real fluids to select the refrigerants which maximize the system COP. This methodology has been adopted to preliminary identify the best working fluid for aircraft ECS. The optimal refrigerants resulting from this approach have been tested in the *DesOptECS MultiPoint* optimization framework for the case study of a short-haule, single-aisle aircraft, as reported in Ch. 5.

3.4. CONCLUSIONS

This chapter documents novel energy system design methods. In particular, these methods have been developed to obtain the preliminary optimal design of aircraft/rotorcraft environmental control systems based on vapour compression cycles powered by a high-speed radial compressor. These methods allow the designer to perform the thermodynamic cycle optimization, the preliminary design of the main components, and the working fluid simultaneously.

The steady-state models of the various system components have been developed using the Modelica acausal modelling language, and are collected in the *DeSimECS* library. Three methods are described and they differ mainly for the preliminary design of the centrifugal compressor. The preliminary design of the compressor can be obtained with i) a mean-line code implemented in *DeSimECS*; ii) *TurboSim*, a Python *in-house* design tool, and iii) a data-driven model. The resulting design optimization frameworks are coded in Python, make use of an open-source genetic optimization algorithm, and are called *DeSimECS Lite*, *DeSimECS TurboEd*, and *DeSimECS TurboAI*, respectively.

The problems associated with the robustness of the system simulations involved in *DeSimECS Lite* have been overcome in *DeSimECS TurboEd* by decoupling the centrifugal compressor design from the rest of the system optimization and performing its design with *TurboSim*. However, the computational cost associated with *DeSimECS TurboEd* can be large due to the large number of design variables. To overcome this issue, in *DeSimECS TurboAI*, a data-driven model has been used for the compressor design, and its optimization has been decoupled from the rest of the system. Additionally, a multi-point design optimization framework, named *DeSimECS MultiPoint*, is illustrated. *DeSimECS MultiPoint* allows to obtain the system design providing the optimal performance depending on several aircraft operating conditions. The suite of optimal integrated system design frameworks is completed by the implementation of a methodology for the selection of the optimal refrigerants for the vapour compression cycle system, implemented in the software *OptiFluidECS*.

NOMENCLATURE

Acronyms

ACM	Air Cycle Machine
CHEX	Compact Heat Exchanger
CV	Control Volume
DesOptECS	Design and Optimization of Energy Conversion Systems
DeSimECS	Design and Simulation of Energy Conversion Systems
ECS	Environmental Control System
FV	Finite Volume
GA	Genetic Algorithm
HEX	Heat exchanger
MB	Moving Boundary
NTU	Number of Thermal Units
PHEX	Plate Heat Exchanger
VCC	Vapour Compression Cycle

Roman letters

A	Heat transfer surface [m^2]
b	Fins height [m]
Bo	Boiling number [-]
$C_1 - C_5$	Constant parameters
C_D	Drag coefficient [-]
C_p	Pressure recovery factor [-]
c_u	Tangential component of the absolute velocity [$m \cdot s^{-1}$]
Co	Convection number [-]
D	Diameter, Drag [N], Heat exchanger depth [m]
F	Force [N]
f	Friction factor [-]
F_d	Fins depth [m]
F_{fl}	Fluid dependent parameter
F_p	Fins pitch [m]
Fr	Froude number [-]
G	Mass flux [$kg \cdot (m^{-2} \cdot s^{-1})$]
h	Heat transfer coefficient [$W \cdot (m^2 \cdot K)^{-1}$], Specific enthalpy [$J \cdot kg^{-1}$]
j	Colburn factor [-]
K	Constant [-]
k	Thermal conductivity [$W \cdot (m \cdot K)^{-1}$], Compressor shape factor [-]
l	Tube length [m]
L_h	Louver height [m]
L_l	Louver length [m]
L_p	Louver pitch [m]
L_{plate}	Plate length [m]
m	Segment number [-]
$\dot{m}$	Mass flow rate [$kg \cdot s^{-1}$]
M_r	Molecular weight [-]
M_{U_2}	Outlet tip Mach number [-]
$M_{w_{1,s}}$	Inlet relative Mach number at shroud [-]
n=0.25	Constant [-]
Nu	Nusselt number [-]
p	Pressure [Pa]
p_{gauge}	Gauge pressure [Pa]
P_t	Tube pitch [m]
Pr	Prandtl number [-]
q	Heat flux [$J \cdot m^{-2}$]
R	Radius [m]
Re	Reynolds number [-]
Re_{Lp}	Reynolds number based on the louver pitch [-]

Re_x	Reynolds number based on logarithmic spiral through diffuser length [-]
s	Slip ratio [-]
T	Temperature [K]
T_h	Tube height [m]
T_p	Tube pitch [m]
U	Impeller blade speed [$\mathrm{m{\cdot}s^{-1}}$], Overall heat transfer coefficient [$\mathrm{W{\cdot}(m^2{\cdot}K)^{-1}}$]
v	Absolute flow velocity [$\mathrm{m{\cdot}s^{-1}}$]
V	Volume [$\mathrm{m^3}$]
W_f	Dissipated specific work due to friction [$\mathrm{J{\cdot}kg^{-1}}$]
We	Weber number [-]
x	Vapour quality [-]
y=0.4	Sizing coefficient [-]

Greek letters

α_2	Impeller outlet absolute angle [deg]
β_tt	Total-to-total pressure ratio [-]
$\beta_\mathrm{1,s}$	Inlet blade metal angle at shroud [deg]
γ_{Pv}	Isentropic pressure-volume exponent [-]
δ_f	Fins thickness [m]
δ_mc	Minichannel thickness [m]
δ_pipe	Pipe wall thickness [m]
δ_t	Flat tube thickness [m]
ϵ	Effectiveness [-], Relative roughness [-]
ϵ_k	Dispersion energy [K]
η_c	Surface effectiveness [-]
η_f	Fins efficiency [-]
Θ	Louver angle [deg]
μ	Dynamic viscosity [Pa·s], Dipole moment [-]
ρ	Density [$\mathrm{kg{\cdot}m^{-3}}$]
σ	Segment diameter [Å]
σ_max	Maximum allowable material stress [Pa]
Φ	Two-phase multiplier
Φ_t	Compressor swallowing capacity [-]
Φ'	Modified mass flow function [-]
Ψ	Compressor loading coefficient [-]
Ω	Rotational speed [rpm]

Superscripts and subscripts

air	Air stream
cb	Cabin
compr	compressor
cr	Critical
env	Environmental
f	Fins
fan	Ram air fan
fresh	Fresh air stream
h	Hydraulic
i	Internal
int	Intermediate
intcool	Intercooler
L	Liquid phase
out	Outlet
pp	Pinch-point
ram	Ram air stream
rec	Recirculated air stream
s	Impeller shroud
sat	Saturation
S1	First stage compressor
S2	Second stage compressor
t	Total thermodynamic condition, Tube
V	Dry vapour phase
1	Compressor impeller inlet
2	Compressor impeller outlet
3	Compressor diffuser inlet
4	Compressor diffuser outlet
∞	Free-stream conditions

REFERENCES

[1] J. V. Vargas and A. Bejan. “Integrative thermodynamic optimization of the environmental control system of an aircraft”. In: *International Journal of Heat and Mass Transfer* 44.20 (Oct. 2001), pp. 3907–3917. ISSN: 0017-9310. DOI: `10.1016/S0017-9310(01)00033-3`.

[2] I. Pérez-Grande and T. J. Leo. “Optimization of a commercial aircraft environmental control system”. In: *Applied Thermal Engineering* 22.17 (Dec. 2002), pp. 1885–1904. ISSN: 1359-4311. DOI: `10.1016/S1359-4311(02)00130-8`.

[3] M. Sielemann, T. Giese, B. Oehler, and M. Gräber. “Optimization of an Unconventional Environmental Control System Architecture”. In: *SAE International Journal of Aerospace* 4.2 (2011), pp. 1263–1275. DOI: `10.4271/2011-01-2691`.

[4] Modelica Association. *Modelica Language Specification, Version 3.5*. Tech. rep. 2021.

[5] Z. Duan, H. Sun, C. Wu, and H. Hu. “Multi-objective optimization of the aircraft environment control system based on component-level parameter decomposition”. In: *Energy* 245 (Apr. 2022), p. 123330. ISSN: 0360-5442. DOI: `10.1016/J.ENERGY.2022.123330`.

[6] L. Chen, F. Liu, Z. Xu, M. Zhu, Q. Liu, L. Zhuang, J. Wen, B. Dong, and Z. Liu. “Thermodynamic Optimization of Aircraft Environmental Control System Using Modified Genetic Algorithm”. In: *Processes 2022, Vol. 10, Page 721* 10.4 (Apr. 2022), p. 721. ISSN: 2227-9717. DOI: `10.3390/PR10040721`.

[7] T. Planès, S. Delbecq, V. Pommier-Budinger, and E. Bénard. “Modeling and Design Optimization of an Electric Environmental Control System for Commercial Passenger Aircraft”. In: *Aerospace 2023, Vol. 10, Page 260* 10.3 (Mar. 2023), p. 260. ISSN: 2226-4310. DOI: `10.3390/AEROSPACE10030260`.

[8] A. Mannini. “Vapor Cycle versus Air Cycle Environmental Control System: selection criteria on modern helicopters”. In: *Twentieth European Rotorcraft Forum*. Amsterdam, 1994, p. 14.

[9] A. Mannini. “The Environmental Control System for a modern helicopter: a blend of new technologies”. In: *Twenty-first European Rotorcraft Forum*. Saint-Petersburg, Russia, 1995, p. 11.

[10] ESDU. *Drag and pressure recovery characteristics of auxiliary air inlets at subsonic speeds*. 2004.

[11] B. A. Emmet Mossman, o. M. Randall, and M. Field. *An experimental investigation of the design variables for NACA submerged duct entrances*. 1947.

[12] J. S. Dennard. *The Total-Pressure Recovery and Drag Characteristics of Several Auxiliary Inlets at Transonic Speeds*. 1959.

[13] N. K. Delany. *An investigation of submerged air inlets on a 1/4-scale model of a typical fighter-type airplane*. 1948.

[14] J. A. Axelson and R. A. Taylor. *Preliminary Investigation of the Transonic Characteristics of an NACA Submerged Inlet*. 1950.

[15] J. L. Frank. *Pressure-distribution and Ram-recovery Characteristics of NACA Submerged Inlets at High Subsonic Speeds.* 1950.

[16] J. Selna and B. A. Schlaff. *An Investigation of the Drag and Pressure Recovery of a Submerged Inlet and a Nose Inlet in the Transonic Flight Range with Free-fall Models.* 1951.

[17] K. M. McCreath and A. J. W. Smith. "Boundary Layer Influence on the Performance of Submerged Intakes". In: *The Aeronautical Journal* 71.680 (Aug. 1967), pp. 581–583. ISSN: 0368-3931. DOI: `10.1017/S0001924000055056`.

[18] B. Zohuri. "Heat Exchangers". In: *Application of Compact Heat Exchangers For Combined Cycle Driven Efficiency In Next Generation Nuclear Power Plants* (2016), pp. 125–160. DOI: `10.1007/978-3-319-23537-0`.

[19] S. G. Kandlikar. "Fundamental issues related to flow boiling in minichannels and microchannels". In: *Experimental Thermal and Fluid Science* 26.2-4 (June 2002), pp. 389–407. ISSN: 0894-1777. DOI: `10.1016/S0894-1777(02)00150-4`.

[20] R. Shah and D. Sekulic. *Fundamentals of heat exchanger design.* 2003. DOI: `10.1002/9780470172605`.

[21] M. H. Kim and C. W. Bullard. "Performance Evaluation of a Window Room Air Conditioner With Microchannel Condensers". In: *Journal of Energy Resources Technology* 124.1 (Mar. 2002), pp. 47–55. ISSN: 0195-0738. DOI: `10.1115/1.1446072`.

[22] S. Bendapudi, J. E. Braun, and E. A. Groll. "A comparison of moving-boundary and finite-volume formulations for transients in centrifugal chillers". In: *International Journal of Refrigeration* 31.8 (Dec. 2008), pp. 1437–1452. ISSN: 0140-7007. DOI: `10.1016/J.IJREFRIG.2008.03.006`.

[23] H. Schmidt, A. Wellenhofer, S. Muschelknautz, J. Schmidt, F. Schmidt, D. Mewes, A. Mersmann, and J. Stichlmair. "L2 Two-Phase Gas-Liquid Flow". In: *VDI Heat Atlas* (2010), pp. 1117–1180. DOI: `10.1007/978-3-540-77877-678`.

[24] "VDI Heat Atlas". In: *VDI Heat Atlas* (2010). DOI: `10.1007/978-3-540-77877-6`.

[25] M. H. Kim and C. W. Bullard. "Air-side thermal hydraulic performance of multi-louvered fin aluminum heat exchangers". In: *International Journal of Refrigeration* 25.3 (May 2002), pp. 390–400. ISSN: 0140-7007. DOI: `10.1016/S0140-7007(01)00025-1`.

[26] Y. J. Chang and C. C. Wang. "A generalized heat transfer correlation for Iouver fin geometry". In: *International Journal of Heat and Mass Transfer* 40.3 (Feb. 1997), pp. 533–544. ISSN: 0017-9310. DOI: `10.1016/0017-9310(96)00116-0`.

[27] R. W. Lockhard and R. C. Martinelli. "Proposed correlation of data for isothermal two-phase, two-component flow in pipes". In: *Chemical Engineering Progress* 45 (1949), pp. 39–48.

[28] D. Chisholm. "Pressure gradients due to friction during the flow of evaporating two-phase mixtures in smooth tubes and channels". In: *International Journal of Heat and Mass Transfer* 16.2 (Feb. 1973), pp. 347–358. ISSN: 0017-9310. DOI: `10.1016/0017-9310(73)90063-X`.

[29] V. Gnielinski. "On heat transfer in tubes". In: *International Journal of Heat and Mass Transfer* 63 (Aug. 2013), pp. 134–140. ISSN: 0017-9310. DOI: `10.1016/J.IJHEATMASSTRANSFER.2013.04.015`.

[30] S. G. Kandlikar. "A General Correlation for Saturated Two-Phase Flow Boiling Heat Transfer Inside Horizontal and Vertical Tubes". In: *Journal of Heat Transfer* 112.1 (Feb. 1990), pp. 219–228. ISSN: 0022-1481. DOI: 10.1115/1.2910348.

[31] M. M. Shah. "Improved correlation for heat transfer during condensation in conventional and mini/micro channels". In: *International Journal of Refrigeration* 98 (Feb. 2019), pp. 222–237. ISSN: 0140-7007. DOI: 10.1016/J.IJREFRIG.2018.07.037.

[32] W. Kast, H. Nirschl, E. S. Gaddis, K.-E. Wirth, and J. Stichlmair. "L1 Pressure Drop in Single Phase Flow". In: *VDI Heat Atlas* (2010), pp. 1053–1116. DOI: 10.1007/978-3-540-77877-6-70.

[33] J. Schmidt and L. Friedel. "Two-phase pressure drop across sudden contractions in duct areas". In: *International Journal of Multiphase Flow* 23.2 (Apr. 1997), pp. 283–299. ISSN: 0301-9322. DOI: 10.1016/S0301-9322(96)00056-0.

[34] M. S. Yadav, S. A. Giri, and V. C. Momale. "Sizing analysis of louvered fin flat tube compact heat exchanger by genetic algorithm". In: *Applied Thermal Engineering* 125 (Oct. 2017), pp. 1426–1436. ISSN: 1359-4311. DOI: 10.1016/J.APPLTHERMALENG.2017.07.119.

[35] H. Martin. "N6 Pressure Drop and Heat Transfer in Plate Heat Exchangers". In: *VDI Heat Atlas* (2010), pp. 1515–1522. DOI: 10.1007/978-3-540-77877-6-109.

[36] B. Palm, J. Claesson, B. Bj¨, and B. Palm. "Plate Heat Exchangers: Calculation Methods for Singleand Two-Phase Flow". In: *Heat Transfer Engineering* 27.4 (May 2006), pp. 88–98. ISSN: 01457632. DOI: 10.1080/01457630500523949.

[37] H. Martin. "A theoretical approach to predict the performance of chevron-type plate heat exchangers". In: *Chemical Engineering and Processing: Process Intensification* 35.4 (Jan. 1996), pp. 301–310. ISSN: 0255-2701. DOI: 10.1016/0255-2701(95)04129-X.

[38] M. G. Cooper. "Heat Flow Rates in Saturated Nucleate Pool Boiling-A Wide-Ranging Examination Using Reduced Properties". In: *Advances in Heat Transfer* 16.C (Jan. 1984), pp. 157–239. ISSN: 0065-2717. DOI: 10.1016/S0065-2717(08)70205-3.

[39] Applying Aspen HTFS Technology. *Aspen Exchanger Design & Rating*. 2008.

[40] ASME B31.5. *Refrigeration Piping and Heat Transfer Components*. 2019.

[41] CS-25 Amendment 3. *Certification Specifications for Large Aeroplanes*. 2017.

[42] A. Giuffré, P. Colonna, and M. Pini. "Design Optimization of a High-Speed Twin-Stage Compressor for Next-Gen Aircraft Environmental Control System". In: *Journal of Engineering for Gas Turbines and Power* 145.3 (Mar. 2023). ISSN: 0742-4795. DOI: 10.1115/1.4056022.

[43] A. Giuffré, P. Colonna, and M. Pini. "The Effect of Size and Working Fluid on the Multi-Objective Design of High-Speed Centrifugal Compressors". In: *International Journal of Refrigeration* 143 (Nov. 2022), pp. 43–56. ISSN: 01407007. DOI: 10.1016/j.ijrefrig.2022.06.023.

[44] D. Rusch and M. Casey. "The design space boundaries for high flow capacity centrifugal compressors". In: *Journal of Turbomachinery* 135.3 (Mar. 2013). ISSN: 15288900. DOI: 10.1115/1.4007548.

[45] T. W. von Backström. "A Unified Correlation for Slip Factor in Centrifugal Impellers". In: *Journal of Turbomachinery* 128.1 (Jan. 2006), pp. 1–10. ISSN: 0889-504X. DOI: 10.1115/1.2101853.

[46] J. Tiainen, A. Jaatinen-Värri, A. Grönman, P. Sallinen, J. Honkatukia, and T. Hartikainen. "Validation of the Axial Thrust Estimation Method for Radial Turbomachines". In: *International Journal of Rotating Machinery* 2021 (2021). ISSN: 15423034. DOI: 10.1155/2021/6669193.

[47] H. Nguyen-Schäfer. "Rotordynamics of automotive turbochargers: Linear and nonlinear rotordynamics-bearing design-rotor balancing". In: *Rotordynamics of Automotive Turbochargers: Linear and Nonlinear Rotordynamics-Bearing Design-Rotor Balancing* 9783642275180 (June 2012), pp. 1–326. DOI: 10.1007/978-3-642-27518-0/COVER.

[48] D. Japikse. "Centrifugal compressor design and performance". In: *Wilder, VT: Concepts ETI, Inc, 1996.* (1996).

[49] J. Larjola. *Centrifugal Compressors, the Fundamentals of Design.* Tech. rep. Lappeenranta University of Technology, Department of Energy Technology, 1988.

[50] H. W. Oh, E. S. Yoon, and M. K. Chung. "An optimum set of loss models for performance prediction of centrifugal compressors". In: *Proceedings of the Institution of Mechanical Engineers, Part A: Journal of Power and Energy.* 211.4 (June 1997), pp. 331–338. ISSN: 09576509. DOI: 10.1243/0957650971537231.

[51] J. D. Stanitz. *One-dimensional Compressible Flow in Vaneless Diffusers of Radial- and Mixed-flow Centrifugal Compressors, Including Effects of Friction, Heat Transfer and Area Change.* 1952.

[52] F. De Bellis, A. Grimaldi, D. T. Rubino, R. Amirante, and E. Distaso. "Accurate radial vaneless diffuser one-dimensional model". In: *Journal of Engineering for Gas Turbines and Power* 137.8 (Aug. 2015). ISSN: 15288919. DOI: 10.1115/1.4029482.

[53] J. E. Coppage, F. Dallenbach, H. P. Eichenberger, G. E. Hlavaka, E. M. Knoernschild, and N. Van Lee. *Study of supersonic radial compressors for refrigeration and pressurization systems.* Wright Air Development Center, 1995.

[54] W. Jansen. "A method for calculating the flow in a centrifugal impeller when entropy gradient are present". In: *Institution of Mechanical Engineers Internal Aerodynamics* (1970).

[55] J. F. Johnston and R. C. Dean. "Losses in Vaneless Diffusers of Centrifugal Compressors and Pumps: Analysis, Experiment, and Design". In: *Journal of Engineering for Power* 88.1 (Jan. 1966), pp. 49–60. ISSN: 0022-0825. DOI: 10.1115/1.3678477.

[56] J. W. Daily and R. E. Nece. "Chamber Dimension Effects on Induced Flow and Frictional Resistance of Enclosed Rotating Disks". In: *Journal of Basic Engineering* 82.1 (Mar. 1960), pp. 217–230. ISSN: 0021-9223. DOI: 10.1115/1.3662532.

[57] R. H. Aungier. "Mean Streamline Aerodynamic Performance Analysis of Centrifugal Compressors". In: *Journal of Turbomachinery* 117.3 (July 1995), pp. 360–366. ISSN: 0889-504X. DOI: 10.1115/1.2835669.

[58] A. Urbańczyk, J. Wright, D. Cowden, I. T. Solutions, H. Y. ÖZDERYA, B. Agostini, M. Greminger, J. Buchanan, huskier, M. Boyd, M. S. de León Peque, P. Boin, B. Weissinger, C. Osterwood, moeb, nopria, A. Kono, HLevering, W. Turner, W. Saville, A. Grunichev, Bernhard, D. Anderson, G. Ebner, I. Krasin, M. Ulianko, P. Thelen, bsilvereagle, jwhevans, and x. xeaon xix. *CadQuery/cadquery 2.0.1.* July 2020. DOI: 10.5281/zenodo.3955119.

[59] M. Van Der Geest, H. Polinder, J. A. Ferreira, and M. Christmann. "Power density limits and design trends of high-speed permanent magnet synchronous machines". In: *IEEE Transactions on Transportation Electrification* 1.3 (Oct. 2015), pp. 266–276. ISSN: 23327782. DOI: 10.1109/TTE.2015.2475751.

[60] D. Eckardt. “Instantaneous Measurements in the Jet-Wake Discharge Flow of a Centrifugal Compressor Impeller”. In: *Journal of Engineering for Power* 97.3 (July 1975), pp. 337–345. ISSN: 0022-0825. DOI: `10.1115/1.3445999`.

[61] D. Eckardt. “Detailed Flow Investigations Within a High-Speed Centrifugal Compressor Impeller”. In: *Journal of Fluids Engineering* 98.3 (Sept. 1976), pp. 390–399. ISSN: 0098-2202. DOI: `10.1115/1.3448334`.

[62] D. Eckardt. *Investigation of the jet-wake flow of a highly loaded centrifugal compressor impeller*. 1978.

[63] D. Japikse. “A Critical Evaluation of Three Centrifugal Compressors With Pedigree Data Sets: Part 5—Studies in Component Performance”. In: *Journal of Turbomachinery* 109.1 (Jan. 1987), pp. 1–9. ISSN: 0889-504X. DOI: `10.1115/1.3262064`.

[64] J. Schiffmann and D. Favrat. “Experimental investigation of a direct driven radial compressor for domestic heat pumps”. In: *International Journal of Refrigeration* 32.8 (Dec. 2009), pp. 1918–1928. ISSN: 01407007. DOI: `10.1016/j.ijrefrig.2009.07.006`.

[65] J. Schiffmann and D. Favrat. “Design, experimental investigation and multi-objective optimization of a small-scale radial compressor for heat pump applications”. In: *Energy* 35.1 (Jan. 2010), pp. 436–450. ISSN: 0360-5442. DOI: `10.1016/J.ENERGY.2009.10.010`.

[66] A. Giuffré, F. Ascione, C. D. Servi, and M. Pini. “Data-driven modeling of high-speed centrifugal compressors for aircraft Environmental Control Systems”. In: *International Journal of Refrigeration* 151 (July 2023), pp. 354–369. ISSN: 0140-7007. DOI: `10.1016/J.IJREFRIG.2023.03.019`.

[67] Dassault Systèmes AB. *Dymola: Dynamic Modeling Laboratory*. 2022.

[68] F. Casella and C. Richter. “ExternalMedia: A Library for Easy Re-Use of External Fluid Property Code in Modelica”. In: *Proceedings 6th International Modelica Conference* (Mar. 2008), pp. 157–161.

[69] F. Ascione, P. Colonna, and C. M. De Servi. “Integrated design optimization method for novel vapour-compression-cycle-based environmental control systems”. In: *Applied Thermal Engineering* 236 (Jan. 2024), p. 121261. ISSN: 1359-4311. DOI: `10.1016/J.APPLTHERMALENG.2023.121261`.

[70] A. Giuffré. “Integrated design optimization of electrically-driven vapour compression cycle systems for aircraft: powered by high-speed centrifugal compressors”. PhD thesis. Delft: Delft University of Technology, 2024. DOI: `10.4233/uuid:b4f6a4a4-2e48-4bbe-9093-3f1368282f63`.

[71] A. Bardow, K. Steur, and J. Gross. “Continuous-molecular targeting for integrated solvent and process design”. In: *Industrial and Engineering Chemistry Research* 49.6 (Mar. 2010), pp. 2834–2840. ISSN: 08885885. DOI: `10.1021/IE901281W`.

[72] J. Gross and J. Vrabec. “An equation-of-state contribution for polar components: Dipolar molecules”. In: *AIChE Journal* 52.3 (Mar. 2006), pp. 1194–1204. ISSN: 1547-5905. DOI: `10.1002/AIC.10683`.

[73] T.-H. Chung, L. L. Lee, and K. E. Starting. “Applications of Kinetic Gas Theories and Multiparameter Correlation for Prediction of Dilute Gas Viscosity and Thermal Conductivity”. In: *J. R. A.; Matovlch,. A. Ind. Eng. Chem. Fundam* 23.8 (1984), p. 209.

[74] S. R. Sastri and K. K. Rao. “A simple method to predict surface tension of organic liquids”. In: *The Chemical Engineering Journal and the Biochemical Engineering Journal* 59.2 (Oct. 1995), pp. 181–186. ISSN: 0923-0467. DOI: `10.1016/0923-0467(94)02946-6`.

4

INTEGRATED DESIGN OPTIMIZATION OF A NOVEL ELECTRICALLY-DRIVEN HELICOPTER ECS USING LOW-GWP REFRIGERANTS AS WORKING FLUID

Nobody made a greater mistake than he
who did nothing because he could do only a little.

Edmund Burke

The Environmental Control System (ECS) is the main utilizer of non-propulsive power among the aircraft subsystems. Onboard helicopters, the ECS is based on the Vapour Compression Cycle (VCC) concept, and the standard refrigerant is R-134a. The objective of this study is to evaluate the impact of replacing the conventional scroll compressor with a high-speed centrifugal compressor operating with a low-GWP refrigerant as the prime mover of the VCC system. The case study is the ECS of a large helicopter and the sizing operating condition is that of the helicopter on the ground on a hot and humid day. The working fluids identified as potential alternatives to R-134a are the haloolefins R-1233zd(E), R-1234ze(Z), R-1224yd(Z) and R-1336mzz(Z). An integrated design optimization method has been employed to simultaneously account for the design of the VCC system, its main components, and the selection of the working fluid. The model of the VCC system has been coded with the acausal Modelica language. The design of the high-speed compressor has been performed with an in-house program validated with experimental data. The objectives of the optimization are the maximization of the Coefficient of Performance (COP) and the minimization of the system weight. The results show that the use of haloolefins in place of R-134a allows the design of lighter and more efficient VCC systems. In particular, the refrigerant R-1234ze(Z) enables the identification of an optimal design point featuring a 12% increase in COP and a 26% reduction in weight.

4.1. INTRODUCTION

Traditionally, the Environmental Control System (ECS) of large passenger helicopters features a Vapour Compression Cycle (VCC) system operating with R-134a. However, the temperature lift in the refrigeration loop is provided by a mechanically-driven scroll compressor. In this context, the novelties of the proposed ECS configuration are the use of an electrically-driven high-speed centrifugal compressor and a low-Global Warming Potential (GWP[1]) refrigerant. Centrifugal compressors are more compact and are characterized by higher performance than scroll compressors, whose isentropic efficiency does not exceed 70% [1]. Moreover, centrifugal compressors can be operated with gas bearings, thus avoiding oil contamination in the refrigerant loop.

As discussed in Ch. 2, the global warming emergency has urged legislative bodies to establish regulations about the use of fluorinated greenhouse gases (F-gas) [2, 3]. Several recent studies deal with the transition to low-GWP refrigerants for VCC systems by investigating the use of haloolefins, i.e., hydrofluoroolefins (HFOs) and hydrochlorofluoro-olefins (HCFOs), envisioned as the next-generation refrigerants. However, none of these studies consider aircraft or rotorcraft ECS as the application. Among the investigated applications, air conditioning aboard passenger vehicles is arguably the application most similar to that of interest in this work, apart from the aspect of mass production. It is thus no coincidence that helicopter VCC systems are often made of components originally developed for automotive air conditioning. In this regard, Mohanraj and Abraham [4] provided an exhaustive review of refrigerants considered as alternative options to the state-of-the-art R-134a working fluid for automotive air conditioning systems. In particular, among the HFOs, R-1234yf and R-1234ze are indicated as the two most suitable drop-in substitutes of R-134a, thanks to their similar thermodynamic properties. In general, their use leads to a slight performance decrease (Coefficient Of Performance (COP) and cooling capacity) of the VCC system. Moreover, they require certain safety measures given their, though mild, flammability. The same considerations are reported by Prabakaran *et al.* [5]. As mentioned in Ch. 2, during the atmospheric degradation of haloolefins, trifluoroacetic acid (TFA), a substance that is harmful to aquatic life, is produced. Therefore, haloolefins are envisioned as a temporary solution in VCC systems. At the same time, hydrocarbons will be the preferred option in the longer term, thanks to their excellent combination of thermodynamic and environmental properties. However, the molar yield of the degradation of haloolefins in the atmosphere can be rather small, as low as 2% in the case of R-1233zd(E) [6–8]. The only exception is R-1224yd(Z) whose TFA molar yield is 97% [8]. One can argue that low TFA-yield haloolefins can be adopted in aviation if they allow for a better performance of the ECS, given the small number of aircraft and rotorcraft and the higher maintenance standards compared to cars.

Few research studies have addressed the design of centrifugal compressors for VCC systems operating with low-GWP refrigerants [9, 10]. If working fluid selection is included in the system analysis, investigations are limited to studies considering just two working fluids belonging to the class of the HFOs, i.e., R-1234yf and R-1234ze(E), treated as drop-in replacements of R-134a [11, 12].

The current chapter concerns the study of the impact of low-GWP refrigerants on the optimal design of a VCC system for the ECS of a large passenger helicopter. Ascione *et al.* [13] performed an exploratory study by testing a large number of low-GWP refrigerants for the same ECS configuration considered here. From the analysis of the cycle thermodynamic performance, the authors identified four haloolefins as potential alternatives to the state-of-the-art R-134a, namely R-1233zd(E), R-1224yd(Z), R-1234ze(Z) and R-1336mzz(Z). This study aims to expand

---

[1] The authors refer to the GWP_{100} index, which provides an estimate of the environmental impact of a substance with respect to that of the CO_2 over a time horizon of 100 years.

the previous work by investigating the effect of these low-GWP refrigerants on the optimal design of the VCC-based ECS of a large passenger helicopter. The design optimization of the VCC system is carried out with an in-house integrated design framework, capable of simultaneously optimizing the thermodynamic cycle and the preliminary design of the main components, i.e., the heat exchangers (HEXs) and the high-speed centrifugal compressor.

The chapter is structured as follows. First, the VCC system layout for large helicopters is described. Next, the multi-objective optimization problem is introduced, by specifying the design space, objective functions, and constraints. Thereafter, the results of the optimization are then presented, together with the analysis of the effect of the working fluid on the design of the main system components. Finally, the main outcomes of the study are summarised.

4.2. ENVIRONMENTAL CONTROL SYSTEM

The selected test case is the optimal design of the ECS of a large helicopter, thus capable of transporting 20 passengers and 2 pilots. The system consists of two sub-systems: one for cabin heating and another for cooling. Due to the relatively low flying altitudes, hence the low power requirement, cabin heating is simply achieved by mixing hot air bled from the engine with fresh air. The cabin air cooling system is based on VCC technology, and it consists of two separate loops, one for cockpit cooling and the other for cabin cooling. This research focuses on the integrated design optimization of the rotorcraft cooling loop, hereinafter indicated simply as ECS. Two separate VCC systems provide cooling to the cabin and the cockpit. Each refrigeration loop is equipped with a dedicated condenser with an independent cooling air intake and fan. An intercooler (or economizer) is installed to further reduce the temperature of the condensed refrigerant upstream of the expansion valve. In this way, for a fixed cooling demand, the vapour quality of the refrigerant entering the evaporator decreases, thus allowing for a reduction of the refrigerant mass flow rate within the system, and enabling a reduction of the power absorbed by the compressor [14]. The baseline VCC system, namely the one currently adopted for many rotorcraft models, uses a mechanically driven scroll compressor to pressurize the working fluid. Each refrigeration loop features an evaporator. The cockpit evaporator is located under the floor in the nose of the helicopter, while the cabin evaporator is usually positioned in the aft part of the helicopter. The condenser unit consists of three HEXs in parallel on the refrigerant side and in series on the air side. Both condenser and evaporator have independent air intakes and electrically-driven fans. A filter is eventually added in front of the evaporator to avoid contamination of cabin air with sand, dust or other pollutants from the environment. To guarantee passengers comfort, the ARP292 [15] standard prescribes a target mass flow rate of air for each evaporator, i.e., 4.5 $\mathrm{g \cdot s^{-1}}$ of fresh air for the cabin and 5.6 $\mathrm{g \cdot s^{-1}}$ for the cockpit, keeping the air humidity below 65%. Cabin air pressurization is not needed due to the relatively low flight altitude, thus allowing for a ratio of recirculated to fresh air significantly larger with respect to the one of a typical aircraft ECS. Figure 4.1 illustrates a schematic of the standard installation arrangement of the VCC system onboard helicopters.

The novel VCC system benchmarked against the baseline case features a twin-stage high-speed electrically-driven centrifugal compressor, in place of the commonly used scroll compressor. Such design choice allows for higher efficiency, lower weight, and improved compactness. Furthermore, being electrically-driven, the compressor can be placed far from the Main Gear Box (MGB), which is typically located in the upper portion of the vehicle. This enables the use of a shorter hose connecting the evaporator outlet with the compressor suction port. This piping operates at the lowest system pressure level, hence a reduction of the pressure drop in this section may beneficially influence the system efficiency, especially when operating with low-density refrigerants. Two compression stages are

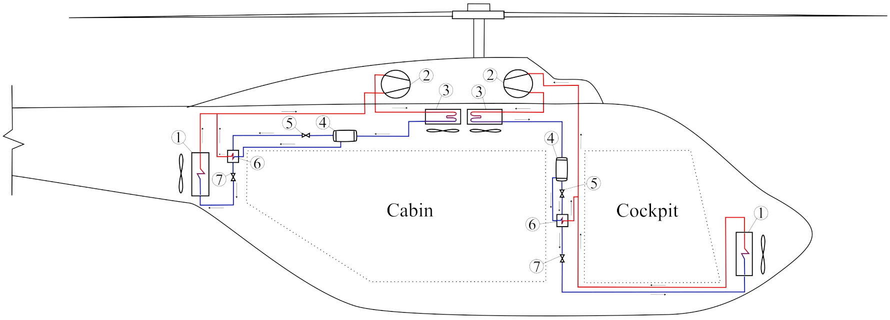

Figure 4.1.: Installation arrangement of the Environmental Control System components onboard the helicopter: 1) Evaporator, 2) Compressor, 3) Condenser unit, 4) Liquid tank, 5) Expansion valve, 6) Intercooler, 7) Expansion valve.

needed to meet the required temperature lift. The two compressor wheels are mounted in a back-to-back configuration to balance their axial thrust, thus allowing for the use of gas bearings. Figure 4.2a shows a simplified process flow diagram of a single VCC system pack.

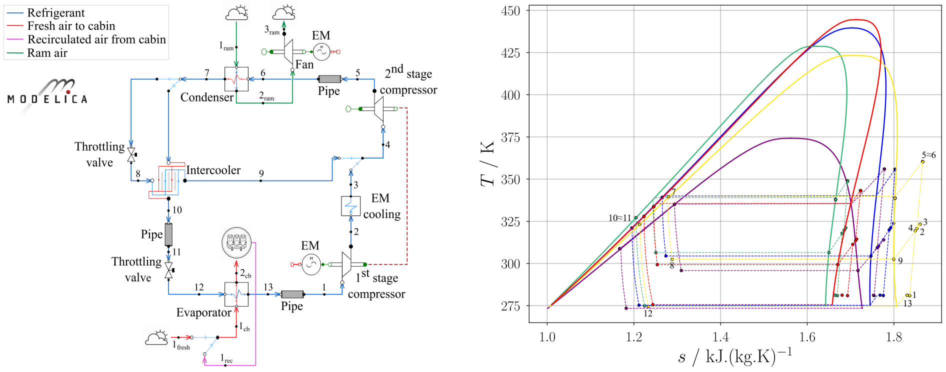

(a)

(b)

Figure 4.2.: (a) Graphical interface of the Modelica model of the VCC-based ECS onboard large helicopters. (b) T-s chart of the thermodynamic processes of the VCC system for each working fluid selected for the system optimization, i.e., — R-134a ($N = -1.10$), — R-1233zd(E) ($N = 3.92$), — R-1224yd(Z) ($N = 4.91$), — R-1234ze(Z) ($N = 1.50$), — R-1336mzz(Z) ($N = 9.24$).

The working fluid commonly adopted for the helicopter ECS is the hydrofluorocarbon (HFC) R-134a [16]. In this work, the refrigerants R-1233zd(E), R-1224yd(Z), R-1234ze(Z) and R-1336mzz(Z) have been tested as possible alternative refrigerants. Table 4.1 lists the main thermodynamic properties and characteristics of the selected haloolefins in comparison to those of R-134.

Table 4.1.: List of the main thermodynamic properties of the working fluids tested for the helicopter ECS optimization [17, 18].

ASHRAE designation	**R-134a**	**R-1233zd(E)**	**R-1224yd(Z)**	**R-1234ze(Z)**	**R-1336mzz(Z)**
Chemical Formula	CH_2FCF_3	$CF_3CH{=}CHCl$	$CF_3CF{=}CHCl$	$CF_3CH{=}CFH$	$CF_3CH{=}CHCF_3$
Category	HFC	HCFO	HCFO	HFO	HFO
Safety class	A1	A1	A1	A2L	A1
GWP	1300	1	<1	1	2
ODP	0	0	0	0	0
ALFT	13.4 years	26 days	21 days	16.4 days	22 days
NBP / °C	−26	18.2	14.6	9.7	33.4
N^a / -	−1.10	3.92	4.91	1.50	9.24
M / g·mol^{-1}	102.0	130.5	148.5	114.0	164.1
T_C / °C	101	166.5	155.5	150.1	171.3
p_C / bar	40.6	36.2	33.4	35.3	29.0
$\rho_{x=1}\|_{T=0°C}$ / kg·m^{-3}	14.4	2.8	3.8	3.6	1.8

---

[a] The values of molecular complexity are estimated assuming that saturated vapour properties approximate those of the ideal gas, namely: $N \approx \frac{Cp}{0.7R} - \frac{\log 10}{0.49}\frac{7}{3}(\omega+1)$ [19].

Figure 4.2b shows a comparison of the thermodynamic cycles on the T-s chart of these working fluids. Ascione *et al.* [13] demonstrated that the system COP increases if these refrigerants are used in place of R-134a. In particular, if the cooling capacity and the evaporation temperature are fixed, the following observations are valid: i) in the case of isentropic dew-line fluids (R-1233zd(E) and R-1234ze(Z)), the large latent heat of evaporation causes a reduction of the cycle mass flow rate, with a consequent decrease of the compressor power demand; ii) in the case of dry fluids (R-1336mzz(Z) and R-1224yd(Z)), despite the small latent heat of evaporation, the shape of the saturated liquid and vapour curves allows for a significant reduction of the losses associated with vapour superheating along the compression.

4.3. CASE STUDY

The integrated design optimization of the system described in Sec. 4.2 has been performed, accounting simultaneously for the selection of the optimal working fluid. This study relies on the optimization framework *DesOptECS TurboEd*, whose methodology is described in Sec. 3.3 and illustrated in Fig. 3.8. The system has been modelling resorting to the Modelica language [20], using the components from the *DeSimECS* (Design and Simulation of Energy Conversion Systems) (see Sec. 3.2). To overcome the issues associated with the numerical solver in the case of complex system models, the preliminary design model of the twin-stage centrifugal compressor is decoupled from the Modelica system model, thus the compressor design is performed using the in-house code *TurboSim*, described in Sec. 3.2.4.

The integrated design optimization framework described has been tested on the design of a VCC system for a large rotorcraft ECS (20 passengers and 2 pilots). The design point of the system is representative of a critical operating case: the helicopter is on the ground on a hot and humid day, i.e., the temperature is 40 °C and the relative humidity 40%. Table 4.2 lists the operating parameters chosen for the system simulation. Furthermore, the complete list of parameters selected for the design of the system HEXs can be found in Tab. 4.3. For the multi-louvered fins and minichannels HEXs, key geometric parameters such as tube, fin, and minichannel thickness, along with fin pitch, were set based on manufacturing constraints. The tube geometry and the number of minichannels were kept constant to reduce design variables. For the intercooler, due to its lower heat load, only one core dimension was optimized, while other parameters remained fixed to limit the complexity of the optimization problem.

The multi-objective optimization (MOO) problem features as objective functions the COP and the system weight. More specifically, the weight is estimated by accounting for that of the three HEXs, the piping, and the centrifugal compressor. Following the indication of the industrial partners, the materials selected for the compressor and the heat exchangers are respectively the 2219-T852 aluminium alloy and the Aluminium 3003.

Table 4.2.: Operating parameters for the ECS in the case of helicopter on the ground on a hot and humid day.

Helicopter ECS system for cabin air conditioning		
Refrigerant loop		
Evaporation temperature	$T_{\mathrm{air,env}}$ / °C	0
Evaporator cooling duty	$\dot{Q}_{\mathrm{eva}}$ / kW	12.5
Air side		
Environmental air temperature	$T_{\mathrm{air,env}}$ / °C	40
Recirculated cabin air temperature	$T_{\mathrm{air,rec}}$ / °C	28
Ram air mass flow rate	$\dot{m}_{\mathrm{ram}}$ / $\mathrm{kg \cdot s^{-1}}$	1.1
Fresh cabin air mass flow rate	$\dot{m}_{\mathrm{fresh,cb}}$ / $\mathrm{kg \cdot s^{-1}}$	0.1
Recirculated cabin air mass flow rate	$\dot{m}_{\mathrm{rec,cb}}$ / $\mathrm{kg \cdot s^{-1}}$	0.5

Table 4.3.: Geometrical parameters of multi-louvered fins and minichannels within condenser and evaporator, and of the flat plate chevron type HEX used as intercooler.

Evaporator			**Condenser**		
Tube height	T_{h} / mm	2	Tube height	T_{h} / mm	1.93
Tube wall thickness	δ_{t} / mm	0.4	Tube wall thickness	δ_{t} / mm	0.4
Tubes pitch	T_{p} / mm	9.4	Tubes pitch	T_{p} / mm	2.33
Number of minichannels	N_{mc} / -	16	Number of minichannels	N_{mc} / -	12
Minichannels wall thickness	δ_{mc} / mm	0.35	Minichannels wall thickness	δ_{mc} / mm	0.3
Fins pitch	F_{p} / mm	3	Fins pitch	F_{p} / mm	1.4
Fins thickness	δ_{f} / mm	0.12	Fins thickness	δ_{f} / mm	0.115

Intercooler		
Number of passes (both refrigerant streams)	N_{pass} / -	1
Number of channels per pass (both refrigerant streams)	N_{channel} / -	40
Flat plate width	W_{plate} / mm	120
Port diameter	D_{port} / mm	30
Amplitude sinusoidal corrugation pattern	Λ / mm	1.5
Wave length corrugation pattern	a / mm	10
Flat plate thickness	δ_{plate} / mm	0.4
Plate inclination angle	β_{plate} / deg	60

The optimization problem consists of 24 design variables whose range of variation is set the same for all the considered working fluids, and 26 inequality constraints (Tab. 4.4). The stochastic optimization algorithm chosen for this application is the Non-Sorted Genetic Algorithm II (NSGA-II) implemented in the open-source Python library Pymoo [21]. Each population consists of 10 individuals for each design variable, for a total of 220 individuals.

The initial points are sampled differently according to the variable type, i.e., with random sampling for integers, and with the Latin hypercube approach for the real number variables. The thermodynamic and transport properties of the working fluids have been calculated using a well-known commercial program [18]. A unique Modelica system model is used to test all the different refrigerants, hence, any difference in the computational time needed to reach convergence is only dependent on the complexity of the equation of state model. On average, 7 days of computational time is needed to reach convergence on a standard desktop workstation with a CPU Intel(R) Xeon(R) CPU E5-1620 v3 featuring 8 logical cores.

4.4. RESULTS

A Pareto front of optimal solutions is obtained for each working fluid, aside from R-1336mzz(Z) (Fig. 4.3) because if this is the working fluid the algorithm could not determine any non-dominated solution due to the violation of some of the constraints related to the centrifugal compressor design, as discussed in Sec. 4.4.2. Figure 4.3 shows that, compared to R-134a, low-GWP refrigerants always allow for more efficient and lighter system designs. In particular, R-1234ze(Z) can be deemed as the best working fluid, enabling a 12% increase in efficiency and a 26% reduction in weight. Despite the enhancement in terms of COP with respect to R-134a, the use of R-1233zd(E) is always associated with the design of heavier system components if compared to the other two HFOs. Finally, if R-1224yd(Z) is the working fluid, the system exhibits a performance that is a compromise between that of R-1233zd(E) and R-1234ze(Z).

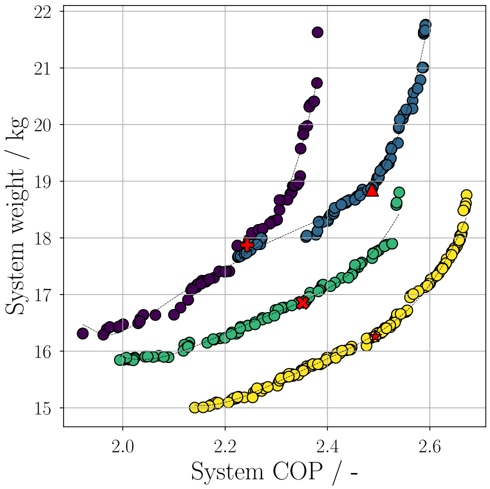

Figure 4.3.: Pareto fronts associated with the considered working fluids resulting from the system optimization in terms of system weight and COP. The working fluids are (●) R-134a, (●) R-1233zd(E), (●) R-1224yd(Z),(●) R-1234ze(Z). Optimal system design points selected according to the approach discussed in Sec. 4.4.3 (✚, ▲, ✖ ,★).

In this work, the COP has been defined as the ratio between the evaporator cooling capacity and the total electric power needed to drive all the turbomachinery installed in the system, i.e., the fan and the centrifugal compressor

Table 4.4.: Design variables and constraints values selected for the design optimization problem.

Design variables			
Variable	Symbol	Min. value	Max. value
Louver angle (evap. and cond.)	Θ / deg	25	35
Louver pitch (evap. and cond.)	L_p / mm	0.50	3
Louver length (evap. and cond.)	L_l / mm	2.13	18.5
Evaporator height	H_{eva} / mm	100	700
Condenser height	H_{cond} / mm	100	500
HEX depth (evap. and cond.)	D_{HEX} / mm	20	60
Compression ratio (1^{st}, 2^{nd} stage)	β_{tt} / -	2	4
Swallowing capacity (1^{st}, 2^{nd} stage)	Φ_{t1} / -	0.02	0.20
Shape factor (1^{st}, 2^{nd} stage)	k / -	0.65	0.95
Absolute outlet angle (1^{st}, 2^{nd} stage)	α_2 / deg	60	75
Number of blades (1^{st}, 2^{nd} stage)	N_{bl} / -	10	20
Diffuser to outlet impeller radius ratio (1^{st}, 2^{nd} stage)	R_3/R_2 / -	1.2	2
Loading coefficient (2^{nd} stage)	Ψ / -	0.65	1
Refrigerant mass flow rate (1^{st} stage)	$\dot{m}_{refr}$ / kg·s^{-1}	0.05	0.15

Constraints values			
Variable	Symbol	Min. value	Max. value
HEX width (evap. and cond.)	W_{HEX} / mm	50	800
Refrigerant velocity (evap. and cond.)	v_{refr} / m·s^{-1}	-	20
Air velocity (evap. and cond.)	v_{air} / m·s^{-1}	-	20
ΔT pinch point (condenser)	$\Delta T_{pp,cond}$ / K	5	20
Refrigerant pressure drop (evap. and cond.)	Δp_{refr} / bar	-	0.8
Air pressure drop (evap. and cond.)	Δp_{air} / Pa	-	400
Inlet hub radius (1^{st}, 2^{nd} stage)	$R_{1,hub}$ / mm	2.35	-
Outlet blade height (1^{st}, 2^{nd} stage)	$H_{2,blade}$ / mm	0.6	-
Outlet relative blade angle (1^{st}, 2^{nd} stage)	$\beta_{2,blade}$ / deg	-45	-10
Rotational speed (1^{st}, 2^{nd} stage)	Ω / krpm	10	200
Inlet relative Mach at shroud (1^{st}, 2^{nd} stage)	$M_{w_{1,s}}$ / -	-	1.4
Outlet relative Mach at shroud (1^{st}, 2^{nd} stage)	$M_{w_{2,s}}$ / -	-	0.98
Absolute Mach at diffuser outlet (1^{st}, 2^{nd} stage)	M_3 / -	-	0.70
Net axial thrust twin-stage compr.	F_{axial} / N	0	26

$$\mathrm{COP} = \frac{\dot{Q}_\mathrm{eva}}{\dot{W}_\mathrm{compr} + \dot{W}_\mathrm{fan}}. \tag{4.1}$$

As expected, the electric power demand decreases as a function of the system efficiency (Fig. 4.4). In particular, the power needed to drive the fan varies in a range from 0.10 kW to 0.38 kW, depending on the pressure drop in the ram air stream delivered to the condenser. The root cause of the difference in terms of system COP between the working fluids is the centrifugal compressor power demand, which ranges from 4.5 kW to 6.5 kW.

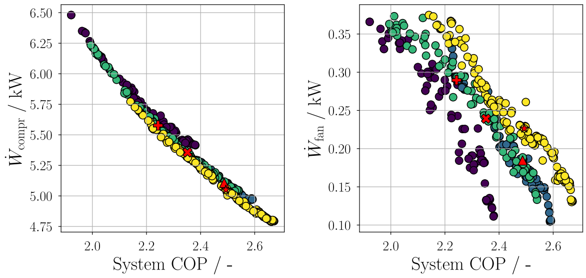

Figure 4.4.: From left to right: centrifugal compressor and ram air fan electric power demand as a function of the system COP. Working fluids: (●) R-134a, (●) R-1233zd(E), (●) R-1234ze(Z), (●) R-1224yd(Z).

Figure 4.5 displays the breakdown of the total system weight into those of the main system components as a function of the COP and the prescribed refrigerant. The piping weight is included in the overall calculation, but it is not shown in Fig. 4.5 since its value is negligible with respect to those of the HEXs and the compressor. The heaviest system component is the compressor. Its weight ranges from 8.3 kg to 8.8 kg and it decreases for more efficient system designs, since the compressor power demand is reduced. According to the methodology described in Sec. 4.2, the weight of the Electronic Control Unit (ECU) is independent of the working fluid and equal to 7.5 kg, therefore the differences observed among the working fluids are only associated with the sizing of the compressor wheel, the casing, and the electric motor. The compressor weight calculation depends on parameters, e.g. wall thickness, and back face disk thickness, which are meant to be selected only for detail design. Therefore, the values of weight reported in this manuscript are approximate and they are only meant to indicatively show the dependence between working fluid and compressor weight, which is not expected to exceed a maximum of 2.5 kg given the small values of electric power demand. The results confirm that the use of the HFOs leads to the design of a larger compressor with respect to R-134a. Among the HFOs, R-1234ze(Z) would lead to the heaviest optimal compressor designs. Even if its vapour density is similar to that of R-1224yd(Z), a larger amount of refrigerant mass flow rate is needed in the VCC loop because of the small specific enthalpy difference across the evaporator (Fig. 4.6). Thus, larger flow passages are required within the compressor.

Among the HEXs, the condenser is the heaviest component and its weight variation as a function of the system COP is the widest among all the system components (Fig. 4.5). The condenser weight is almost independent of the choice of the working fluid since its sizing is a consequence of the ram air pressure drop, thus the electric fan power consumption minimization. Hence, heavier condensers, featuring large ram air frontal areas, are necessary for high-efficiency systems.

Contrarily, the evaporator weight is independent of the COP, but it is strongly influenced by

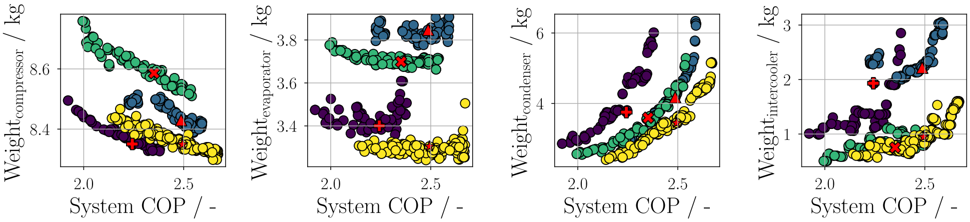

Figure 4.5.: Trend of the weight of the main system components as a function of the system COP. Working fluids: (●) R-134a, (●) R-1233zd(E), (●) R-1234ze(Z), (●) R-1224yd(Z). From left to right: centrifugal compressor, evaporator, condenser, and intercooler.

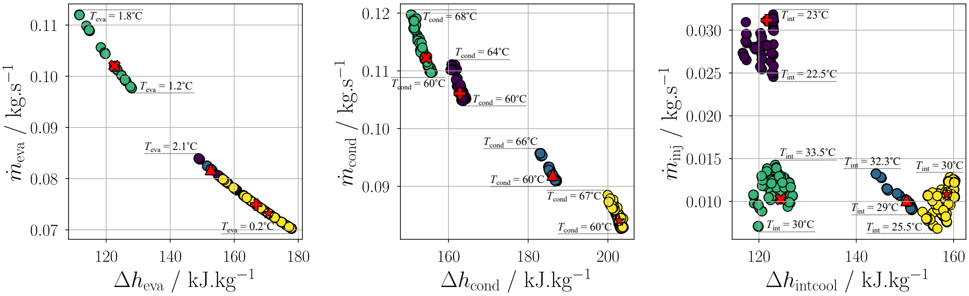

Figure 4.6.: Refrigerant mass flow rate as a function of the specific enthalpy variation for each heat exchanger, and corresponding range of operating temperature. From left to right: evaporator, intercooler and condenser. Working fluids: (●) R-134a, (●) R-1233zd(E), (●) R-1234ze(Z), (●) R-1224yd(Z).

the choice of the working fluid. The heaviest devices are designed in the case of R-1233zd(E). Among the selected HFOs, this refrigerant is characterized by the lowest density, implying the need for larger flow passages to limit the velocity of the refrigerant, hence the associated pressure drops. Note that, for a prescribed cooling capacity in the evaporator, the specific enthalpy variation of R-1233zd(E) is similar to the one of R-134a (Fig. 4.6). Therefore, the refrigerant mass flow rate is comparable, and any difference in the HEX weight can only be associated with the effect of the fluid density. In the case of R-1224yd(Z), despite the similarities in terms of thermodynamic properties with R-1234ze(Z), the evaporator weight is different. Figure 4.6 shows that the mass flow rate of R-1224yd(Z) within the evaporator is larger as compared with that calculated for the other refrigerants. This aspect, combined with the effect of the flow density, makes the size of this HEX similar to the one for the R-1233zd(E) system. In the case of R-1234ze(Z), the optimal designs correspond to evaporators whose weights are closer to those for R-134a. This is explained considering that, despite the large difference in terms of flow density, the mass flow rate of this refrigerant is the lowest if compared to those computed for the other haloolefins, thanks to the large latent heat of evaporation. This effect compensates for the effect associated with the low flow density, leading to compact evaporators.

Finally, the results show that the sizing of the intercooler is similar for all the working fluids. Its weight oscillates between 0.5 kg and 3 kg. The only variable influencing the intercooler sizing, hence its weight, is the plate length (L_{plate}). The heat duty of this HEX ranges from 1 kW to 2 kW in the case of the haloolefins, and it increases from 3 kW to 4 kW for R-134a.

The heaviest component is sized for the case of R-1233zd(E). Despite the similar values of the mass flow rate of R-1224yd(Z) and R-1234ze(Z) (Fig. 4.6), the lower refrigerant density of R-1233zd(E) implies larger flow passages, therefore a bulkier and heavier component (Fig. 4.5).

4.4.1. HEAT EXCHANGERS DESIGN

According to the adopted design requirements, the cooling capacity of the evaporator is specified and equal to 12.5 kW. From Eqn. 4.1, the only variable which affects the evaporator sizing in case the system COP is to be maximized is the pressure drop associated with the refrigerant flow. Figure 4.7 illustrates the trend of the three dimensions of the evaporator core as a function of the refrigerant pressure drop.

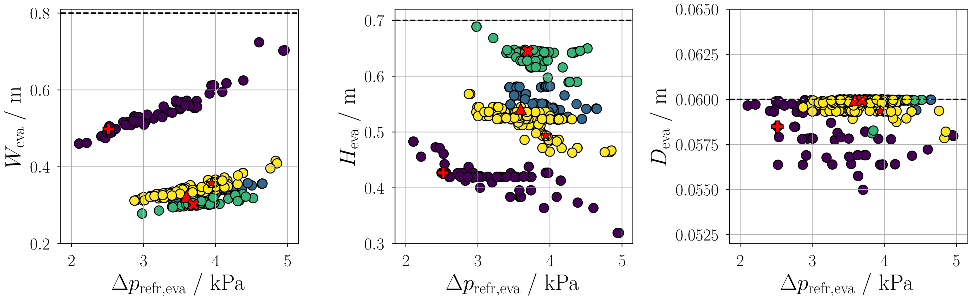

Figure 4.7.: Trend of the three dimensions of the evaporator core (from left to right: width, height, and depth) as a function of pressure drop associated with the refrigerant flow. Working fluids:(●) R-134a, (●) R-1233zd(E), (●) R-1234ze(Z), (●) R-1224yd(Z).

The optimal evaporator designs are characterized by a short width and a large height. These designs feature a large number of short tubes to decrease the refrigerant velocity and shorten the flow path. The optimal depth of the evaporator is the same for all the fluids, and its value corresponds to the upper bound of the range selected for this design variable (see Tab. 4.4). Notice that the value of H_{eva} is larger in the case of haloolefins, because of the larger frontal area needed to reduce the flow speed in the case of low-density refrigerants and obtain a pressure drop in the same range as that calculated for R-134a. Table 4.5 lists the values of the fin geometrical parameters and of the variables related to the aerothermal performance of the evaporator, calculated as an average of the values related to the optimal designs. In the case of low-GWP refrigerants, the flow velocity is almost double that of R-134a, with a consequent similar trend for the heat transfer coefficient. Such high values allow the design of compact-size evaporators despite the limitations associated with the fluid density when operating at low-pressure levels. Finally, the size of the fins is similar, independently from the working fluid. The same is valid for the performance of the ram air side, as reported in Tab. 4.5.

As opposed to the design of the evaporator, the condenser sizing is driven by the need to minimize the fan power demand, hence the ram air pressure drop. As reported by Ascione *et al.* [13], in the case of ground operating conditions, the required ram air mass flow rate is approximately equal to 1.1 $\mathrm{kg \cdot s^{-1}}$, see the design specifications listed in Tab. 4.2. Hence, to enhance the system efficiency while minimizing friction losses, the condenser must feature a large ram air frontal area (Fig. 4.8). Figure 4.4 shows that the electric fan power demand and the air pressure drop are almost independent from the selected working fluid. Therefore, the minimum ram air pressure drop is achieved in correspondence with the largest value of

Table 4.5.: Values defining the optimal fins geometry and the aerothermal performance of the evaporator. These values are calculated as an average of those related to optimal designs for each refrigerant.

Variable	**Symbol**	**R-134a**	**R-1233zd(E)**	**R-1224yd(Z)**	**R-1234ze(Z)**
Louver angle	Θ / deg	34.5	34.1	34.7	33.8
Louver length	L_l / mm	10.6	5.90	7.10	7.40
Louver pitch	L_p / mm	0.50	0.50	0.50	0.50
Refrigerant flow velocity	v_{refr} / m·s^{-1}	2.5	5.7	5.8	5.4
Refrigerant heat transfer coefficient	h_{refr} / kW·m^{-2}·K^{-1}	1.97	6.07	5.05	5.13
Air flow velocity	v_{air} / m·s^{-1}	2.3	2.8	2.7	2.9
Air heat transfer coefficient	h_{air} / W·m^{-2}·K^{-1}	121	133	142	128
Air pressure drop	Δp_{air} / Pa	173	218	208	230

condenser width, see Tab. 4.4. Finally, the optimal condenser depth does not depend on the adopted working fluid and corresponds to the minimum value that this variable can assume within the prescribed design space (Fig. 4.8).

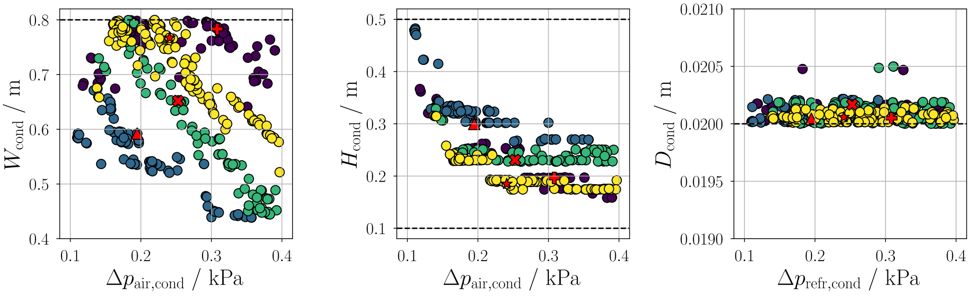

Figure 4.8.: Trend of the three dimensions of the condenser core (from left to right: width, height and depth) as a function of pressure drop associated with the ram air flow. Working fluids:(●) R-134a, (●) R-1233zd(E), (●) R-1234ze(Z), (●) R-1224yd(Z).

Table 4.6 summarizes the fin geometry of the condenser for all the refrigerants. The fin geometry is very similar for all the fluids, except for the louver pitch, whose largest values are calculated in the case of haloolefins. This can be justified considering that larger flow pitches allow for lower pressure drops to guarantee an optimal trade-off between friction loss reduction and HEX compactness on the ram air side.

Table 4.6.: Optimal condenser fin design parameters. These values are calculated as an average of the optimal design points over the Pareto front of each refrigerant.

Variable	**Symbol**	**R-134a**	**R-1233zd(E)**	**R-1224yd(Z)**	**R-1234ze(Z)**
Louver angle	Θ / deg	29.2	28.5	28.8	29.5
Louver length	L_l / mm	9.5	10.6	10.7	9.2
Louver pitch	L_p / mm	1.9	2.6	2.6	2.9

As discussed thus far, for a constant ram air mass flow rate, the optimal condenser dimensions are independent of the working fluid selection, and the same is valid for the airflow velocity. Consequently, the range of variation of the heat transfer coefficient is similar for all refrigerants on both sides of the condenser, as shown in Fig. 4.9. Finally, for what regards the refrigerant side, the effect of flow density has a strong influence on the evaporator sizing. Since the global size of the HEX, the condensation temperature, and the refrigerant mass flow rate (see Fig. 4.6) are comparable for all the working fluids, condensers designed for haloolefins are always characterized by higher flow velocities if compared to those designed for R-134a. As a consequence, larger pressure drops occur on the refrigerant side, while the heat transfer coefficient varies in the same range of values as those calculated in case R-134a is the working fluid.

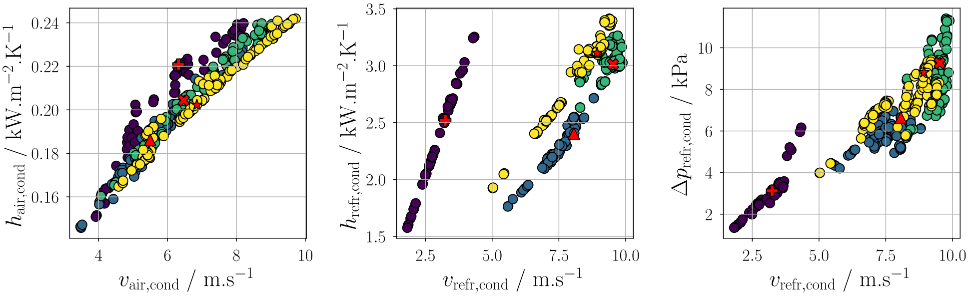

Figure 4.9.: Condenser aerothermal performance. From left to right: ram air heat transfer coefficient as a function of the air velocity. Refrigerant stream heat transfer coefficient as a function of the refrigerant velocity inside the condenser tubes. Pressure drop associated with the refrigerant stream as a function of the refrigerant speed within the condenser tubes. Working fluids:(●) R-134a, (●) R-1233zd(E), (●) R-1234ze(Z), (●) R-1224yd(Z).

4.4.2. COMPRESSOR DESIGN

Table 4.7 lists the average value of the design variables used for the centrifugal compressor design. These values are calculated as an average of the optimal design points over the values of the Pareto front obtained for each refrigerant. The loading coefficient is similar for each compressor stage and does not vary significantly with the working fluid. The values of the flow coefficient and the shape factor are higher for the first stage than the second stage, and this is true also for the pressure ratio and the isentropic efficiency (Fig. 4.10). The reason is that there is an optimal trade-off between the interstage pressure, and thus the split of the compressor duty among the two stages, which maximizes the system efficiency and the need to satisfy the constraint on the maximum net axial thrust. The design of the second stage is technologically more challenging due to the lower volumetric flow rate associated with the higher density of the fluid. Hence, the optimal twin-stage compressor design features an unequal split of the total-to-total pressure ratio, which is lower for the second stage, in order to limit the inherent efficiency penalty. These considerations are valid for all fluids, except for the case of R-134a, and agree with the findings reported by Giuffreé *et al.* [9].

In the case of R-134a, the optimal designs are characterized by higher pressure ratios of the second stage as compared to the values of the first stage (Fig. 4.10). This is due to the higher influence of the prescribed set of constraints on the design of such compressor. The higher density of R-134a with respect to that of the other refrigerants leads to the design of a

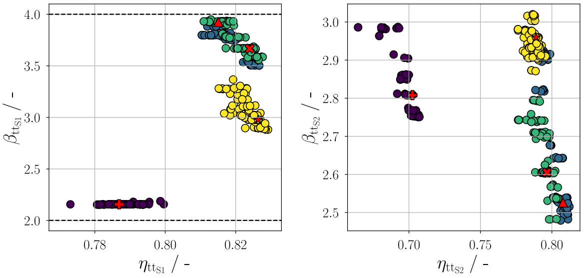

Figure 4.10.: Total-to-total compression ratio as a function of the isentropic efficiency of the first stage (left) and the second stage (right) of the centrifugal compressor. Working fluids:(●) R-134a, (●) R-1233zd(E), (●) R-1234ze(Z), (●) R-1224yd(Z).

compressor featuring a higher rotational speed, smaller dimensions, and a higher net axial thrust. The consequence thereof is a sizeable limitation of the feasible design space and ultimately the choice of very low values of the flow coefficient for both stages. Notice that the selection of a low flow coefficient for the second stage is believed to strongly penalize the operating range of the machine, thus generally leading to a sub-optimal design [9]. However, the maximization of the compressor operating range is not included in the set of design optimization variables, thus leading to optimal designs for R-134a featuring a higher pressure ratio and a low flow coefficient in the second stage.

Table 4.7.: Optimal design variables for the twin-stage centrifugal compressor design. These values are calculated as an average of the optimal design points over the Pareto front associated with each refrigerant.

		R-134a		**R-1233zd(E)**		**R-1224yd(Z)**		**R-1234ze(Z)**	
Variable	Symbol	Stage 1	Stage 2	Stage 1	Stage 2	Stage 1	Stage 2	Stage 1	Stage 2
Swallowing capacity	Φ_{t1} / -	0.07	0.03	0.15	0.07	0.12	0.06	0.16	0.07
Loading coefficient	Ψ / -	0.65	0.72	0.70	0.70	0.68	0.68	0.65	0.71
Shape factor	k / -	0.82	0.75	0.94	0.84	0.90	0.85	0.92	0.84
Outlet absolute flow angle	α_2 / deg	68	73	69	70	69	71	67	71
Diffuser to outlet impeller radii ratio	R_3/R_2 / -	1.45	1.35	1.50	1.35	1.47	1.42	1.80	1.40

Figure 4.11 shows the trend of the impeller hub radius as a function of the rotational speed and of the blade height at the impeller outlet with respect to the volumetric flow rate. As compared to R-134a, haloolefins allow for larger impeller wheels for both compressor stages, as a result of the larger volumetric flow rate, thus overcoming all the challenges associated with manufacturability. Large compressor wheels inherently lead to a reduction of the rotational speed (Fig. 4.12). To comply with the limit on the maximum axial thrust, the rotational speed in the case of R-134a is comparable with that associated with R-1234ze(Z). Therefore, the compressors designed for these two refrigerants have similar ranges of impeller size (Fig. 4.11). Figure 4.12 shows the trend of the net axial thrust of the twin-stage centrifugal compressor as a function of the rotation speed. For the considered design case, a maximum admissible value of the axial force equal to 26 N has been selected. The results show that the optimal compressor designs obtained for the haloolefins have a large margin of safety with respect to this limit.

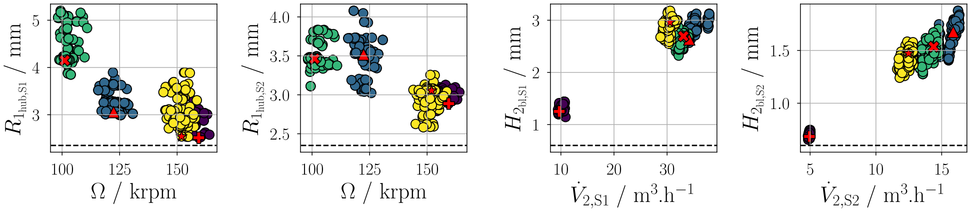

Figure 4.11.: Twin-stage centrifugal compressor impeller sizing. From left to right: trend of the impeller inlet radius at the hub as a function of the compressor rotational speed for both the first and the second stages. Outlet blade height as a function of the volumetric flow rate of both the first and second compressor stages. Working fluids:(●) R-134a, (●) R-1233zd(E), (●) R-1234ze(Z), (●) R-1224yd(Z).

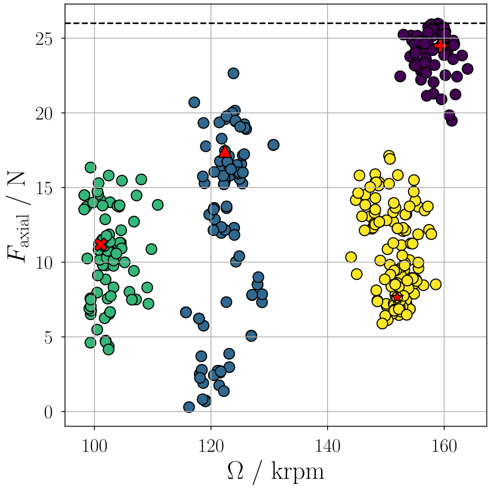

Figure 4.12.: Trend of the net axial thrust as a function of the rotational speed of the twin-stage centrifugal compressor and the working fluid ((●) R-134a, (●) R-1233zd(E), (●) R-1234ze(Z), (●) R-1224yd(Z)).

As mentioned in Sec. 4.4, the VCC system design optimization has also been performed in case refrigerant R-1336mzz(Z) is the working fluid. However, the optimization algorithm could not converge to any set of non-dominated solutions because of the violation of the non-linear constraint associated with the maximum admissible value of inlet relative Mach number at the impeller shroud ($M_{\mathrm{w}_{1,\mathrm{s}}}$), as reported in Tab. 4.4. With reference to the properties listed in Tab. 4.1, R-1336mzz(Z) is a promising alternative to R-134a: this refrigerant is not flammable or toxic, and it features the lowest value of vapour density and the highest molecular complexity among all the considered working fluids. However, higher molecular complexity implies large Mach number values of the flow through the compressor channels, as discussed in Sec. 2.4. Designs for which $M_{\mathrm{w}_{1,\mathrm{s}}}$ exceeds 1.4 are discarded to limit the losses associated with secondary flow and mixing due to shock interaction within the rotor flow channels, as discussed by Rusch and Casey [22]. However, to investigate whether any R-1336mzz(Z) compressor design was feasible, the constraint on the maximum inlet Mach number at the impeller shroud has been relaxed and its value set to 1.6. In this case, the system optimization converged to a limited set of non-dominated solutions. However, the optimal compressor designs feature values of design mass flow rates which are very close to those at the chocking point. Thus, despite the attractive properties of R-1336mzz(Z), the results of the system optimization reveal that the design of a twin-stage centrifugal compressor is unfeasible. Feasible compressor designs might be obtained with more than two stages.

4.4.3. OPTIMAL SYSTEM DESIGNS

For each working fluid, a single optimal design has been selected among those forming the Pareto front resulting from the solution of the MOO procedure (Fig. 4.3). It is common practice in aerospace engineering to identify the optimal system design solution as the one enabling the minimum aircraft specific fuel consumption. This quantity is defined as a linear combination of the penalties associated with system weight, power off-take and ram air drag. However, in the case of the helicopter operating on the ground, the ram air drag penalty cannot be accounted for as an objective function. Therefore, a multi-criteria decision-making algorithm based on the Augmented Scalarization Function (ASF) decomposition method has been selected [23]. A decomposition method requires the definition of a vector of weights with a number of elements equal to the number of objective functions and formed by positive float numbers, whose sum is unitary. Such a vector defines how predominant is each one of the objectives with respect to the others for the selection of a single optimal design point out of all the non-dominated solutions forming the Pareto front. The decomposition transforms the MOO procedure into a set of single-objective optimization problems. However, since the individual objective functions usually feature different scales of values, normalization is always needed, thus

$$\bar{f}_q(x) = \frac{f_q(x) - c}{\hat{z}_q^{\mathrm{N}} - \hat{z}_q^*}, \quad \forall q = 1, \ldots, Q \tag{4.2}$$

where $\hat{z}_q^*$ and $\hat{z}_q^{\mathrm{N}}$ are respectively the ideal point and the nadir point. They are known as boundary points since they define the range of the solutions to the optimization problem. In particular, the ideal point corresponds to the best of each objective function in the design space

$$\hat{z}_q^* = \min\{f_q(x) \mid x \in \Omega\}. \tag{4.3}$$

The nadir point is the worst value for each objective function in the design space

$$\hat{z}_q^{\mathrm{N}} = \max\{f_q(x) \mid x \in \Omega\}. \tag{4.4}$$

Afterwards, the ASF decomposition method is applied. Its mathematical expression is

$$\min\left\{g^{\mathrm{ASF}}(x \mid w, z^*) = \max\left\{\frac{1}{w_i} \mid f_i(x) - z_i^* \mid\right\}\right\} \tag{4.5}$$

Here, the same weight has been assigned to both objective functions, since they are assumed to be equally important for the definition of the best design point. Table 4.8 reports a list of the main system design parameters, corresponding to the optimal points forming the Pareto front associated with each refrigerant.

In the case of haloolefins as working fluids, the corresponding optimal designs are similar, due to the comparable thermodynamic properties of these refrigerants. The optimal operating temperature levels are the same. With respect to the temperature in the evaporator, since the outlet flow temperature is fixed and set equal to 0 °C, any difference in the flow temperature

Table 4.8.: List of the main system design parameters corresponding to the optimal design points chosen from the Pareto front associated with each working fluid.

Variable	Symbol	(✚) **R-134a**		(▲) **R-1233zd(E)**		(✖) **R-1224yd(Z)**		(★) **R-1234ze(Z)**	
System efficiency	COP / -	2.20		2.50		2.30		2.50	
System weight	weight / kg	17.9		18.9		16.9		16.2	
Evaporation temperature [a]	T_{eva} / °C	0.2		1.6		1.5		1.3	
Intermediate temperature	T_{int} / °C	22.6		32.3		31.3		26.5	
Condensation temperature	T_{cond} / °C	61.2		61.7		62.0		61.5	
Evaporation pressure	p_{eva} / bar	2.87		0.42		0.50		0.63	
Intermediate pressure	p_{int} / bar	6.20		1.67		1.84		1.87	
Condensation pressure	p_{cond} / bar	17.4		4.22		4.80		5.53	
Fan electric power	$\dot{W}_{\mathrm{fan}}$ / kW	0.30		0.20		0.20		0.20	
Condenser									
Heat duty	$\dot{Q}_{\mathrm{cond}}$ / kW	17.3		17.1		17.3		17.0	
Weight	weight$_{\mathrm{cond}}$ / kg	3.80		4.20		3.60		3.50	
Global dimensions	$W_{\mathrm{cond}} \times H_{\mathrm{cond}} \times D_{\mathrm{cond}}$ / m×m×m	0.78×0.20×0.02		0.60×0.30×0.02		0.65×0.23×0.02		0.77×0.18×0.02	
Air pressure drop	$\Delta p_{\mathrm{air,cond}}$ / kPa	0.31		0.19		0.20		0.20	
Air heat transfer coeff.	$h_{\mathrm{air,cond}}$ / $\mathrm{W \cdot m^{-2} \cdot K^{-1}}$	308		195		253		241	
Air velocity	$v_{\mathrm{air,cond}}$ / $\mathrm{m \cdot s^{-1}}$	6.30		5.50		6.50		6.85	
Refrigerant pressure drop	$\Delta p_{\mathrm{refr,cond}}$ / kPa	3.12		6.65		9.26		8.82	
Refrigerant heat transfer coeff.	$h_{\mathrm{refr,cond}}$ / $\mathrm{W \cdot m^{-2} \cdot K^{-1}}$	2520		2405		3013		3112	
Refrigerant velocity	$v_{\mathrm{refr,cond}}$ / $\mathrm{m \cdot s^{-1}}$	3.24		8.06		9.52		8.93	
Evaporator									
Weight	weight$_{\mathrm{eva}}$ / kg	3.40		3.90		3.70		3.30	
Global dimensions	$W_{\mathrm{eva}} \times H_{\mathrm{eva}} \times D_{\mathrm{eva}}$ / m×m×m	0.50×0.43×0.06		0.32×0.54×0.06		0.30×0.64×0.06		0.36×0.49×0.06	
Air pressure drop	$\Delta p_{\mathrm{air,eva}}$ / Pa	190		228		208		227	
Air heat transfer coeff.	$h_{\mathrm{air,eva}}$ / $\mathrm{W \cdot m^{-2} \cdot K^{-1}}$	125		132		128		133	
Air velocity	$v_{\mathrm{air,eva}}$ / $\mathrm{m \cdot s^{-1}}$	2.50		3.0		2.70		3.0	
Refrigerant pressure drop	$\Delta p_{\mathrm{refr,eva}}$ / kPa	2.52		3.6		3.7		3.9	
Refrigerant heat transfer coeff.	$h_{\mathrm{refr,eva}}$ / $\mathrm{W \cdot m^{-2} \cdot K^{-1}}$	2005		6111		5061		5085	
Refrigerant velocity	$v_{\mathrm{refr,eva}}$ / $\mathrm{m \cdot s^{-1}}$	2.10		5.5		5.7		5.5	
Intercooler									
Heat duty	$\dot{Q}_{\mathrm{intcool}}$ / kW	3.80		1.50		1.30		1.70	
Weight	weight$_{\mathrm{intcool}}$ / kg	1.90		2.20		0.80		0.95	
Twin-stage centrifugal compressor									
Centrifugal compressor power	$\dot{W}_{\mathrm{compr}}$ / kW	5.60		5.10		5.40		5.0	
Rotational speed	Ω / krpm	159		122		101		152	
Axial thrust	F_{ax} / N	24		18		11		8	
		1st stage	2nd stage	1st stage	2nd stage	1st stage	2nd stage	1st stage	2nd stage
Compression ratio	β_{tt} / -	2.2	2.80	4.0	2.50	3.7	2.60	3.0	3.0
Total-to-total efficiency	η_{tt} / -	0.79	0.70	0.82	0.81	0.82	0.80	0.83	0.80
Mass flow rate	$\dot{m}_{\mathrm{refr}}$ / $\mathrm{kg \cdot s^{-1}}$	0.07	0.11	0.08	0.09	0.10	0.11	0.07	0.08
Swallowing capacity	Φ_{t1} / -	0.07	0.03	0.14	0.08	0.12	0.06	0.16	0.07
Loading coefficient	Ψ / -	0.67	0.71	0.70	0.71	0.69	0.70	0.65	0.70
Shape factor	k / -	0.85	0.76	0.95	0.84	0.90	0.86	0.94	0.84
Number of blades	N_{bl} / -	13	16	15	18	18	18	20	20
Outlet absolute flow angle	α_2 / deg	67.6	73.3	68.0	70.0	69.4	71.2	67.0	71.3
Outlet blade angle	$\beta_{2,\mathrm{bl}}$ / deg	-25.9	-33.1	-22.0	-27.5	-32.2	-32.3	-44.0	-39.3
Inlet impeller radius at hub	$R_{1,\mathrm{hub}}$ / mm	2.50	2.90	3.06	3.52	4.15	3.46	2.54	3.05
Outlet blade height	H_2 / mm	1.25	0.68	2.63	1.68	2.70	1.54	2.96	1.47
Diffuser to outlet impeller radii ratio	R_3/R_2 / -	1.40	1.35	1.48	1.32	1.47	1.43	1.76	1.38
Inlet relative Mach at shroud	$M_{\mathrm{w1,s}}$ / -	0.78	0.71	1.29	0.85	1.20	0.80	1.25	0.92

---

[a] The temperature at the outlet of the evaporator is imposed equal to 0 °C for all the working fluids. The effect of the pressure drop generates a temperature glide and a consequent increase of the temperature at the evaporator inlet.

at the inlet is due to the effect of the temperature glide associated with the pressure drop, which is always higher in the case of haloolefins with respect to R-134a. For the same levels of operating temperature, the corresponding saturation pressures are inherently lower as compared to the benchmark fluid. In particular, the use of haloolefins implies evaporators operating at sub-atmospheric pressures, which poses some technological challenges associated with their mechanical design. The optimal system designs obtained if haloolefins are the working fluids allow to achieve higher COP with respect to those for which R-134a is the working fluid. In particular, R-1234ze(Z) would allow to achieve the best thermodynamic performance and a lower weight if compared to those calculated for the benchmark case, with a COP that is 9% higher and a weight that is almost 10% lower. The fan electric power demand does not vary depending on the working fluid of the system, hence, the difference in system efficiency can only be associated with the electric power needed to drive the compressor, which is 10% lower in case R-1234ze(Z) is the working fluid, since the required refrigerant mass flow rate is lower. At the same time, the design of the twin-stage centrifugal compressor is very compact and features a high rotational speed, in excess of 150 krpm. With respect to the designs obtained for the other two haloolefins, due to the combination of a lower overall pressure ratio and power demand and low flow density, the impeller wheel diameters are smaller and the flow passages are larger.

4.5. CONCLUSIONS

The effect of the working fluid on the optimal design of a novel concept of environmental control system aboard helicopters has been analysed. The proposed system is based on the vapour compression cycle principle and adopts as the prime mover a small-scale high-speed centrifugal compressor in place of the traditional scroll compressor. The considered working fluids are R-1233zd(E), R-1234ze(Z), R-1224yd(Z) and R-1336mzz(Z). These refrigerants are haloolefins, and they are likely to become next-generation refrigerants, thanks to their low global warming potential. The benchmark case is the optimal system for which the state-of-the-art refrigerant R-134a is the working fluid. Steady-state and lumped parameter models of the main system components have been developed using the acausal Modelica modelling language. The optimization framework *DesOptECS TurboEd* has been coded to integrate the in-house compressor design tool *TurboSim* within the Modelica system model, using Python. Such a method allows for the system cycle calculations, simultaneously calculating the preliminary design of the system components. A multi-objective optimization has been performed using a gradient-free algorithm. The objective functions are maximum system COP and minimum system weight. The test case is the ECS of a large passenger helicopter. The system has been optimized for a single critical operating point: the helicopter is on the ground on a hot and humid day.

The main conclusions drawn from this work are summarised as follows:

i) A Pareto front of optimal design solutions is obtained for all the working fluids, except for R-1336mzz(Z). The results show that system efficiency can only be enhanced at the expense of heavier heat transfer equipment.

ii) High efficiency system designs, featuring lightweight components are possible also with haloolefins as working fluids. Among these fluids, R-1234ze(Z) is identified as the best replacement for R-134a, allowing to obtain a maximum COP increase equal to 12% and a maximum weight reduction of 26%.

iii) The adoption of haloolefins as working fluids results in heavier evaporators. The low vapour density of these refrigerants leads to designs featuring a large number of minichannels, so that the flow velocity, and hence the associated friction losses can be kept within acceptable values.

iv) The condenser is the heaviest component among the heat exchangers installed in the system. Its weight increases with the system COP, within a range from 3 kg to 6 kg. This trend is independent of the refrigerant choice. The optimal condenser designs feature large flow passages on the air stream to limit the ram air pressure drop, hence the associated fan electric power consumption.

v) The design of a twin-stage high-speed centrifugal compressor is feasible. The use of haloolefins allows for compressor efficiency of up to 80%. Thanks to the low vapour density of these refrigerants, larger flow passages and impeller wheels radii can be obtained, overcoming the challenges associated with small-capacity centrifugal compressor manufacturability. Despite the limited size of the compressor, the rotational speed never exceeds a maximum of 160 krpm. Gas bearings can be used for the rotor since the net axial thrust never exceeds 26 N.

vi) R-1336mzz(Z) is not suitable for the considered application. Because of its high molecular complexity, the flow speed of sound at the suction port of the compressor is inherently low. This makes the thermo-fluid dynamic design of the compressor challenging because of the losses associated with secondary flows and mixing due to shock interaction within the rotor flow channels. Furthermore, a safe operation of the compressor would be challenging, since the design mass flow rate is close to the choking.

NOMENCLATURE

Acronyms

ALFT	Atmospheric lifetime
ASF	Augmented Scalarization Function
CO_2	Carbon dioxide
COP	Coefficient Of Performance
DeSimECS	Design and Simulation of Energy Conversion Systems
ECS	Environmental Control System
ECU	Electronic Control Unit
F-gas	Fluorinated greenhouse gases
GWP	Global Warming Potential
HCFO	Hydrochlorofluoro-olefin
HEX	Heat Exchanger
HFC	Hydrofluorocarbon
HFO	Hydrofluoroolefin
MGB	Motor Gear Box
MOO	Multi-objective optimization
NBP	Normal Boiling Point [°C]
NSGA	Non-Sorted Genetic Algorithm
ODP	Ozone Depletion Potential
R-1224yd(Z)	cis-1-Chloro-2,3,3,3-Tetrafluoropropane
R-1234yf	2,3,3,3-Tetrafluoropropene
R-1233zd(E)	trans-1-Chloro-3,3,3-trifluoropropene
R-1234ze(Z)	cis-1,3,3,3-Tetrafluoropropene
R-134a	1,1,1,2-Tetrafluoroethane
R-1336mzz(Z)	cis-1,1,1,4,4,4-hexafluoro-2-butene
TFA	Trifluoracetic acid
VCC	Vapour Compression Cycle

Roman letters

A	Heat transfer area [m^2]
c_p	Specific heat capacity at constant pressure [J·(kg·K)$^{-1}$]
D	Depth [m], Diameter [m]
f	Objective function
F	Force [N]
g	Inequality constraint
h	Specific enthalpy [J·kg^{-1}]
H	Height [m], Blade height [m]
k	Shape factor [-]
L	Length [m]
L_l	Louver length [m]
L_p	Louver pitch [m]
$\dot{m}$	Mass flow rate [kg·s^{-1}]
M	Molar mass [g·mol^{-1}], Mach number [-]
N	Molecular complexity [-]
p	Pressure [Pa]
$\dot{Q}$	Thermal power [W]
R	Gas constant [J·(kg·K)$^{-1}$], Radius [m]
s	Specific entropy [J·(kg·K)$^{-1}$]
T	Temperature [°C]
U	Impeller blade speed [m·s^{-1}]
v	Flow velocity [m·s^{-1}]
V	Volume [m^3]
x	Design variable
W	Width [m]
$\dot{W}$	Power [W]

Greek letters

α	Absolute angle [deg]
β	Compression ratio [-]

δ	Thickness [m]
η	Efficiency [-]
Ω	Rotational speed [rpm]
Φ_t	Swallowing capacity [-]
Ψ	Loading coefficient [-]
ρ	Density [kg·m^{-3}]
Θ	Louver angle [deg]

Superscripts and subscripts

air	Air flow stream
ax	Axial
bl	Compressor impeller blades
C	Critical property
cb	Cabin air stream
compr	Compressor
cond	Conduction
eva	Evaporator
env	Environment
fan	Fan
fresh	Fresh air stream
h	Impeller hub
hub	Compressor hub
in	Inlet section
max	Maximum value
mc	Minichannels
min	Minimum value
ram	Ram air stream
rec	Recirculated air stream
refr	Refrigerant
t	Total thermodynamic state
tt	Total-to-total
s	Compressor shroud
w	Relative velocity
1	Compressor impeller inlet
2	Compressor impeller outlet
3	Compressor diffuser outlet

REFERENCES

[1] G. F. Hundy, A. R. Trott, and T. C. Welch. *Refrigeration, Air Conditioning and Heat Pumps*. Fifth edition. Butterworth-Heinemann, 2016. ISBN: 978-0-08-100647-4.

[2] E. A. Heath. "Amendment to the Montreal Protocol on Substances that Deplete the Ozone Layer (Kigali Amendment)". In: *International Legal Materials* 56 (Feb. 2017), pp. 193–205.

[3] European Commission. *Proposal for a regulation of the European parliament and of the council on fluorinated greenhouse gases, amending Directive (EU) 2019/1937 and repealing Regulation (EU) No 517/2014*. Tech. rep. May 2022.

[4] M. Mohanraj and J. D. A. P. Abraham. "Environment friendly refrigerant options for automobile air conditioners: a review". In: *Journal of Thermal Analysis and Calorimetry* 147.1 (2022), pp. 47–72. ISSN: 1588-2926. DOI: `10.1007/s10973-020-10286-w`.

[5] R. Prabakaran, D. M. Lal, and S. C. Kim. "A state of art review on future low global warming potential refrigerants and performance augmentation methods for vapour compression based mobile air conditioning system". In: *Journal of Thermal Analysis and Calorimetry* 148.2 (2023), 417'–449.

[6] M. P. Sulbaek Andersen, J. A. Schmidt, A. Volkova, and D. J. Wuebbles. "A three-dimensional model of the atmospheric chemistry of E and Z-CF3CH=CHCl (HCFO-1233(zd) (E/Z))". In: *Atmospheric Environment* 179 (Apr. 2018), pp. 250–259. ISSN: 1352-2310. DOI: `10.1016/J.ATMOSENV.2018.02.018`.

[7] C. Arpagaus, R. Kuster, M. Prinzing, F. Bless, M. Uhlmann, E. Büchel, S. Frei, J. Schiffmann, and S. S. Bertsch. "High temperature heat pump using HFO and HCFO refrigerants-system design and experimental results". In: *Refrigeration science and technology proceedings. 25th IIR international congress of refrigeration*. 2019, pp. 4239–4247.

[8] C. Arpagaus and S. Bertsch. "Experimental comparison of HCFO and HFO R-1224yd(Z), R-1233zd(E), R-1336mzz(Z), and HFC R-245fa in a high temperature heat pump up to 150 ∘C supply temperature". In: *18th International Refrigeration and Air Conditioning Conference*. Purdue University, 2021.

[9] A. Giuffré, P. Colonna, and M. Pini. "Design Optimization of a High-Speed Twin-Stage Compressor for Next-Gen Aircraft Environmental Control System". In: *Journal of Engineering for Gas Turbines and Power* 145.3 (Mar. 2023). ISSN: 0742-4795. DOI: `10.1115/1.4056022`.

[10] A. Giuffré, P. Colonna, and M. Pini. "The Effect of Size and Working Fluid on the Multi-Objective Design of High-Speed Centrifugal Compressors". In: *International Journal of Refrigeration* 143 (Nov. 2022), pp. 43–56. ISSN: 01407007. DOI: `10.1016/j.ijrefrig.2022.06.023`.

[11] F. Molés, J. Navarro-Esbrí, B. Peris, A. Mota-Babiloni, and Á. Barragán-Cervera. "Theoretical energy performance evaluation of different single stage vapour compression refrigeration configurations using R1234yf and R1234ze(E) as working fluids". In: *International Journal of Refrigeration* 44 (Aug. 2014), pp. 141–150. ISSN: 0140-7007. DOI: `10.1016/J.IJREFRIG.2014.04.025`.

[12] A. Yataganbaba, A. Kilicarslan, and I. Kurtbaş. “Exergy analysis of R1234yf and R1234ze as R134a replacements in a two evaporator vapour compression refrigeration system”. In: *International Journal of Refrigeration* 60 (Dec. 2015), pp. 26–37. ISSN: 0140-7007. DOI: `10.1016/J.IJREFRIG.2015.08.010`.

[13] F. Ascione, C. M. De Servi, O. Meijer, V. Pommé, and P. Colonna. “Assessment of an Inverse Organic Rankine cycle system for the ECS of a large rotorcraft adopting a high-speed centrifugal compressor and a low GWP refrigerant”. In: *Proceedings of the 6th International Seminar on ORC Power Systems*. Ed. by Technical University of Munich. Technical University of Munich, 2021. DOI: `10.14459/2021mp1633127`.

[14] A. Mannini. “The Environmental Control System for a modern helicopter: a blend of new technologies”. In: *Twenty-first European Rotorcraft Forum*. Saint-Petersburg, Russia, 1995, p. 11.

[15] ARP292. “Air Conditioning Helicopter General Requirements”. In: *SAE International* (2014). DOI: `10.4271/ARP292`.

[16] ARP731C. “General Requirements for Application of Vapor Cycle Refrigeration Systems for Aircraft”. In: *SAE International* (2015). DOI: `10.4271/ARP731C`.

[17] ANSI/ASHRAE Standard 34. *Designation and Safety Classification of Refrigerants*. Tech. rep. 2022.

[18] E. W. Lemmon, I. H. Bell, M. L. Huber, and M. O. McLinder. *NIST Standard Reference Database 23: Reference Fluid Thermodynamic and Transport Properties-REFPROP, Version 10.0, National Institute of Standards and Technology*. 2018. DOI: `10.18434/T4/1502528`.

[19] C. M. Invernizzi. *Closed Power Cycles Thermodynamic Fundamentals and Applications*. Londono: Springer, 2013. ISBN: 978-1-4471-5139-5. DOI: `10.1007/978-1-4471-5140-1`.

[20] Modelica Association. *Modelica Language Specification, Version 3.5*. Tech. rep. 2021.

[21] J. Blank and K. Deb. “Pymoo: Multi-Objective Optimization in Python”. In: *IEEE Access* 8 (2020), pp. 89497–89509. ISSN: 21693536. DOI: `10.1109/ACCESS.2020.2990567`.

[22] D. Rusch and M. Casey. “The design space boundaries for high flow capacity centrifugal compressors”. In: *Journal of Turbomachinery* 135.3 (Mar. 2013). ISSN: 15288900. DOI: `10.1115/1.4007548`.

[23] A. P. Wierzbicki. “A mathematical basis for satisficing decision making”. In: *Mathematical Modelling* 3.5 (Jan. 1982), pp. 391–405. ISSN: 0270-0255. DOI: `10.1016/0270-0255(82)90038-0`.

.

5

MULTI-POINT MULTI-OBJECTIVE DESIGN OPTIMIZATION OF AIRCRAFT ECS

Only when the last tree has died
and the last river been poisoned
and the last fish been caught,
we will realize we cannot eat money.

Cree Indian Proverb

A promising solution to improve the efficiency of aircraft Environmental Control Systems (ECS) is based on the adoption of Vapour Compression Cycle (VCC) technology powered by a high-speed electrically-driven centrifugal compressor. The objective of this study is to assess an optimal design methodology capable of including the selection of the working fluid of the VCC among the system optimization variables. The optimal working fluid is obtained with a Continuous-Molecular Targeting to Computer-Aided Molecular Design (CoMT-CAMD) method, whereby the thermodynamic properties of the working fluid are estimated with the PC-SAFT equation of state model. This model allows to define a so-called optimal pseudo-fluid whose molecular describers are optimized simultaneously with the design of the thermodynamic cycle and the preliminary design of the ECS components (heat exchangers, compressor, piping, etc.). With this method and the analysis of the results, the natural refrigerants 1-butene and 1-butyne have been selected as optimal working fluids for a test case, that of the ECS for short-haul single-aisle airliner, such as the Airbus A320. Then, the use of these refrigerants has been simulated in the multi-point and multi-objective optimization of the aircraft ECS test case, whose objective functions are the minimization of the system power consumption, the drag penalty associated with the ram air, and the system weight. The study was performed for three operating points of the aircraft, i.e., standard flying at cruise, flying at cruise with one ECS pack failure, and hot ground operating conditions. The results have been compared with those obtained in the case the working fluid is the state-of-the-art refrigerant R-134a. The use of natural refrigerants allows for the reduction of the drag penalty, especially in the case of 1-butene. In case 1-butyne is the working fluid, it is possible to design lightweight systems whose electric power consumption is similar to that of the benchmark system. However, the analysis shows that using either of the two natural refrigerants does not lead to a significant reduction in fuel weight penalty when compared to the system using R-134a as the working fluid.

5.1. INTRODUCTION

THE air conditioning technology currently used for the Environmental Control System (ECS) onboard passenger airliners is the Air Cycle Machine (ACM), as discussed in Sec. 1.2. The Vapour Compression Cycle (VCC) system, which is already employed for the ECS of business jets and helicopters (see Ch. 4), was identified as a promising alternative to the ACM [1]. Thus far, the lack of research, the low power density of the compressor, and the safety risks associated with the use of some refrigerants have hampered the adoption of such a system for medium and large passenger aircraft. The motivation for this research is that the weight and fuel consumption of the ECS can be reduced by adopting a VCC system powered by an electrically-driven high-speed miniature centrifugal compressor. Within this research framework, Giuffré [2] performed an integrated design optimization of both the ACM and the VCC system for the ECS of a single-aisle, short-haul passenger aircraft, e.g., A320, over three points of the operating envelope in order to evaluate the possible benefits of the new technology. The results show that the electric power consumption and the global weight of the VCC-based ECS are lower with respect to that based on the ACM, at the expense of a slight increase of the drag caused by the ram air ducts. The working fluid of the simulated VCC-based ECS is R-134a, the state-of-the-art refrigerant for aerospace applications [3].

As discussed in Ch. 2.3, the latest international regulations [4, 5] prescribe a gradual phase-out of fluorinated greenhouse gases (F-gas) from the refrigeration sector. For this reason, hydrofluorocarbons (HFCs) are being progressively replaced by *fourth-generation refrigerants*, e.g., haloolefins and natural refrigerants, characterized by values of Global Warming Potential (GWP) comparable to or lower than that of CO_2. Despite their excellent environmental properties, haloolefins are considered a temporary solution, since these substances may react in the atmosphere and one of the decomposition products may be trifluoroacetic acid (TFA), a substance that is harmful to aquatic life [6]. Therefore, natural refrigerants are considered the only long-term solution for VCC technology. Many studies concern the performance analysis of refrigeration systems adopting natural refrigerants as working fluid [7, 8]. The main obstacle to their adoption is their high flammability [9] and the associated safety risks, which can be mitigated by *ad hoc* technological solutions, i.e., limited refrigerant charge, leak detection sensors, alarms, and forced ventilation [7].

The choice of the optimal working fluid for systems implementing a closed thermodynamic cycle is a non-trivial task that has a crucial influence on both the system performance and the design of its components. Typically, fluid selection relies either on consolidated industrial practice, common knowledge, or the iterative assessment by means of system simulations of multiple fluid candidates for which thermo-physical properties are available. However, this approach is arguably time-consuming and may lead to suboptimal solutions. To address the limitations of the current fluid selection practice, Computer Aided Molecular Design (CAMD) methods have been developed. According to this approach, different molecular groups are combined to identify the optimal fluid molecule or the molecule of novel working fluids that are optimal for a given application. This method is based on fluid property models based on the so-called group-contribution equation of states [10, 11]. CAMD methods are commonly used in research for the chemical industry for the optimal synthesis of unconventional solvents, polymers, refrigerants and mixtures to reduce process costs and environmental impact [11]. Lately, CAMD techniques have been employed to develop integrated energy systems design frameworks where the working fluid is optimized along with the system thermodynamic processes. This approach is known as CAMPD (Computer-Aided Molecular and Process Design) and the concept was first successfully tested with a preliminary design exercise of an Organic Rankine Cycle (ORC) system by Papadopoulos *et al.* [12], albeit the modelling of the system and its component was rather simplistic. The authors solved a multi-objective optimization (MOO) problem to identify unconventional working fluids, by optimizing desirable macroscopic thermo-physical properties. Then, the use of the set of optimal fluids was assessed by means of ORC system simulations to evaluate their economic, thermodynamic, safety and environmental performance. Papadopoulos *et al.* [13] extended the CAMD method to identify optimal binary mixtures as working fluids for ORC systems.

The development of CAMD methods has benefited from the development of sophisticated physically-based models for the estimation of fluid thermodynamic properties, such as the Statistical Associating Fluid Theory (SAFT) equation of state [14], which have allowed the calculation of properties starting from a limited amount of information related to its molecule. Among the CAMD methods based on the SAFT equation of state, Bardow *et al.* [15] proposed the Continuous-Molecular Targeting to Computer-Aided Molecular Design (CoMT-CAMD) method: the PC-SAFT [16] equation of state model allows to define any fluid molecule by means of molecular describers associated with the physical structure of the molecule. Following this approach, it is possible to optimize the performance of a system by treating the working fluid as a hypothetical substance whose molecular describers are included among the other variables of the optimal design problem. The optimization provides therefore an optimal but hypothetical working fluid as a result. The fluid parameters associated with the PC-SAFT model are then used to identify a set of real substances whose properties are similar to those of the optimal hypothetical fluid. Lampe *et al.* [17] further tested the CoMT-CAMD approach for the maximization of the net power output of a geothermal ORC plant. The authors were able to identify 10 promising working fluids from a database of 200 substances. Lampe *et al.* [18] adopted the CoMT-CAMD method for the identification of the optimal working fluid of an ORC power plant. The authors assessed a single framework for the optimization of both the thermodynamic process of the system and the preliminary design of the radial turbine.

The research documented in this chapter is about applying the CoMT-CAMD approach to the case of the optimal design of an electrically-driven VCC-based ECS for the aircraft. To this end, an exemplary test case was selected, namely that of the optimization of the preliminary design of a system for short-haul single-aisle airliners, such as the Airbus A320. The implementation of the method consists of a numerical procedure that can be subdivided into two main steps. First, a single-objective optimization problem is solved, whereby the Coefficient of Performance (COP) of the VCC system is maximized by optimizing simultaneously the parameters representing the working fluid molecular structure, the design of the centrifugal compressor, and the thermodynamic process. The optimal molecular parameters are, then, used to identify the substances which better approximate the ideal working fluid. A database of a few halogenated refrigerants[1] and non-polar hydrocarbons has been considered for this purpose. Successively, the assessment of the optimal organic compounds is carried out by solving the multi-point and multi-objective optimization of the preliminary design of the ECS. Three system operating conditions are considered: hot ground, cruise operation, and the case of a faulty ECS pack during cruise. Furthermore, the results of the multi-point and multi-objective optimization associated with each refrigerant have been compared to those obtained in a previous study in which R-134a was the working fluid [2].

The chapter is structured as follows. First, the VCC system layout suitable for a single-aisle, short-haul passenger aircraft is described. Then, the methodology is introduced and the implementation of the CoMT-CAMD method for working fluid optimization and the associated results are discussed. Next, the multi-point and multi-objective optimization of the ECS system for the assessment of the optimal refrigerants identified through the CoMT-CAMD method is described, by specifying the design space, objective functions, and constraints.

---

[1] Halogenated organic compounds feature halogen substituent (F, Cl, Br, or I), which are not present in non-halogenated substances.

Thereafter, the results of the optimization are presented together with the analysis of the impact of the working fluid on the VCC system performance and the design of the main system components. The optimal system designs are finally compared with the optimal design of a system employing R-134a as the working fluid. The main outcomes of the study are then summarised and recommendations are stated.

5.2. TEST CASE

The selected test case concerns the optimal design of the VCC system for the ECS of a short-haul single-aisle passenger airliner, such as the A320. Typically, this type of aircraft features two twin ECS packs to ensure redundancy in the event of pack failure during flight. Each pack nominally supplies 50% of the required airflow, but it can operate at 180% of the nominal flow rate in case one pack fails [19]. Three operating conditions of the aircraft are considered to optimize the design, e.g., ground, cruise, and faulty-pack. In particular, the so-called faulty-pack operating condition, i.e., the condition due to the failure of one ECS pack, is critical. Figure 5.1 shows a simplified process flow diagram of the aircraft ECS for the selected operating conditions.

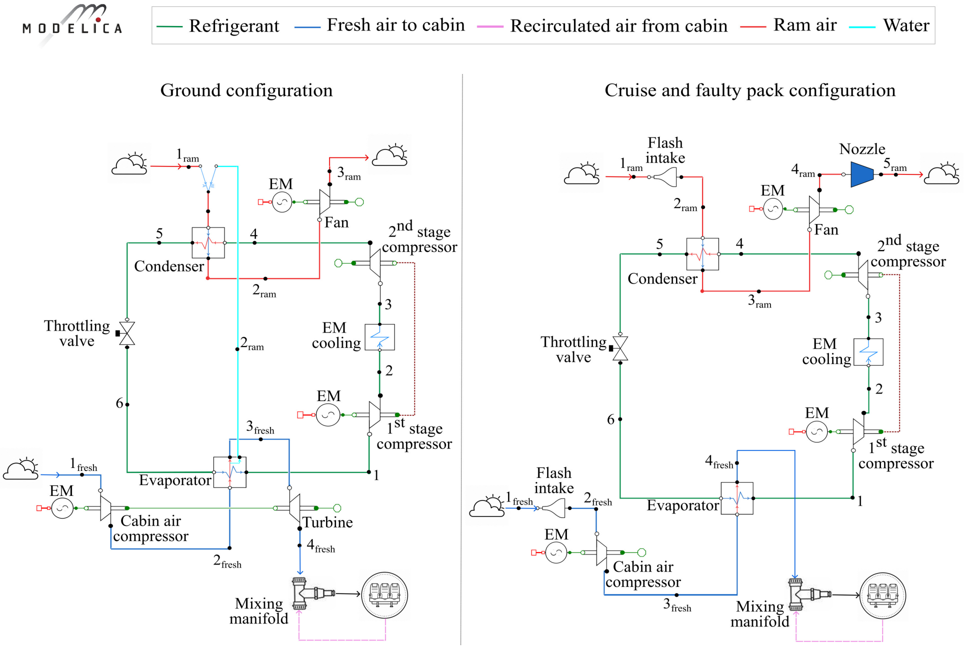

Figure 5.1.: Graphical interface of the Modelica system models representing the simplified process flow diagram of the ECS selected as a test case. Left: System model for the simulation of ground operating conditions. Right: System model for the simulation of the cruise conditions in both the case of normal operation and of a faulty ECS pack.

The key feature of the VCC system analyzed in this work is that the prime mover of the system is a high-speed miniature centrifugal compressor. The compressor, referred to as refrigerant compressor (RC), is electrically driven. To comply with the high temperature lift between the evaporator and the condenser, the compressor is designed with two stages, which are mounted in a back-to-back configuration to balance their axial thrust and to allow for the use of gas bearings.

Ram air is directly drawn from the surrounding environment through a dedicated intake and duct, and it is used as a heat sink for the condenser, before being exhausted again in the environment. At cruise operating conditions, passenger airliners can reach an altitude of up to 12 km. Therefore, the cabin needs pressurization to preserve a safe and comfortable environment for the passengers and the aircraft crew. This is achieved using two independent cabin air compressors (CACs) which are regulated to maintain the pressure in the cabin always higher than 75 kPa [20], as well as to supply sufficient fresh air to the aircraft occupants.

According to the AC 25-20 advisory circular of the Federal Aviation Administration [20], every passenger in the cabin should be provided with at least 6 $\text{g}\cdot\text{s}^{-1}$ of fresh air. During standard operation, 50% of the cabin air is recirculated by dedicated fans. This air stream is purified through filters before being combined in the mixing manifold with fresh air from the ECS pack. In the case of the A320 aircraft, this means that each ECS pack operates with almost 0.5 $\text{kg}\cdot\text{s}^{-1}$ of fresh air if at cruise. The fraction of recirculated air in the flight deck compartment is often lower to provide a greater margin in terms of airflow for avionics cooling [19].

In normal operating conditions, the fresh air supplied by the ECS packs needs to be cooled before being mixed with the recirculated air to achieve the targeted air temperature in the cockpit and passenger cabin. This cooling process is performed in the evaporator of the VCC system. Moreover, in the case of ground operation, the cabin also requires air dehumidification. As the recirculated air is indirectly cooled and dehumidified via the fresh air stream, the temperature required at the outlet of the ECS pack can be relatively low. To limit the temperature drop that the VCC system must provide, the cold air from the evaporator is further expanded in a turbine to achieve the targeted temperature level before entering the mixing manifold. The condensed water recuperated downstream of the evaporator is then injected into the ram air stream to increase its cooling capacity. In the case of cruise operating conditions, being the fresh air already dry and the cooling capacity requested to ECS pack lower, the dehumidification system and the turbine are bypassed. Thus, the air cooling is due only to the evaporator.

5.3. METHODOLOGY

The design methodology used for this case study is explained in detail in Sec. 3.3 and it is briefly summarized here for clarity. The devised optimal design procedure integrates the CoMT-CAMD method for working fluid selection and consists of the following main steps:

1. *Identification of the optimal ideal fluid for the given application.*
   The thermodynamic processes and the preliminary design of the centrifugal compressor are optimized together with the parameters representing the working fluid molecular structure to maximize the COP of the VCC system. This single-objective optimization problem is solved for a simplified system model where the heat exchangers (HEXs) preliminary design is neglected. This model has been implemented using the Python programming language since it is currently not possible to programmatically modify the parameters of the PC-SAFT equation of state using the compiled Modelica model. The resulting optimization and simulation framework is called *OptiFluidECS*, as mentioned in Sec. 3.3. To obtain bounds for the molecular parameters that ensure that the ideal fluid is made of realistic molecules, the optimization is repeated for each class of fluids and the result is the validity range for each of the molecular parameters. This procedure and the results obtained from this analysis are discussed in detail in Sec. 5.4.

2. *Search for molecules similar to the ideal working fluid.*
   The molecular parameters representing the optimal fluid, which is an ideal fluid or *pseudo-fluid* whose molecule is defined by the optimal value of the molecular describers, are used to identify a comprehensive list of substances for each fluid class. This is the last procedure of the CoMT-CAMD method implemented into *OptiFluidECS*. Subsequently, the resulting optimal fluids are tested as working fluids using the same optimization framework allowing for the selection of the *pseudo-fluid*, in order to rank them and verify the feasibility of the compressor design. The only difference with respect to the optimization problem solved in the initial step of the design procedure is that the molecular parameters are not included among the optimization variables and their values are specific for each substance being evaluated. The outcome of this design step is presented in Sec. 5.4.3.

3. *Assessment of the fluid candidates selected through the CoMT-CAMD method.*
   Once the optimal working fluids are identified, they are assessed as refrigerants for the VCC system by solving a multi-point and multi-objective optimization problem in which both the thermodynamic cycle and the design of the components are optimized. The *in-house* design framework *DesOptECS MultiPoint*, described in Sec 3.3, has been used for this purpose. Detailed information about the system model and the definition of the optimization problem are provided in Sec. 5.5. The results are discussed in Sec. 5.6.

5.4. PSEUDO-FLUID MODELLING AND OPTIMIZATION

As treated in Ch. 4, the working fluid has a crucial influence on VCC system performance, on component design and on many other operational and safety aspects. Therefore, the inclusion of the working fluid molecule among the variables of the automated design optimization problem is relevant. To this end, Bardow *et al.* [15] proposed the CoMT-CAMD method for the selection of the optimal solvent in industrial chemical processes. The method relies on the predictive capabilities of the PC-SAFT equation of state model, whereby the parameters of the fluid model are related to the molecular structure and intermolecular forces [16]: molecules are modelled as chains of spheres, interacting through van der Waals forces, hydrogen, and polar bonds. Every molecule is described by a limited set of parameters. If self-associating molecules are neglected, these are the number of segments per chain molecule (m) and the segment diameter (σ), which provide information about the molecular geometry; the dispersion energy (ϵ_k) and the dipole moment (μ), which defines the attractive forces. These molecular parameters are included among the system optimization design variables to identify the most suitable hypothetical molecule, named *pseudo-fluid*, for the considered application. A *pseudo-fluid* is, therefore, a fluid that does not necessarily exist, but whose molecular parameters are within the bounds of realistic values. Subsequently, the optimal set of molecular parameters is used to select a list of real fluids whose molecular characteristics and thus properties are close to those of the *pseudo-fluid*. The advantage of this method is twofold: i) the optimal molecule is identified through a systematic approach, avoiding the computationally expensive and possibly non-robust procedure of computing the solution of a complex optimization problem associated with each possible working fluid; ii) the possibility of identifying unconventional working fluids, which may be overlooked if a conventional empirical approach is adopted.

5.4.1. MODEL

For the process calculations, the PC-SAFT equation of state is complemented with a correlation for the *pseudo-fluid* specific isobaric heat capacity in the ideal gas state (c_p^{ig}), and for the molar mass (M) in order to obtain a complete fluid thermodynamic model. In the case of real substances, the value of M is known from its molecular formula, while the dependency of c_p^{ig} on the temperature is provided by fluid property databases, or obtained with group contribution methods. In the case of a pseudo-fluid, c_p^{ig} and M need to be estimated starting from molecular describers. The method proposed by Stavrou *et al.* [21] and based on quantitative structure property relationships (QSPR) has been used for this purpose, which provides

$$M = \beta_1 \cdot (m \cdot \epsilon_k) + \beta_2 \cdot (m\sigma^3) + \beta_3 \cdot (m\sigma^3 \cdot \epsilon_k) + \beta_4 \cdot (m\sigma^3 \mu); \tag{5.1}$$

$$c_p^{\mathrm{ig}} = \gamma_0 + \gamma_1 \cdot (m \cdot \epsilon_k) + \gamma_2 \cdot (m\sigma^3) + \gamma_3 \cdot (m\sigma^3 \cdot \epsilon_k). \tag{5.2}$$

where β and γ are coefficients, and μ is the dipole moment of the molecule.

To ensure the reliability of the adopted QSPR relationships, specific sets of β and γ coefficients are defined for each of the two categories of working fluids considered in this study, namely halogenated substances and non-polar ($\mu = 0$) hydrocarbons. The complete list of the fluids considered for the fitting of the coefficients, with their molecular parameters, is reported in Tab. A.1 and A.2 of the Appendix A. The dataset defined for halogenated substances includes the data of 26 fluids, while that for hydrocarbons encompasses the properties of 56 fluids. Further details about the fitting of the coefficients and the accuracy of the QSPR relationships in Eqs. 5.1 and 5.2 are provided in Sec. A.2 and A.3.

In addition to thermodynamic properties, also the transport properties of the *pseudo-fluid* must be determined to perform the sizing of the system components. Thus, the molecular describers are also used to estimate the thermal conductivity and viscosity with the method by Chung *et al.* [22]. The correlation proposed by Sastri and Rao [23] is used to predict the surface tension.

The equations forming the system model are implemented in the *OptiFluidECS* Python program and solved. This model is a simplified version of the Modelica model developed for the multi-point and multi-objective optimization procedure aimed at assessing the best working fluid, according to the method treated in Chap. 3. The Python model does not include the procedure for the preliminary design of the HEXs and does not account for the associated pressure drops. Only the preliminary design of the centrifugal compressor is performed together with the process simulations, since this component is the most critical from a design point of view, as demonstrated by Giuffré *et al.* [24]. The design of the centrifugal compressor is performed by integrating the *in-house* tool *TurboSim* within the process calculations. Conversely, the CAC, the fan and the turbine performance are simply given by an estimate of the isentropic efficiency, namely 0.75 for the CAC, 0.65 for the fan, and 0.8 for the turbine.

5.4.2. OPTIMIZATION

The preliminary design optimization is carried out for the most critical design point, i.e., the aircraft is on the ground on a hot day. The operating conditions and the system parameters chosen for this case study are listed in Tab. 5.1.

The solution of the optimization problem relies on the genetic algorithm (GA) implemented in the open-source Python package Pymoo [25]. The objective function is the minimization of the total electric power consumption of the ECS system, which results from the sum of the power demand of the CAC, refrigerant compressor, and ram air fan. The design problem includes 14 non-linear inequality constraints (g_j) pertaining to the centrifugal compressor design. The design variables are also 14 and they can be split into two groups: i) 11 variables associated with the design of the system and the centrifugal compressor (x_{sys}), and ii) 3 molecular parameters defining the molecule of the *pseudo-fluid* (x_{fluid}). Table 5.2 lists the

Table 5.1.: Parameters defining the operating specifications of the aircraft ECS and corresponding the operating parameters of the VCC system adopted for the design optimization problem which is solved to determine the optimal *pseudo-fluid*.

Operating conditions		
Fresh air mass flow rate (one ECS pack)	$\dot{m}_{\text{fresh}}$ / kg·s^{-1}	0.5
Environmental air temperature	T_{env} / K	311.15
Environmental air pressure	p_{env} / kPa	101.325
Temperature air delivered by the ECS pack	T_{ECS} / K	256.95
Pressure air delivered by the ECS pack	p_{ECS} / kPa	102.40
VCC operating parameters		
Evaporation temperature	T_{eva} / K	268.15 and 273.15
Temperature lift	ΔT_{lift} / K	50 to 80
Pinch point temperature difference evaporator	$\Delta T_{\text{pp,eva}}$ / K	13
Superheating degree evaporator	$\Delta T_{\text{sh,eva}}$ / K	9
Subcooling degree condenser	$\Delta T_{\text{sc,cond}}$ / K	9

ranges of values chosen for the design variables and the constraints of the problem. Following the guidelines by Stavrou *et al.* [21], the identification of a real fluid starting from the results of the optimization problem resulting in the definition of the optimal *pseudo-fluid* is possible only if the search space for the 3 design variables associated with the *pseudo-fluid* molecular structure is limited by the fronts of the convex hull formed by the molecular parameters of the k real substances among which the molecules resembling the most the *pseudo-fluid* are searched. The convex hull fronts are defined by a set of m linear inequality constraints to restrict the search space as shown in Fig. 5.2. Then, the optimization problem can be mathematically expressed as

$$\begin{aligned} \min \quad & \dot{W}_{\text{el,sys}} = f(x_{\text{sys}}, x_{\text{fluid}}) \\ \text{s.t.} \quad & \begin{cases} g_j(x_{\text{sys}}, x_{\text{fluid}}) \le 0, & j = 1, \dots, J \\ x^{(\text{L})}_{\text{sys}_n} \le x_{\text{sys}_n} \le x^{(\text{U})}_{\text{sys}_n}, & n = 1, \dots, N \\ A \cdot x_{\text{fluid}_m} \le b, & m = 1, \dots, 3 \end{cases} \end{aligned} \tag{5.3}$$

where the matrix A and the vector b of the last inequality constraint depend on the considered category of working fluids.

As reported in Tab. 5.1, the system optimization has been carried out for two different levels of evaporation temperature (268.15 K and 273.15 K). Additionally, four values of temperature lift have been considered, ranging from 50 K to 80 K. It follows that, in total, eight optimization problems have been solved for each category of fluid.

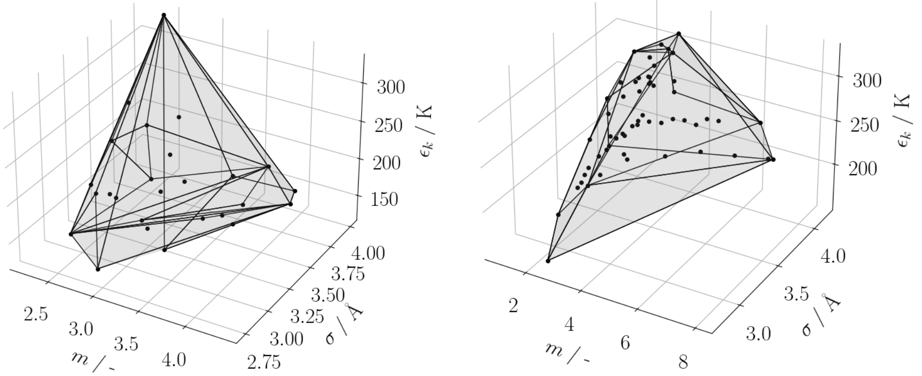

Figure 5.2.: Convex hull limiting the search space for the *pseudo-fluid* molecular parameters m, σ and ϵ_k in the case of halogenated fluids (left) and non-halogenated fluids (right).

5.4.3. PSEUDO-FLUID MAPPING AND OPTIMAL WORKING FLUID SELECTION

The search space for the real molecules with characteristics similar to those of the *pseudo-fluid* must be bound with minimum and maximum values of the molecular describers, therefore eight system optimization runs for each class of fluids are performed to determine these values. Within the realm of CAMD methods, this operation was termed *mapping of the pseudo-fluid onto real substances*. The results of this procedure are reported in Tab. 5.3, where the range of the optimal PC-SAFT molecular parameters for both halogenated and non-halogenated working fluids is highlighted in bold. These ranges have been extended by ±10% to enable the identification of a comprehensive list of fluids for each class. The refrigerants resulting from the mapping procedure are listed in Tab. 5.4.

To minimize the environmental impact of the proposed design solutions, only mediums with a GWP closer or lower than that of CO_2 ($GWP = 1$) have been selected. Therefore, the refrigerants R-22, R-124, and R-152a have been excluded from the analysis. Among the non-halogenated fluids, 1,3-butadiene and diethyl ether have been discarded due to their high toxicity [26, 27]. In particular, 1,3-butadiene is also included among the cancerous substances [26].

The remaining nine optimal real fluids have been assessed with the *OptiFluidECS* framework previously used for the *pseudo-fluid* optimization. The difference with the prior analysis is that, in this case, the molecular parameters are not included anymore among the design variables of the problem. Moreover, the thermo-physical properties have been estimated using the reference equations of state for the selected fluids implemented in a well-known computer program [28]. However, this commercial database does not include cyclobutane, for which the PC-SAFT equation of state has been used as an alternative. The operating conditions of the system are analogous to those listed in Tab. 5.1. However, the evaporation temperature and the VCC system temperature lift are set constant at 273.15 K and 70 K, respectively. The objective of this additional optimization study, whose main results are reported in Tab. 5.5, is to rank the identified refrigerants in terms of expected system COP and verify the feasibility of the compressor design, to eventually narrow down the potential fluid candidates for the final multi-point multi-objective optimization.

Table 5.2.: Values of the design variables and constraints selected for the ECS design optimization problem resulting in the identification of the optimal *pseudo-fluid.*

Design variables (x_{sys})			
Variable	Symbol	Min. value	Max. value
Ram air mass flow rate	$\dot{m}_{ram}$ / kg·s^{-1}	2.2	3
Compression ratio (1st stage)	β_{tt} / -	2	4
Swallowing capacity (1st, 2nd stage)	Φ_{t1} / -	0.02	0.20
Shape factor (1st, 2nd stage)	k / -	0.65	0.95
Absolute outlet angle (1st, 2nd stage)	α_2 / deg	60	75
Diffuser to outlet impeller radius ratio (1st, 2nd stage)	R_3/R_2 / -	1.2	2
Loading coefficient (1st stage)	ψ / -	0.65	1

Constraints			
Variable	Symbol	Min. value	Max. value
Inlet hub radius (1st, 2nd stage)	$R_{1,hub}$ / mm	2.35	-
Outlet blade height (1st, 2nd stage)	$H_{2,blade}$ / mm	0.8	-
Volute radius (1st, 2nd stage)	R_{volute} / mm	-	50
Outlet relative blade angle (1st, 2nd stage)	$\beta_{2,blade}$ / deg	-45	-10
Inlet relative Mach at shroud (1st, 2nd stage)	$M_{w_{1,s}}$ / -	-	1.4
Absolute Mach at diffuser outlet (1st, 2nd stage)	M_3 / -	-	0.70
Rotational speed (1st, 2nd stage)	Ω / krpm	30	150
Net axial thrust twin-stage compr.	F_{axial} / N	0	400

Design variables (x_{fluid}): halogenated fluids			
Variable	Symbol	Min. value	Max. value
Segment number	m / -	2	4.5
Segment diameter	σ / Å	2.7	4
Dispersion energy	ϵ_k / K	120	335

Design variables (x_{fluid}): non-halogenated fluids			
Variable	Symbol	Min. value	Max. value
Segment number	m / -	1.0	8.0
Segment diameter	σ / Å	2.7	4.2
Dispersion energy	ϵ_k / K	150	333

The results disclose that, in the case of R-1224yd(Z), it is not possible to design a centrifugal compressor compliant with the constraints listed in Tab. 5.2. This is due to the high molecular complexity of this refrigerant that results in a low speed of sound, thus a Mach number at the diffuser inlet (M_3) for the first stage of the compressor above the maximum allowable value. The compressor design is also unfeasible when cyclopentane and cyclobutane are adopted as working fluids. Specifically, in the case of cyclopentane, the values of Mach number at the diffuser inlet (M_3) and volute radius (R_{volute}) exceed the maximum limits chosen as constraints. Similarly to R-1224yd(Z), the large value of M_3 is associated with the high

Table 5.3.: Optimal sets of the *pseudo-fluid* molecular parameters obtained by means of system optimization calculations associated with working fluids which are either halogenated or non-halogenated compounds. The numbers in bold indicate the minimum and maximum values for each optimal molecular descriptor.

Halogenated fluids				**Non-halogenated fluids**			
Test case	**Segment number m / -**	**Segment diameter σ / Å**	**Dispersion energy ϵ_k / K**	**Test case**	**Segment number m / -**	**Segment diameter σ / Å**	**Dispersion energy ϵ_k / K**
$T_{\text{eva}} = 268.15$ K $\Delta T_{\text{lift}} = 50$ K	**3.07**	3.12	**196.84**	$T_{\text{eva}} = 268.15$ K $\Delta T_{\text{lift}} = 50$ K	2.41	3.32	237.24
$T_{\text{eva}} = 268.15$ K $\Delta T_{\text{lift}} = 60$ K	3.05	3.12	196.76	$T_{\text{eva}} = 268.15$ K $\Delta T_{\text{lift}} = 60$ K	2.52	3.17	225.99
$T_{\text{eva}} = 268.15$ K $\Delta T_{\text{lift}} = 70$ K	2.81	3.15	203.66	$T_{\text{eva}} = 268.15$ K $\Delta T_{\text{lift}} = 70$ K	**2.20**	3.33	235.16
$T_{\text{eva}} = 268.15$ K $\Delta T_{\text{lift}} = 75$ K	2.91	**3.11**	196.09	$T_{\text{eva}} = 268.15$ K $\Delta T_{\text{lift}} = 80$ K	2.37	3.24	231.56
$T_{\text{eva}} = 273.15$ K $\Delta T_{\text{lift}} = 50$ K	3.05	**3.15**	200.36	$T_{\text{eva}} = 273.15$ K $\Delta T_{\text{lift}} = 50$ K	2.37	3.31	240.50
$T_{\text{eva}} = 273.15$ K $\Delta T_{\text{lift}} = 60$ K	2.83	3.15	203.34	$T_{\text{eva}} = 273.15$ K $\Delta T_{\text{lift}} = 60$ K	2.33	3.31	241.70
$T_{\text{eva}} = 273.15$K $\Delta T_{\text{lift}} = 70$ K	**2.78**	3.19	**210.10**	$T_{\text{eva}} = 273.15$ K $\Delta T_{\text{lift}} = 70$ K	**2.79**	**3.08**	**218.43**
$T_{\text{eva}} = 273.15$ K $\Delta T_{\text{lift}} = 80$ K	2.95	3.11	196.49	$T_{\text{eva}} = 273.15$ K $\Delta T_{\text{lift}} = 80$ K	2.22	**3.38**	**245.96**

molecular complexity, thus the relatively low speed of sound of cyclopentane. Additionally, cyclopentane is characterized by a low saturated vapour density at the prescribed evaporation pressure. This characteristic leads to an increase in volumetric flow rate and compressor size. The same considerations apply to the case of cyclobutane. Such working fluid has properties similar to those of 1-butyne, for instance, the saturation pressure levels and vapour density, but it has a molecular complexity even higher than that of cyclopentane. It results that the design of the first stage is unfeasible due to the violation of the constraints on the maximum inlet Mach number and volute radius. For the selected inlet thermodynamic conditions, the design space boundaries do not allow for any feasible compressor design.

Regarding the other molecules for which the compressor design is feasible (see Tab. 5.5), the highest value of COP is obtained for the case of 1-butyne (COP = 2.2), followed by propyne, 1-butene, and dimethyl ether, which exhibit essentially the same performance (COP = 2.1) being the difference in the estimated COP lower than the uncertainty of the numerical calculations. The fluid with the lowest COP is propane (COP = 1.85), a medium largely used in the refrigeration industry for small cooling capacity applications. The choice of the best refrigerant is also driven by other technological and safety-related considerations. 1-butene has the advantage over the other fluids of featuring an evaporation pressure above the atmospheric pressure. This aspect is crucial in the case of flammable fluids, as the risks of inward air leakage which could prompt fluid autoignition is minimized if the evaporator operates at super-atmospheric conditions. In conclusion, among the fluids identified through the *pseudo-fluid* property mapping, two optimal refrigerants have been selected for the multi-point and multi-objective optimization of VCC system of the aircraft ECS: 1-butyne and 1-butene. The former has been chosen because it enables maximum system efficiency, a key aspect for the application at hand given that the ECS is the non-propulsive system

Table 5.4.: Fluids selected from the database of halogenated and non-halogenated fluids using the results of the mapping of the *pseudo-fluid* optimal parameters so that their molecular parameters are as close as possible to the optimal *pseudo-fluid*.

Halogenated fluids

Fluid name	**Segment number m / -**	**Segment diameter σ / Å**	**Dispersion energy ϵ_k / K**	**GWP / -**	**ODP / -**	**Safety class**	**Molecular complexity N / -**
R-1224yd(Z)	3.23	3.40	194.93	<1	0	A1	4.91
R-124	3.05	3.32	183.5	609	0.02	A1	2.18
R-152a	2.72	3.10	192.12	124	0	A2	-3.12
R-22	2.55	3.10	185.47	1810	0.04	A1	-4.44

Non-halogenated fluids

Fluid name	**Segment number m / -**	**Segment diameter σ / Å**	**Dispersion energy ϵ_k / K**	**GWP / -**	**ODP / -**	**Safety class**	**Molecular complexity N / -**
1-butene	2.29	3.64	222.00	1	0	A3	1.37
1-butyne	2.77	3.29	212.72	<1	0	A3	1.02
1,3-butadiene	2.23	3.59	228.60	1	0	B3	0.59
Cyclobutane	2.13	3.60	251.9	<1	0	A3	7.64
Cyclopentane	2.36	3.71	265.83	11	0	A3	4.72
Diethyl ether	2.97	3.51	220.09	<1	0	B3	7.79
Dimethyl ether	2.31	3.25	211.06	1	0	A3	-2.20
Propane	2.00	3.62	208.11	3.30	0	A3	-1.31
Propyne	2.43	3.13	207.63	<1	0	A3	-3.14

5

aboard the aircraft responsible for the highest energy consumption, while the latter has been preferred as its adoption may entail operational and safety-related advantages thanks to the super-atmospheric evaporating pressure, at the expense of a limited COP reduction.

Figure 5.3 shows the comparison of the VCC system thermodynamic cycle for the two optimal refrigerants and for the reference fluid R-134a in the $T-s$ diagram. For a prescribed cooling capacity, both natural refrigerants are characterized by a larger latent heat of evaporation compared to R-134a, resulting in a lower refrigerant mass flow rate in the refrigeration loop. This difference is more significant in the case of 1-butyne.

5.5. MULTI-POINT MULTI-OBJECTIVE OPTIMIZATION

The system models used for the exemplary multi-point, multi-objective optimization of the VCC system of the ECS of an airliner (the Airbus A320) have been coded in the acausal modelling language Modelica [29]. The component models are steady-state and zero-dimensional, and are part of the *DeSimECS* (Design and Simulation of Energy Conversion Systems) library described in Sec. 3.2. The compressor preliminary design relies on the *in-house* computer programme *TurboSim* [30], while the system models include a simplified model of the compressor whose parameters are tuned on the results of the design performed with *TurboSim*. For more details about the integration of the centrifugal compressor preliminary design procedure into the thermodynamic cycle calculations, the reader is referred to Sec. 3.3. Conversely, the HEXs preliminary design (or rating) is performed via the component models of the Modelica code. Finally, the thermodynamic and transport properties

Table 5.5.: Results of the system optimization for the real working fluids selected through the mapping procedure.

Variable	**Symbol**	**1-butene**		**1-butyne**		**Dimethyl ether**		**Propane**		**Propyne**	
VCC system efficiency	COP / -	2.1		2.2		2.1		1.85		2.1	
System electric power demand	$\dot{W}_{\mathrm{el}}$ / kW	21.9		21.1		22.03		24.9		21.6	
Refrigerant mass flow rate	$\dot{m}_{\mathrm{refr}}$ / kg·s^{-1}	0.18		0.14		0.16		0.21		0.13	
Evaporation pressure	p_{eva} / bar	1.3		0.7		0.3		0.5		0.3	
Condensation pressure	p_{cond} / bar	9.6		7.0		1.8		2.6		1.6	
Saturated vapour density at evaporation temperature	$\rho_{\mathrm{v}}(T_{\mathrm{eva}})$ / kg·m^{-3}	3.35		1.80		5.82		10.35		2.65	
		S1	S2	S1	S2	S1	S2	S1	S2	S1	S2
Total-to-total compression ratio	β_{tt} / -	4	1.87	2.66	3.62	4	1.7	3.59	1.52	4	1.77
Total-to-total efficiency	η_{tt} / -	0.79	0.76	0.81	0.77	0.72	0.75	0.73	0.79	0.71	0.76
Flow coefficient	Φ_{t1} / -	0.08	0.08	0.17	0.04	0.03	0.04	0.03	0.04	0.03	0.03
Isentropic loading coefficient	Ψ_{is} / -	0.79	0.93	0.87	0.82	0.83	0.65	0.85	0.94	0.95	0.89
Outlet absolute flow angle	α_2 / deg	73.2	64.5	74.9	73.7	71.4	72.2	69.7	73.1	74.9	74.9
Shape factor	k / -	0.94	0.89	0.90	0.88	0.80	0.86	0.81	0.73	0.91	0.86
Diffuser to impeller outlet radii ratio	R_3/R_2 / -	1.45	1.60	1.26	143	1.55	1.85	1.54	1.36	1.40	1.22
Impeller inlet hub radius	$R_{1,\mathrm{hub}}$ / mm	3.0	2.7	4.6	3.9	4.7	2.6	4.4	3.5	3.0	2.6
Impeller outlet blade height	$H_{2,\mathrm{blade}}$ / mm	1.72	1.25	4.11	1.12	0.81	0.97	0.80	1.20	0.83	0.86
Volute radius	R_{volute} / mm	48.4	37.5	50.0	49.8	49.1	39.2	44.5	27.8	46.0	29.6
Rotational speed	Ω / krpm	143.6		126.9		146.8		147.2		141.5	
Net axial thrust	F_{axial} / N	14.1		10.8		26.8		40.0		24.3	

of the working fluids are computed using a reference computer program [28].

The Python optimization framework, named *DesOptECS MultiPoint* [2] (Sec. 3.3), integrates *TurboSim* and a Modelica modelling and simulation environment [31] and it is used to obtain the optimal ECS design for each of the specific points of the operating envelope considered in the design problem, i.e., ground condition, standard flying at cruise, and faulty-pack condition at cruise (see Fig. 5.1 for the simplified process flow diagrams of the corresponding system models). The design point used for the sizing of the main system components is that of aircraft operation on the ground and on a hot and humid day, as this is the most demanding condition in terms of cooling duty of the ECS pack. The system off-design performance is, then, evaluated for the other two operating points. More specifically, the HEXs are sized at ground operating conditions, which correspond to the design point. Then, the resulting geometry is used as input for the off-design models of the system in the case of cruise and faulty-pack operating conditions. In the case of the centrifugal compressor, at the design point, the optimizer provides a vector of inputs to *TurboSim* including the compression ratio, the refrigerant mass flow rate, the flow inlet conditions and the required set of non-dimensional

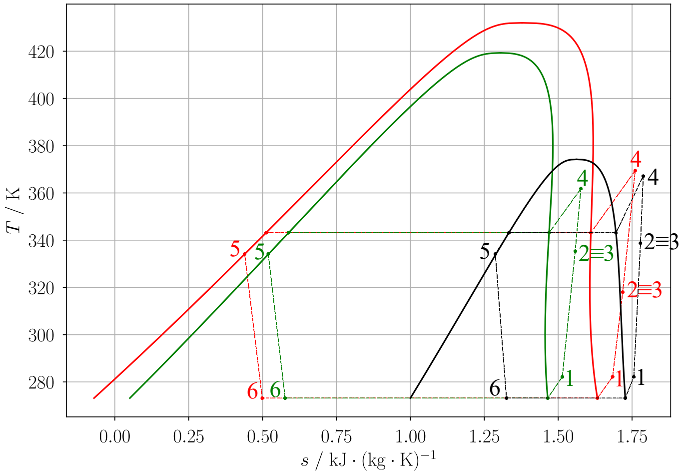

Figure 5.3.: $T-s$ chart of the selected working fluids (—) 1-butyne, (—) 1-butene, compared to (—) R-134a. The numbering refers to the state points in Fig. 5.1

.

parameters (see Ch. 3). If the compressor design is feasible, the selected design parameters and the geometry resulting from the design are stored as inputs for the off-design analysis. During the off-design analysis, the optimizer selects new values of compression ratio, mass flow rate and inlet conditions. The compressor feasibility in these operating conditions is verified if i) the compressor operating condition corresponds to a stable operating point of the compressor map, and ii) the actual compression ratio resulting from the off-design analysis stands within a 5% deviation from the value prescribed by the optimizer. The resulting values of efficiency and compression ratio for the compressor in each operating condition are used as input for the simplified compressor model used in the Modelica model of the system, and the simulation is then executed. If the conditions are not met, the simulation is discarded. The thermal loads of each aircraft mission phase have been determined using a cabin thermal model obtained with components of the *in-house* Modelica library *DynTherM* (Dynamic modelling and simulation of Thermal Management systems) [32] and are reported in Tab. 5.6.

Table 5.6.: Specifications of the operating conditions used for the multi-point multi-objective optimization of the exemplary aircraft ECS.

Variable	**Symbol**	**Ground**	**Cruise**	**Faulty-pack**
Fresh air mass flow rate	$\dot{m}_{\mathrm{fresh}}$ / kg·s^{-1}	0.5	0.5	0.88
Environmental air temperature	T_{env} / K	311.15	216.65	216.65
Environmental air pressure	p_{env} / kPa	101.32	19.68	19.68
Environmental air humidity	Φ_{env} / %	22	0	0
Air temperature delivered by ECS pack	T_{ECS} / K	256.95	276.55	273.69
Air pressure delivered by ECS pack	p_{ECS} / kPa	102.4	76.27	76.25

The objective functions of the optimization problem are the net electric power consumption ($\dot{W}_{\mathrm{el}}$), the drag penalty associated with the ram airflow (D), and the total system weight. The system weight accounts for the contribution of the HEXs, the RC, the CAC, and the working fluid charge. The 3003 and 2219-T852 Aluminium alloys have been chosen as materials for the HEXs and the compressor wheels and casing, respectively. The optimization algorithm evaluates the objective functions as a weighted average of the values of the chosen figures of merit estimated for each operating point. The values of the weights have been selected considering that: i) the drag penalty is null in case of ground operating conditions; ii) the cruise phase is typically the longest over the operating envelope; iii) the case of a faulty ECS pack during flight is an emergency condition, an unusual occurrence, for which the ECS performance needs to be verified just for safety purposes. The net electric power demand is then estimated as

$$\dot{W}_{\mathrm{el}} = 0.3\dot{W}_{\mathrm{el,g}} + 0.6\dot{W}_{\mathrm{el,c}} + 0.1\dot{W}_{\mathrm{el,fp}}, \tag{5.4}$$

while the drag penalty is calculated as

$$D = 0.8D_{\mathrm{c}} + 0.2D_{\mathrm{fp}}. \tag{5.5}$$

Regarding the third figure of merit, the system weight depends on the sizing of the components; therefore, it is computed only at ground conditions.

The optimization problem has been solved with the Non-Sorted Genetic Algorithm (NSGA-II) implemented in the open-source Python package Pymoo [25]. The optimization problem consists of 27 design variables (Tab. 5.8) and 41 nonlinear inequality constraints (Tab. 5.9), whose ranges of variation are taken equal for all the selected working fluids. The geometrical parameters of evaporator and condenser that have been fixed constant for this study case are listed in Tab. 5.7. At each iteration of the algorithm, the population of candidate solutions consists of 10 individuals for each design variable. The design vector of each solution is initialized by sampling the design variables in the chosen range of variation using the Latin Hypercube approach.

Table 5.7.: Geometrical parameters of multi-louvered fins and minichannels within condenser and evaporator.

		Evaporator	**Condenser**
Tube height	T_{h} / mm	1.93	1.3
Tube wall thickness	δ_{t} / mm	0.4	0.4
Tubes pitch	T_{p} / mm	9.3	7.6
Number of minichannels	N_{mc} / -	10	16
Minichannels wall thickness	δ_{mc} / mm	0.35	0.35
Fins pitch	F_{p} / mm	1.4	1.0
Fins thickness	δ_{f} / mm	0.12	0.12
Fins height	F_{h} / mm	7.4	6.3
Louver length	L_{l} / mm	6.3	5.0
Louver pitch	L_{p} / mm	1.4	1.0
Louver angle	Θ / deg	27	37

Table 5.8.: Design variables selected for the multi-point multi-objective design optimization of the ECS of an exemplary aircraft (Airbus A320).

Design variables (x_{sys})				
Operating point	Variable	Symbol	Min. value	Max. value
G	Ram air mass flow rate	$\dot{m}_{\text{ram}}$ / kg·s^{-1}	2.5	3.5
G	Evaporation temperature	T_{eva} / K	253.15	268.15
G, C, FP	Superheating degree	ΔT_{sh} / K	3	10
G, C, FP	Subcooling degree	ΔT_{sc} / K	3	10
G	Evaporator height	H_{eva} / m	0.3	1.0
G	Evaporator depth	Z_{eva} / m	0.03	0.40
G	Condenser height	H_{cond} / m	0.5	1.2
G	Condenser depth	Z_{cond} / m	0.03	0.4
G	Compression ratio CAC	$\beta_{\text{tt,CAC}}$ / -	1.8	2.0
G	Swallowing capacity CAC	$\Phi_{\text{t1,CAC}}$ / -	0.08	0.15
G	Loading coefficient CAC	$\psi_{\text{is,CAC}}$ / -	0.75	0.90
G	Absolute outlet angle CAC	$\alpha_{\text{2,CAC}}$ / deg	60.0	70.0
G, C, FP	Compression ratio CC (1st, 2nd stage)	$\beta_{\text{tt,S1-S2}}$ / -	2.0	4.0
G	Swallowing capacity CC (1st stage)	$\Phi_{\text{t1,S1}}$ / -	0.08	0.15
G	Swallowing capacity CC (2nd stage)	$\Phi_{\text{t1,S2}}$ / -	0.04	0.10
G	Loading coefficient CC (1st stage)	$\psi_{\text{is,S1}}$ / -	0.65	0.85
G	Absolute outlet angle CC (1st, 2nd stage)	$\alpha_{\text{2,S1-S2}}$ / deg	60.0	75.0

5.6. RESULTS

The results of the optimization exercise outlined in this section serve to demonstrate the validity of the CoMT-CAMD method used for the selection of the optimal working fluids for the selected application of the aircraft ECS. However, due to the complexity of the optimization problem, the intricate dependency of the design variables and the limited database of fluids considered for the analysis, these results cannot be generalized to establish guidelines for the aircraft ECS design when resorting to hydrocarbons.

The optimization converges to a set of non-dominated solutions that define a Pareto surface for both the case of 1-butene and 1-butyne as working fluids of the VCC system (Fig. 5.4). Figure 5.5 shows the non-dominated solutions projected on each plane of the three-dimensional chart, which facilitates the analysis of the trend of each objective function

Table 5.9.: Values of the constraints of the multi-point multi-objective design optimization of the ECS of an exemplary aircraft (Airbus A320).

		Constraints values		
Working fluid	Variable	Symbol	Min. value	Max. value
1-butene, 1-butyne	Fan power	$\dot{W}_{\mathrm{el,fan}}$ / kW	-	10
1-butene, 1-butyne	Evaporator width	W_{eva} / m	0.05	2.0
1-butene, 1-butyne	Pinch-point temperature evaporator	ΔT_{eva} / K	0.5	-
1-butene	Refrigerant velocity evaporator	$v_{\mathrm{refr,eva}}$ / m·s^{-1}	-	40
1-butyne	Refrigerant velocity evaporator	$v_{\mathrm{refr,eva}}$ / m·s^{-1}	-	50
1-butene, 1-butyne	Air velocity evaporator	$v_{\mathrm{air,eva}}$ / m·s^{-1}	-	40
1-butene, 1-butyne	Refrigerant pressure drop evaporator	$\Delta p_{\mathrm{refr,eva}}$ / kPa	-	100
1-butene, 1-butyne	Air pressure drop evaporator	$\Delta p_{\mathrm{air,eva}}$ / kPa	-	10
1-butene, 1-butyne	Condenser width	W_{cond} / m	0.05	2.0
1-butene, 1-butyne	Pinch-point temperature condenser	ΔT_{cond} / K	0.5	-
1-butene, 1-butyne	Refrigerant velocity condenser	$v_{\mathrm{refr,cond}}$ / m·s^{-1}	-	40
1-butene, 1-butyne	Air velocity evaporator	$v_{\mathrm{air,cond}}$ / m·s^{-1}	-	40
1-butene, 1-butyne	Refrigerant pressure drop condenser	$\Delta p_{\mathrm{refr,cond}}$ / kPa	-	50
1-butene	Air pressure drop condenser	$\Delta p_{\mathrm{air,cond}}$ / kPa	-	2.0
1-butyne	Air pressure drop condenser	$\Delta p_{\mathrm{air,cond}}$ / kPa	-	10
1-butene, 1-butyne	Inlet hub radius CAC	$R_{\mathrm{1,hub,CAC}}$ / mm	3.25	-
1-butene, 1-butyne	Outlet blade height CAC	$H_{\mathrm{2,blade,CAC}}$ / mm	1.4	-
1-butene, 1-butyne	Volute radius CAC	R_{volute} / m	-	0.35
1-butene, 1-butyne	Outlet relative blade angle CAC	$\beta_{\mathrm{2,blade,CAC}}$ / deg	-50	-10
1-butene, 1-butyne	Absolute Mach at diffuser outlet CAC	$M_{\mathrm{3,CAC}}$ / -	-	0.70
1-butene, 1-butyne	Outlet tip blade speed CAC	$U_{\mathrm{2,CAC}}$ / m·s^{-1}	-	600
1-butene, 1-butyne	Rotational speed CAC	Ω_{CAC} / krpm	0.6	10
1-butene, 1-butyne	Inlet hub radius (1$^{\mathrm{st}}$, 2$^{\mathrm{nd}}$ stage)	$R_{\mathrm{1,hub,S1-S2}}$ / mm	3.25	-
1-butene, 1-butyne	Outlet blade height (1$^{\mathrm{st}}$ stage)	$H_{\mathrm{2,blade,S1}}$ / mm	1	-
1-butene, 1-butyne	Outlet blade height (2$^{\mathrm{nd}}$ stage)	$H_{\mathrm{2,blade,S2}}$ / mm	0.8	-
1-butene, 1-butyne	Volute radius (1$^{\mathrm{st}}$, 2$^{\mathrm{nd}}$ stage)	$R_{\mathrm{volute,S1-S2}}$ / m	-	0.35
1-butene, 1-butyne	Outlet relative blade angle (1$^{\mathrm{st}}$, 2$^{\mathrm{nd}}$ stage)	$\beta_{\mathrm{2,blade,S1-S2}}$ / deg	-45	-10
1-butene, 1-butyne	Absolute Mach at diffuser outlet (1$^{\mathrm{st}}$, 2$^{\mathrm{nd}}$ stage)	$M_{\mathrm{3,S1-S2}}$ / -	-	0.80
1-butene, 1-butyne	Outlet tip blade speed (1$^{\mathrm{st}}$, 2$^{\mathrm{nd}}$ stage)	$U_{\mathrm{2,S1-S2}}$ / m·s^{-1}	-	600
1-butene, 1-butyne	Rotational speed (1$^{\mathrm{st}}$, 2$^{\mathrm{nd}}$ stage)	$\Omega_{\mathrm{S1-S2}}$ / krpm	0.6	10
1-butene, 1-butyne	Net axial thrust twin-stage compr.	F_{axial} / N	0	400

in relation to the other two. For comparison purposes, these results are displayed together with those of the same system optimization but employing refrigerant R-134a as the working fluid, which were documented by Giuffré [2].

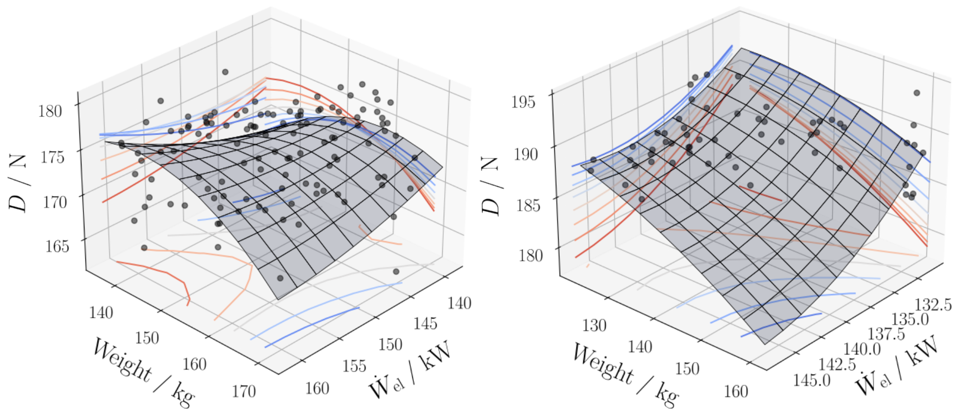

Figure 5.4.: Pareto surfaces resulting from the multi-point and multi-objective optimization of the preliminary design of an exemplary ECS in case 1-butene (left) and 1-butyne (right) are the working fluids.

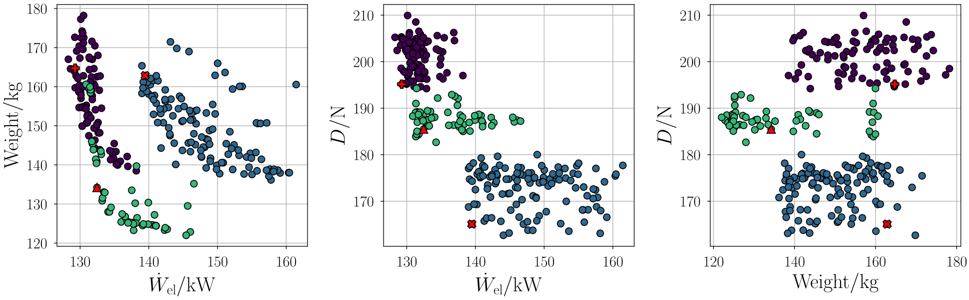

Figure 5.5.: Non-dominated solutions of the three objective functions of the multi-point optimization of the preliminary design of an exemplary ECS. Working fluids: (●) R-134a, (●) 1-butene, and (●) 1-butyne. Optimal system design solutions corresponding to the minimum system specific fuel consumption (✚, ✖, ▲). The results of benchmark case for which R-134a is the working fluid are taken from Ref. [2] and are used here for comparison purposes.

The results show that the use of the natural refrigerants 1-butene and 1-butyne as working fluids does not result in a reduction of the total electric power demand of the ECS system, if compared to R-134a. The electric power consumption of a VCC-based ECS operating with R-134a ranges between 130 kW and 140 kW. The system weight trend is characterized by an inverse proportionality with the power demand of the system and it varies from 140 kg to 180 kg, while the drag penalty is independent of the other two variables and it ranges between

195 N and 210 N. In the case of 1-butene, the electric power demand increases on average by approximately 15%, while the system weight remains within the same range of values as that of the benchmark system. 1-butene allows for the largest reduction (approximately 15%) of drag penalty if compared to the benchmark system. However, such optimal value of ram air drag penalty is still above the minimum value of 135 N obtained in the case of a bleedless ACM-based ECS [2]. In the case of 1-butyne, the system electric power consumption is comparable to or slightly larger than that of the benchmark system. Furthermore, the use of this working fluid implies the design of ECS characterized by a reduction of 15% in weight and 7% in ram air drag penalty. Based on the selected criteria, and for this exemplary system design optimization problem, 1-butyne is the working fluid allowing to achieve the best system performance if compared to that achievable if 1-butene and R-134a are the working fluids.

The cooling duty required by the ECS in the three selected operating points varies in a similar range of values independently from the working fluid. It is the lowest in the case of the aircraft flying at cruise, and the highest for the critical case of failure of one ECS pack. Note that for this operating condition, the evaporator cooling duty, in the case of the two natural refrigerants, varies in an appreciable range, of approximately 10 kW, while for cruise and on-ground operation this quantity is almost constant. The reason is the large variation in CAC efficiency observed for each solution of the Pareto front when the CAC has to supply the cabin with an air mass flow rate double that of cruise conditions. In general, since 1-butene and 1-butyne are characterized by large latent heat of evaporation, the refrigerant mass flow rate within the VCC loop is 1.8 to 2.7 times lower when compared to R-134a (Fig. 5.6).

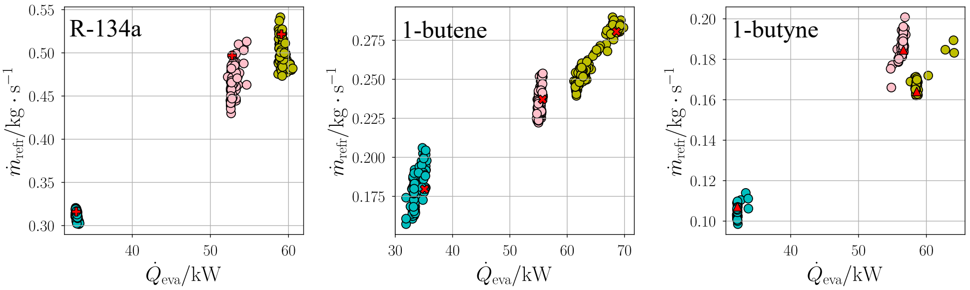

Figure 5.6.: Mass flow rate of the VCC system working fluid as a function of the evaporator cooling capacity. Operating conditions of the ECS system: (●) ground, (●) faulty-pack, and (●) cruise.

The size and the weight of the components are mostly affected by the fluid volumetric flow rate and the maximum flow velocity adopted in the HEXs tubes. As the selected natural refrigerants feature a low vapour density, the volumetric flow rate is larger than that estimated for the benchmark system, despite the significantly lower mass flow rate. In particular, the volumetric flow rate is the highest for 1-butyne. However, the weight of the system components for this fluid tends to be lower than that estimated for the other two molecules, as it is possible to adopt higher fluid velocity in the HEXs without causing excessive pressure drops (see Fig. 5.12 and 5.14).

The total electric power consumption is calculated as the sum of the power demand of the ram air electric fan, the CAC, and the RC. The results show that, for all three operating points, the compression ratio of the CAC is similar (see Tab. 5.10). Consequently, as the mass flow rate of air is a design specification, the compressor power demand does not vary significantly. The same is valid for the ram air fan. Figure 5.8 shows that the optimizer identifies as optimal in terms of system performance values of ram air mass flow rate at each operating point which are similar independently from the working fluid. Therefore, the differences in total electric power demand shown in Fig. 5.5 are due only to the power consumption of the RC, in particular at cruise. It is possible to demonstrate that the compressor power consumption is a function of five quantities: the flow heat capacity rate $\dot{C}$, the fluid generalized polytropic exponent γ_{pv}, and the compressor total-to-total pressure ratio, the inlet temperature, as well as the efficiency. The last two quantities and γ_{pv} do not vary significantly among the considered fluids. The higher compressor power consumption observed in case 1-butene is the working fluid is then due to a combination of high flow heat capacity rate and large compression ratio compared to the other two working fluids (see Fig. 5.7).

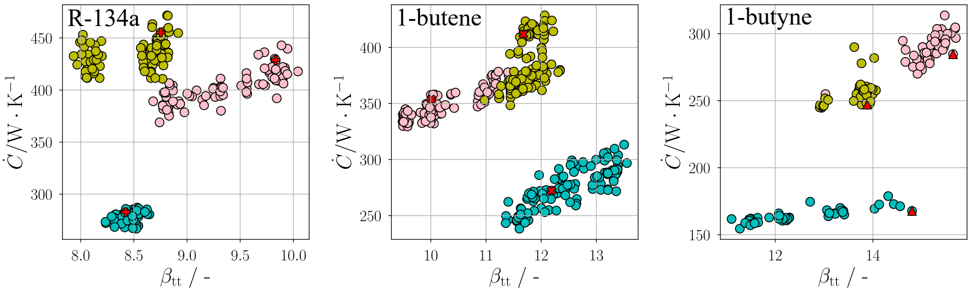

Figure 5.7.: From left to right: heat capacity rate as a function of the total-to-total compression ratio of the twin-stage centrifugal compressor of the VCC system. Operating conditions of the ECS system: (●) ground, (●) faulty-pack, and (●) cruise.

The ram air drag penalty at cruise is calculated by subtracting the thrust generated in the nozzle from the drag occurring in the flush intakes. For a fixed geometry of the nozzle, the thrust exclusively depends on the ram air mass flow rate and its velocity, since the total pressure recovery in the intake is similar, independently from the working fluid of the VCC system, and the pressure drop in the condenser is relatively low. In turn, the airflow speed is directly proportional to the working fluid temperature. As already mentioned, the ram air mass flow rate is comparable for all the selected test cases. If the ECS operates with 1-butene as the working fluid, the condenser heat duty is the largest and the condensation temperature is the highest, independently from the considered operating condition(Fig. 5.8). Therefore, for a fixed ram air mass flow rate, the air temperature at the condenser outlet is the highest compared to the other two test cases. This results in a higher ram nozzle thrust, and therefore lower drag.

To facilitate the comparison of the system performance depending on the working fluid, a single figure of merit has been considered, i.e., the fuel weight penalty (W_{f_0}). This quantity provides an estimate of the aircraft fuel consumption due to the ECS weight, aerodynamic drag caused by ram air ducts, and electric power consumption. The fuel weight penalty is calculated as the sum of these three contributions, according to the definition provided by the AIR1168-8A SAE report [33]

$$W_{\mathrm{f}_0} = W_{\mathrm{f}_0}\Big|_{\mathrm{weight}} + W_{\mathrm{f}_0}\Big|_{\mathrm{power}} + W_{\mathrm{f}_0}\Big|_{\mathrm{drag}}, \tag{5.6}$$

where

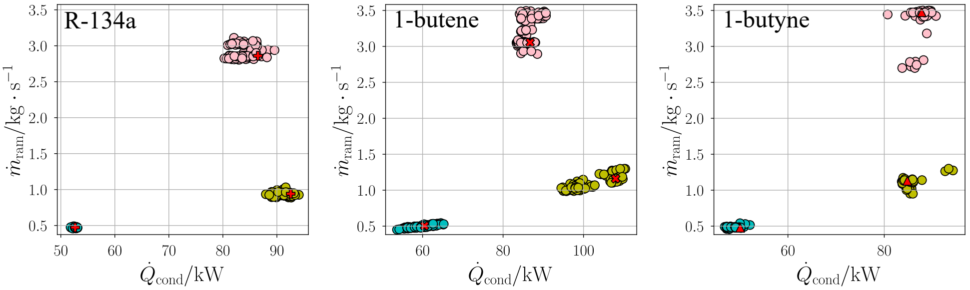

Figure 5.8.: From left to right: ram air mass flow rate as a function of the condenser heat duty. Operating conditions of the ECS system: (●) ground, (●) faulty-pack, and (●) cruise.

$$\begin{cases} W_{\mathrm{f}_0}\Big|_{\text{weight}} = W_{\mathrm{F}}\left[\exp\left(\frac{SFC_{\mathrm{th}}\tau}{L/D}\right)-1\right], \\[2ex] W_{\mathrm{f}_0}\Big|_{\text{power}} = \dot{W}_{\mathrm{el}}\cdot SFC_{\mathrm{P}}\frac{L/D}{SFC_{\mathrm{th}}}\left[\exp\left(\frac{SFC_{\mathrm{th}}\tau}{L/D}\right)-1\right], \\[2ex] W_{\mathrm{f}_0}\Big|_{\text{drag}} = \dot{m}_{\mathrm{ram}}\cdot v_{\mathrm{air}}\cdot\frac{L/D}{g}\left[\exp\left(\frac{SFC_{\mathrm{th}}\tau}{L/D}\right)-1\right]. \end{cases} \tag{5.7}$$

More specifically, the first term is associated with the weight of the ECS system, the second term is related to the electric power consumption, while the third term refers to the ram air drag penalty. The values of the constants in Eqn. 5.7 have been considered independent of the flight phase and are equal to those suggested by Bender [34] for the case study of the Airbus A320 aircraft.

Figure 5.9 shows values of the fuel weight penalty as a function of the design objective function, whereby the lowest values are indicated with red markers. The results show that with 1-butyne as the working fluid, it is possible to design an aircraft ECS whose specific fuel consumption is lower than that estimated for the benchmark system, i.e., that with a VCC system adopting R-134a as working fluid. However, the improvement is significantly limited: the fuel weight penalty is reduced by almost 3 kg in comparison to the benchmark value of approximately 85 kg. Such improvement is achieved despite the slightly higher electric power consumption, thanks to the lower system weight and drag. 1-butene as working fluid is a suboptimal choice, despite those designs allow for a significantly lower ram air drag. Table 5.10 lists the most significant variables characterizing the optimal ECS designs depending on the working fluid and the operating point.

The mass of the working fluid charge is on average equal to 650 g for both 1-butene and 1-butyne. The use of flammable refrigerants might be relevant from a regulatory point of view. However, to contextualize the problem, it might be helpful to compare the situation to regulations valid for domestic or commercial applications of VCC systems. According to the existing safety guidelines [35, 36], the maximum allowable limit for the mentioned applications with highly flammable refrigerants is 500 g, regardless of the room size. Therefore, it can be argued that the flammability of the selected hydrocarbons is not a critical limitation for their adoption in VCC systems aboard aircraft, considering the sophisticated technology and maintenance of systems developed in the aerospace industry, and the significantly lower price of these compounds. In the following, a detailed analysis of the influence of the working fluid choice on the design of the main system components, namely the HEXs, the CAC, and the RC

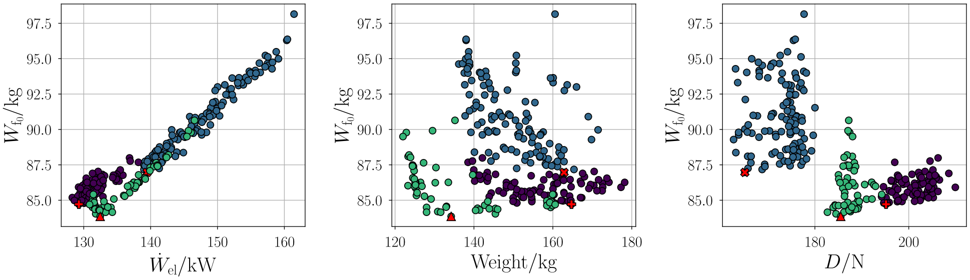

Figure 5.9.: Aircraft fuel weight penalty associated with the ECS as a function of the design objective functions. Working fluids: (●) R-134a, (●) 1-butene, (●) 1-butyne. Red markers indicate the values corresponding to optimal system design solutions in case of (✚) R-134a, (✖) 1-butene, and (▲) 1-butyne are the working fluids.

Table 5.10.: List of the most significant variables characterizing the optimal ECS designs depending on the working fluid and the operating point. Optimal designs are associated with the minimum fuel weight penalty due to the ECS.

Working fluid		**R-134a**			**1-butene**			**1-butyne**		
Operating point		**G**	**C**	**FP**	**G**	**C**	**FP**	**G**	**C**	**FP**
Evaporator duty	$\dot{Q}_{\text{eva}}$ / kW	52.8	32.8	59.1	55.7	35.1	68.6	56.6	32.1	58.6
Condenser duty	$\dot{Q}_{\text{cond}}$ / kW	86.5	52.7	92.6	86.7	60.5	108	87.8	50.1	84.8
Refrigerant compressor electric power	$\dot{W}_{\text{el,compr}}$ / kW	36.2	20.4	35.9	33.3	27.4	42.2	33.5	19.3	28.1
Fan electric power	$\dot{W}_{\text{el,fan}}$ / kW	1.6	0	0	2.5	0	0	4.6	0	0
CAC electric power	$\dot{W}_{\text{el,CAC}}$ / kW	34.4	54.6	94.8	40	57.2	105.3	42.5	53.9	94.3
Ram air mass flow rate	$\dot{m}_{\text{ram}}$ / kg · s^{-1}	2.9	0.5	0.9	3.1	0.5	1.2	3.5	0.5	1.1
Refrigerant mass flow rate	$\dot{m}_{\text{refr}}$ / kg · s^{-1}	0.5	0.3	0.5	0.24	0.18	0.28	0.18	0.11	0.16
Evaporation temperature	T_{eva} / K	267.6	275.2	270.2	267.6	272.4	263.1	266.3	267.7	259.1
Evaporation pressure	p_{eva} / bar	2.38	3.15	2.63	1.04	1.25	0.87	0.54	0.56	0.38
Condensation temperature	T_{cond} / K	345.7	352.9	345.1	344.5	363.7	342	345.3	348.5	325.0
Condensation pressure	p_{cond} / bar	22.40	26.19	22.11	9.89	14.85	9.36	7.41	8.02	4.34
Compression ratio 1st stage	$\beta_{\text{tt,S1}}$ / -	3.22	3	3.06	3	3.7	3.2	4.0	3.9	3.8
Compression ratio 2nd stage	$\beta_{\text{tt,S2}}$ / -	3.05	2.8	2.85	3.3	3.3	3.6	3.9	3.8	3.7
Total-to-total efficiency 1st stage	$\eta_{\text{tt,S1}}$ / -	0.82	0.81	0.81	0.71	0.78	0.70	0.67	0.74	0.67
Total-to-total efficiency 2nd stage	$\eta_{\text{tt,S2}}$ / -	0.75	0.67	0.77	0.70	0.71	0.71	0.72	0.74	0.72
Rotation speed RC	Ω_{RC} / krpm	105.7	103.2	106.1	144.3	146.8	147.4	167.5	164.9	160.4
Compression ratio CAC	$\beta_{\text{tt,CAC}}$ / -	1.70	2.76	2.73	1.84	2.87	3.0	1.91	2.73	2.71
Total-to-total efficiency CAC	$\eta_{\text{tt,CAC}}$ / -	0.86	0.87	0.87	0.82	0.80	0.75	0.78	0.81	0.75
Rotational speed CAC	Ω_{CAC} / krpm	20.9	28.2	28.0	18.9	25.3	27.3	24.0	28.4	29.4

is provided. The discussion is limited to the two natural refrigerants.

5.6.1. HEAT EXCHANGERS DESIGN

The two HEXs of the aircraft ECS, i.e., the evaporator and the condenser, are sized for ground operating conditions, and then their performance is evaluated in the case of the other two operating points. The reader can refer to Fig. 3.2 and 3.3 in Ch. 3 for the schematics of the

HEXs geometry.

Figure 5.10 shows the optimized dimensions of the condenser core, namely the width (W), the height (H), and the depth (D), as a function of the condenser weight. The width and the height are the two dimensions of the airstream frontal area of the HEX. The height determines the number of tubes on the refrigerant side, while the depth is directly proportional to the flat tube width, and consequently the width of the minichannels on the working fluid side. The results show that the HEX width is the only dimension that influences the condenser weight, according to a direct proportionality law.

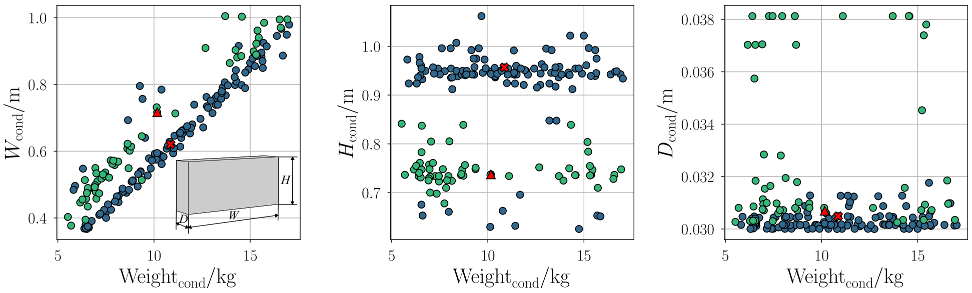

Figure 5.10.: From left to right: condenser width, height and depth of the HEX core as a function of weight. Working fluids: (●) 1-butene, (●) 1-butyne.

The optimal design of the condenser is associated with the refrigerant and the airflow velocity being adjusted to achieve the best trade-off between the pressure drop over the air stream and the compactness of the device. The ram air pressure drop decreases with increasing HEX width and decreasing depth. The increase in HEX height, together with the decrease in width, allows for a reduction of the refrigerant pressure drop in the condenser. The ram air mass flow rate does not depend on the working fluids and this is valid for all operating conditions, therefore differences in air velocity and pressure drop are only associated with variations of the ram air side frontal area. Therefore, Fig. 5.11 shows that, if 1-butyne is the working fluid, the ram air pressure drop is the highest. Optimal designs for which the minimum fuel weight penalty of the ECS is minimal are those for which pressure drop associated with ram air is minimal, though this results in a larger weight of the condenser.

The optimal condenser designs are characterized by high values of HEX height, not only to reduce the pressure drop on the ram air side but also to limit the pressure drop in the refrigerant flow. In particular, the number of tubes on the refrigerant side is directly proportional to the height of the condenser. In the case of 1-butene, this dimension is on average equal to 0.95 m and it is 20% larger compared to that of 1-butyne, while the width and depth of the condenser vary in a similar range of values. The optimal depth is approximately 30 mm, which corresponds to the lower bound set for this quantity in the optimization problem constraints (see Tab. 5.9. The differences in condenser height can only be explained as the result of different local optima found by the optimization algorithm for the 1-butyne case, as both the volumetric flow rate and the velocity of 1-butene within the condenser tubes (Fig. 5.12) are lower than those of 1-butyne.

Figure 5.13 shows that the optimal design of the evaporator strongly depends on the working fluid.

VCC system performance is particularly sensitive to the pressure drop associated with the refrigerant flow in the evaporator. Therefore, the width of the evaporator, corresponding to the length of the refrigerant tubes, is shorter if compared to the width of the condenser. The

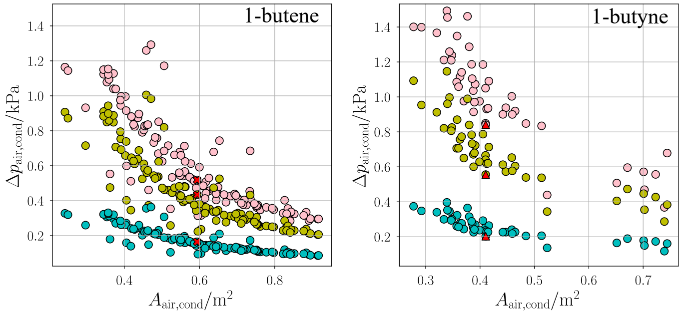

Figure 5.11.: From left to right: variation of the pressure drop on the air side of the condenser as a function of the frontal area of the HEX for the working fluids 1-butene, and 1-butyne. Operating conditions of the ECS system: (●) ground, (●) faulty-pack, and (●) cruise.

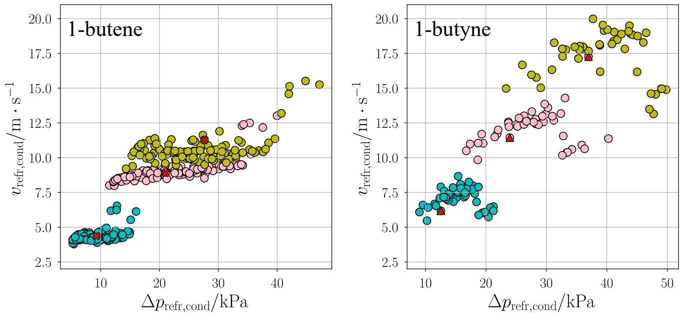

Figure 5.12.: From left to right: velocity of the refrigerant within the condenser tubes as a function of the corresponding pressure drop. Operating conditions of the ECS system: (●) ground, (●) faulty-pack, and (●) cruise.

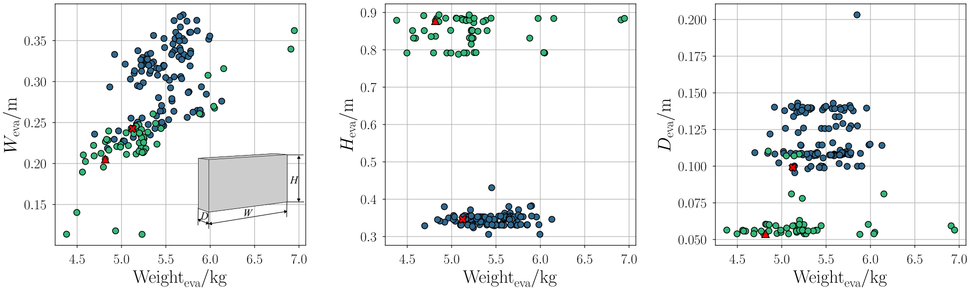

Figure 5.13.: From left to right: width, height and depth of the evaporator core as a function of the weight. Working fluids: (●) 1-butene, (●) 1-butyne.

optimal height values of 1-butyne evaporator are more than double those calculated for the 1-butene evaporator, while the depth is almost half. These dimensions are tuned by the optimizer to comply with the constraint on the maximum velocity of the refrigerant, which is set to 50 $\mathrm{m \cdot s^{-1}}$ for all the operating conditions of the ECS. To maximize the flow passage area in the evaporator the optimizer explores two different strategies: in the case of 1-butene, the depth of the evaporator is maximized, while in the case of 1-butyne the number of flat tubes is increased by adopting larger HEX heights. The vapour velocity tends to be higher for 1-butyne, though the pressure drop across the evaporator is lower, as shown in Fig. 5.14.

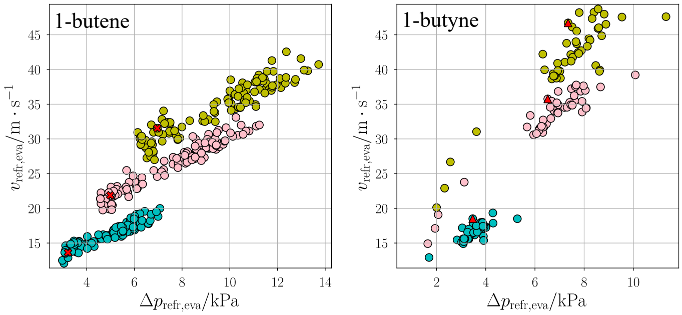

Figure 5.14.: From left to right: velocity of the refrigerant within the evaporator tubes as a function of the corresponding pressure drop. Operating conditions of the ECS system: (●) ground, (●) faulty-pack, and (●) cruise.

5.6.2. TURBOMACHINERY DESIGN

CABIN AIR COMPRESSOR

The function of the CAC is the pressurization of the cabin, therefore its design is independent of the working fluid of the VCC system. Due to the adopted model implementation strategy, all the components are sized for the conditions corresponding to on-ground operation. While on-ground operating conditions are the most critical for the sizing of VCC system components, this is not the case for the CAC, as the compression ratio required to pressurize the ambient air is the lowest and it is approximately equal to 1.8. Optimal designs are characterized by high values of flow coefficient (Φ_{t1}), ranging between 0.11 and 0.15, and isentropic loading coefficient (ψ_{is}), varying from 0.84 to 0.89. The rotational speed is relatively high and it varies between 22 to 25 krpm. In the other two operating points, i.e., during cruise flight under standard conditions and in the case of a faulty-pack, ambient air is rarefied, therefore the CAC compression ratio is higher, ranging between 2.8 and 3.0. In the case of a faulty ECS pack, the air mass flow rate of the CAC is double that of cruise operation and the compression ratio is much higher, resulting in a reduction of the total-to-total efficiency (η_{tt}), varying between 0.7 and 0.78, as compared to the other two operating conditions.

REFRIGERANT COMPRESSOR

The design of the RC is complex since it depends both on the properties of the working fluid and on the operating conditions of the aircraft. Even if the density of 1-butene and 1-butyne is lower than that of R-134a, optimal 1-butene and 1-butyne compressors feature smaller size and higher rotational speed, because of the significantly lower mass flow rate and higher speed of sound of these working fluids (Fig. 5.6). Moreover, to comply with the required temperature lift of the system, these compressor designs feature larger compression ratios for both stages. As a result, the total-to-total efficiency (η_{tt}) of 1-butene and 1-butyne compressors is 10% lower if compared to optimal R-134a compressors.

The design of the centrifugal compressor must comply with constraints associated with fluid-dynamic, manufacturing, and structural aspects. This turbomachine features two stages mounted in a back-to-back configuration to balance the net axial force. The two impellers are installed on a common shaft, thus they rotate at the same speed. In the design calculation of the compressor, this condition is enforced by adapting the isentropic loading coefficient (ψ_{is}) of the second stage to match the rotational speed (Ω) determined while designing the first stage. The results show that, in general, due to the lower flow density, the impeller dimensions of the first stage of the compressor are larger than those of the second stage (Fig. 5.15). In the case of 1-butyne, since the volumetric flow rate is larger for all the operating conditions, the diameter of the compressor wheel is slightly bigger than that of the 1-butene compressor. Moreover, the compressor designed for 1-butyne is characterized by a higher flow coefficient, and lower loading coefficient(Fig. 5.16 and 5.15). The consequence is that the peripheral speed of the two impellers of 1-butyne compressor is higher, thus the rotational speed, given that the size of the wheels of the two compressors is similar (Fig. 5.16). Furthermore, the optimal values of the flow coefficient of the first stage are systematically higher than those of the second stage, and this outcome is in agreement with the findings of Giuffré *et al.* [30] (Fig. 5.15).

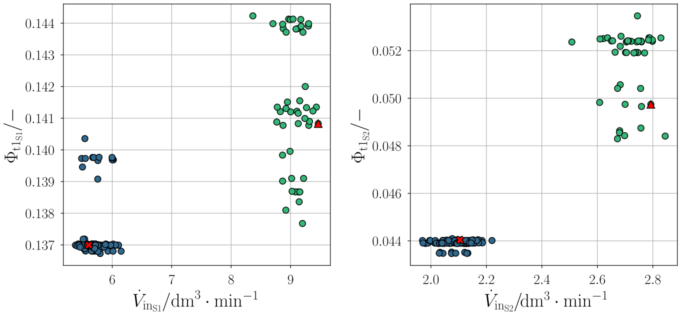

Figure 5.15.: From left to right: flow coefficient of the first and of the second stage of the centrifugal compressor as a function of the inlet volumetric flow rate. Working fluids: (●) 1-butene, (●) 1-butyne.

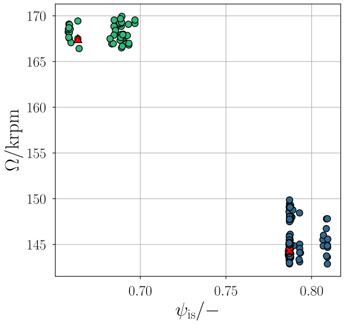

Figure 5.16.: Rotational speed as a function of the isentropic loading coefficient for ground operating conditions. Working fluids: (●) 1-butene, (●) 1-butyne.

In the case of the 1-butyne compressor, the compression ratios of the first and of the second stage are significantly higher than those of the 1-butene compressor, and they are close to the prescribed upper limit, which is set to 4 (Fig. 5.17). Despite the high values of compression ratio, the total-to-total efficiency of the compressor is similar to that estimated for the 1-butene compressor, with average values of approximately 72%.

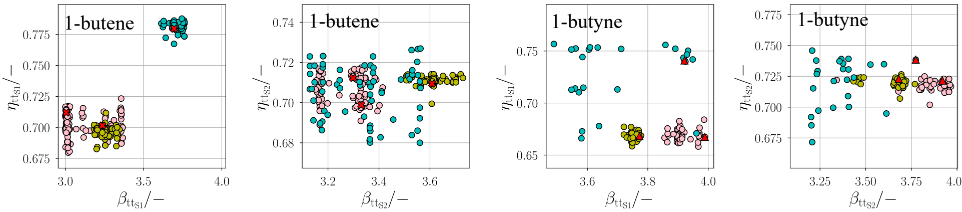

Figure 5.17.: From left to right: total-to-total efficiency of the first and second stage of the refrigerant centrifugal compressor as a function of the compression ratio. Operating conditions of the ECS system: (●) ground, (●) faulty-pack, and (●) cruise.

5.7. CONCLUSIONS

A methodology for the concurrent selection of the optimal refrigerant and optimization of the design of a Vapour Compression Cycle system for aircraft Environmental Control System was developed and tested with a study case, namely that of the ECS of a short-haul, single-aisle passenger airline, i.e., the Airbus A320. The prime mover of the VCC system is an electrically-driven high-speed centrifugal compressor. The working fluid selection method implements the principles of the Continuous-Molecular Targeting to Computer-Aided Molecular Design (CoMT-CAMD) approach proposed by Bardow *et al.* [15], which, in turn, relies on the Pertubated-Chain Statistical Associating Fluid Theory equation of state model for the computation working of fluid properties. Therefore, a substance is defined by a set of molecular describers, which are optimized to maximize the COP of the VCC system while facilitating the design of the centrifugal compressor. This is achieved with the *in-house* Python programme *OptiFluidECS* supporting an interface with the software *TurboSim* for the centrifugal compressor design. The result is a hypothetical optimal working fluid, referred to as *pseudo-fluid*. Working fluids featuring molecular descriptors similar to those of the *pseudo-fluid* were searched in a database consisting of 26 halogenated substances and 56 non-polar non-halogenated refrigerants. The application of this procedure leads to the selection of 1-butene and 1-butyne as the optimal refrigerants for the VCC system of the ECS test case. The working fluid selection is based on various criteria, including the predicted system COP, the design feasibility of the compressor, the environmental footprint, as well as considerations regarding safety of operation.

A multi-point and multi-objective integrated design optimization of the exemplary VCC system was carried out to assess these two refrigerants as working fluids. For this analysis, the VCC system model was implemented in a computer code using the Modelica modelling language. The software allows for the preliminary design of all the system components. The Python *in-house TurboSim* program provides the centrifugal compressor design and it is integrated within the Modelica system model. The system design optimization framework *DesOptECS MultiPoint* is coded in Python, and relies on an interface with the Modelica executable [31] for system simulations.

The optimization study considers three aircraft operating points, namely: ground operation during hot weather conditions, standard flying at cruise, and fault of one ECS pack during cruise. A gradient-free optimization algorithm has been chosen to minimize the three objective functions of the problem, i.e., system weight, drag penalty associated with the ram air, and system electric power consumption. The resulting optimal ECS designs associated with the two optimal natural refrigerants were compared with those obtained in case R-134a is the working fluid, which is referred to as the benchmark case.

The main conclusions of this study are summarized as follows:

i) a CoMT-CAMD methodology has been successfully developed and applied to the case of the design optimization of a VCC-based aircraft ECS. 1-butene and 1-butyne were singled out as the optimal working fluids belonging to the class of non-polar non-halogenated compounds. Despite their high flammability, natural refrigerants have been selected due to their promising thermodynamic properties and almost null GWP;

ii) the optimal design solutions on the Pareto surfaces resulting from the multi-point and multi-objective ECS design optimization do not feature lower power consumption than those associated with the benchmark system. However, the use of the two selected natural refrigerants as working fluids allows for the reduction of the drag penalty associated with the needed ram air, reaching a maximum decrease of 15% in the case 1-butene is the working fluid. If 1-butyne is the VCC system working fluid, some optimal solutions also allow for system designs with a 15% reduction in system weight and an electric power consumption varying approximately in the same values estimated for the benchmark system (130 - 140 kW). Overall, the analysis of the optimal system designs corresponding to the minimum fuel weight penalty results only in 3 kg reduction of fuel weight penalty in the case of 1-butyne, as compared to the benchmark value of 85 kg;

iii) the overall design optimization leads to condensers for which the pressure drop associated with the ram air stream is minimal, while ensuring adequate refrigerant velocity within the tubes. However, when low vapour density refrigerants are used, pressure drop associated with the refrigerant flow can rise, especially for system operating points for which the required refrigerant mass flow rate is large, as in the case of cruise and faulty-pack operating conditions. To address this issue, condenser designs with more flat tubes can be adopted to increase the flow passage area for the refrigerant stream;

iv) the design of the evaporator is mainly influenced by the need to minimize the pressure drop associated with the refrigerant stream. Therefore, the evaporator is designed with a shorter width compared to the condenser. To keep the pressure drop and the velocity of the refrigerant within the selected boundaries, the optimization algorithm has adopted two design strategies: an increased number of tubes in the case of 1-butyne, and maximization of the evaporator depth for 1-butene;

v) the cabin air compressor performance is penalized by the choice of the design point, that is at ground conditions. However, the most critical conditions for the cabin air compressor arise when the aircraft flies at cruise in standard conditions and when one ECS pack is faulty. In such cases, the environmental air is rarefied, and a higher pressure ratio is necessary for cabin air pressurization, which causes a significant drop in the efficiency of this compressor, up to 20% compared to the efficiency at design point. In future works, a procedure to design the CAC for more critical operating points will be devised;

vi) the refrigerant compressor design depends both on the working fluid and the operating point of the system. If the working fluid is one of the two selected natural refrigerants, the required refrigerant mass flow rate in the VCC system is lower than that of the benchmark system, leading to compressor designs with smaller flow passages and a higher rotational speed. However, due to the thermodynamic properties of these fluids, the temperature lift of the VCC system requires the turbomachinery to operate with a high compression ratio, which causes a decrease in the efficiency of up to 10%. In the case of the 1-butyne compressor, the compression ratios of both compressor stages are systematically higher than those of the 1-butene compressor. Compared to 1-butene, optimal compressor designs are characterized by a lower isentropic loading coefficient, and higher peripheral blade speed at the compressor outlet, which results in an increased rotational speed ranging between 165 and 170 krpm. The flow coefficient values of both compressor stages are higher in the case of the 1-butyne compressor due to its larger volumetric flow rate.

The findings of this investigation are meant to prove the validity of the adoption of the CoMT-CAMD method for the exemplary test case of the environmental control system for a passenger aircraft, like the A320. The results successfully pinpoint two unconventional molecules which show performance comparable to those of the state-of-the-art refrigerant for vapour compression cycle-based systems, but with improved environmental properties. However, the outcome of this work does not provide general design guidelines for aircraft ECS in the case hydrocarbons are selected as working fluid. The reason is twofold: i) the database of working fluids selected for the CoMT-CAMD method is limited to few halogenated compounds and non-polar hydrocarbons compounds; ii) the optimization problem is very complex, due to the high level of detail of the components models, the large number of design variables and constraints, and the number of selected operating conditions. Therefore, the optimal solutions derive from complex non-linear relations among the variables which are not trivial to generalize without a large number of sampling working fluids.

Future work may focus on the realization of a single design framework integrating the working fluid optimization within the multi-point and multi-objective system design optimization. Moreover, the recommendation is to extend the database of working fluids with polar hydrocarbon substances, which have been neglected in this work for the sake of simplicity. An additional recommendation is to extend this research to the use of blends of hydrofluoroolefins and natural refrigerants as working fluids, resulting in optimal compounds with favourable thermodynamic properties and low flammability. The high flammability of the refrigerant adopted for the aircraft environmental control system, in fact, still represents a limitation according to the current aerospace certification authorities.

NOMENCLATURE

Acronyms

ACM	Air Cycle Machine
CAC	Cabin Air Compressor
CAMD	Computer-Aided Molecular Design
CAMDP	Computer-Aided Molecular and Process Design
CO_2	Carbon dioxide
CoMT-CAMD	Continuous-Molecular Targeting to Computer-Aided Molecular Design
COP	Coefficient Of Performance
DeSimECS	Design and Simulation of Energy Conversion Systems
DymTherM	Dynamic modelling and simulation of Thermal Management systems
ECS	Environmental Control System
F-gas	Fluorinated greenhouse gases
GA	Genetic Algorithm
GWP	Global Warming Potential
HEX	Heat exchanger
HFC	Hydrofluorocarbon
MOO	Multi-Objective Optimization
NSGA-II	Non-Sorted Genetic Algorithm-II
ODP	Ozone Depletion Potential
ORC	Organic Rankine Cycle
PC-SAFT	Pertubed-Chain Statistical Associating Fluid Theory
QSPR	Quantitative Structure-Property Relationship
R-134a	1,1,1,2-Tetrafluoroethane
TFA	Trifluoroacetic acid
VCC	Vapour Compression Cycle

Roman letters

$\dot{C}$	Heat capacity rate $[\mathrm{W{\cdot}K^{-1}}]$
D	Drag [N]
F	Force [N]
f	Objective function [-]
g	Gravitational acceleration $[\mathrm{m{\cdot}s^{-2}}]$
H	Height [m]
k	Shape factor [-]
L	Lift [N]
M	Molecular mass $[\mathrm{g{\cdot}mol^{-1}}]$, Mach number [-]
m	Number of segments per chain molecule [-]
$\dot{m}$	Mass flow rate $[\mathrm{kg{\cdot}s^{-1}}]$
N	Molecular complexity [-]
ϵ_k	Dispersion energy [K]
c_p^{ig}	Specific isobaric heat capacity $[\mathrm{J{\cdot}(kg{\cdot}K)^{-1}}]$
p	Pressure [Pa]
$\dot{Q}$	Heat [W]
R	Radius [m]
s	Specific entropy $[\mathrm{J{\cdot}(kg{\cdot}K)^{-1}}]$
SFC_{P}	Power specific fuel consumption $[\mathrm{lb{\cdot}(hp{\cdot}h)^{-1}}]$
SFC_{th}	Thrust specific fuel consumption $[\mathrm{lb{\cdot}(hp{\cdot}h)^{-1}}]$
T	Temperature [K]
v	Velocity $[\mathrm{m{\cdot}s^{-1}}]$
W	Width [m]
W_{f_0}	Fuel weight penalty [kg]
$\dot{W}$	Power [W]
x	Optimization variable [-]

Z	Depth [m]

Greek letters

α	Absolute flow angle [deg]
β	Compression ratio [-], Relative flow angle [deg]
γ_{pv}	Fluid polytropic exponent [-]
σ	Segment diameter [Å]
μ	Dipole moment [-]
Φ	Swallowing capacity [-]
ψ	Loading coefficient [-]
Ω	Rotational speed [rpm]

Superscripts and subscripts

1	Inlet compressor impeller
2	Outlet compressor impeller
3	Inlet diffuser
$w_{1,\mathrm{s}}$	Inlet relative velocity at shroud
c	Cruise
cab	Cabin air flow
cond	Condenser
ECS	ECS pack
el	Electric
env	Ambient conditions
eva	Evaporator
fresh	Fresh air flow
fp	Faulty-pack
g	Hot ground
pp	Pinch-point
ram	Ram air flow
sc	Subcooling
sh	Superheating
tt	Total-to-total

REFERENCES

[1] K. Linnett and R. Crabtree. “What’s Next in Commercial Aircraft Environmental Control Systems?” In: *SAE Transactions* 102 (1993), pp. 639–653.

[2] A. Giuffré. “Integrated design optimization of electrically-driven vapour compression cycle systems for aircraft: powered by high-speed centrifugal compressors”. PhD thesis. Delft: Delft University of Technology, 2024. DOI: `10.4233/uuid:b4f6a4a4-2e48-4bbe-9093-3f1368282f63`.

[3] ARP731C. “General Requirements for Application of Vapor Cycle Refrigeration Systems for Aircraft”. In: *SAE International* (2015). DOI: `10.4271/ARP731C`.

[4] E. A. Heath. “Amendment to the Montreal Protocol on Substances that Deplete the Ozone Layer (Kigali Amendment)”. In: *International Legal Materials* 56 (Feb. 2017), pp. 193–205.

[5] European Commission. *Proposal for a regulation of the European parliament and of the council on fluorinated greenhouse gases, amending Directive (EU) 2019/1937 and repealing Regulation (EU) No 517/2014*. Tech. rep. May 2022.

[6] M. Mohanraj and J. D. A. P. Abraham. “Environment friendly refrigerant options for automobile air conditioners: a review”. In: *Journal of Thermal Analysis and Calorimetry* 147.1 (2022), pp. 47–72. ISSN: 1588-2926. DOI: `10.1007/s10973-020-10286-w`.

[7] B. Palm. “Hydrocarbons as refrigerants in small heat pump and refrigeration systems – A review”. In: *International Journal of Refrigeration* 31.4 (June 2008), pp. 552–563. ISSN: 0140-7007. DOI: `10.1016/J.IJREFRIG.2007.11.016`.

[8] N. Abas, A. R. Kalair, N. Khan, A. Haider, Z. Saleem, and M. S. Saleem. “Natural and synthetic refrigerants, global warming: A review”. In: *Renewable and Sustainable Energy Reviews* 90 (July 2018), pp. 557–569. ISSN: 1364-0321. DOI: `10.1016/J.RSER.2018.03.099`.

[9] ANSI/ASHRAE Standard 34. *Designation and Safety Classification of Refrigerants*. Tech. rep. 2022.

[10] L. Y. Ng, F. K. Chong, and N. G. Chemmangattuvalappil. “Challenges and opportunities in computer-aided molecular design”. In: *Computers & Chemical Engineering* 81 (Oct. 2015), pp. 115–129. ISSN: 0098-1354. DOI: `10.1016/J.COMPCHEMENG.2015.03.009`.

[11] N. D. Austin, N. V. Sahinidis, and D. W. Trahan. “Computer-aided molecular design: An introduction and review of tools, applications, and solution techniques”. In: *Chemical Engineering Research and Design* 116 (Dec. 2016), pp. 2–26. ISSN: 0263-8762. DOI: `10.1016/J.CHERD.2016.10.014`.

[12] A. I. Papadopoulos, M. Stijepovic, and P. Linke. “On the systematic design and selection of optimal working fluids for Organic Rankine Cycles”. In: *Applied Thermal Engineering* 30.6-7 (May 2010), pp. 760–769. ISSN: 1359-4311. DOI: `10.1016/J.APPLTHERMALENG.2009.12.006`.

[13] A. I. Papadopoulos, M. Stijepovic, P. Linke, P. Seferlis, and S. Voutetakis. "Toward optimum working fluid mixtures for Organic Rankine Cycles using molecular design and sensitivity analysis". In: *Industrial and Engineering Chemistry Research* 52.34 (Aug. 2013), pp. 12116–12133. ISSN: 08885885. DOI: 10.1021/ie400968j.

[14] W. G. Chapman, K. E. Gubbins, G. Jackson, and M. Radosz. "SAFT: Equation-of-state solution model for associating fluids". In: *Fluid Phase Equilibria* 52.C (Dec. 1989), pp. 31–38. ISSN: 0378-3812. DOI: 10.1016/0378-3812(89)80308-5.

[15] A. Bardow, K. Steur, and J. Gross. "Continuous-molecular targeting for integrated solvent and process design". In: *Industrial and Engineering Chemistry Research* 49.6 (Mar. 2010), pp. 2834–2840. ISSN: 08885885. DOI: 10.1021/IE901281W.

[16] J. Gross and J. Vrabec. "An equation-of-state contribution for polar components: Dipolar molecules". In: *AIChE Journal* 52.3 (Mar. 2006), pp. 1194–1204. ISSN: 1547-5905. DOI: 10.1002/AIC.10683.

[17] M. Lampe, M. Stavrou, H. M. Bucker, J. Gross, and A. Bardow. "Simultaneous optimization of working fluid and process for organic rankine cycles using PC-SAFT". In: *Industrial and Engineering Chemistry Research* 53.21 (May 2014), pp. 8821–8830. ISSN: 15205045. DOI: 10.1021/ie5006542.

[18] M. Lampe, C. de Servi, J. Schilling, A. Bardow, and P. Colonna. "Toward the integrated design of organic rankine cycle power plants: A method for the simultaneous optimization of working fluid, thermodynamic cycle, and turbine". In: *Journal of Engineering for Gas Turbines and Power* 141.11 (Nov. 2019). ISSN: 15288919. DOI: 10.1115/1.4044380.

[19] I. Martinez. *Aircraft environmental control system.* Tech. rep. 2014.

[20] Federal Aviation Administration. *AC 25-20 - Pressurization, ventilation and Oxigen systems assessment for subsonic flight including high altitude operation.* 1996.

[21] M. Stavrou, M. Lampe, A. Bardow, and J. Gross. "Continuous Molecular Targeting–Computer-Aided Molecular Design (CoMT–CAMD) for Simultaneous Process and Solvent Design for CO2 Capture". In: *Industrial & Engineering Chemistry Research* 53.46 (2014), pp. 18029–18041. DOI: 10.1021/ie502924h.

[22] T.-H. Chung, L. L. Lee, and K. E. Starting. "Applications of Kinetic Gas Theories and Multiparameter Correlation for Prediction of Dilute Gas Viscosity and Thermal Conductivity". In: *J. R. A.; Matovlch,. A. Ind. Eng. Chem. Fundam* 23.8 (1984), p. 209.

[23] S. R. Sastri and K. K. Rao. "A simple method to predict surface tension of organic liquids". In: *The Chemical Engineering Journal and the Biochemical Engineering Journal* 59.2 (Oct. 1995), pp. 181–186. ISSN: 0923-0467. DOI: 10.1016/0923-0467(94)02946-6.

[24] A. Giuffré, F. Ascione, C. D. Servi, and M. Pini. "Data-driven modeling of high-speed centrifugal compressors for aircraft Environmental Control Systems". In: *International Journal of Refrigeration* 151 (July 2023), pp. 354–369. ISSN: 0140-7007. DOI: 10.1016/J.IJREFRIG.2023.03.019.

[25] J. Blank and K. Deb. "Pymoo: Multi-Objective Optimization in Python". In: *IEEE Access* 8 (2020), pp. 89497–89509. ISSN: 21693536. DOI: 10.1109/ACCESS.2020.2990567.

[26] R. L. Melnick and J. Huff. "1,3-Butadiene: Toxicity and carcinogenicity in laboratory animals and in humans". In: *Reviews of Environmental Contamination and Toxicology* 124 (1992), pp. 111–144. ISSN: 01795953. DOI: 10.1007/978-1-4612-2864-6.

[27] F. Monticelli. "Diethyl Ether". In: *Encyclopedia of Toxicology: Third Edition* (Jan. 2014), pp. 138–139. DOI: 10.1016/B978-0-12-386454-3.00987-8.

[28] E. W. Lemmon, I. H. Bell, M. L. Huber, and M. O. McLinder. *NIST Standard Reference Database 23: Reference Fluid Thermodynamic and Transport Properties-REFPROP, Version 10.0, National Institute of Standards and Technology*. 2018. DOI: 10.18434/T4/1502528.

[29] Modelica Association. *Modelica Language Specification, Version 3.5*. Tech. rep. 2021.

[30] A. Giuffré, P. Colonna, and M. Pini. "The Effect of Size and Working Fluid on the Multi-Objective Design of High-Speed Centrifugal Compressors". In: *International Journal of Refrigeration* 143 (Nov. 2022), pp. 43–56. ISSN: 01407007. DOI: 10.1016/j.ijrefrig.2022.06.023.

[31] Dassault Systèmes AB. *Dymola: Dynamic Modeling Laboratory*. 2022.

[32] A. Giuffré, P. Colonna, and C. D. Servi. "Dynamic thermal model of passenger aircraft for the estimation of the cabin cooling and heating requirements". In: *Applied Thermal Engineering* 244 (May 2024), p. 122641. ISSN: 1359-4311. DOI: 10.1016/J.APPLTHERMALENG.2024.122641.

[33] SAE International Information Report. *Aircraft Fuel Weight Penalty Due to Air Conditioning*. June 2011. DOI: 10.4271/AIR1168/8A.

[34] D. Bender. "Exergy-Based Analysis of Aircraft Environmental Control Systems and its Integration into Model-Based Design". PhD thesis. Berlin: Technischen Universität Berlin, 2019.

[35] IEC 60335-2-40:2022. *Household and similar electrical appliances - Safety - Part 2-40: Particular requirements for electrical heat pumps, air-conditioners and dehumidifiers*. Tech. rep. 2022.

[36] IEC 60335-2-89:2019. *Household and similar electrical appliances - Safety - Part 2-89: Particular requirements for commercial refrigerating appliances and ice-makers with an incorporated or remote refrigerant unit or motor-compressor*. Tech. rep. 2023.

II

Inverse organic Rankine cycle Integrated System (IRIS) Setup

6

DESIGN AND COMMISSIONING OF THE IRIS FACILITY

> *Men argue. Nature acts.*
>
> François Voltaire

This chapter documents the detailed design and the commissioning of a novel experimental test rig, called Inverse organic Rankine cycle Integrated System (IRIS). The setup has been conceived for testing the performance of Vapour Compression Cycle (VCC) systems and some of their components for aircraft Environmental Control System (ECS) applications in different operating conditions, and for validating the numerical models developed for systems and components simulation and optimal design. The facility implements a single-stage compression refrigeration cycle with two test sections: a volumetric compressor test bed and an air-cooled condenser test bed. The evaporator is heated by a glycol-water mixture, warmed up in an independent loop. The facility has been designed to operate with R-1233zd(E) as working fluid, but it may be operated with other working fluids with appropriate modifications. The successful commissioning of the facility is documented by discussing the data recorded during steady-state operation at the design operating point, together with the operation of the setup during start-up and shut-down procedures. The system cooling capacity is equal to 17.88 ± 0.8 kW, *which is slightly larger than the design value of* 15.5 kW. *The difference has a positive effect on the system efficiency, which is 4% higher than the one calculated at design. The plans for the facility are also briefly outlined.*

Parts of this chapter have been published in

- F. Ascione, C. M. De Servi, O. Meijer, V. Pommé, and P. Colonna. “Assessment of an Inverse Organic Rankine cycle system for the ECS of a large rotorcraft adopting a high-speed centrifugal compressor and a low GWP refrigerant”. In: *Proceedings of the 6th International Seminar on ORC Power Systems. Ed. by Technical University of Munich.* Technical University of Munich, 2021. DOI: 10.14459/2021mp1633127.
- F. Ascione, A. J. Head, P. Colonna, C. M. De Servi. “Design and commissioning of the IRIS: a setup for aircraft Vapour Compression Cycle-based Environmental Control System testing". In: *Proceedings of the ASME Turbo Expo 2024: Turbomachinery Technical Conference and Exposition. Volume 5: Cycle Innovations.* London, United Kingdom. June 24–28, 2024. V005T06A006. ASME. DOI: 10.1115/GT2024-123714.

6.1. INTRODUCTION

Experimental investigation is still essential for the validation of the numerical models and the assessment of new technologies. In the literature, a few examples of experimental facilities for aircraft Environmental Control System (ECS) testing are reported. The majority of these setups have been designed to reproduce the Balance Of Plant (BoP) of the Air Cycle Machine (ACM) [1, 2]. Small test rigs of VCC systems are employed for research on avionics cooling [3, 4]. To contribute to research on novel systems and components for aircraft cabin air thermal management, a novel experimental test rig, called Inverse organic Rankine cycle Integrated System (IRIS), has been designed and commissioned at the Propulsion & Power Laboratory of the TU Delft Aerospace Engineering faculty. The setup has been conceived for testing the performance of Vapour Compression Cycle (VCC) systems for aircraft ECS applications in different operating conditions, for testing high-speed centrifugal compressors and condensers for these systems, and for validating *in-house* simulation and optimal design software for VCC systems and components.

The facility consists of a BoP which realizes a single-stage compression refrigeration cycle (Fig. 6.1). It accommodates two test sections: a compressor testing setup and an air-cooled condenser test bed. The evaporator is heated by a glycol-water mixture, warmed up in an independent loop. An electronic expansion valve controls the degree of superheating of the refrigerant vapour at the compression suction port. The setup was designed with the low-Global Warming Potential (GWP) refrigerant R-1233zd(E) as the working fluid. This fluid is an alternative to the state-of-the-art R-134a refrigerant. Other working fluids, pure or mixture could be used in the future, with appropriate modifications to the setup. The system is designed for a cooling capacity of 15.5 kW.

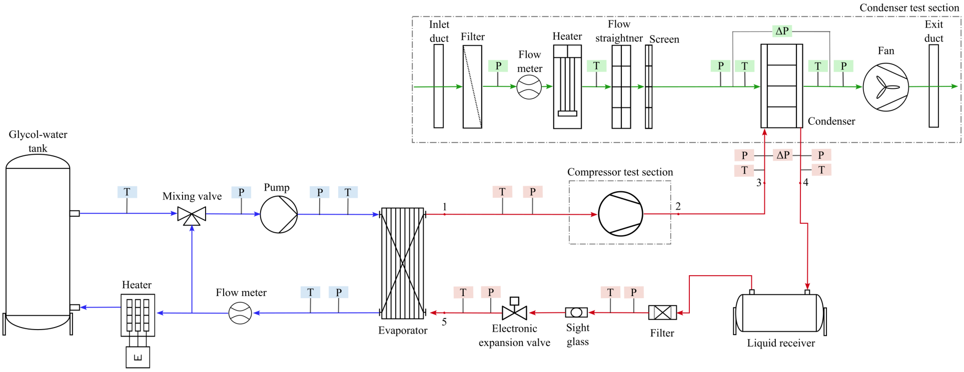

Figure 6.1.: Simplified P&ID of the IRIS setup illustrating the working fluid loop together with the glycol-water loop (—) used to transfer thermal energy to the evaporator of the refrigerant loop (—), and the condenser test section where the working fluid condenses as energy is transferred as heat to ambient air (—).

The IRIS setup would allow exploring the use of a variety of haloolefins with similar thermodynamic properties to R-1233zd(E). The condenser test bed design is flexible in the sense that different kinds of air-to-refrigerant heat exchangers can be installed and tested. At the time of writing, the compressor test section accommodates a piston compressor, which in the future will be replaced by the high-speed centrifugal compressor introduced in Ch. 2. Some of the envisaged experiments aim to assess the performance of the aircraft VCC system in different operating conditions and to characterize the performance maps of the compressor.

This chapter documents the detailed design and the commissioning of the IRIS setup. First, the design requirements and the selection criteria of the system configuration and the working fluid are illustrated. Then, the choice of hardware, measurement instrumentation and control procedures is reported in relation to the objectives of the future experimental campaigns. Finally, the commissioning of the facility is documented by discussing the data recorded during operation at steady-state at the design operating point, together with the operation of the setup during start-up and the shut-down procedures. The design operating condition corresponds to a temperature of evaporation equal to 20 °C, and a temperature lift between condensation and evaporation of 45 °C. For this operating point, the piston compressor reaches a pressure ratio equal to 4.15 with a refrigerant mass flow rate of 0.105 $\mathrm{kg \cdot s^{-1}}$. The values of temperature and pressure are measured at all the relevant state points of the thermodynamic cycle.

6.2. DESIGN REQUIREMENTS AND WORKING FLUID SELECTION

The IRIS setup has been conceived to test the performance of the VCC system for aircraft and rotorcraft ECS. As VCC systems are already state-of-the-art technology for helicopter cabin air cooling, the preliminary design of the IRIS setup has been carried out considering the requirements of this application. Helicopter ECSs are sized for a critical operating condition, i.e., the helicopter is on the ground on a hot and humid day [5], and the design requirements of the setup comply with this specific case. The corresponding design cooling duty of the IRIS is 15.5 kW. The temperature of the environmental air entering the ram air duct is equal to 40 °C with a humidity level of 40%. The refrigerant condensation temperature is set to 65 °C. In the case of volumetric compressors, to allow for safe operation, the suction pressure should always be higher than the atmospheric pressure.

The idea underpinning the conceptualization of the IRIS setup is to design a simple and flexible facility. To comply with these requirements and with logistic constraints, there are two differences in the IRIS setup as compared to the traditional helicopter ECS configuration: i) the absence of the intercooler in the BoP, ii) the utilization of a plate heat exchanger as the evaporator, whereas the refrigerant is warmed up by a mixture of 20% ethylene glycol and water, instead of air.

The selection of the working fluid of the refrigeration loop is based on the findings from a study on the preliminary design of helicopter ECSs [6]. A steady-state model of the system was developed using the acausal modelling language Modelica to assess the thermodynamic performance of the system as a function of several low-GWP working fluids and to verify the feasibility of the design of its components. Various refrigerants were considered, such as haloolefins and hydrocarbons, as reported in Tab. 6.1. The thermodynamic and transport properties of the working fluids were calculated using a well-known software library [7]. The effect of working fluids on the performance was compared and ranked in terms of system Coefficient Of Performance (COP) to preliminarily identify the optimal refrigerants (Fig. 6.2). The system COP is strongly influenced by the operating pressure between the two compression stages, hereinafter indicated as the intermediate pressure of the system, which is reported on the abscissa of Fig. 6.2. The best performance is achieved if refrigerants belonging to the group of the haloolefins are the working fluids, i.e., R-1233zd(E), R-1336mzz(Z), R-1224yd(Z) and R-1234ze(Z). The COP improvement due to the adoption of new working fluids compared to the COP associated with R-134a ranges from 12% to 15%. R-1233zd(E) is identified as the optimal working fluid and selected as the design refrigerant for the IRIS setup.

Similarly to what was done in the case of the study on the helicopter ECS preliminary design [6], a simplified zero-dimensional and steady-state model of the IRIS setup has been developed using the causal Modelica language (Fig. 6.3 (left)). The design operating conditions

Table 6.1.: Main properties of low-GWP refrigerants considered as working fluids for the preliminary design of the IRIS setup.

Refrigerant class	**ASHRAE name**	**T_c / K**	**p_c / bar**	**NBP / K**	**M / g·mol^{-1}**	**N / -**	**GWP**	**ODP**	**Safety group**
HFC	R-134a	374.21	40.49	247.08	109.03	−1.10	1300	0	A1
	R-32	351.26	57.82	221.5	52.02	-1.93	677	0	A2L
	R-152a	386.41	45.17	249.13	66.05	-0.56	138	0	A2
HFO	R-1234yf	367.85	33.82	243.67	114	−0.038	0	0	A2L
	R-1243zf	376.93	35.18	247.73	96.05	0.097	4	0	A2
	R-1234ze(E)	382.51	36.35	254.18	114.04	1.78	1	0	A2L
	R-1234ze(Z)	423.37	35.31	282.88	114.04	1.49	1	0	A2L
	R-1336mzz(Z)	444.5	29.03	306.6	164.06	9.24	2	0	A1
HCFO	R-1233zd(E)	439.6	36.24	2.84	130.05	3.92	5	0	A1
	R-1224yd(Z)	428.69	33.37	287.77	148.49	4.91	<1	0	A1
Natural refrigerants	Isobutane	407.81	36.29	261.4	58.12	3.03	4	0	A3
	Propylene	364.21	45.55	225.53	42.08	−2.622	2	0	A3
	Propane	369.89	42.51	231.04	44.10	−1.313	3	0	A3

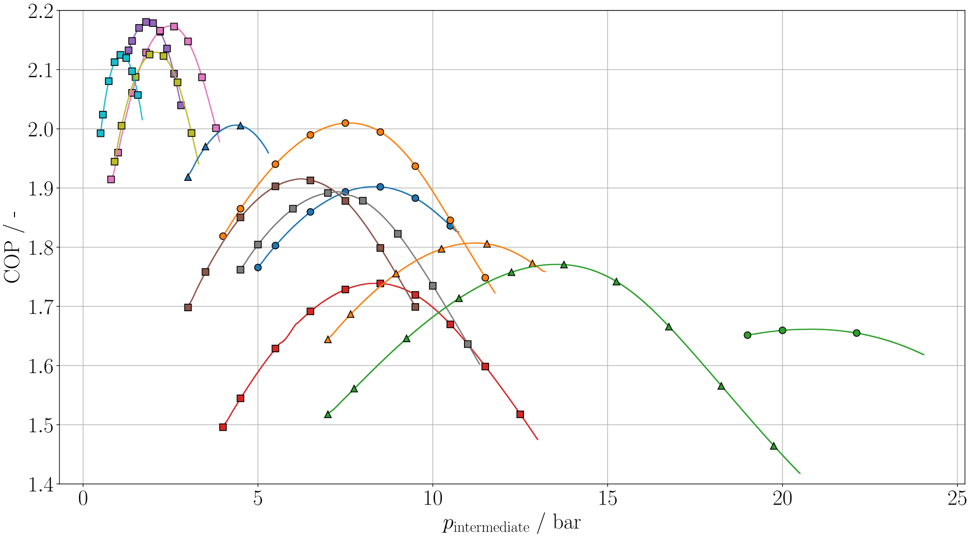

Figure 6.2.: COP as a function of the intermediate pressure estimated for the exemplary helicopter ECS considered for the design of the IRIS. The COP is calculated for several working fluids, namely (●) R-134a, (●) R-152a, (●) R-32, (■) R-1234yf, (■) R-1233zd(E), (■) R-1234ze(E), (■) R-1234ze(Z), (■) R-1243zf, (■) R-1224yd(Z), (■) R-1336mzz(Z), (▲) Isobutane, (▲) Propane, (▲) Propylene.

of the R-1233zd(E) loop have been estimated for each state point of the thermodynamic cycle (Tab. 6.2). The predicted cooling duty of the setup in nominal conditions is 15.5 kW. The refrigerant mass flow rate is equal to 0.105 kg·s^{-1}. The subcooling and the superheating degree are set to 5 K. Figure 6.3 (right) shows the vapour compression cycle in the T–s chart of the refrigerant. The system simulations are performed considering an inlet temperature of the glycol-water stream in the evaporator of 45 °C at atmospheric pressure. The temperature decrease is equal to 10 K and the fluid volumetric flow rate is 1.30 $\mathrm{m^3 \cdot h^{-1}}$. On the condenser side, the inlet air is at a temperature of 40 °C at atmospheric pressure with a mass flow rate of 1.4 $\mathrm{kg \cdot s^{-1}}$. The outlet temperature is estimated to be equal to 54 °C. The predicted system COP is 3.60.

Table 6.2.: Preliminary design specifications of the IRIS setup refrigeration loop. The state points refer to the P&ID in Fig. 6.1.

Refrigeration loop			
State point	***T* / °C**	***p* / bar**	***x* / -**
1	25	1.08	Superheated vapour
2≡3	80.18	4.48	Superheated vapour
4	60.76	4.45	Subcooled liquid
5	20	1.08	0.26

Refrigerant mass flow rate	$\dot{m}_{\mathrm{refr}}$ / $\mathrm{kg{\cdot}s^{-1}}$	0.105
Evaporator heat duty	$\dot{Q}_{\mathrm{eva}}$ / kW	15.5
Condenser heat duty	$\dot{Q}_{\mathrm{cond}}$ / kW	19.8
Compressor power demand	$\dot{W}_{\mathrm{compr}}$ / kW	4.30

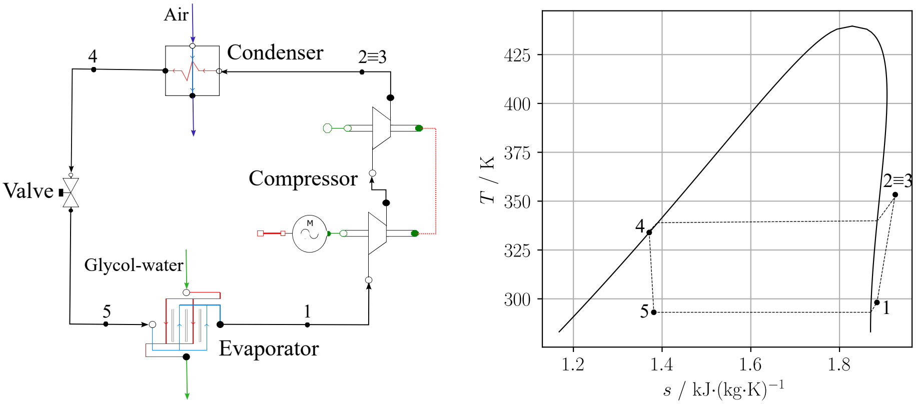

Figure 6.3.: Left: schematic of the Modelica model used for the preliminary design of the vapour compression cycle of the IRIS facility. Right: representation in the temperature-entropy diagram of R-1233zd(E) of the processes calculated for the vapour compression cycle of the IRIS facility. The thermodynamic states of the working fluid at the inlet and outlet of components are indicated with the same number on the P&ID in Fig. 6.1.

6.3. DETAILED DESIGN

Figure 6.6 shows the Piping and Instrumentation Diagram (P&ID) of the facility. The system includes three different fluid circuits hereinafter referred to as

- *heating loop*, providing thermal energy input to the evaporator, whose working fluid is a mixture of ethylene glycol and water;
- *cooling loop*, a suction-type wind tunnel for condenser testing;
- *refrigeration loop*, namely the VCC system, whose working fluid is therefore R-1233zd(E).

According to the ANSI/ISA standard 5.1 [8], the components and the instrumentation are identified by standardized symbols and tags. The tags consist of a series of letters and numbers used to identify the component type and its location in the setup. For instance, the tag PT2001 indicates a pressure transducer located in line section 200X, which, in this case, identifies the heating loop. A complete legend of the abbreviations used for the section lines, the equipment and the instrumentation is reported in Fig. 6.6.

Figure 6.4 shows three-dimensional CAD drawings of the IRIS setup. The heating and the refrigeration loop of the IRIS setup are installed in an isolated room. Within the room, the components are mounted on an aluminium frame, thus realizing a compact layout (Fig. 6.4 (left)). The cooling loop is located outside the room in an L-shaped structure that houses a wind tunnel (Fig. 6.4 (right)). A fan positioned at the exit port sucks in environmental air. The condenser is installed inside the tunnel and connected with the rest of the refrigeration loop located in the cabinet via two hoses. The external structure is designed to protect the components of the wind tunnel and it features several removable panels that provide easy access to components and instrumentation of the loop for maintenance, replacement or to add further measurement sensors to the condenser test section (Fig. 6.4 (right)). Figure 6.5 shows photographs of the IRIS setup.

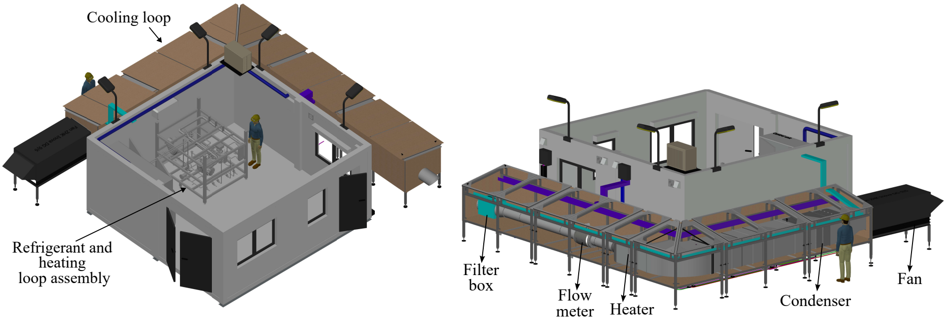

Figure 6.4.: Left: isometric view of the IRIS showing the refrigeration and heating loops within the laboratory room. Right: isometric view of the cooling loop L-shaped wind tunnel.

6.3.1. HEATING LOOP

The heating loop serves as the continuous thermal energy source for the refrigerant within the evaporator (HX0002 in Fig. 6.6). The working fluid is an antifreeze, a mixture of 20% ethylene glycol and 80% water. The fluid is stored in an insulated tank (R2001) in carbon steel and distributed by *Pacetti*. Three offset dividers are installed inside the tank to optimise the thermal distribution of the fluid: the inlet flange is located at the bottom, while the outlet port is at the top of the receiver. The reservoir has a capacity of 300 l, a maximum operating pressure equal to 8 bar(a), and it has a 20 mm thick external cladding in PVC for thermal

Figure 6.5.: Left: photograph of the inside of the IRIS laboratory room. Right: photograph of the cooling loop wind tunnel.

insulation. The hot fluid is circulated by the *Wilo* pump (P2001), whose speed is regulated by an integrated differential pressure controller. Three speed ranges can be manually selected. The pump also features an integrated venting function allowing for the automatic pump liquid discharge. During the warming up of the loop, the three-way mixing valve (MV2001), whose stem position is regulated via a motorized actuator, is fully open in position A-B, thus the glycol-water mixture flows only through the evaporator. Upon returning to the tank, the electric heater (H2001) warms up the fluid until the working fluid temperature at the evaporator inlet reaches a given set-point value. Then, the electric heater is turned off, and the water temperature at the evaporator inlet is kept constant by controlling the glycol-water mass flow rate directed from the tank to the evaporator through the mixing valve. The mixing valve allows for the recirculation of a part of the fluid from the outlet of the evaporator (C) with the hot fluid stream from the tank (A). This allows to regulate the temperature in the evaporator, independently from the heater. The electric heater (H2001) features a series of tubular elements fixed in a flange connection and mounted in a vessel that can be connected to the hoses of the setup. Thereby, the water-glycol blend is heated by direct contact with the heating elements inside the vessel. Thermostats prevent temperature overshoots above 80 °C to protect the heater elements. The device installed in the heating loop has a maximum heating power of 19.5 kW. Finally, to protect the loop from pressure buildup which may be caused by an increase in the water temperature, an expansion receiver (ER2001) is positioned downstream of the tank. The nominal diameter of the hoses of the heating loop is 22 mm, and they are insulated with polyethylene foam sleeves.

Table 6.3 lists further technical information about the models of the components described thus far.

6.3.2. COOLING LOOP

In the cooling loop, air is used to cool down and liquefy the refrigerant flow within the condenser (HX1001 in Fig. 6.6). In the same fashion as a suction-type wind tunnel, the fan (F1001) is located downstream of the test section and it sucks environmental air into the duct. At the tunnel inlet section, there is a box hosting a *systemair* F7 fibreglass filter (AF1001) to keep the incoming air free of any pollutants. The duct has a circular cross-section from the inlet to the location of the electric heater (H1001) such that it can accommodate the flow meter (F1001). Then, a diffuser with an outlet rectangular section is situated upstream of the

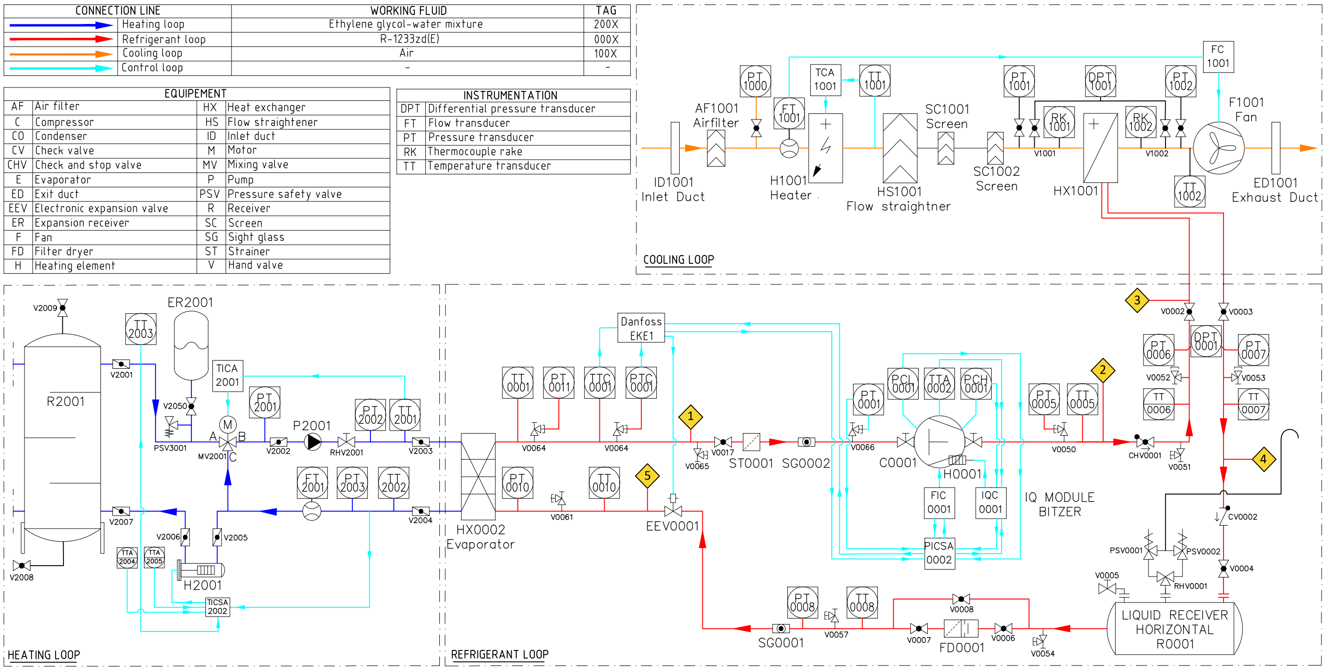

CONNECTION LINE		WORKING FLUID	TAG
🟦	Heating loop	Ethylene glycol-water mixture	200X
🟥	Refrigerant loop	R-1233zd(E)	000X
🟧	Cooling loop	Air	100X
🟦	Control loop	-	-

EQUIPEMENT			
AF	Air filter	HX	Heat exchanger
C	Compressor	HS	Flow straightener
CO	Condenser	ID	Inlet duct
CV	Check valve	M	Motor
CHV	Check and stop valve	MV	Mixing valve
E	Evaporator	P	Pump
ED	Exit duct	PSV	Pressure safety valve
EEV	Electronic expansion valve	R	Receiver
ER	Expansion receiver	SC	Screen
F	Fan	SG	Sight glass
FD	Filter dryer	ST	Strainer
H	Heating element	V	Hand valve

INSTRUMENTATION	
DPT	Differential pressure transducer
FT	Flow transducer
PT	Pressure transducer
RK	Thermocouple rake
TT	Temperature transducer

Figure 6.6.: Piping and Instrumentation Diagram (P&ID) of the IRIS setup.

Table 6.3.: Specifications of the components of the heating loop.

Component	**Tag**	**Model**	**Specifications**
Tank	R2001	*Pacetti* TLR-G2	• capacity 300 l; • max. operating pressure 8 bar; • operating temperature range −10 °C- +65 °C
Mixing valve + actuator	MV2001	*Belimo* H515B + LV24A-SZ-TPC	• 3-way globe valve; • operating temperature range −10 °C- +120 °C
Pump	P2001	*Wilo* Yonos PICO 25/1-8	• fix rotational speed; • max. operating pressure 10 bar; • operating temperature range −10 °C- +95 °C
Electric heater	H2001	*Heating Group International*	• power 19.5 kW 3×100 V; • max. pressure 200 bar(g); • max. operating temperature 80 °C
Expansion receiver	ER2001	*Flamco* Flexcon Premium 18/0.5	• capacity 18 l 3×100 V; • max. pressure 3 bar; • max. operating temperature 120 °C
Pressure safety valve	PSV3001	*Falmco* Prescofiller	• max. operating pressure 3 bar;
Hand valve	V2001-V2007	*Sigeval* FL(w)	• butterfly valve; • max. operating pressure 16 bar; • operating temperature range −40 °C- +210 °C
Hand valve	V2008, V2009	*Comap* V111006001	• ball valve; • max. operating pressure 30 bar; • operating temperature range −5 °C- +90 °C
Hand valve	V2050	*Comap* V111003001	• ball valve; • max. operating pressure 30 bar; • operating temperature range −5 °C- +90 °C

heater (H1001). To comply with the design specifications, the electric air heater (H1001) is installed upstream of the test section to increase the air stream temperature entering the condenser (HX1001) up to a set point value. A flow straightener (HS1001) and two screens (SC1001 and SC1002) will be soon installed upstream of the condenser to promote flow uniformity. To guarantee good reliability of the measurements, the ANSI/ASHRAE Standard 41.2-2022 ANSI/ASHRAE Standard 41.2-2022 [9] prescribes that the length of the duct between the flow straighteners and the test section should be at least equal to the so-called *development length* of five times the hydraulic diameter of the test section. In the cooling loop, the test section is the condenser itself, whose frontal dimensions on the air side are 0.79 m × 0.71 m, thus a distance of approximately 4 m separates the flow straighteners and the condenser. The condenser is currently a microchannel heat exchanger with multilouvered fins on the air side by *KALTRA*. A variable-speed centrifugal fan (F1001) by *euroclima* is situated upstream of the exhaust duct (ED1001). The fan box is equipped with a silencer to reduce the noise during operation. The exit door incorporates movable buffers which open when the setup operations are started and whose position is regulated via a *BELIMO* electric actuator

Table 6.4 lists technical information about the components of the cooling loop.

6.3.3. REFRIGERATION LOOP

The evaporator of the VCC system (HX0002 in Fig. 6.6) is a brazed plate heat exchanger with a countercurrent flow arrangement manufactured by *ALFA LAVAL*. The refrigerant, warmed up by the glycol-water mixture flow, evaporates and reaches a superheated vapour state upstream of the compressor (C0001), currently a semi-hermetic ECOLINE 4HE-18Y-40P reciprocating

Table 6.4.: Specifications of the components of the cooling loop.

Component	**Tag**	**Model**	**Specifications**
Air filter	AF1001	*systemair* BFR 355-400 F7 Filter	• filter class ePM1 50%; • media type Fiber glass
Electric heater	H1001	*systemair* RB100-50/68-4 400V/3	• power 68 kW 3×400 V; • max. operating temperature 50 °C; • operating mass flow rate range $2.7-18$ $\mathrm{m^3 \cdot h^{-1}}$; • min. air velocity 1.5 $\mathrm{m \cdot s^{-1}}$
Condenser	HX1001	*KALTRA* K90172-OEM	• flow arrangement 2-pass; • pressure rating 45 bar
Fan	F1001	*systemair* 22-251-2131/001	• variable rotational speed; • design flow rate 4.30 $\mathrm{m^3 \cdot h^{-1}}$; • motor power 3.65 kW 3×400 V $-$ 50 Hz
Exhaust duct baffles + actuator	ED1001	*systemair* + *BELIMO* LF24-SR	-

compressor manufactured by *Bitzer*. The internal kinematics are lubricated with the BSE55 polyolester oil. The compressor is equipped with an internal oil heater which ensures the oil lubricity even after long standstill periods. The volumetric machine is driven by an electric motor with a maximum input power of 22 kW, and it features an external frequency inverter. The compressor is equipped with an integrated IQ (in-phase/quadrature) module which is used for high-pressure switch, data log, alarm history and Modbus RTU communication. Downstream of the compressor, the superheated refrigerant enters the condenser, where it undergoes the processes of desuperheating, condensation and subcooling due to the effect of the air of the cooling loop. The condensate enters the receiver (R0001), where the refrigerant charge is stored. This component is followed by the filter drier (FD0001) and the sight glass (SG0001). The filter drier is used to trap coarse particulate or any copper shavings and to capture any moisture dissolved in the fluid. The sight glass is an optical access to check whether there are any gas bubbles in the fluid, which would indicate that the refrigerant charge is low. Downstream the receiver, the refrigerant is expanded back to the evaporation pressure by means of the electronic expansion valve EEV0001 Colibri Electric expansion valve ETS 12C from *Danfoss*, equipped with a *Danfoss EKE1* superheat controller. This device regulates the refrigerant charge delivered to the evaporator to maintain the proper superheating degree and to prevent even a small amount of liquid from being ingested by the reciprocating compressor, thus causing its failure. A sight glass (SG0002) is installed upstream of the compressor suction port, providing optical access to this critical section of the loop. Polyethylene foam sleeves cover all the piping for thermal insulation.

Table 6.5 provides additional information about the components of the refrigeration loop.

6.4. INSTRUMENTATION, DATA ACQUISITION AND CONTROL

A data acquisition and control (DAQ&C) system is used to acquire and record data from the sensors and to control the system by delivering appropriate signals to the various actuators. The core of the DAQ&C system is the *National Instrument* (NI) compactRIO (cRIO) 9056 controller, which can accommodate a maximum of eight NI input/output (I/O) modules, handling digital or analog signals. In addition, the Modbus communication protocol is used to exchange data between the DAQ&C system of the facility and the *Danfoss* EKE 1C superheat controller, and the *Bitzer* compressor IQ module. The DAQ&C is connected to a computer via

Table 6.5.: Specifications of the components of the refrigeration loop.

Component	**Tag**	**Model**	**Specifications**
Evaporator	HX0002	*ALFA LAVAL* CB110-20L	• flow arrangement countercurrent; • plate material Alloy 316; • number of passes 1
Compressor	C0001	*Bitzer* Ecoline 4HE-18Y	• displacement 73.7 $m^3 \cdot h^{-1}$; • max. suction pressure 19 bar; • max. discharge pressure 32 bar; • oil type BSE55; • max. motor power 22 kW
Liquid receiver	R0001	*Bitzer* F2002HP	• volume receiver 20 l; • max. pressure 33 bar; • min. temperature -10 °C; • max. temperature 120 °C;
Electric valve	EEV0001	*Danfoss* Colibri ETS 12C	• max. operating pressure 50 bar(g) • inlet refrigerant temperature $-40...70$ °C;
Filter drier	FD0001	*Danfoss* DCR0485	• max. pressure 46 bar; • temperature range $-40...70$ °C; • volume 1.94 l
Sight glass (liquid flow)	SG0001	*AWA* SL15	• max. pressure 120 bar
Sight glass	SG0002	*Danfoss* SGS N type	• max. pressure 52 bar
Strainer	ST0001	*Danfoss* FIA SS65-150	• max. pressure 52 bar
Hand valve	V0002-V0004	*Danfoss* SVA-S SS 20	• butt weld valve; • max. pressure 52 bar; • operating temperature $-60...150$ °C
Hand valve	V0006-V008	*Danfoss* SVA-S SS 15	• butt weld valve; • max. pressure 52 bar; • operating temperature $-60...150$ °C
Hand valve	V0017	*Danfoss* SVA-S SS 65	• butt weld valve; • max. pressure 52 bar; • operating temperature $-60...150$ °C
Check and stop valve	CHV0001	*Danfoss* SCA 20	• butt weld valve; • max. pressure 52 bar; • operating temperature $-60...150$ °C
Check valve	CV0002	*Danfoss* CHV-X SS 20	• butt weld valve; • max. pressure 52 bar; • operating temperature $-60...150$ °C

an Ethernet/IP (Industrial communication Protocol) and runs the *IRIS* LabView program. The software features a graphical user interface allowing the operator to easily control, monitor and record the process variables in real time (Fig. 6.7). Table 6.6 lists the characteristics of the modules hosted in the cRIO-9056 and the hardware connected to each of them.

6.4.1. INSTRUMENTATION

The heating loop is equipped with three temperature and pressure transducers (Fig. 6.6). Each pressure and temperature sensor transmits a $4-20$ mA output signal to the 16-channel 24-bit A/D input modules NI-9208 of the compactRIO (cRIO-9056). The glycol-water volumetric flow rate circulating within the loop is monitored with an electromagnetic flow meter (FT2001 in Fig. 6.6) located downstream of the evaporator (HX0002). The working principle of this transducer relies upon Faraday's law of magnetic induction, i.e., a voltage is induced in a

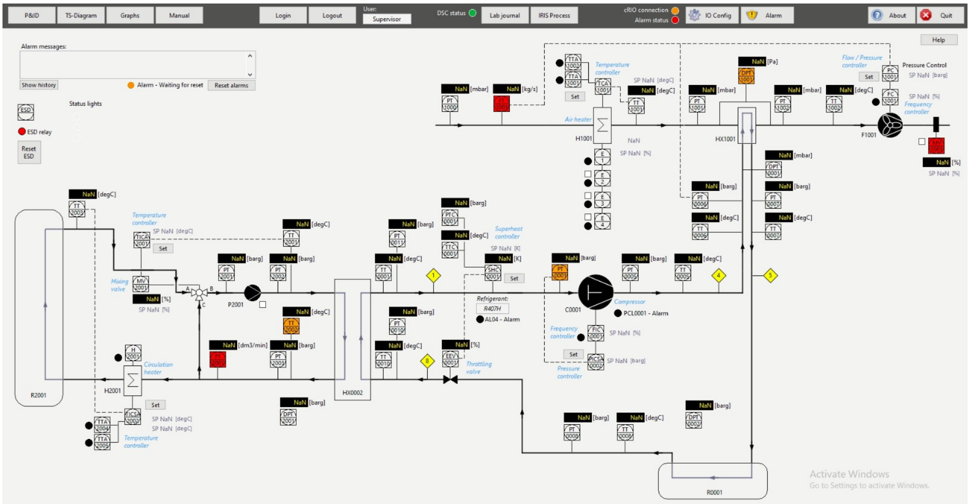

Figure 6.7.: Graphical user interface of the *IRIS* LabView program providing data acquisition and supervisory control functionality to the IRIS setup.

Table 6.6.: Input Output modules currently equipping the NI cRIO-9056 controller.

Model	**Quantity**	**Type**	**Range**	**Channels**	**Description**
Analog					
NI-9208	3	Current input	4 – 20 mA	16	Temperature, pressure and flow transmitters
NI-9264	1	Voltage output	0 – 10 V	16	Compressor frequency control, air heater control, mixing valve control
NI-9202	1	Voltage input	0 – 10 V	16	Differential pressure transducer, mixing valve actuator
Digital					
NI-9375	1	Input/Output	-	32	Alarms, pump enable, air heater enable, water heater enable, fan enable
Thermocouple					
NI-9214	2	Thermocouple type T	-	16	Thermocouple rake

conductor moving through a magnetic field. In this case, the moving conductor is the working fluid. The induced voltage is proportional to the velocity of the fluid and it is amplified by two measuring electrodes. The volumetric flow rate is calculated by multiplying the velocity by the known pipe cross-sectional area. Also in this case, the measured value is transmitted via a 4 – 20 mA output signal to a NI-9208 A/D input module of the cRIO-9056 controller.

The cooling loop is instrumented with three pressure transducers and two temperature transducers (Fig. 6.6). Each pressure and temperature sensor transmits a 4 – 20 mA signal to the NI-9208 module of the compactRIO (cRIO-9056). A differential pressure transducer (DPT1001) monitors the airflow pressure drop across the condenser test section. The air volumetric flow rate is measured and recorded via the ultrasonic flow meter (FT1001). This device is directly connected to a temperature and a pressure sensor, which provide the process measurements needed for the calculation of the corrected volumetric flow rate. All these pieces of equipment provide an 4 – 20 mA signal to the compactRIO controller. Finally, according to the current design of the IRIS setup, in the near future two thermocouple rakes will be installed at the inlet and at the outlet of the condenser test section to measure the airflow temperature distribution. These frames have been designed to accommodate 9 and 20 thermocouples respectively.

The refrigerant loop is equipped with six temperature and pressure transducers, located in the most significant sections of the loop to allow for the system and the components energy balances, i.e., in the proximity of the inlet and the outlet ports of each main component, see Fig. 6.6. A differential pressure transducer (DPT0001) measures the pressure drop of the refrigerant flow across the condenser. All sensors output a 4 – 20 mA signal to the NI-9208 A/D input module of the cRIO-9056 controller.

Table 6.7 lists all the relevant data about the instrumentation installed in the IRIS setup.

Table 6.7.: Specifications of the process sensors equipping the IRIS setup.

Loop	**Property**	**Tag**	**Model**	**Signal**	**Range**	**Accuracy (Type B)**
Heating loop	Temperature	TT2001-TT2003	*WIKA* TR21-B	4 – 20 mA	0…+150 °C	Class A[a] + ±0.25 K[b]
	Pressure	PT2001	*WIKA* S-20	4 – 20 mA	−1…+5 bar(g)	±0.25% of span
	Pressure	PT2002, PT2003	*WIKA* S-20	4 – 20mA	0…+4 bar(g)	±0.25% of span
	Flow rate	FT2001	*Endress+Hauser* Proline Promag W 400	4 – 20 mA	0…75 $dm^3 \cdot min^{-1}$	±0.5%
Cooling loop	Temperature	TT1001, TT1002	*WIKA* TR36	4 – 20 mA	0…+150 °C	Class A + ±0.25 K
	Pressure	PT1000	*WIKA* S-20	4 – 20 mA	−300…+300 mbar(g)	±0.25% of span
	Pressure	PT1001, PT1002	*WIKA* S-20	4 – 20 mA	−500…+500 mbar(g)	±0.25% of span
	Differential pressure	DPT1001	*Siemens* QBM4100-1U	4 – 20 mA	−50…+50 mbar	±3% full scale
	Flow rate	FT1001	*KROHNE* Optisonic 7300	4 – 20 mA	0.4…1.4 $kg \cdot s^{-1}$	±1.5%
	Temperature	-	*KROHNE* Optitemp TRA-P10	4 – 20 mA	0…100 °C	±0.1% of span
	Pressure	-	*KROHNE* Optibar PM 3050	4 – 20 mA	0…0.4 bar	±0.2%
Refrigerant loop	Temperature	TT0001-TT0008	*WIKA* TR21-B	4 – 20 mA	0…+150 °C	Class A + ±0.25 K
	Temperature	TT0010	*WIKA* TR21-B	4 – 20 mA	−10…+150 °C	Class A + ±0.25 K
	Pressure	PT0001, PT0010	*WIKA* S-20	4 – 20 mA	−1…+0.6 bar(g)	±0.25% of span
	Pressure	PT0005, PT0006	*WIKA* S-20	4 – 20 mA	0…6 bar(g)	±0.25% of span
	Pressure	PT0007, PT0008	*WIKA* S-20	4 – 20 mA	0…4 bar(g)	±0.25% of span
	Differential pressure	DPT0001	*WIKA* DPT-20	4 – 20 mA	−500…+500 mbar	±0.25% of span

---

[a] Tolerance value of the measuring element according to IEC 60751, as documented in the WIKA sensor datasheet.

[b] Measuring deviation of the transmitter per IEC 62828, as documented in the WIKA sensor data sheet.

6.4.2. CONTROL STRATEGY

To ensure the correct and safe functionality of the IRIS setup during the start-up, operation and shut-down procedures, six control loops have been implemented (Fig. 6.6).

The refrigerant loop is controlled by two loops, i.e., the superheat controller (SHC0001) and the pressure controller (PICSA0002). The SHC0001 control loop sets the superheating degree at the evaporator outlet to prevent any liquid droplet from reaching the compressor suction port. This is achieved by regulating the opening of the EEV0001 valve. The controller hardware includes: i) a pressure sensor (PTC0001) to measure the evaporation pressure, ii) a temperature sensor (TIC0001) to monitor the refrigerant temperature at the evaporator outlet,

iii) the expansion valve (EEV0001), iv) the *Danfoss* EKE 1C controller, v) a *Danfoss* EKE 2U power supply for backup purposes. Figure 6.8 shows a picture of these components. A control algorithm is programmed in the firmware of the *Danfoss* EKE 1C controller, where both the temperature and the pressure sensors are directly wired. The EKE 1C unit determines the value of the superheating degree as a difference between the temperature measured at the outlet of the heat exchanger and the saturation temperature at the evaporation pressure. The controller regulates the opening of the EEV0001 expansion valve to match the calculated degree of superheating with a given set point value. During the commissioning of the setup, this controller has been configured to automatically calculate the minimum stable set point of the superheating degree within an operating range provided by the operator.

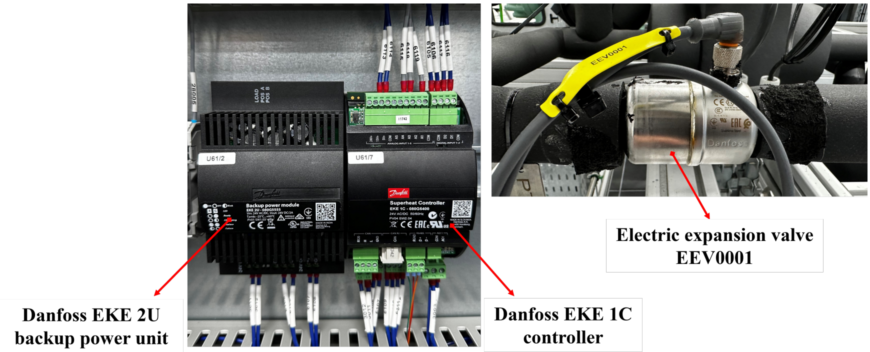

Figure 6.8.: Main components of the superheating control system (SHC0001 in Fig. 6.6): *Danfoss* electric expansion valve (EEV0001), EKE 1C *Danfoss* superheat controller, and *Danfoss* EKE 2U back-up power unit.

The PICSA0002 control loop sets the compressor suction pressure (PT0001) by varying the rotational speed of the compressor via the *Bitzer* Varypack frequency inverter (FIC0001). The control algorithm, a proportional–integral–derivative (PID) feedback, is implemented cRIO-9056. The purpose of this control loop is to prevent subatmospheric inlet conditions, which can cause damage to the compressor components. In the event that the pressure at the compressor inlet is too low during operation, a low-pressure switch (PCL0001) is triggered, causing an immediate shut-down of the loop. Additionally, the compressor IQ module is connected to a high-pressure switch (PCH0001) to protect the compressor from any pressure overshoot. Figure 6.9 shows a photograph of the compressor with its control system.

In the cooling loop, the TCA1001 control loop regulates the airflow temperature entering the condenser (TT1001). This control algorithm is implemented in the cRIO-9056 and it is based on a PID logic. The heater (H1001) is composed of four heating elements with a power capacity of 17 kW each. During operation, the heating power of the first element can be regulated, while the other three can only be turned on or off. The cooling loop includes also an air flow rate controller, directly implemented in the cRIO-9056 using a PID feedback mechanism. This control system regulates the fan (FC1001) rotational speed to tune the air mass flow rate to a specific set point value.

In the heating loop, there are two temperature control systems, namely, TICSA2002 and TICA2001. The TICSA2002 control loop is implemented in the cRIO-9056, and it is based on an on/off control logic. If the temperature TT2003 falls below a set point value, the heater turns on. The controller TICA2001, integrated into the cRIO-9056, leverages a PID control logic and it is active only during the operation of the refrigerant loop. The goal is to keep the

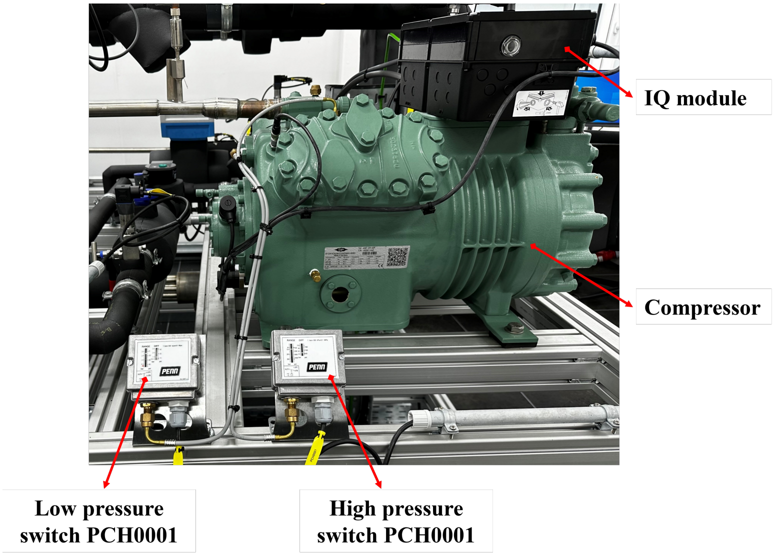

Figure 6.9.: The *Bitzer* ECOLINE reciprocating compressor equipped with the IQ module, the low-pressure switch (PCL0001), and the high-pressure switch (PCH0001).

glycol-water temperature at the evaporator inlet constant by regulating the opening of the MV2001 three-way mixing valve. During start-up, the valve operates in position A-B, and the working fluid flows from the receiver to the evaporator. During operation, to keep the glycol-water temperature constant at the evaporator inlet, a part of the colder fluid from the evaporator outlet is recirculated into the port C of the valve to be mixed with the hot fluid from the tank. The valve opening is regulated based on the offset between the set point and the process value of the temperature TT2001.

6.4.3. SAFETY INTERLOCKS

In addition to the control loops, other process variables are monitored and can trigger warnings, alarms or emergency shutdowns, depending on the event severity. Table 6.8 lists alarm controls programmed for each loop of the IRIS setup.

When a warning occurs, the operator is notified through the GUI of the IRIS LabView program. The process variable associated with the warning is highlighted in orange. If instead an alarm is triggered, the process variable is displayed in red. Moreover, during operation, the GUI provides a list of all the triggers to enable at-a-glance inspection.

In addition, a traffic light mounted on the outside of the electric cabinet within the lab room (see Fig. 6.5) and always visible to the operators notifies them about the system status. The green light indicates that the loops are not in operation while the IRIS software is running and the control cabinet is powered. The yellow light means that both the heating and cooling loops are in operation, while the refrigerant loop is not active yet. The red light pinpoints that either the compressor is enabled or the shutdown procedure has been triggered. In case of an emergency, the operator can manually shut down the setup using the Emergency Shutdown (ESD) button mounted on the frame of the refrigerant loop (see Fig. 6.5).

Table 6.8.: Alarms and warnings. The event severity is classified as high-high (HH), high (H), low (L), low-low (LL).

Heating loop					
Tag	**Description**	**Value and Action**			
		HH	H	L	LL
TTA2004	Heater H2001 overheating	xxx, shutdown + alarm	-	-	-
TTA2005	Heater H2001 overheating	xxx, shutdown + alarm	-	-	-
PTA2002	Pressure downstream pump P2001	2.9 bar(g), shutdown + alarm	-	-	0.2 bar(g), shutdown + alarm
DPT2001	Pressure drop evaporator HX0001	-	20 kPa, warning	-	-
FT2001	Glycol-water flow rate	-	-	-	0.2 $dm^3 \cdot min^{-1}$, shutdown + alarm

Cooling loop					
Tag	**Description**	**Value and Action**			
		HH	H	L	LL
DPTA1001	Pressure drop condenser HX0002	-	5 Pa, warning	-	-
TCA1001	Heater H1001 temperature	50 °C, shutdown + alarm	-	5 °C, warning	-
TTA1002	Heater H1001 overheating	50 °C, shutdown + alarm	-	-	-
FT1001	Mass flow rate in FT1001	-	-	-	0.8 $kg \cdot s^{-1}$, shutdown + alarm
MV1001	Baffles opening	-	-	-	70%, shutdown + alarm

Refrigerant loop					
Tag	**Description**	**Value and Action**			
		HH	H	L	LL
PCL0001	Compressor low pressure switch	1	-	-	-
PTA0005	Compressor high pressure	8 bar(g), shutdown + alarm	-	-	-
PTA0001	Evaporator pressure	-	-	-	−0.1 bar(g), shutdown + alarm

6.5. COMMISSIONING

Before the refrigerant was charged, a pressure and leakage test was successfully performed following the guidelines of the DIN EN 378-2 [10] standard. This safety procedure is used to prove the leak tightness of the components. The test is performed using dry nitrogen, an odourless and inert gas. An electronic device is used to detect any gas leakage. The low-pressure and the high-pressure lines are tested separately with a maximum pressure of 8 bar and 15 bar, respectively. For each test, the loop hoses were filled in with nitrogen, and the pressure was increased to the prescribed test value and kept constant for 15 minutes. After the successful completion of the leakage test, the refrigerant loop was filled with 6.7 kg of R-1233zd(E). Approximately 300 l of 20% ethylene-glycol and water solution were charged into the tank of the heating loop.

The IRIS setup was successfully commissioned to ensure the correct installation and operation of all the hardware of the system. The process variables were recorded until the steady-state operating conditions were reached. The results were compared with the requirements and specifications defined during the design phase.

6.5.1. SEQUENCE OF OPERATION

An automated procedure has been implemented in the *IRIS* LabView program to control the start-up, operation and shut-down phases of the facility. The activation of the refrigerant loop is only possible if the heating and cooling loops have reached their prescribed operating conditions. The initial phase of the start-up process of the facility, thus, involves a series of steps to put in operation the heating and the cooling loops.

In the start-up sequence of the heating loop, the P2001 pump (refer to Fig. 6.6 for tags and location of the devices) is turned on first to enable the circulation of the glycol-water mixture. Then, the H2001 electric heater is activated and the control TICSA2002 loop is initiated. The procedure ends once the set point temperature at the evaporator inlet (TT2001) is reached. At the same time, the operation of the cooling loop is initiated. First, the baffles installed at the outlet section of the wind tunnel are opened. Then, the F1001 fan is switched on and its speed control (FC1001) is activated until the air flow rate reaches the set point value. Finally, the air temperature controller (TCA1001) is activated and the electric H1001 heater warms up the airflow. The procedure ends when the air temperature at the condenser inlet (TT1001) is equal to the desired value.

Once the start-up procedures of both the heating and the cooling loop are terminated, the refrigerant loop is activated. To allow for a safe operation of the compressor, the superheat controller (SHC0001) is enabled and the compressor starts operating only once the refrigerant pressure in the loop is above a set point value of 0.25 bar(g). When this condition is achieved, the PICSA0002 pressure controller is activated and the FIC0001 frequency inverter regulates the inlet pressure of the compressor to match the design value. The SHC0001 superheat control system remains active throughout the operation. While the refrigerant loop is running, the TICA2001 temperature controller of the heating loop is activated to maintain the TT2001 temperature constant and equal to the design set point value.

The shut-down procedure is essentially the reverse of the start-up procedure. Initially, the procedure to turn off the refrigerant loop is performed. First, the compressor is gradually slowed down. Then, all the controllers of the loop are disabled. Thereafter, the termination sequences of the heating loop and the cooling loop take place simultaneously. First, the heating sources and the associated controllers are switched off. Following a fixed cooldown interval, the flow rate is interrupted by switching off both the P2001 pump and the FC1001 fan.

6.5.2. RESULTS

The commissioning of the setup was executed with the primary objective of ensuring that the design specifications of the refrigerant loop were met. More specifically, the objective was to verify that the system achieves the design cooling capacity when operating at the design values of evaporation and condensation pressure and temperature (Tab. 6.2). Preliminary tests were conducted in advance to test the hardware, the software and the alarm system.

The heating loop pump (P2001) operates at a constant rotational speed, thus the glycol-water volumetric flow rate is constant and equal to 1.44 $\mathrm{m^3 \cdot h^{-1}}$ (Fig. 6.10). This value is higher than the design value (1.3 $\mathrm{m^3 \cdot h^{-1}}$) due to the lower pressure drops in the heating loop. As the rotational speed of the P2001 pump cannot be adapted, the setpoint value of the glycol-water temperature at the evaporator (HX0002) inlet has been reduced with respect to the design conditions to account for the higher glycol-water mass flow rate and achieve the targeted cooling capacity of the refrigeration loop.

Figure 6.11 shows the variation over time of temperature values related to the glycol-water flow, along with the refrigerant temperature upstream and downstream of the evaporator. If the TICSA2002 control (refer to Fig. 6.6) is active, the heater turns off automatically once the TT2003 set point value is reached. However, preliminary tests revealed that after some time,

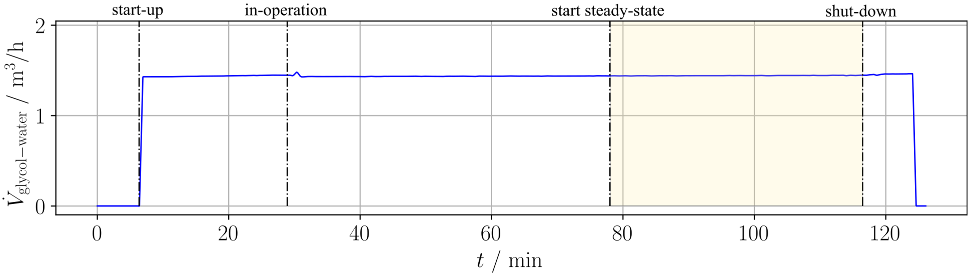

Figure 6.10.: Recording of the FT2001 volumetric flow rate of glycol-water mixture over time, see Fig. 6.6. The time interval highlighted with the shaded band indicates the period in which the process can be considered at steady-state.

during steady-state operation, the TT2003 temperature rapidly decreases. Although the heater turns on again, due to the high thermal inertia of water inside the tank, the rise of the TT2003 temperature is rather slow. Consequently, some time is needed to restore the desired operating conditions of the setup. To avoid this situation during the commissioning, in the TICSA2002 control, the set point of the TT2003 temperature was maintained sufficiently high such that the H2001 heater was kept active throughout the entire test duration to avoid any abrupt decrease in the temperature at the outlet of the tank (TT2003).

During the start-up phase, the temperature of the glycol-water mixture increases linearly in all the different loop sections. Once the TT2003 temperature reaches the set point value of 49 °C, the refrigerant loop starts operating since, in the cooling loop, the process variables have already reached steady-state conditions (Fig. 6.14). After $t = 29$ min from the beginning of the test, the compressor turns on and the refrigerant starts circulating within the evaporator and absorbing thermal energy from the glycol-water flow, therefore the inlet and outlet temperatures (TT22001 and TT2002) rapidly drop. From the moment the compressor starts operating, the TICA2001 controller is activated, and the MV2001 valve opening is regulated to achieve the TT2001 set point temperature of 40.8 °C. The TT2001 set point was lowered with respect to the design value of 45 °C. This is because, as previously discussed, the glycol-water volumetric flow rate in the loop is slightly higher than assumed in the preliminary design phase of the setup. Therefore, a lower inlet temperature is required to maintain the evaporation temperature of the refrigerant in the evaporator close to the design point.

Figure 6.12 reports the recording of the mixing valve opening over time. As explained before, the heater was kept on throughout the experiment. As a consequence, the TT2003 temperature upstream of the valve increases during the test. Since the volumetric flow rate of glycol-water circulating in the loop is constant, the valve opening increases linearly to recirculate a larger amount of water from C to B, thus maintaining the TT2002 temperature close to the set point value. However, the PID control causes oscillations in the valve regulation, which are propagated to all the temperature trends.

The temperature of the refrigerant entering the evaporator (TT0010) did not undergo significant variations during the test, and its mean value is equal to 22.6 °C. The temperature at the outlet (TT0001) is regulated by the EEV0001 controller, which sets the optimal superheating degree, whose mean value is 4 K. Figure 6.13 shows the recording over time of the superheating degree at the evaporator outlet, together with the percentage opening of the EEV001 electric valve. These variables are critical for the safe operation of the compressor and, hence of the system. When the refrigeration loop starts operating, the EEV0001 valve opens by a small fraction, thus allowing for a high degree of superheating to protect the

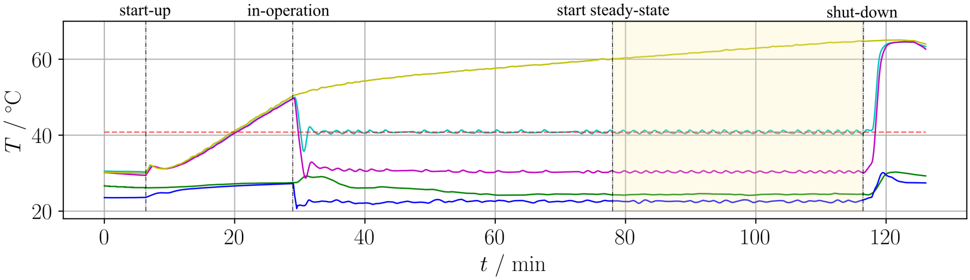

Figure 6.11.: Temporal recordings of temperature values related to the heating loop and refrigerant loop, see Fig.6.6. Heating loop: TT2003(—), TT2001 (—), and TT2002 (—). Refrigerant loop: TT0010 (—), and TT0001 (—). The set point value of the TICA2001 controller is also indicated (- -). The time interval highlighted with the shaded band indicates the period in which the process in the refrigerant loop can be considered at steady-state.

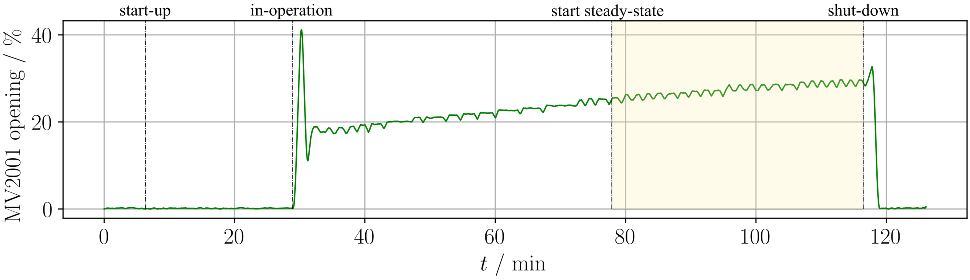

Figure 6.12.: MV2001 mixing valve percentage opening over time (refrigerant loop, see Fig. 6.6).

compressor. During operation, the valve opening and consequently the flow rate through the evaporator increase, while the superheating degree decreases until it stabilizes around a mean value which allows for the safe and optimal operation of the compressor at the given suction pressure. When this condition occurs, after about $t = 78$ min from the start of the test, the process in the refrigerant loop can be considered steady-state according to the criteria by [11]: the percentage variation of all the monitored variables of the refrigerant loop remains within ±0.4% of their mean value.

During the steady-state operation, the average pressure drop of the refrigerant and the water-glycol flow within the evaporator are equal to 1.4 kPa and 5.1 kPa, respectively. The IRIS setup was kept running in steady-state conditions for approximately 38 min. Then the compressor was shut down, together with the H2001 heater. Once both the compressor and the heater are turned off, the temperatures in the heating loop rapidly increase, then, once also the pump is turned off, all temperature values reach a steady condition and afterwards they slowly decrease due to passive cooling.

Figure 6.14 shows the variation over time of the temperatures of the airflow and the refrigerant upstream and downstream of the condenser. Once the start-up phase of the refrigerant loop is initiated, the F1001 fan is activated. Then, the H1001 heater is turned on and the TCA1001 control loop is activated. The temperature of the air entering the condenser (TT1001) is regulated to keep its set point value of 38 °C. At the same time, the FC1001 flow

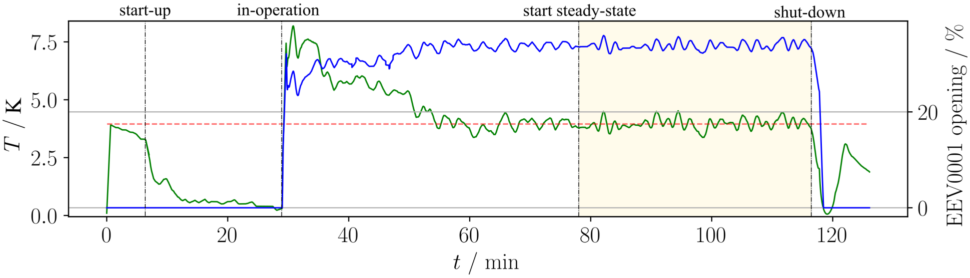

Figure 6.13.: Superheating degree (measured in T0001 compared to the saturation temperature at the PT0001 pressure level) as a function of time (—), see Fig. 6.6. The average value of the superheating degree during steady-state operation (- -) is also indicated. Corresponding percentage opening of the EEV0001 valve during the test (—). The time interval highlighted with the shaded band indicates the period in which the process in the refrigerant loop can be considered at steady-state.

control regulates the fan speed to maintain an air mass flow rate equal to the setpoint value of 1.13 $\mathrm{kg \cdot s^{-1}}$ (Fig. 6.15).

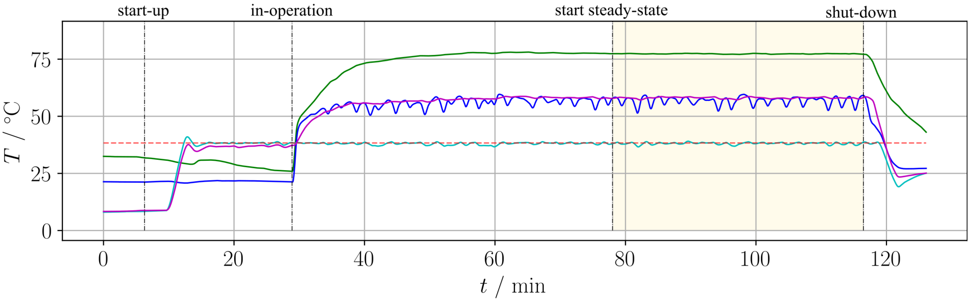

Figure 6.14.: Temporal recordings of temperature values related to the cooling loop and the refrigerant loop, see Fig. 6.6. Cooling loop: TT1001 (—), and TT1002 (—). Refrigerant loop: TT0006 (—) and TT0007 (—). The set point value of the TCA1001 controller is also indicated (- -). The time interval highlighted with the shaded band indicates the period in which the process in the refrigerant loop can be considered at steady-state.

During preliminary tests, it was observed that it was not possible to heat the inlet air temperature up to the design value of 40 °C when the environmental temperature was too low. These tests were performed during winter, and the environmental air temperature was equal to 9 °C. In this condition, the H1001 electric heater underwent overheating, causing a critical alarm to go off and the immediate shutdown of the loop. Therefore, during the commissioning test, the set point value of TT1001 was lowered to 38 °C. As a consequence, in order to obtain the design condensation pressure of 3.48 bar(g), the condenser cooling air mass flow rate was reduced to 1.13 $\mathrm{kg \cdot s^{-1}}$ with respect to the design value of 1.40 $\mathrm{kg \cdot s^{-1}}$. The average air temperature downstream of the condenser (TT1002) during steady-state was 58 °C. The recorded values of the airflow temperature oscillate over time. Oscillations are more pronounced downstream of the condenser (TT1002) since the sensor is mounted closer

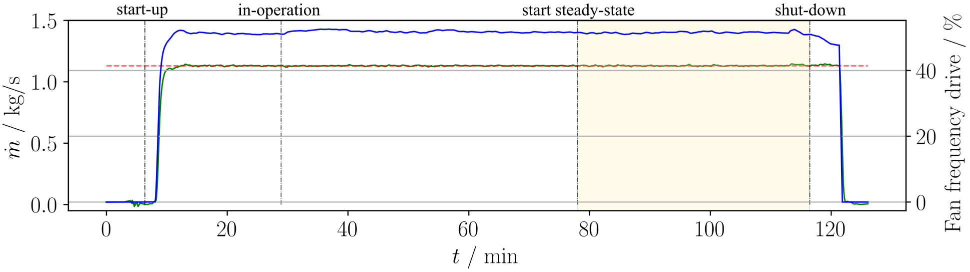

Figure 6.15.: Recording of the FT1001 mass flow rate of air over time (—), see Fig. 6.6. The set point value of the FC1001 controller is also indicated (- -). Corresponding adjustable-frequency drive of the FC1001 fan during the test (—). The time interval highlighted with the shaded band indicates the period in which the process in the refrigerant loop can be considered at steady-state.

to the heat exchanger outlet section, where the temperature gradients are larger. Despite the oscillations are within acceptable limits, the control system could be improved by regulating the inlet temperature of the airflow to achieve the desired condensation pressure. In this way, the air inlet temperature set point (TT1001) must not be repeatedly tuned by the operator to reach the desired condensation pressure, thus allowing for a more stable operation of the setup.

In any case, the refrigerant temperatures upstream (TT0006) and downstream (TT0007) of the condenser do not oscillate during steady-state operation. Their mean values are equal to 77 °C and 56 °C, respectively. The pressure drops across the condenser hot and cold streams recorded during steady-state operation are 0.46 bar on the refrigerant side, and 102 Pa on the air side. Once the shut-down process starts, first the heater is turned off and the fan keeps operating for a few minutes to allow for a rapid cooling of the components.

Figure 6.16 reports the temporal recording of the refrigerant pressure upstream (PT0001) and downstream (PT0005) of the compressor during the commissioning test. As soon as the compressor turns on, the FIC0001 control is activated and it regulates the compressor rotational speed to meet the suction pressure set point value of 0.08 bar(g). Downstream of the compressor, the flow pressure reaches a steady state value of 3.7 bar(g). The design condensation pressure of 3.48 bar(g) is achieved at the inlet of the condenser (PT0006) to account for the pressure losses occurring within the hose connecting the compressor outlet and the condenser. At the shut-down time, the compressor is the first component to be turned off, and the pressure of the refrigerant within the loop rapidly decreases.

6.6. Nominal system performance and uncertainty quantification

The analysis of Type A uncertainty [12] associated with the measurements of process variables was not performed because the signals are affected by oscillations and repeatability measurements were not performed, therefore it was not possible to perform statistical analysis on the data. Only Type B uncertainty associated with the manufacturer-certified accuracy of the sensors was therefore considered. These values are reported in Tab. 6.7.

The thermodynamic performance of a refrigeration system is expressed in terms of coefficient of performance (COP), defined as the ratio between the VCC system cooling power

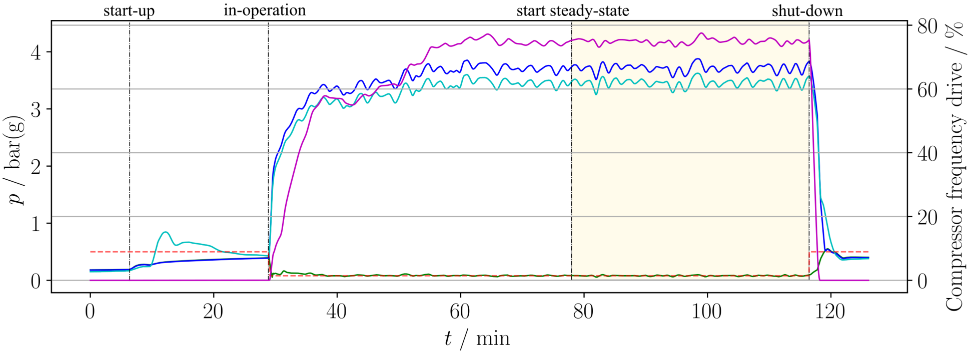

Figure 6.16.: Temporal recordings of pressure values related to the refrigerant loop: PT0001(—), PT0005 (—), and PT0006 (—), see Fig. 6.6. The set point value of the PICSA0002 controller is also indicated (- -). Percentage regulation of the C0001 compressor frequency drive via the FIC0001 controller during the test(—). The time interval highlighted with the shaded band indicates the period in which the process in the refrigerant loop can be considered at steady-state.

and the power demand of the compressor, namely

$$\mathrm{COP} = \frac{\dot{Q}_{\mathrm{eva}}}{\dot{W}_{\mathrm{compr}}}. \tag{6.1}$$

Since the IRIS setup is not equipped with a transducer to measure the refrigerant mass flow rate, the heat duty of both the evaporator and the condenser can be determined from the steady-state energy balance applied to the water-glycol, thus

$$\dot{Q}_{\mathrm{eva}} = \rho_{\mathrm{g-w}} \dot{V}_{\mathrm{g-w}} c_{p_{\mathrm{g-w}}} (T_{2001} - T_{2002}), \tag{6.2}$$

and to the airflow stream, which reads

$$\dot{Q}_{\mathrm{cond}} = \rho_{\mathrm{a}} \dot{V}_{\mathrm{a}} c_{p_{\mathrm{a}}} (T_{1002} - T_{1001}). \tag{6.3}$$

The density of the fluid (ρ) and the isobaric heat capacity (c_p) are calculated with a validated program for the estimation of thermophysical properties of fluids [7]. Hence, the value estimated for the evaporator cooling duty is equal to 17.88 ± 0.8 kW, while that of the condenser heat duty is 22.50 ± 0.25 kW.
The refrigerant mass flow rate can be estimated as

$$\dot{m}_{\mathrm{refr}} = \frac{\dot{Q}_{\mathrm{cond}}}{\Delta h_{\mathrm{cond}}} \tag{6.4}$$

where the specific enthalpy of condensation Δh_{cond} is the difference between the specific enthalpy values calculated with a computer program [7] using as input the pressure and pressure values measured for state points 3 and 4, therefore upstream and downstream of the condenser (see Fig. 6.6). The average value of refrigerant mass flow rate estimated during the steady-state operation of the setup is equal to 0.12 $\mathrm{kg \cdot s^{-1}}$, thus 12% higher than the design value (see Tab. 6.2).

The mechanical power transferred to the fluid by the compressor rotor is calculated as

$$\dot{W}_{\text{compr}} = \dot{m}_{\text{refr}} \Delta h_{\text{compr}}, \tag{6.5}$$

where Δh_{compr} is the specific enthalpy difference across the discharge and suction ports of the compressor, calculated using a well-known computer programme [7] given the temperature and pressure of the state points 2 and 1 (see Fig. 6.6). The compressor power is estimated to be equal to 4.75 ± 1 kW. Therefore, the estimated coefficient of performance is $\text{COP} = 3.76 \pm 0.48$.

The uncertainty associated with the variables involved in the estimation of the COP, which are a function of measured quantities, was calculated by means of the law of error propagation [12], assuming a 95% confidence interval. In particular, assuming constant values of density and heat capacity, the uncertainty associated with the evaporator and the condenser duty includes only the contribution of the uncertainty of the temperature and the volumetric flow rate measurements. Under the assumption that the process variables measured by the sensors are unrelated, the uncertainty $u(\dot{Q})$ is given by,

$$u(\dot{Q}) = \sqrt{\left(\frac{\partial \dot{Q}}{\partial \dot{V}} u(\dot{V})\right)^2 + \left(\frac{\partial \dot{Q}}{\partial T} u(T)\right)^2}. \tag{6.6}$$

The compressor power was estimated from the energy balance associated with the refrigeration cycle as $\dot{W}_{\text{compr}} = \dot{Q}_{\text{eva}} - \dot{Q}_{\text{cond}}$. Therefore, its overall uncertainty $u(\dot{W}_{\text{compr}})$ depends only on the uncertainties associated with the heat duty of the evaporator $u(\dot{Q}_{\text{eva}})$ and the condenser $u(\dot{Q}_{\text{cond}})$ and is therefore given by

$$u(\dot{W}_{\text{compr}}) = \sqrt{\left(\frac{\partial \dot{W}_{\text{compr}}}{\partial \dot{Q}_{\text{eva}}} u(\dot{Q}_{\text{eva}})\right)^2 + \left(\frac{\partial \dot{W}_{\text{compr}}}{\partial \dot{Q}_{\text{cond}}} u(\dot{Q}_{\text{cond}})\right)^2}. \tag{6.7}$$

Hence, according to the definition of COP (in Eq. 6.1), the uncertainty of the system COP can be obtained as

$$u(\text{COP}) = \sqrt{\left(\frac{\partial \text{COP}}{\partial \dot{Q}_{\text{eva}}} u(\dot{Q}_{\text{eva}})\right)^2 + \left(\frac{\partial \text{COP}}{\partial \dot{W}_{\text{compr}}} u(\dot{W}_{\text{compr}})\right)^2}. \tag{6.8}$$

Table 6.9 lists the mean values of temperature and pressure of each state point of the refrigerant loop obtained from signals acquired during steady-state operation at nominal conditions. The values are compared to design values. Figure 6.17 shows the T–s diagrams of the working fluid indicating the thermodynamic cycle associated with the processes occurring in the IRIS setup. The temperature and entropy values are estimated starting from the process variables measured during the commissioning. The chart also shows the same thermodynamic cycle calculated with design values. The comparison shows that i) the system can operate at temperature levels which are very close to the temperatures calculated with design values, ii) the measured pressure drops are larger than those estimated with design values, especially for the condenser for which the measured refrigerant pressure drop is 15 times larger than what was estimated with design calculations, iii) the pressure drop associated with the hose connecting the compressor outlet to the condenser was neglected, while its measured value is 0.25 bar. Such pressure drop negatively impacts the compressor power consumption, which is larger as the compressor is controlled so as to comply with the design value of the condensation pressure. At steady-state, the evaporator cooling duty is larger than its design value, therefore the measured COP of the refrigerant cycle of the IRIS setup is 4% higher than the design value.

Table 6.9.: Comparison between temperature and pressure values of the main state points of the refrigerant cycle of the IRIS setup measured during commissioning at nominal conditions and the corresponding design values. The numbering of the state points refers to those indicated in the P&ID of Fig. 6.6.

	Design values		**Measured values**	
State point	***T* / °C**	***p* / bar**	***T* / °C**	***p* / bar**
1	25	1.08	24.4	1.09
2	80.18	4.48	79.5	4.70
3	80.18	4.48	77.3	4.45
4	60.76	4.45	56.8	4.0
5	20	1.08	22.6	1.15

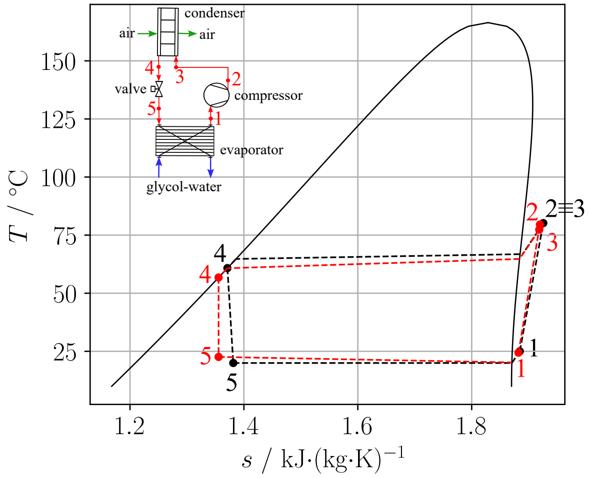

Figure 6.17.: Representation in the T-s diagram of R-1233zd(E) of the processes occurring in the refrigerant loop of the IRIS setup. Temperature and entropy values estimated from the process variables measured during the commissioning (- -), and calculated with the design values (- -). The thermodynamic states numbering refers to the P&ID in Fig. 6.6.

6.7. CONCLUSIONS AND FUTURE WORK

This chapter documents the design and the commissioning of the IRIS setup. The purpose of this facility is to test the performance of Vapour Compression Cycle systems and its main components for the aircraft Environmental Control System. The experiments aim to provide data for developing novel design guidelines for such a system under different aircraft operating conditions and to validate the *in-house* numerical models developed for the system and components simulations and design optimization. A single balance of plant realizes a single-stage compression refrigeration cycle incorporating two test sections: one for the volumetric compressor and another for the air-cooled condenser. The design working fluid is R-1233zd(E). The design cooling capacity of the system is 15.5 kW. The facility was successfully commissioned. The hardware and the control system were tested by starting, reaching nominal operating conditions and shutting down the setup. Data of the process flow variables in each loop of the setup were recorded during all the procedures. The facility was operated at steady-state nominal conditions for about 40 min, proving that the IRIS can stably operate at specified conditions. The average values of inlet temperature and pressure at the compressor suction port are equal to 22.6 °C and 0.08 bar(g), respectively. The mean value of condensation pressure is 3.48 bar(g). The system cooling capacity is slightly larger than the design value and it is equal to 17.88 ± 0.8 kW. This positively affects the estimation of the COP which is 4% higher than its design value.

Future experimental tests are planned to evaluate the operation and performance of the IRIS setup at off-design conditions. In particular, the evaporator and the condensation pressure of the refrigerant loop can be adjusted by varying the operating conditions of the heating and cooling loops. These tests will also allow to characterize the volumetric compressor efficiency at various compression ratios and refrigerant mass flow rates. Additionally, the condenser test section equipment is going to be completed with the installation of thermocouple rakes. The condenser performance will be characterized in terms of heat transfer coefficient and pressure drop, by varying the inlet thermodynamic conditions, and the mass flow rate of both the refrigerant and the air stream.

In the near future, the IRIS setup will be employed to test innovative high-speed oil-free centrifugal compressors running on gas bearings. The plan is to modify the existing design of the setup to accommodate the turbomachinery supplied by Aeronamic and test its performance under different operating conditions. The Propulsion & Power group is also developping *in-house* models for centrifugal compressor design that include fluid-dynamic and rotor-dynamic aspects in an automated framework. The ambition is to design and manufacture a prototype of the turbomachinery and test it in the IRIS setup. The testing activity will support the improvement of the numerical tools and their validation. To enable future research activities, modifications and revisions to the current design of the IRIS setup will be necessary. Particular attention should be given to the risk of surge for the compressor, especially during the start-up of the refrigerant loop. The pressure oscillations were recorded during this phase before the system reached steady-state conditions. Therefore, an anti-surge control must be included in the system, and the development of a dynamic model of the IRIS setup could be beneficial to correctly predict the system dynamic behaviour and design the control loops correctly. Envisaged experiments may include the replacement of the design refrigerant of the IRIS with another fluid. However, it is recommended to carefully review the compatibility with the installed components and the material of their sealing. The future version of the IRIS setup would significantly contribute to research on centrifugal compressors and their performance analysis for the aerospace sector and eventually for domestic heat pump applications.

NOMENCLATURE

Acronyms

ACM	Air Cycle Machine
BoP	Balance of Plant
COP	Coefficient Of Performance
DAQ&C	Data Acquisition and Control
ECS	Environmental Control System
GWP	Global Warming Potential
HCFO	Hydroclorofluoroolefins
HFC	Hydrofluorocarbons
IRIS	Inverse organic Rankine cycle Integrated System
MEA	More Electric Aircraft
NBP	Normal Boiling Point [K]
ODP	Ozone Depletion Potential
PID	Proportional–Integral–Derivative
P&ID	Piping and Instrumentation Diagram
PLC	Programmable Logic Controller
R-1233zd(E)	trans-1-Chloro-3,3,3-trifluoropropene
VCC	Vapour Compression Cycle

Roman letters

c_p	Specific heat at constant pressure [$\mathrm{J \cdot (kg \cdot K)^{-1}}$]
h	Specific enthalpy [$\mathrm{J \cdot kg^{-1}}$]
M	Molar mass [$\mathrm{g \cdot mol^{-1}}$]
N	Molecular complexity [-]
$\dot{m}$	Mass flow rate [$\mathrm{kg \cdot s^{-1}}$]
p	Pressure [Pa]
$\dot{Q}$	Thermal power [W]
s	Entropy [$\mathrm{J/(kg \cdot K)^{-1}}$]
T	Temperature [K]
$\dot{u}$	Uncertainty
$\dot{V}$	Volumetric flow rate [$\mathrm{m^3 \cdot s^{-1}}$]
$\dot{W}$	Mechanical power [W]
x	Vapour quality [-]

Greek letters

ρ	Density [$\mathrm{kg \cdot m^{-3}}$]

Superscripts and subscripts

a	Airflow
c	Critical thermodynamic point
compr	Compressor
cond	Condenser
eva	Evaporator
g-w	Glycol-water flow
refr	Refrigerant
v	Saturated vapour

REFERENCES

[1] H. Zhao, Y. Hou, Y. Zhu, L. Chen, and S. Chen. “Experimental study on the performance of an aircraft environmental control system”. In: *Applied Thermal Engineering* 29.16 (Nov. 2009), pp. 3284–3288. ISSN: 1359-4311. DOI: 10.1016/J.APPLTHERMALENG.2009.05.002.

[2] S. H. Chowdhury, F. Ali, and I. K. Jennions. “Development of a Novel Ground Test Facility for Aircraft Environmental Control System”. In: *Journal of Thermal Science and Engineering Applications* 15.8 (June 2023). ISSN: 1948-5085. DOI: 10.1115/1.4062553.

[3] E. Tayfun, C. Fethiye, C. Aykut, O. Recep, and S. Mustafa Fazil. “Experimental and numerical investigation of a compact vapor compression refrigeration system for cooling avionics in harsh environment”. In: *Applied Thermal Engineering* (Sept. 2023), p. 121663. ISSN: 1359-4311. DOI: 10.1016/J.APPLTHERMALENG.2023.121663.

[4] S. Mancin, C. Zilio, G. Righetti, and L. Rossetto. “Mini Vapor Cycle System for high density electronic cooling applications”. In: *International Journal of Refrigeration* 36.4 (June 2013), pp. 1191–1202. ISSN: 0140-7007. DOI: 10.1016/J.IJREFRIG.2012.12.008.

[5] ARP292. “Air Conditioning Helicopter General Requirements”. In: *SAE International* (2014). DOI: 10.4271/ARP292.

[6] F. Ascione, C. M. De Servi, O. Meijer, V. Pommé, and P. Colonna. “Assessment of an Inverse Organic Rankine cycle system for the ECS of a large rotorcraft adopting a high-speed centrifugal compressor and a low GWP refrigerant”. In: *Proceedings of the 6th International Seminar on ORC Power Systems*. Ed. by Technical University of Munich. Technical University of Munich, 2021. DOI: 10.14459/2021mp1633127.

[7] E. W. Lemmon, I. H. Bell, M. L. Huber, and M. O. McLinder. *NIST Standard Reference Database 23: Reference Fluid Thermodynamic and Transport Properties-REFPROP, Version 10.0, National Institute of Standards and Technology*. 2018. DOI: 10.18434/T4/1502528.

[8] American National Standard. *ANSI/ISA-5.1-2009, Instrumentation symbols and identification*. Tech. rep. 2009.

[9] ANSI/ASHRAE Standard 41.2-2022. *Standard methods for air velocity and airflow measurement*. 2022.

[10] DIN EN 378-2. *Refrigerating systems and heat pumps - Safety and environmental requirements - Part 2: Design, construction, testing, marking and documentation*. 2018.

[11] B. Woodland, J. Braun, E. Groll, and W. Horton. “Experimental Testing of an Organic Rankine Cycle with Scroll-Type Expander”. In: *International Refrigeration and Air Conditioning Conference* (Jan. 2012).

[12] ISO/IEC Guide 98-3:2008. *Uncertainty of measurement. Part 3: Guide to the expression of uncertainty in measurement*. 2008.

7

CONCLUSIONS AND RECOMMENDATIONS

The greatest threat to our planet is the belief that
someone else will save it.

Robert Swan

7.1. CONCLUSIONS

THE urgent demand for environmentally friendly means of transportation has spurred industry and academia to investigate electrified system solutions for the next generation of passenger aircraft. In this societal framework, the work presented in this dissertation is part of a research project whose objective is to assess a novel more sustainable technology for aircraft Environmental Control Systems (ECS). The ECS is the main consumer of non-propulsive power among the aircraft auxiliary systems, its fuel consumption reaching maximum 3% of the total, depending on the aircraft and the mission.

The driving idea of this project is that the environmental footprint of the ECS can be reduced by resorting to the electrically-driven Vapour Compression Cycle (VCC) technology as a replacement for the traditional Air Cycle Machine (ACM), as explained in Chapter 1. VCC-based ECS systems are nowadays employed only onboard helicopters and business jets. This system configuration was abandoned in case of airliners because of the large weight and limited efficiency of its main components, particularly the volumetric compressor. The latest advancements in compact heat exchangers (HEXs) and high-speed centrifugal compressor technologies offer a solution to the existing limitations, making the VCC system suitable for aircraft ECS, as outlined in Chapter 2.

The work documented in this thesis is focused on the development of a novel integrated system design method and its application to analyze the feasibility and the performance optimisation of VCC-based environmental control systems powered by a high-speed electrically-driven centrifugal compressor. One of the research objectives is also to investigate the use of alternative working fluids belonging to the category of low Global Warming Potential (GWP) refrigerants as substitutes for the state-of-the-art R-134a. The design and optimization of the aircraft ECS is a complex multi-disciplinary problem. The objective is to minimize the specific fuel consumption, defined as a linear combination of drag penalty, system weight and thermodynamic efficiency, and dependent on the aircraft operating conditions and the preliminary design of the main system components. Therefore, an integrated system optimization method has been developed to allow for the contemporary optimization of the ECS thermodynamic processes, the preliminary design of its main components and the selection of the best working fluid for different operating conditions in an automated fashion.

This method, presented in Chapter 3, has been applied to two relevant cases, whose choice was agreed with the industrial partners of the project.

The first study case is a large rotorcraft hosting 20 passengers and 2 pilots, as documented in Chapter 4. Four refrigerants belonging to the class of haloolefins have been heuristically selected and considered as working fluid for system optimization. The objective was to determine whether more efficient and lightweight systems can be designed if resorting to low-GWP haloolefins as working fluid, in place of the traditionally used R-134a. Therefore, the optimization objective functions are maximum system Coefficient Of Performance (COP) and minimum system weight. The optimization has been carried out for the operating condition of rotorcraft on the ground on a hot and humid day, indicated as the critical operating point by one of the industrial partners. The main outcomes of the research study conducted for this application are summarized as follows:

i) A novel methodology for integrated design and optimization of complex energy systems has been developed. It has been proved that it is possible to account simultaneously for system performance and the preliminary design of the main system components, i.e., HEXs, centrifugal compressor and hoses. The working fluid within the refrigeration loop can be varied to account for the effect of the refrigerant on the objective functions. Five high molecular complexity haloolefins, i.e., R-1233zd(E), R-1234ze(z), R-1224yd(Z), and R-1336mzz(Z) have been heuristically selected and successfully tested as alternatives to the R-134a.

ii) The Pareto fronts obtained from the system optimization reveal that the use of haloolefins allows for the design of high-efficiency and lightweight components. The results show that any increase in the system COP comes at the expense of heavier system components. By resorting to high-molecular complexity haloolefins, in the case of the temperature of evaporation and the VCC system cooling capacity being fixed, it is possible to enhance the system efficiency as compared to refrigerant R-134a. In particular, a characteristic of the relation between thermodynamic properties of the working fluid, i.e., the positive slope of the saturated vapour curve in the T-s chart of the fluid, explains the lower losses associated with vapour superheating along the compression process. The large latent heat of evaporation enables the reduction of the refrigerant mass flow rate within the loop. Among the selected refrigerants, R-1234ze(Z) allows to obtain a 12% increase of COP and a maximum weight reduction of 26% compared to a system employing R-134a as working fluid.

iii) The design of a twin-stage high-speed centrifugal compressor running on gas bearings is possible if haloolefins are the working fluid. The rotational speed and the total-to-total efficiency of the turbomachinery can reach the maximum values of 160 krpm and 80%, respectively. The low density of these refrigerants makes it possible to design larger flow passages and impeller wheel diameters, which overcomes the challenges associated with manufacturing miniature compressors for small-capacity systems.
The R-1336mzz(Z) refrigerant is unsuitable for the selected application. The high molecular complexity of this fluid results in an excessively low speed of sound of the flow. Therefore, the fluid-dynamic losses associated with shock interaction within the rotor flow channels lead to inefficient compressor designs.

iv) Bulkier heat transfer equipment is designed if a haloolefin is the working fluid. The low vapour density of these working fluids detrimentally affects the size of the evaporator, since a large number of minichannels is necessary to reduce the overall flow velocity inside the tubes and keep the friction losses within acceptable ranges of values. The condenser is the heaviest component of the system. It is characterized by a large frontal area on the ram air stream to limit the pressure drop in the ram air duct and reduce the ram air fan electric power demand.

The second case study, reported in Chapter 5, is that of the ECS of a single-aisle short-haul passenger aircraft, i.e., the A320. The optimization objective is the same, therefore the minimization of drag penalty, system weight and electric power consumption. The design optimization considers three operating points of the aircraft, namely ground conditions, standard flying at cruise and flying with faulty ECS pack conditions. In this case, an automated fluid selection method based on the modeling of fluid properties using the Perturbed-Chain Statistical Associating Fluid Theory (PC-SAFT) equation of state has been integrated into the optimization framework. The research objective is to demonstrate that it is possible to automatically treat the working fluid as one of the optimization variables of the system and its main components. In this way, it is possible to consider within the design optimization process refrigerants that have never been taken into account for the selected application, and whose selection is tailored to the operating conditions of the system. The main findings of this research are reported as follows:

i) The integrated design optimization framework for VCC-based aircraft ECS has been successfully extended by integrating the Continuous-Molecular Targeting to Computer-Aided Molecular Design (CoMT-CAMD) method for optimal working fluid selection. This approach is based on the use of the PC-SAFT equation of state for the estimation of the properties of the working fluid. It allows for the identification of any substance by means of its molecular describers which can be retrieved from a comprehensive database. Therefore, these molecular parameters can be included among the design variables of the system optimization problem. Using this method, starting from a database of 26 halogenated substances and 56 non-polar non-halogenated refrigerants, it was possible to identify two optimal refrigerants for the aircraft ECS, i.e., 1-butene and 1-butyne.

ii) A multi-point and multi-objective optimization of the preliminary design of aircraft ECS has been successfully performed using 1-butene and 1-butyne as the working fluid of the VCC system. The results have been compared with those obtained in the case of the benchmark case whereby the working fluid is R-134a. With the selected natural refrigerants, the optimal system designs are characterised by a lower drag penalty associated with the ram air. In the case of 1-butyne, it is possible to obtain aircraft ECS design solutions featuring lighter components and electric power consumption comparable to that of the benchmark case. Therefore, 1-butene is identified as the preferable working fluid between the two natural substances, even if its use leads to a rather small reduction in fuel weight penalty compared to the benchmark case.

iii) Optimal condenser designs are characterized by a large frontal area on the ram air side to minimize the drag penalty and the ram air fan power demand. The size of the evaporator depends on friction losses caused by the refrigerant flowing through channels. The optimal evaporator design must comply with the pressure drop specification also when the system operates in off-design conditions leading to low evaporation temperature, i.e., cruise conditions. In these cases, the flow density reduces and more tubes are required to limit the flow velocity. In particular, in the case of 1-butyne, since the flow density and the refrigerant mass flow rate are lower compared to 1-butene, the evaporator is thus bulkier.

iv) In the case of 1-butene and 1-butyne, the calculated total-to-total efficiency of the centrifugal compressor is ten percentage points lower than that estimated if R-134a is the working fluid. The thermodynamic properties of the natural refrigerants lead to a low mass flow rate within the VCC system and high compression ratios. Consequently, optimal compressor designs are characterized by small wheel dimensions and high rotational speed, which negatively affect the performance.

As part of this research project, a novel experimental setup called Inverse organic Rankine cycle Integrated System (IRIS) was realized and commissioned at the Propulsion & Power Laboratories of the TU Delft Aerospace Engineering faculty. The IRIS setup implements a single-stage compression refrigeration cycle. For the commissioning, an off-the-shelf volumetric compressor was selected to limit the risks of initial operation. Soon this compressor will be substituted with a high-speed centrifugal compressor.

This facility has been conceived to validate *in-house* system and components models and the novel design methods developed within the project. The results of the numerical analysis presented in this dissertation demonstrate that the latest technological advancements in high-speed compressor and compact heat exchanger technologies allow in principle to overcome the limitations associated with adoption of the VCC configuration for aircraft cabin cooling. For the purpose of providing experimental evidence, the IRIS setup was designed to comprise two independent test sections, one for electrically-driven compressor testing and another for evaluating the aerothermal performance of an air-cooled condenser. Another important characteristic of this setup is that the working fluid is next-generation refrigerant R-1233zd(E). The system was designed for a cooling capacity of 15.5 kW, which corresponds to the typical demand of the ECS of the large helicopter selected as a well-assessed test case. A detailed description of the equipment, the control system, and the operating procedures of the IRIS is provided in Chapter 6. The IRIS setup was successfully commissioned and all relevant data were acquired during steady-state operation at the design operating point, as well as during the start-up and shut-down procedures. The main outcomes from these first experimental tests are:

i) The IRIS setup can be continuously operated in steady-state conditions meeting the design specifications of the refrigerant loop. In particular, the design values of pressure at the inlet of both the compressor and condenser, respectively equal to 0.08 bar(g) and 3.48 bar(g), were successfully reached. Because of equipment limitations, it was necessary to adjust the operating conditions of both the heating and cooling loops from the design conditions to achieve the design values of temperature and pressure within the refrigerant loop.

ii) The pressure drop associated with the refrigerant flow through the heat exchangers channel is underestimated by the numerical models. The outcome of the experimental test shows that, in the case of the condenser, the measured refrigerant pressure drop is 15 times higher than the calculated design value. The numerical model of the experimental facility used for the design of the system neglects the presence of the long hose connecting the compressor outlet port to the condenser inlet section. The experimental results show that the omission of this component from the system model is a limitation since the measured pressure drop associated with the pipe is equal to 0.25 bar, thus it is not negligible.

iii) To maintain the desired condensation pressure and compensate for any pressure losses within the hose that connects the compressor and the condenser, the flow downstream of the compressor needs to reach a higher pressure. Therefore, the mechanical power transferred to the fluid by the compressor, equal to 4.75 kW, is larger by 9% if compared to the design value. Despite this difference, the system performance is not negatively affected. The cooling duty of the IRIS setup is estimated to be equal to 17.88 kW, which is 15% larger than the design value. Therefore, the calculated system COP is 4% higher if compared to the benchmark design condition.

7.2. LIMITATIONS AND RECOMMENDATIONS

The limitations of this study are discussed together with recommendations for further research as follows.

i) The models of the components of aircraft ECS used for the simulations were developed using the Modelica language. However, in the case of steady-state simulations, the complexity of the system model can cause numerical problems during the model initialization, thus compromising the successful convergence of the simulation. In the case of system optimization, it is difficult to choose the correct set of initial conditions for each set of design variables. This represents a limiting aspect of this optimization method since the design space of the solutions could be narrower than the real one. Convergence properties and robustness of the numerical solution procedure have been achieved by decoupling the procedure to optimize the design of some components from that of the entire system. For example, it was proven that utilizing a data-driven model of the compressor in place of the detailed physics-based model reduces not only the computational costs, but it also improves the robustness and stability of the solver (see Chapter 3). The same approach could be adopted also for the design of HEXs. In this way, the Modelica model of the system can be simplified by replacing the detailed physics-based models of the heat exchangers with data-driven models featuring as input variables only the effectiveness and the pressure drop calculated with the surrogate models. The complexity of the set of equations describing the ECS model would be reduced, the accuracy of the results would not be compromised and the computational cost of simulations and therefore of the entire design opimization would be much lower.

ii) The CoMT-CAMD method described in Chapter 5 for the selection of the optimal refrigerant was integrated into a simplified framework for VCC systems optimization. This method does not account for the effect of the working fluid on components sizing, thus limiting the validity of the results. Future code improvements should include the procedures for the preliminary design of the heat exchangers. Alternatively, a tailored interface between the software used for the calculation of the thermodynamic and transport properties of the working fluid and the Modelica executable could allow for the use of the PC-SAFT equation of state for the optimization of the pseudo-fluid when executing simulations of the Modelica model of the system.

iii) The refrigerant optimization, documented in Chapter 5, relies on the database of molecular describers of only two classes of pure fluids: a few halogenated substances and non-polar non-halogenated compounds. However, additional suitable solutions could be identified if the design space would also include polar non-halogenated refrigerants. As stated in the conclusions of Chapter 5, natural refrigerants feature good thermodynamic properties and they are an attractive option for small-capacity refrigeration systems. However, their use for VCC-based aircraft ECS may be limited due to safety concerns related to their high flammability. Therefore, in future research, the CoMT-CAMD method could be applied to model blends of haloolefins and natural refrigerants to identify working fluids offering a good balance between low flammability and the possibility of achieving good thermodynamic efficiency.

iv) The numerical models of the heat exchangers described in Chapter 3 include a set of semi-empirical correlations to estimate the pressure drop and the heat transfer coefficient of the refrigerant flow. However, some of these correlations are valid only for specific classes of working fluid. Future research on blends or natural refrigerants should better evaluate the validity of the current correlations and, if possible, improve them. A similar limitation affects the semi-empirical equations used to compute the fluid-dynamic losses affecting the channels of the centrifugal compressor.

v) Experimental campaigns are planned to characterize the validated system and component models using measurements performed with the data acquisition system of the IRIS setup, both in design and off-design conditions.The volumetric compressor currently installed in the setup was designed for the refrigerant R-1234ze(E) as working fluid. One of the research objectives is to assess the performance map of the electrically-driven compressor operating with R-1233zd(E). However, this is only possible if measurements of the refrigerant mass flow rate are available, therefore a clamp-on ultrasonic flow meter downstream of the condenser will be installed. This sensor allows for non-intrusive measurements of the liquid volumetric flow rate.

vi) The air-cooled condenser test section of the IRIS setup should be equipped with additional instruments if the research objective is to characterise the aerothermal performance of heat exchanger. As discussed in Chapter 2, the demand for lightweight and efficient thermal management devices is paving the way for the development of additive-manufactured HEXs with complex fin and channel geometries. Significant efforts are being made to develop numerical models, but their validation is limited due to the lack of experimental data. In this framework, the cooling loop of the IRIS setup is a suitable test bed for the characterization of different kinds of air-cooled HEXs. For this purpose, additional instrumentation would be needed. First, thermocouple rakes will be installed upstream and downstream of the HEX to analyse the temperature profile of the flow, and to investigate the effect of the fins geometry and of the HEX material on the efficiency of the heat transfer. In addition, a rake of Pitot probes upstream and downstream of the condenser in correspondence with the cross-section of the device would allow retrieving the velocity profile of the flow. These data would be useful essential to validate the results of the CFD simulations. Furthermore, testing different HEXs topologies, possibly also with different tilt angles, would be a valuable contribution to the development of novel correlations for the heat transfer coefficient and the friction factor prediction.

vii) Relevant research can be done by evaluating the effect of using different low-GWP haloolefins or natural refrigerants as the working fluid of the IRIS setup. However, possible technological limitations must be taken into account. Unless the novel refrigerant is considered as a drop-in replacement of the current working fluid, the design of the IRIS setup should be adapted. Significant attention points are the pressure and temperature levels of operation, and the compatibility of the novel fluid with the existing hardware and sealing materials. Furthermore, in the case of flammable refrigerants, safety regulations impose the addition of a ventilation system and the certification that the volume occupied by the IRIS setup is an ATEX zone.

viii) The research plan includes the modification of the IRIS setup described in this dissertation to replace the volumetric compressor with a high-speed centrifugal compressor. However, some limiting aspects need to be considered. During the start-up phase of the refrigerant loop, several oscillations of the flow pressure at the inlet section of the compressor were recorded during the commissioning phase. In the case of a centrifugal compressor, these oscillations can cause surge and component failure. Therefore, an anti-surge control loop must be added to the refrigerant loop. In this regard, the development of a dynamic numerical model of the IRIS setup would be a useful tool for the preliminary design of the control loop. The volumetric compressor currently installed in the loop is oil-lubricated, and traces of oil mixed with the refrigerant could be present in the piping and other components of the loop. In the case of the centrifugal compressor, any residual oil that impinges on the compressor blades could gravely damage the rotor. To enable the safe operation of the IRIS setup, all the hardware installed in the refrigerant loop must be properly cleaned, or, if not possible, substituted before installing the turbomachine.

ix) During the commissioning of the IRIS setup, some limitations of the existing hardware were identified. In particular, during the operation of the heating loop, it was not possible to obtain that the temperature of the hot water at the outlet of the tank remains constant. Over time, the fluid temperature started decreasing and, even if the electric heater of the loop turns on, the thermal inertia of the water in the tank is too high to allow for a sufficiently quick increase of the temperature. To overcome this problem, a recirculation pump could be installed to mix the water and to make the temperature of the fluid stored in the tank more uniform. Alternatively, both the heater and the tank could be replaced with a tank equipped with an internal heater to ensure uniform and efficient heating of the liquid in the tank given a set point temperature value at the outlet of the tank. Furthermore, during the commissioning of the IRIS setup, it was observed that in the cooling loop, the maximum temperature of the air entering the condenser is limited because of the overheating of the internal elements of the electric heater. This is especially critical during very cold days, when the ambient air temperature is low. A possible solution could be to replace the heater with another model allowing to achieve higher air temperature.

x) As discussed in Chapter 6, during the operation of the IRIS setup, the prescribed pressure of condensation of the refrigerant loop was reached by manually selecting the optimal air mass flow rate of the cooling loop, while regulating the inlet air temperature so that it remains constant. This method can be improved by including an additional control loop that regulates the airflow inlet temperature and the mass flow rate simultaneously for a fixed set point value of condensation pressure. In this way, the two loops would be easily interconnected, and manual tuning would no longer be necessary.

A

PSEUDO-FLUID THERMODYNAMIC MODELLING

A.1. LIST OF FLUIDS

List of halogenated substances (Tab. A.1), and non-polar non-halogenated medium (Tab. A.2) used as databases for the *pseudo-fluid* properties calculation.

Table A.1.: Database of halogenated substances used for the CoMT-CAMD method.

Fluid name	Segment number	Segment diameter	Segment energy parameter
R-11	2.34	3.66	244.68
R-113	2.83	3.74	233.01
R-115	2.76	3.50	170.88
R-116	2.85	3.31	139.14
R-12	2.28	3.53	202.81
R-1224yd(Z)	**3.23**	**3.40**	**194.93**
R-123	2.99	3.48	214.04
R-124	**3.05**	**3.32**	**183.50**
R-125	3.10	3.13	156.89
R-1233xf	2.55	3.66	221.09
R-13	2.22	3.35	160.78
R-1336mzz(E)	3.86	3.31	170.93
R-134a	3.49	2.93	164.26
R-14	2.25	3.11	120.36
R-143a	2.67	3.21	173.01
R-152a	**2.72**	**3.10**	**192.12**
R-218	3.43	3.41	151.14
R-22	**2.55**	**3.11**	**185.47**
R-23	2.96	2.74	140.91
RC318	3.67	3.39	166.18
Hexafluorobenzene	3.77	3.40	221.84
Perfluorobutane	3.73	3.56	164.60
Perfluorocyclohexane	3.79	3.79	193.67
Perfluorotoluene	4.38	3.46	216.71
Perfluoropentane	4.17	3.65	172.00
Titaniumtetrachloride	2.41	3.99	332.70

Table A.2.: Database of non-polar non-halogenated substances used for the CoMT-CAMD method.

Fluid name	Segment number	Segment diameter	Segment energy parameter
1-butene	**2.29**	**3.64**	**222.00**
1-butyne	**2.77**	**3.29**	**212.72**
1-pentene	2.60	3.74	231.99
11-dimethylcyclohexane	2.72	4.16	290.06
11-dimethylcyclopentane	2.79	3.95	264.12
12-dichloroethane	2.60	3.45	285.01
13-butadiene	**2.23**	**3.59**	**228.60**
Benzene	2.46	3.65	287.35
Biphenyl	3.93	3.77	323.23
Butane	2.33	3.71	222.88
Butylbenzene	3.77	3.87	283.07
Carbondioxide	1.51	3.19	163.33
Chlorobenzene	2.65	3.75	315.04
Cyclobutene	**2.13**	**3.60**	**251.90**
Cycloheptane	2.69	3.93	296.29
Cyclohexane	2.53	3.85	278.11
Cyclooctane	2.88	4.01	307.03
Cyclopentane	**2.36**	**3.71**	**265.83**
Cyclopropane	1.87	3.46	231.17
Decane	4.66	3.84	243.87
DEPEG	8.05	3.59	254.28
DiEGDME	4.72	3.43	240.54
Diethylether	**2.97**	**3.51**	**220.09**
Dimethylcarbonate	3.26	3.24	254.14
Dimethylether	**2.31**	**3.25**	**211.06**
Diphenylether	3.78	3.92	332.20
Dodecane	5.31	3.90	249.21
Ethane	1.61	3.52	191.42
Ethene	1.54	3.45	179.37
Ethylbenzene	3.08	3.80	287.35
Ethyne	2.49	2.76	156.17
Heptane	3.48	3.80	238.40
Hexadecane	6.65	3.95	254.70
Hexane	3.06	3.80	236.77
Isobutane	2.26	3.76	216.53
Isooctane	3.14	4.09	249.77
Isopentane	2.56	3.83	230.75
Methane	1.00	3.70	150.03
Methylcyclohexane	2.66	4.00	282.33
Methylcyclopentane	2.61	3.82	265.12
MonoEGDME	3.59	3.35	233.15
m-xylene	3.19	3.76	283.98
Neopentane	2.35	3.95	225.69
Nonane	4.21	3.84	244.51
Octane	3.82	3.84	242.78
o-xylene	3.14	3.76	291.05
p-xylene	3.17	3.78	283.77
PentaEGDME	7.89	3.58	253.93
Pentane	2.69	3.77	231.20
Propane	**2.00**	**3.62**	**208.11**
Propene	1.96	3.54	207.19
Propyne	**2.43**	**3.13**	**207.63**
TetraEGDME	6.82	3.55	250.72
TriEGDME	5.74	3.51	247.93
Toluene	2.81	3.72	285.69
Undecane	4.91	3.89	248.82

A.2. MOLAR MASS PREDICTION

The molar mass M has been predicted using the Quantitative Structure-Property Relationship (QSPR) method, particularly the Eqn. 5.1. The procedure has been iterated twice, once for the halogenated fluids and once for the non-halogenated ones. The coefficients of the fitting are reported in Tab. A.3.

Table A.3.: Values of the coefficients used in the QSPR method to calculate the molar mass M for the halogenated and the non-halogenated fluids. Note that the coefficient β_4 of Eqn. 5.1 is omitted since the method treats all the substances as non-polar ($\mu = 0$).

QSPR coefficients	**Halogenated**	**Non-halogenated**
β_1	$-11.779 \cdot 10^{-2}$	$9.7266 \cdot 10^{-2}$
β_2	$1.79975 \cdot 10^{-2}$	$-5.258 \cdot 10^{-2}$
β_3	$8.36 \cdot 10^{-5}$	$7.38 \cdot 10^{-4}$

Figure A.1 shows the comparison between the values of M taken from a well-assessed database [1] and the ones obtained using the QSPR model for both groups of fluids.

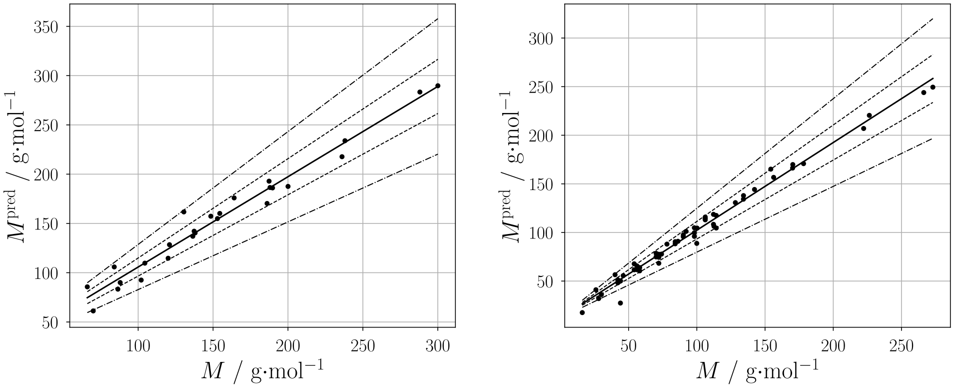

(a) (b)

Figure A.1.: Comparison of the predicted values of molar mass to the values corresponding to the real fluid for the case of (a) halogenated and (b) non-halogenated substances. (—) linear data fitting, (- -) ±10% deviation; (-·) ±25% deviation.

A.3. ISOBARIC HEAT CAPACITY PREDICTION

For both halogenated and non-halogenated fluids, the isobaric heat capacity (c_p^{ig}) has been predicted for three temperature levels, e.g., 200 K, 300 K, and 400 K. The temperature levels comply with the temperature range of operation of the VCC system for aircraft ECS.

Table A.4 lists the values of the coefficient used in Eqn. 5.2 to predict c_p^{ig} using the QSPR method for the group of halogenated fluids. Figure A.2 shows the comparison between the real and the predicted values of c_p^{ig} for the three selected temperature values in the case of halogenated fluids.

Table A.4.: Values of the coefficients used in the QSPR method to calculate the isobaric heat capacity c_p^{ig} for halogenated fluids for three different temperature levels.

Halogenated fluids			
QSPR coefficient	$T = 200\,\mathrm{K}$	$T = 300\,\mathrm{K}$	$T = 400\,\mathrm{K}$
γ_0	$-7.82{\cdot}10^4$	$-5.53{\cdot}10^4$	$-7.33{\cdot}10^4$
γ_1	$2.22{\cdot}10^4$	$1.98{\cdot}10^4$	$3.56{\cdot}10^4$
γ_2	$1.26{\cdot}10^3$	$1.73{\cdot}10^3$	$2.17{\cdot}10^3$
γ_3	$-2.80{\cdot}10^2$	$-1.04{\cdot}10^3$	$-1.87{\cdot}10^3$

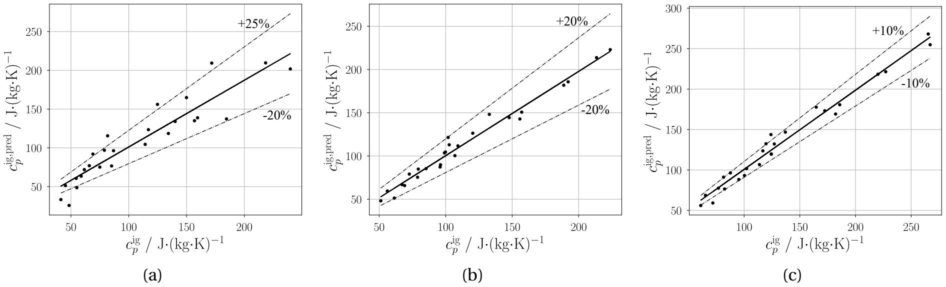

Figure A.2.: Comparison of the predicted values of isobaric heat capacity to the values corresponding to the real fluid for the case of halogenated fluids for (a) $T = 200\,\mathrm{K}$, (b) $T = 300\,\mathrm{K}$, and (c) $T = 400\,\mathrm{K}$.

Table A.5 lists the values of the coefficient used in Eqn. 5.2 to predict c_p^{ig} using the QSPR method for the group of non-halogenated fluids. Figure A.3 shows the comparison between the real and the predicted values of c_p^{ig} for the three selected temperature values in the case of non-halogenated fluids.

Table A.5.: Values of the coefficients used in the QSPR method to calculate the isobaric heat capacity c_p^{ig} for non-halogenated fluids for three different temperature levels.

Non-halogenated fluids			
QSPR coefficient	$T = 200\,\mathrm{K}$	$T = 300\,\mathrm{K}$	$T = 400\,\mathrm{K}$
γ_0	$-9.057{\cdot}10^4$	$-6.50{\cdot}10^4$	$-3.26{\cdot}10^4$
γ_1	$43.69{\cdot}10^3$	$32{\cdot}10^3$	$7.57{\cdot}10^3$
γ_2	$1.43{\cdot}10^3$	$1.59{\cdot}10^3$	$1.54{\cdot}10^3$
γ_3	$-8.26{\cdot}10^2$	$-8.68{\cdot}10^2$	$-3.54{\cdot}10^2$

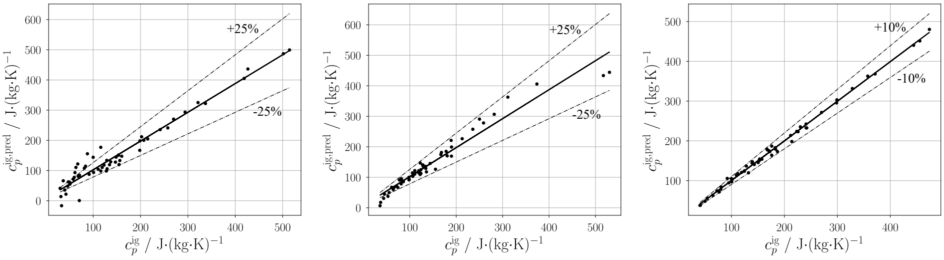

(a)

(b)

(c)

Figure A.3.: Comparison of the predicted values of isobaric heat capacity to the values corresponding to the real fluid for the case of non-halogenated fluids for (a) $T = 200\,\mathrm{K}$, (b) $T = 300\,\mathrm{K}$, and (c) $T = 400\,\mathrm{K}$.

ACKNOWLEDGEMENTS

This journey as a Ph.D. candidate would not have been possible without the support of many people.

First, my deepest gratitude goes to Prof. Piero Colonna for his unwavering support and positivity. Thank you for the technical guidance and all the tips that helped me grow as a researcher. I am grateful to my supervisor, Dr. Carlo De Servi, for his technical and moral support during this journey and for the many hours spent debugging Modelica codes. Special thanks to Dr. Matteo Pini for the many personal and professional conversations we had.

This Ph.D. journey made me feel part of a team, and I want to thank two special people. My colleague and friend, Dr. Andrea Giuffrè, with whom I shared long hours of debugging codes and writing papers. I have learned a lot from you and wish you all the success in your life and career. Thank you to Dr. Adam Head for the countless hours spent on the realization and commissioning of the IRIS project. Your positivity was a great support during challenging times.

Words cannot express my gratitude to my parents. You have always been examples of hard work and discipline, qualities that have rewarded me during these years. You taught me how to be an independent and determined woman and, most importantly, to accept my limits. Thank you to my brother, Fabrizio, you had to act as the big brother so many times, offering careful advice and moments of confidence. You are full of talent, I am convinced you have a bright future ahead.

These years took away one of the most important people in my family, my aunt, to whom I dedicate this dissertation. Once she told me that things are worth pursuing only if your heart makes you consider them important. This has been my strongest motivation in moments of low spirits. I hope I have made my grandma proud in the first time she attends a Ph.D. defence. Thank you to Rosanna, all my aunts, uncles, and cousins for sharing in the successes of my life thus far.

A huge thank you to all the people I have met in the department over the years. Special thanks to all the office mates of room 6.20. Thank you to Evert for helping me correct my Dutch skills. Thank you to Fabio, Lorenzo, Matteo, Alessandro, all the Francescos, Hugo, and Rishikesh for the hours, sometimes noisy, we spent together. A special thank you to Nitish, the first person I met when I arrived here, for our special personal conversations. I wish you a brilliant future. Thank you to Ale Porc. for always cheering up the atmosphere and sharing all the faculty gossip. Thank you to Gioele, the messiest and sweetest friend I got here, for all the special adventures we had together, from complaining at the university to go-karting, sailing, and surfing together.

Thank you to my two favourite ladies, Rosie and Giovanna. I could not believe that, in this jungle of males, I would meet these two beauties. Thank you for all the chats, confidence, gossip, nights of Netflix series, shopping, and laughs. Thank you for being here by my side today.

Last but not least, thank you to Davide, my favourite doctor, cook and fisherman. Thank you for being, first of all, a careful and sincere friend. Your lovely advice, crazy ideas, and unstoppable way of being special made many days special even when least expected.

Thank you to my friend Teresa; distance is never enough for true friends. Thank you to Daniela; without your initial advice, all this would not have been possible.

RINGRAZIAMENTI

Questa esperienza da dottoranda non sarebbe stata possible senza il supporto di tante persone. Innanzitutto, la mia piú profound gratitude va al Prof. Piero Colonna per il suo instancabile supporto e la sua positivitá. Grazie per la guida professionale e per i consigli che mi hanno aiutata a crescere come ricercatrice. Ringrazio il mio supervisore, Dr. Carlo De Servi, per il supporto tecnico e morale durante questi anni e per le numerose ore passate insieme a debuggare codici in Modelica. Uno speciale ringraziamento a Dr. Matteo Pini per le nostre conversazioni professional e non.

Questa esperienza mi ha fatto sentire davvero parte di un gruppo di ricerca, per questo vorrei ringraziare due persone speciali. Il mio collega e amico, Dr. Andrea Giuffré, col quale ho condiviso lunghe sessioni di debugging e di stesura di articoli di ricerca. Ho imparato molto da te e ti auguro il meglio per la tua vita e la tua carriera professionale. Grazie al Dr. Adam Head per le innumerevoli ore passate in laboratorio per la realizzazione del progetto dell'IRIS. La tua positivitá é stata di immenso supporto in momenti difficili.

Le parole non bastano per esprimere la mia gratitudine ai miei genitori. Siete stati un esempio di duro lavoro e disciplina, qualitá che mi hanno ricompensata in questi anni. Mi avete insegnato ad essere una donna independente e determinata e, soprattutto, ad accettare i miei limiti. Grazie a mio fratello, Fabrizio, che ha dovuto farmi da fratello maggiore tante volte con consigli sinceri e affettuosi. Sei un ragazzo talentuoso, sono convinta che un futuro brillante é lí ad aspettarti.

Questi anni hanno portato via una delle persone piú importanti della mia famiglia, mia zia, alla quale dedico questa tesi. Una volta mi ha detto che nella vita vale la pena impegnarsi in qualcosa soltanto se nel nostro cuore sentiamo che sia importante. Queste parole sono state la mia piú grande motivazione i tutti i momenti di scoraggiamento. Spero di ave reso mia nonna orgogliosa, che per la prima volta nella sua vita ha potuto assistere a una cerimonia di dottorato. Grazie a Rosanna, a tutte le zie, agli zii, e ai cugini per aver condiviso con me tutti i traguardi della mia vita sin'ora.

Un immenso grazie a tutte le persone che ho incontrato in questi anni in dipartimento. Un grazie speciale a tutti i colleghi dell'ufficio 6.20. Grazie a Evert per avermi aiutato con la mia scarsa conoscenza dell' Olandese, Grazie a Fabio, Lorenzo, Matteo, Alessandro, tutti i Francesco, Hugo, e Rishikesh, per le ore, talvolta rumorose, che abbiamo passato insieme. Un grazie particolare a Nitish, la prima persona che ho incontrato al mio arrivo qui, per tutte le nostre conversazioni speciali. Ti auguro un fututo brillante. Grazie ad Ale Porc. per avermi sempre risollevato il morale e per tutti i nostri pettegolezzi di facoltá. Grazie a Gioele, il piú disordinato e dolce amico che ho conosciuto qui, per tutte le nostre avventure uniche, dalle lamentele all'universitá alle uscite coi go-kart, in vela e in surf.

Grazie alle due mie ragazze preferite, Rosie e Giovanna. Non avrei mai potuto credere che, in questa giungla di uomini, avrei incontrato queste due bellezze. Grazie per tutte le confidenze, i gossip, le notti di serie Netflix, lo shopping, e le risate.

Ultimo, ma non certo per importanza, un grazie speciale a Davide, il mio dottore, cuoco e pescatore preferito. Grazie per essere, prima di tutto, un amico attento e sincero. I tuoi consigli, le tue idee stravaganti e il tuo modo instancabile di rendere tutto speciale hanno reso unici tanti giorni, anche quando meno me lo aspettavo.

Grazie alla mia amica Teresa, la distanza non é mai abbastanza per le vere amiche. Grazie a Daniela, senza il tuo incoraggiamento iniziale, tutto questo non sarebbe mai accaduto.

ABOUT THE AUTHOR

Federica Ascione was born in Scafati, Italy, on March 5th, 1995. She graduated cum laude in mechanical engineering from the University of Naples Federico II in 2018, specializing in energy systems. Her master thesis concerned the preliminary design of a novel setup for supersonic turbine cascade testing, in collaboration with the von Karman Institute for Fluid-Dynamics.

Following her graduation, she was selected as a research master student at the Von Karman Institute for Fluid-Dynamics. There, she conducted an experimental study on the aerothermal characterization of additive-manufactured heat exchangers for aerospace applications for the European funded project NATHENA. This research experience strongly motivated her to pursue a career as researcher in the field of applied thermodynamics.

In 2019, Federica joined the Propulsion & Power group at Delft University of Technology. Her research there focused on the design, optimization, and testing of a novel Environmental Control System concept for more electric aircraft, in the framework of the NEDEFA project. During her Ph.D. research, she also had the opportunity to supervise master students and interact directly with industrial stakeholders.

Currently, Federica is a post-doctoral researcher involved in the European funded project HyPoTraDe, where she supports the modeling of thermal management systems for fuel cell-battery hybrid-electric powertrain architectures.

Beyond her professional interests in fluid dynamics and heat transfer, Federica is passionate about classical music and art. She loves swimming, cooking and traveling, and she enjoys spending hours exploring museums.

LIST OF PUBLICATIONS

JOURNAL ARTICLES

1. **Ascione, F.**, Galieti, L., Colonna, P., & De Servi, C. M. (2024). Multi-Point Multi-Objective Design Optimization of Aircraft ECS using PC-SAFT equation of state for working fluid selection. *International Journal of Refrigeration.* (To be submitted).

2. **Ascione, F.**, Giuffré, A., Colonna, P., & De Servi, C. M. (2024). Integrated design optimization of a novel electrically-driven helicopter ECS using low-GWP refrigerants as working fluid. *International Journal of Refrigeration.* (Submitted).

3. Giuffré, A., **Ascione, F.**, Colonna, P., & De Servi, C. M. (2024). Integrated Design Optimization of Environmental Control Systems for Next-Generation Aircraft. *Journal of Aircraft.* (Submitted).

4. **Ascione, F.**, Colonna, P., & De Servi, C. M. (2024). Integrated design optimization method for novel vapour-compression-cycle-based environmental control systems. *Applied Thermal Engineering, 236*, 121261. DOI: 0.1016/j.applthermaleng.2023.121261.

5. Giuffré, A., **Ascione, F.**, De Servi, C., & Pini, M. (2023). Data-driven modeling of high-speed centrifugal compressors for aircraft Environmental Control Systems. *International Journal of Refrigeration, 151*, 354-369. DOI: 10.1016/j.ijrefrig.2023.03.019.

CONFERENCE PROCEEDINGS

1. **Ascione, F.**, Head, A. J., Colonna, P., & De Servi, C. M. (2024). Design and commissioning of the IRIS: a setup for aircraft vapour compression cycle-based Environmental Control System testing. In *Proceedings of the ASME Turbo Expo 2024: Turbomachinery Technical Conference and Exposition. Volume 5: Cycle Innovations.* London, United Kingdom. June 24–28, 2024. V005T06A006. ASME. DOI: 10.1115/GT2024-123714.

2. Giuffré, A., **Ascione, F.**, De Servi, C. M., & Pini, M. (2022). Data-driven modeling of high-speed centrifugal compressors for aircraft Environmental Control Systems In *Proceedings of the Global Propulsion and Power Society.*

3. **Ascione, F.**, De Servi, C. M., Meijer, O., Pommé, V., & Colonna, P. (2021). Assessment of an inverse organic Rankine cycle system for the ECS of a large rotorcraft adopting a high-speed centrifugal compressor and a low GWP refrigerant. In *Proceedings of the 6th International Seminar on ORC Power Systems.* DOI: 10.14459/2021mp1633127.

4. **Ascione, F.**, Conrozier, A., Sakly, A., Planquart, P., Hugo, J. M., & Laboureur, D. (2020). Aerothermal characterization of a compact heat exchanger element by additive manufacturing. In *Proceedings of the Aerospace Europe Conference 2020.*